Effect of host anion or cation substitution on the luminescence and stability of lanthanum oxide based phosphors doped with bismuth

by

Babiker Mohammed Jaffar Jabraldar

MSc

A thesis submitted in fulfilment of the requirements for the

Doctor of Philosophy majoring in Physics

in the

Faculty of Natural and Agricultural Sciences

Department of Physics

at the

University of the Free State

Republic of South Africa

Supervisor: Prof. R. E. Kroon

Co-supervisor: Prof. H. C. Swart

Co-supervisor: Prof. Hassan Abdel Halim Abdallah Seed Ahmed

January 2022

Dedication

I dedicate this work to my lovely wife: Abeer Abdalrheem Salim Ahmed; for her endless love, support and encouragement.

To my father and mother; for their support, encouragement, and constant love have sustained me throughout my life.

To my brothers and sisters; for their respect and appreciation.

To all people who were suffering to create peace in my country and the world.

Declaration

I declare that this thesis is my own and that it has not been submitted before for any degree or examination in any other University.

Babiker Mohammed Jaffar Jabraldar

Signature: Date

Acknowledgements

I would like to thank the following individuals and institutions:

❖ My supervisor Prof R.E. Kroon who has supported me throughout my thesis with his patience and knowledge.

❖ Special thanks goes to Prof. H.C. Swart for giving me this opportunity to be part of the Department of Physics family and for his guidance and professional suggestions throughout this thesis as my co-supervisor.

❖ My co-supervisor Prof. Hassan Seed Ahmed for all his support and assistance.

❖ Prof. A. Yousif for being my co-supervisor and assisting me with all the chemistry involved in my project.

❖ Prof Liza Coetzee for measuring XPS and Auger spectra and SEM images.

❖ Dr. Emad Hasabeldaim for assistance with CL and AES measurements.

❖ Mr. Lucas Erasmus for his assistance in doing PLD thin films and PL measurements.

❖ Mrs. Hanlie Grobler, Mrs. Nonkululeko Phili-Mgobhozi, and Mr. E. Lee of the UFS Centre of Microscopy for their assistance in SEM, EDS and CL measurements.

❖ The phosphor group at the University of the Free State for their good discussions.

❖ For all my brothers and sisters from Sudan who are in Bloemfontein of always being together.

❖ Special thanks to Dr. Mohammed Abdul Aziz and his family (his wife Sarah and his kids Fatima and Tasneem) for their assistance.

❖ I thank my colleague Dr. Anwar Elbushra and his wife Sarah for their assistance.

❖ Special thanks to my lovely family, my parents for their support, encouragement, love and constant assistance throughout my life, to my sisters and brothers for their respect, appreciation, encouragement and constant love.

❖ My deep thanks and gratitude goes to the African Laser Centre (ALC) for their financial support.

ABSTRACT

LaOCl:Bi^{3+} phosphor powders were successfully prepared via the solid-state reaction method and compared to LaOBr:Bi^{3+}. Photoluminescence measurements revealed that the phosphors displayed ultraviolet emission around 344 nm for LaOCl:Bi and 358 nm for LaOBr:Bi under excitations of 266 nm and 273 nm, respectively. The optimum Bi doping concentration and annealing temperature were established as 0.7 mol% and 900 °C for both hosts. The scanning electron microscopy data showed that the particles are randomly oriented flat thin plates with diameters close to or larger than 100 nm. The chemical composition of the phosphor was studied by using energy dispersive X-ray spectroscopy, while diffuse reflectance spectroscopy was employed to study the absorption. The ultraviolet emission peaks were assigned to the $^3P_1 \rightarrow {}^1S_0$ transition of the Bi^{3+} ions, while additional relatively weak emissions in the visible range were attributed to Bi clustering. LaOCl:Bi was found to undergo a little degradation while exposed to the atmosphere for several months, while LaOBr:Bi was significantly less stable. The LaOBr:Bi phosphor was also found to degrade rapidly under 254 nm ultraviolet excitation, while LaOCl:Bi did not degrade under the same conditions. X-ray photoelectron spectroscopy measurements indicated that similar surface changes occurred for both samples during UV-exposure, suggesting that the cause of degradation is not primarily related to surface changes, but may be due to the greater probability of forming non-radiative defects in the bulk of LaOBr having the smaller bandgap.

Luminescence properties of bismuth (Bi) doped lanthanum oxyfluoride (LaOF) were investigated experimentally with samples prepared via the solid-state reaction method using ammonium fluoride, lanthanum oxide and bismuth oxide as precursors. Energy dispersive X-ray spectroscopy data showed that the samples were not completely stoichiometric and that the F/O ratio decreased with increasing synthesis temperature. The X-ray diffraction data confirmed that the phosphor powder crystallized in the tetragonal structure for lower synthesis temperatures up to 1000 °C. When prepared at 1100 °C, the LaOF took the rhombohedral form which showed almost no luminescence when doped with Bi. Therefore the investigation focussed on the tetragonal phase of LaOF for which scanning electron microscopy data showed that the shape of the particles did not change when it was doped with Bi. A single broad white luminescence emission band centred at 518 nm was observed by exciting the phosphor at 263 nm. The optimum Bi doping concentration was found to be $La_{1-x}OF:Bi_{x=0.005}$. This sample was stable when exposed to the atmosphere for up

to six months, although its luminescence degraded slowly under a 254 nm ultraviolet lamp. XPS data confirmed that the annealing at 1100 °C and exposure of the sample to UV radiation result in segregation of the Bi^{3+} on the surface of the sample.

Bi^{3+} doped LaOCl and LaOF phosphor thin films were successfully prepared via the pulsed laser deposition technique in vacuum and different Argon (Ar) pressures. All peaks of the XRD patterns of the films were consistent with the tetragonal structure of the LaOCl and LaOF, but in the case of LaOF the signal was weaker and not all peaks were present, suggesting some preferred orientation. The elemental composition of the films were studied by using energy dispersive X-ray spectroscopy, while plan-view and cross-sectional scanning electron microscopy was used to study the morphology of the films. Photoluminescence measurements revealed that the films exhibited emission around 344 nm for LaOCl:Bi and 518 nm for LaOF:Bi under excitations of 266 nm and 263 nm, respectively. The emission peaks were attributed to the $^3P_1 \rightarrow {}^1S_0$ transition of the Bi^{3+} ions. The luminescence from the LaOF:Bi sample was less intense compared to the LaOCl:Bi sample prepared under the same conditions, which was also the case for powder samples. The amount of ablated material present on the substrate was much less for LaOF:Bi compared to LaOCl:Bi, which is attributed to the greater bandgap and hence weaker absorption of the laser pulses for LaOF:Bi.

$La_{2-y}Y_yO_3$ phosphor powders were prepared via the citric acid sol-gel combustion method and their stability was checked after four months of storage in the atmosphere using X-ray diffraction. The material, like La_2O_3, was prone to hydroxylation unless a high proportion of Y was added, which also caused changes in the phases present. Based on its stability and single phase (cubic), the composition $La_{0.5}Y_{1.5}O_3$ was selected for further study with Bi doping. Under an excitation of 333 nm the phosphor presented two emission peaks located at 424 and 529 nm. This corresponded to excitation of Bi^{3+} ions in the non-centrosymmetric C_2 symmetry sites. Blue (424 nm) emission could be excited from the same samples when excited at 371 nm from Bi^{3+} ions on the centrosymmetric S_6 sites, which was similar in colour to the emission of Bi-doped La_2O_3. The optimum doping concentration for $La_{0.5-x}Y_{1.5}O_3$:Bi powder was found to be x = 0.005. The luminescence from this material was not as intense as that from $Y_{2-x}O_3$:$Bi_{x=0.005}$, but there was a significant shift in colour as a result of the added La which meant that emission from the Bi^{3+} ions at the S_6 sites of the alloy was close to that of unstable La_2O_3 on the colour chart.

Bismuth (Bi^{3+}) doped lanthanum gallate ($LaGaO_3$) phosphor powder and thin films were successfully synthesised via the citric acid sol-gel combustion synthesis and pulsed laser deposition (PLD), respectively. Firstly the stability of $La_{2-y}Ga_yO_3$ powders under ambient conditions was assessed. The optical properties of $La_{1-x}GaO_3:Bi_x$ phosphor powders were then investigated. X-ray diffraction data confirmed that the structure of $LaGaO_3$ belong to the orthorhombic perovskite structure with *Pbnm* space group, while diffuse reflectance spectroscopy data showed that the band gap energy of the $LaGaO_3$ host was 4.65 eV. Scanning electron microscopy data showed that the grain size increased with increasing annealing temperature. There was no change in the particle size and morphology when dopant was added to the host. Photoluminescence (PL) and cathodoluminescence (CL) measurements indicated that the phosphor presented efficient ultraviolet emission around 370 nm, which was attributed to transitions between the $^3P_1$ excited state and $^1S_0$ ground state of the Bi^{3+} ions. The optimum Bi doping concentration and annealing conditions for photoluminescence were found to be for $La_{1-x}GaO_3:Bi_{x=0.003}$ and 1200 °C. Thin films of the optimized powder were prepared via PLD. The PL and CL of the $LaGaO_3:Bi^{3+}$ thin films were similar to the powder.

Keywords

LaOCl; LaOBr; LaOF; $LaGaO_3$; $LaYO_3$; Bi^{3+} ions; Photoluminescence; Stability; Cathodoluminescence; PL Degradation

Acronyms

CL	Cathodoluminescence
CRTs	Cathode ray tubes
DRS	Diffuse reflectance spectroscopy
EDS	Energy dispersive spectroscopy
ESCA	Electron spectroscopy for chemical analysis
FEDs	Field emissive displays
FWHM	Full width at half maximum
JCPDS	Joint Committee on Powder Diffraction Standards
LCDs	Liquid crystal displays
LEDs	Light emitting diodes
MMCT	Metal to metal charge transfer
PL	Photoluminescence.
SEM	Scanning electron microscopy.
UV-vis	Ultraviolet-visible
XRD	X-ray diffraction.

Table of Contents

Chapter three

Preparation methods of phosphors

Chapter four

Theory of characterization techniques

Chapter five

Comparative study of the photoluminescence and cathodoluminescence of Bi doped LaOCl and LaOBr phosphor powders

Chapter six

Luminescence properties of Bi doped LaOF phosphor powder

Chapter ten

Conclusions and future work

Chapter one

General introduction

1.1. Overview

Luminescent materials, also known as phosphors, are materials that absorb energy and then emit it in the form of light in the ultraviolet, visible or infrared regions [1]. Phosphor materials have been widely applied in the field of new technology. The main applications are in light emitting diodes (LEDs), light sources (e.g. fluorescent tubes), scintillators and displays [2].

Phosphors are usually composed of a host substance with a wide band gap, activated with little quantities of impurity ions known as activators or luminescent centres, such as transition metal and/or rare-earth ions. These luminescent centres have energy levels that can be excited directly or indirectly by transferring energy. Generally, host substances must have good mechanical, optical and thermal characteristics [3]. There are several types of host materials, such as sulphides, oxides, silicates, halides, selenides, nitrides, oxyhalides or oxynitrides, etc.

In crystalline phosphors, the luminescent centres may arise from the crystalline defects such as interstitial ions and atoms or ion vacancies or from activators that were intentionally inserted into the host material. The luminescent centres which are produced from crystalline defects are known as host-crystal centres, while the luminescent centres produced from activators are called activator centres. Luminescent centres may be simple or complex. Simple luminescent centres are point defects or single activator ions, while the complex centres are pairs or clusters of defects or activator ions, often ions of different kinds [4].

Activator ions are divided into two types. The first type has energy levels that have weak interactions with the host material. Most of the rare earth ions are typical examples of this type. The low lying *f* orbitals are well shielded from their coordination environment, thus giving rise to characteristic line emission spectra from the sharp *f-f* transitions. The second type of activator ions interact strongly with the host lattice. Examples include Mn^{2+}, Eu^{2+} and Ce^{3+} ions where *d*-electrons are involved. The *d*-orbitals have a pronounced interaction with the crystalline host lattice which lifts the degeneracy and leads to distinct energy states, giving rise to broad bands in

the spectrum. The luminescence of Bi^{3+} ions is less intensively studied than the lanthanide and transition metal ions and is of the second type, although it involves *s* electrons, not *d* electrons.

A thin film is a layer of substance prepared on a substrate (usually Si, glass) ranging in thickness from a fraction of nanometres to several micrometres. Luminescence of the thin films receive much attention from both scientific and technological viewpoints. The research interest in luminescent thin films has been reflected in rapid developments in a variety of thin films applications like devices, including flat-panel displays, light sources, solar cells and integrated optics systems [5].

Phosphor materials prepared in the form of thin films have many important advantages over powder phosphors of the same composition because of their good thermal stability, good adhesion to the substrate, good luminescence properties and higher image resolution from small grains [6]. There are several deposition techniques to prepare thin films, including electro-deposition, spin coating, pulsed laser deposition (PLD), evaporation, sputtering method, spray pyrolysis, anodic growth and chemical vapour deposition [7].

The stability of luminescent materials in application conditions is an important issue to move from the laboratory to the industry level and then to general uses: phosphors used in photonic applications must be stable under photon irradiation, and for the use in field emissive displays (FEDs) must be stable under the electron beam irradiation as well.

In this research study, LaOCl, LaOBr, LaOF, $LaYO_3$ and $LaGaO_3$ powders and thin films have been studied as phosphor host lattice, all activated with Bi. Stability, structural and optical characteristics of the synthesized phosphors have been investigated experimentally using a variety of analytical techniques, including: X-ray diffraction, ultraviolet–visible spectroscopy, scanning electron microscopy, energy dispersive spectroscopy, photoluminescence spectroscopy, cathodoluminescence spectroscopy and X-ray photoelectron spectroscopy.

1.2. Problem statement

Lanthanum oxyhalide compounds LaOX (X = Cl, Br and F) have attracted some research interest because of their excellent electrical, magnetic, optical and luminescence properties [8]. In addition, LaOF has high chemical stability, low phonon energy, high refractive and high transparency in the NIR and UV-vis regions [9]. LaOX (X = Cl, Br) compounds belong to the tetragonal PbFCl-type

crystal structure with space group *P*4/*nmm* (No. 129) [10]. In both structures the La^{3+} ions with C_{4v} site symmetry are bonded with four oxygen atoms (La-O) with the same bond length and five halide atoms having two distinct La-X bond lengths [11, 12].

LaOX (X = Cl, Br and F) have already been used as a hosts material to produce phosphors emitting a variety of colours, but mainly when activated with Nd^{3+} and Yb^{3+} [13], Eu^{3+} [14] and Sm^{3+} [15], Tm^{3+} and Ho^{3+} [16]. LaOX (X = Cl, Br) have also been of some interest in the blue emission when activated with Bi^{3+} ions [17, 18], but more studies are required for LaOX (X = Cl, Br) doped with Bi. In addition, there have been no reports yet of LaOF doped with Bi.

For any phosphor to be used in an application, its stability under a particular application environment is an important consideration. Initial work showed that while La_2O_3:Bi is a promising phosphor material for blue light emission, it is unstable when exposed to the atmosphere. It changes to lanthanum hydroxide which is a poor host material and it gives little or no luminescence [19]. While this may have potential as an atmospheric exposure sensor, we wish to investigate methods to stabilize the La_2O_3 host. Initial efforts have considered replacing some O with S to form La_2O_2S:Bi, which we find to be stable but has a reduced luminescence [20]. In this work, lanthanum oxyhalide LaOX (X = Cl, Br and F) and $(La,M)_2O_3$ (M = Y and Ga) phosphor powders and thin films all doped with Bi^{3+} were prepared to compare their stability and suitability for luminescence applications. Alloying La_2O_3 with Y_2O_3 and Ga_2O_3 have been reported in the literature [21, 22]. We propose to investigate and compare these various means to stabilize La_2O_3:Bi.

For the systematic investigation, we firstly investigated the luminescent properties of LaOX (X = Cl, Br and F), $LaYO_3$ and $LaGaO_3$ activated by Bi^{3+} as phosphor powders prepared by solid state reaction method and citric acid sol-gel combustion synthesis, respectively. Then LaOX (X = Cl, F) and $LaGaO_3$ doped Bi were investigated as thin films by using the PLD technique. In order to enhance the light output from the Bi^{3+} ions, we need a systematic investigation of the crystal structure and luminescent properties of our phosphors material. The stability, luminescence properties, morphology and structure were investigated and discussed.

1.3. Research aims

The major aim of the research project is to study the effect of host anion or cation substitution on the luminescence and stability of lanthanum oxide (La_2O_3) based phosphors doped with bismuth. This goal is composed of various objectives which were addressed below:

1. To synthesize LaOX (X = Cl, Br and F) phosphor powders doped with Bi by using the solid state reaction method.
1. To prepare $LaGaO_3$ and $LaYO_3$ phosphor powders doped with Bi by using the sol-gel combustion method.
2. To study the stability of the LaOCl:Bi and LaOBr:Bi phosphor powders in the atmosphere and under UV irradiation.
3. To compare LaOCl:Bi with LaOBr:Bi in terms of its luminescence and stability in the atmosphere and when exposed to UV irradiation.
4. To study the luminescence characteristics of $LaGaO_3$:Bi and $LaYO_3$:Bi phosphor powders.
5. To study the crystal structure of the phosphors and determining the crystallite size by X-ray diffraction.
6. To study the morphology of the phosphors by scanning electron microscopy.
7. To determine the chemical composition of the phosphors by energy dispersive X-ray spectroscopy.
8. Measuring the reflectance of the phosphors and determining the band gap from this data.
9. To prepare thin films of LaOX (X = Cl and F) doped with Bi by using the PLD technique.
10. To prepare $LaGaO_3$:Bi thin films by using the PLD technique.

1.4. Thesis layout

This thesis consists of ten chapters. ***Chapter* (1)** contains a general introduction about the work and aims of the study. ***Chapter* (2)** includes background information on fundamentals of phosphors and luminescence processes. ***Chapter* (3)** gives a brief description of the experimental techniques that were used to synthesize the phosphors. ***Chapter* (4)** gives a brief theoretical description of the characterization techniques of the phosphors. ***Chapter* (5)** presents the comparative study of the photoluminescence and cathodoluminescence of Bi doped LaOCl and LaOBr phosphor powders. Luminescence properties of LaOF doped Bi phosphor powder are reported in ***chapter* (6)**. ***Chapter***

(7) presents the Bi doped LaOCl and LaOF thin films grown by pulsed laser deposition. Stability and Photoluminescence properties of $La_{0.5}Y_{1.5}O_3$ doped Bi phosphor powders are presented in ***chapter* (8)**. ***Chapter* (9)** presents the alloying La_2O_3 with Ga_2O_3 for stable Bi doped phosphor powder and pulsed laser deposited thin films. Finally, a summary of the thesis as well as future work are given in ***chapter* (10)**. The last part of the thesis presents a list of publications from this work.

1.5. References

1. A. Edgar. Luminescent Materials. In: Kasap S., Capper P. (eds) Springer Handbook of Electronic and Photonic Materials. Springer (2017) doi: 10.1007/978-3-319-48933-9_38
2. William M. Yen, Shigeo Shionoya, Hajime Yamamoto. Phosphor Handbook. 2nd Edition. CRC Press, Boca Raton, London New York (2007). ISBN: 0-8493-3564-7
3. S.R. Rotman, Wide-Gap Luminescent Materials: Theory and Application. Kluwer Academic, Dordrecht (1997). ISBN 978-1-4615-4100-4
4. Luminescence center [Online]. Available from https://encyclopedia2.thefreedictionary.com/Luminescent+Center [Accessed 11 October 2021].
5. Yang Zhangab and Jianhua Hao. Metal-ion doped luminescent thin films for optoelectronic applications. *Journal of Materials Chemistry C* 36 (2013) 5607. doi: 10.1039/c3tc31024h
6. Jong Seong Bae, Kyoo Sung Shim, Byung Kee Moon, Byung Chun Choi, Jung Hyun Jeong, Soung-soo Yi, Jung Hwan Kim. Photoluminescence characteristics of $ZnGa_2O_4$–xMx:Mn^{2+} (M=S, Se) thin film phosphors grown by pulsed laser ablation. *Thin Solid Films* 479 (2005) 238 – 244. doi: 10.1016/j.tsf.2004.11.181
7. M. R. Byeon, E. H. Chung, J. P. Kim, T. E. Hong, J. S. Jin, E. D. Jeong, J. S. Bae, Y. D. Kim, S. Park, W. T. Oh, *et al*. The effects for the deposition temperature onto the structural, compositional and optical properties of pulsed laser ablated Cu2ZnSnS4 thin films grown on soda lime glass substrates. *Thin Solid Films* 546 (2013) 387-392. doi: 10.1016/j.tsf.2013.05.032
8. U. Rambabu, A. Mathur, S. Buddhudu. Fluorescence spectra of Eu^{3+} and Tb^{3+}-doped lanthanide oxychloride powder phosphors. *Materials Chemistry and Physics* 61 (1999) 156–162. doi: 10.1016/s0254-0584(99)00122-4
9. Emille M. Rodrigues, Ernesto R. Souza, Jorge H. S. K. Monteiro, Rafael D. L. Gaspar, Italo O. Mazali and Fernando A. Sigoli. Non-stabilized europium-doped lanthanum oxyfluoride

and fluoride nanoparticles well dispersed in thin silica films. *Journal of Materials Chemistry* 22 (2012) 24109–24123. doi: 10.1039/C2JM34901A

10. Kenneth R. Kort and Sarbajit Banerjee. Shape-controlled synthesis of well-defined matlockite LnOCl (Ln: La, Ce, Gd, Dy) nanocrystals by a novel non-hydrolytic approach. *Journal of Inorganic Chemistry* 50 (2011) 5539–5544. doi: 10.1021/ic200114s

11. Jorma Hölsä, Kari Koski, Sari Makkonen, Eija Säilynoja, Hanna Rahiala. X-ray powder diffraction and vibrational spectroscopic investigation of the $LaO(Cl_{1-x}Br_x)$ solid solutions. *Journal of Alloys and Compounds* 249 (1997) 217–220. doi: 10.1016/s0925-8388(96)02632-1

12. Enjie He, Hairong Zheng, Zhenglong Zhang, Xisheng Zhang, Liangmin Xu, Zhenxing Fu, and Yu Lei. Influence of Crystal Structure on the Fluorescence Emission of Eu^{3+}: LaOF Nanocrystals. *Journal of Nanoscience and Nanotechnology* 10 (2010) 1908–1912. doi: 10.1166/jnn.2010.2057

13. Guan. M, Mei. L. F, Huang. Z. H, Yang. C. X, Guo. Q. F, Xia. Z. G. Synthesis and near-infrared luminescence properties of LaOCl:Nd^{3+}/Yb^{3+}. *Journal of Infrared Physics and Technology* 60 (2013) 98-102. doi: 10.1016/j.infrared.2013.03.014

14. Lee. S. S, Park. H. I, Joh. C. H, Byeon. S. H. Morphology-dependent photoluminescence property of red-emitting LnOCl:Eu (Ln = La and Gd). *Journal of Solid State Chemistry* 180 (2007) 3529–3534. doi: 10.1016/j.jssc.2007.10.020

15. Rambabu. U, Reddy. K. R, Annapurna. K, Balaji. T, Satyanarayana. J. V, S. Buddhudu. Fluorescence spectra of Sm^{3+}-doped lanthanide oxychloride powder phosphors. *Journal of Materials Letters* 27 (1996) 59–63. doi: 10.1016/0167-577x(96)80002-4

16. X. Zhang, D. Gao, L. Li. Down- and up-conversion luminescence of Tm^{3+}/Ho^{3+} codoped LaOF nanoparticles. *Journal of Applied Physics* 107 (2010) 123528. doi: 10.1063/1.3436569

17. A. Wolfert and G. Blasse. Luminescence of the Bi^{3+} ion in compounds LnOCl (Ln = La, Y, Gd). *Materials Research Bulletin* 19 (1984) 67–75. doi: 10.1016/0025-5408(84)90011-4

18. Wolfert, A & Blasse, G. Luminescence of Bi^{3+}-activated LaOBr, a system with emission from different states. *Journal of Luminescence* 33 (1985) 213–226. doi: 10.1016/0022-2313(85)90019-5

19. B.M. Jaffar, H.C. Swart, H.A.A. Seed Ahmed, A. Yousif, R.E. Kroon. Stability of Bi doped La_2O_3 powder phosphor and PMMA composites. *Journal of Physics and Chemistry of Solids* 131 (2019) 156-163. doi: 10.1016/j.jpcs.2019.04.004

20. B.M. Jaffar, HC. Swart, H.A.A. Seed Ahmed, A. Yousif, R.E. Kroon. Optical properties and stability of Bi doped La_2O_2S. *Journal of Optical Materials* 95 (2019) 109260. doi: 10.1016/j.optmat.2019.109260

21. B. Jacquier, G. Boulon, G. Sallavuard, F. Gaume-Mahn. Bi^{3+} center in a lanthanum gallate phosphor. *Journal of Solid State Chemistry* 4 (1972) 374–378. doi: 10.1016/0022-4596(72)90152-1

22. D. R. Taikar, Sumedha Tamboli, S. J. Dhoble. Synthesis and photoluminescence properties of red, green and blue emitting $LaYO_3$:M (M = Eu^{3+}, Tb^{3+}, Sm^{3+},Bi^{3+}, Pb^{2+}) phosphors. *Optik* 142 (2017) 183-190. doi: 10.1016/j.ijleo.2017.05.095

Chapter two

Background information

2.1. Fundamentals of phosphors

Phosphors, also known as luminescent materials, are any light-emitting materials when applying an external electromagnetic radiation excitation source [1]. There are several types of excitation sources such as electric field or voltage, photons, electrons, etc. Most luminescent materials are inorganic and can be prepared in the form of powder or thin films [2]. Normally, the phosphor matrix or host is either an insulator or semiconductor with a wide band gap, which is mostly activated via small amount of activator ions (dopants), typically rare earth ions or transition metals are used to act as a centre of the luminescence. An activator is an impurity ion that, when inserted into the host material as a dopant, leads to a centre that can be excited to luminescence. Usually, the concentration of the dopant is mainly low, because the concentration quenching phenomenon occurs at high concentrations. In some cases, when the dopant ion displays weak luminescent intensity, other impurity ions can be added, called co-dopants or co-activators (sensitizer), which absorbs the energy and then transfer it to the original dopant (activator) to improve its luminescence [2]. A sensitizer is therefore an impurity ion that is introduced into the host material to transfer its energy of excitation to a neighbouring activator to cause luminescence.

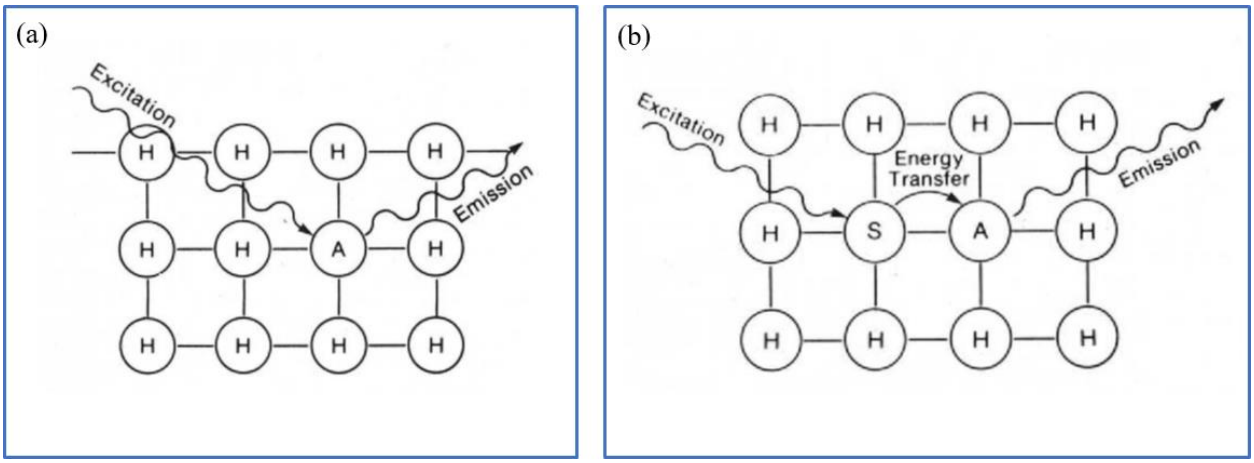

Figure 2.1: Diagrammatic representation of the luminescence process: (a) activator (A) in a host (H) and (b) sensitizer (S) and activator (A) in a host (H). (Reproduced from [3])

Figure 2.1. Shows schematically the role of the activator and sensitizer in the luminescence process [3]. In figure 2.1(a) the emission of light results from direct excitation of the activator atom represented by A (the absorber) surrounded by the host lattice atoms, represented by H, while figure 2.1(b) displays emission of light from A as a result of excitation of an energy transfer from the co-dopant atom (the sensitizer) represented by S.

In general, the phosphors are represented by a formula such as LaOCl:Bi^{3+} (0.7 mol%), where LaOCl represents the host, bismuth (Bi^{3+}) represents the dopant or activator and (0.7 mol%) indicates the concentration of the dopant per mole relative to the host matrix.

Generally, the host material should have characteristic properties such as good chemical and structural stability as well as being transparent to the radiation source with which it is excited [4]. Actually, there are various types of host structure such as alkali-earth sulphides, alkali-earth aluminates, rare-earth oxides, nitrides and oxysulphides, lanthanide oxyhalides, gallates and silicates, etc.

2.2. Types of Light emission

Light is electromagnetic energy which ranges from radio waves to gamma rays [5]. Visible light usually refers to electromagnetic radiation that can be detected by the human eye, which is located between infrared (IR) with low energy and ultraviolet (UV) with high energy, having a wavelength in the range from 400 nm to 700 nm as shown in figure 2.2. Light can be emitted usually by two processes, namely luminescence and incandescence.

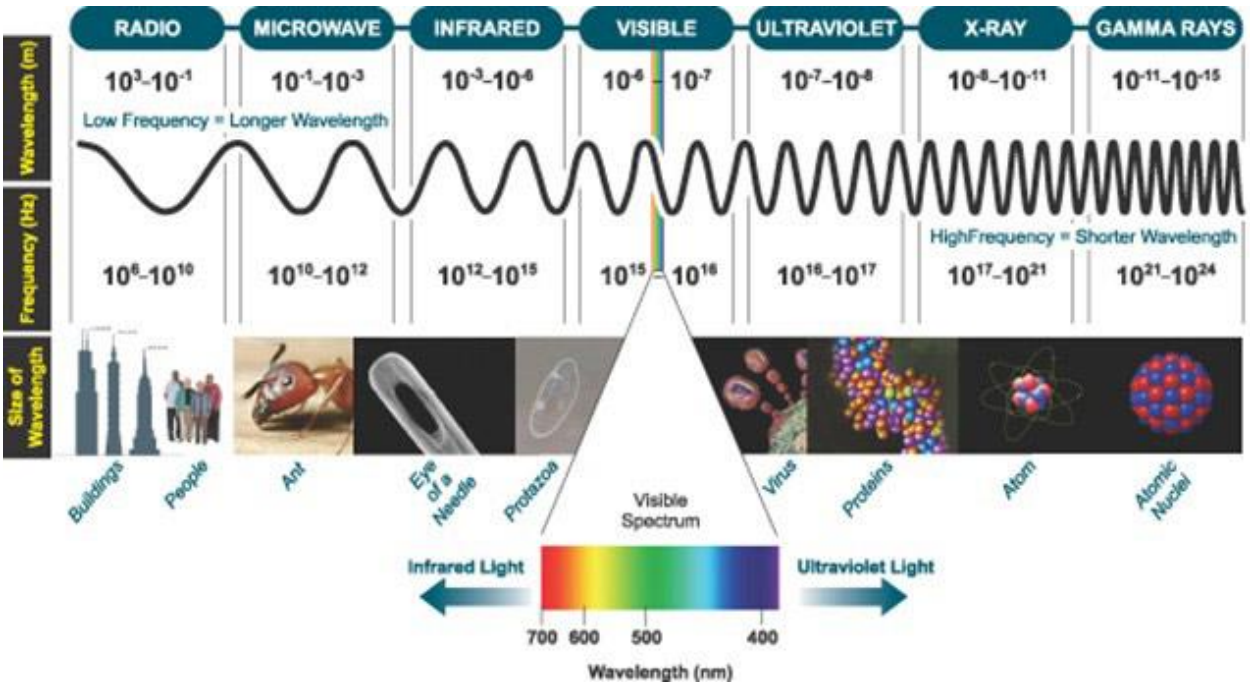

Figure 2.2: Electromagnetic radiation and the range of the visible spectrum that is detectable by the human eye [6].

2.2.1. Incandescence

Incandescence is the emission of light from a hot body due to the heat energy [7]. When an object is heated with enough high energy, it will start to glow. In old incandescent light bulbs, which consists of a tungsten wire, light is produced from heat when an electrical current passes through the wire. When an iron rod is exposed to gas flames or heated in an electric stoves heater or a flame, it will start to glow with a reddish colour, where the red-hot will change to orange and yellow as it becomes hotter. The stars and sun glow via incandescence which releases both light and heat because of the nuclear reactions in its core [8]. Figure 2.3 shows various types of incandescence.

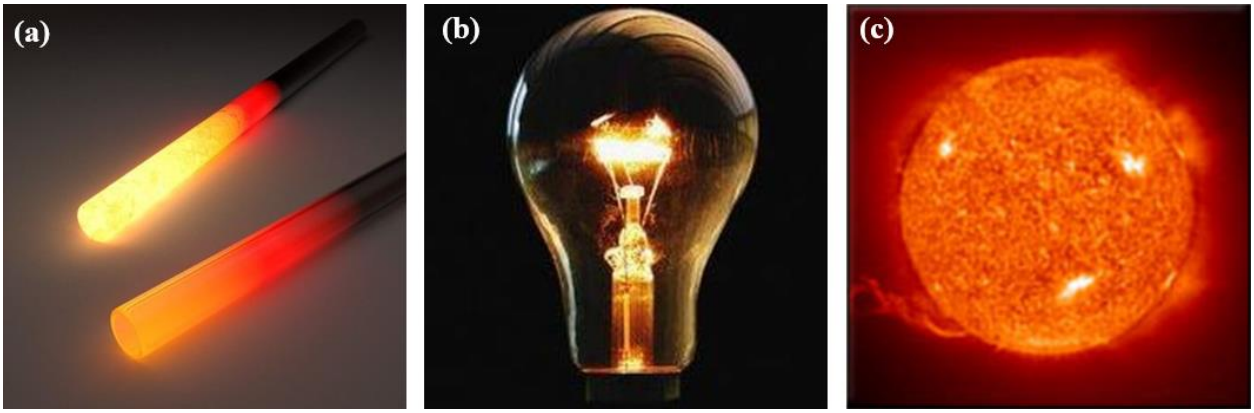

Figure 2.3: Various types of incandescence (a) the rod of iron that glows red when heated in a flame (b) an ordinary light bulb and (c) the sun [9, 10, 11].

2.2.2. Luminescence

Luminescence, which is also known as cold light, is the process of emitting light from any substance when an external energy excitation source is applied. The phenomenon of luminescence occurs due to the absorption of energy by electrons from the external excitation source, thus jumping from the lowest energy level (ground state) to a higher energy level (excited state), where the electrons will fall back to their ground level after a short relaxation time, and releasing their energy in the form of light emission in the visible range [8].

The luminescence can be divided into two categories, fluorescence and phosphorescence, depending upon how long the source continues to emit light after excitation (Figure 2.4). Fluorescence is a rapid luminescence process in which emission from the material stops shortly after the removal of the energy excitation source, whereas phosphorescence is a slow luminescence process whereby the light emission continues to be emitted from the material for a few seconds, minutes or even hours after the source of excitation has stopped. During fluorescence the emission occurs from an excited singlet state and the decay is basically independent of temperature, while in the phosphorescence the emission takes place from an excited triplet state and the decay of phosphorescence exhibits strong temperature dependence [8].

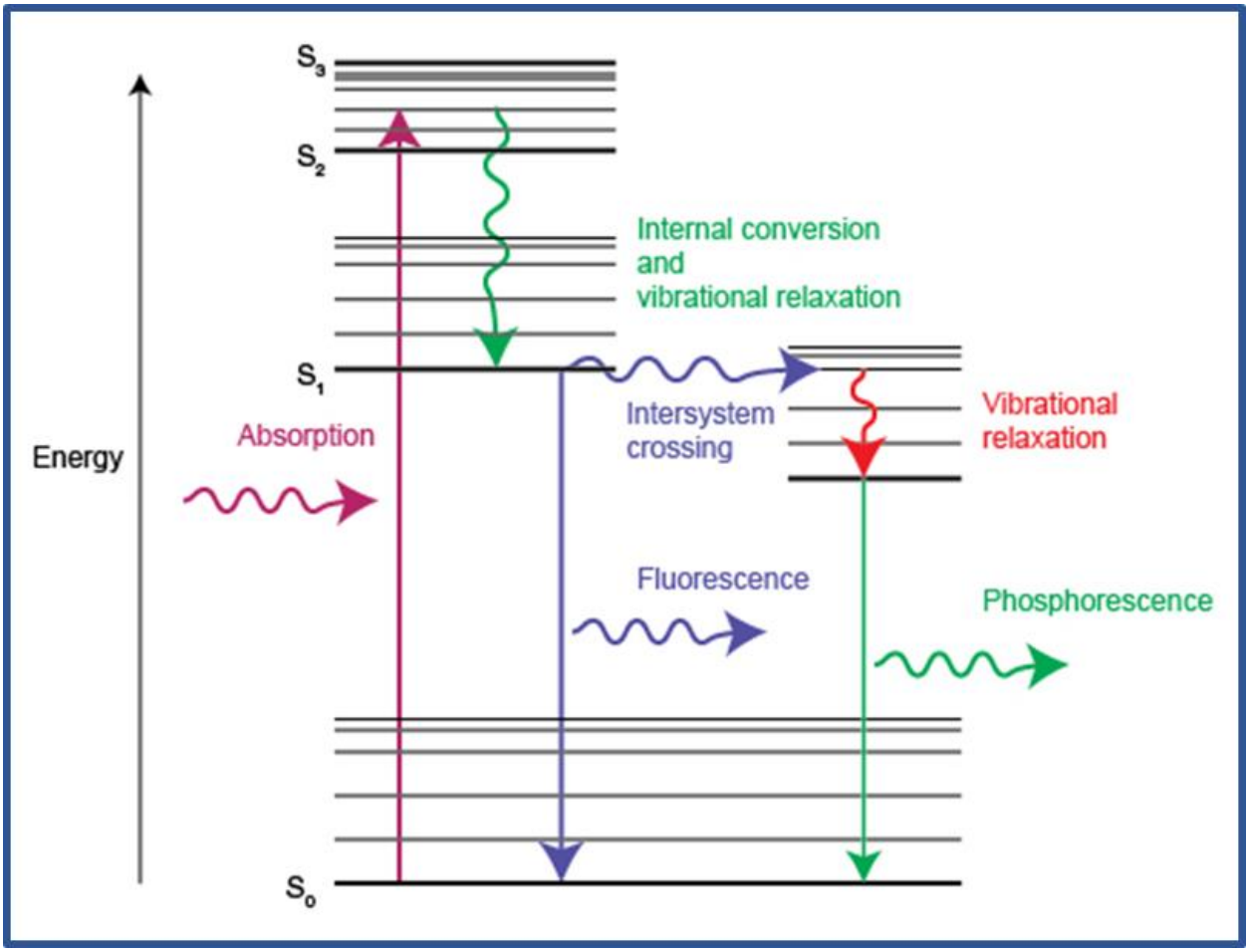

Figure 2.4: Energy level diagram showing absorption, emission, fluorescence and phosphorescence processes [12].

2.3. Types of luminescence

There are different types of luminescence, each classified differently according to the excitation method used, such as photoluminescence, cathodoluminescence and others.

2.3.1. Photoluminescence (PL)

PL is an optical process in which a substance gives emission of light by absorbing incident light (i.e. photons, including ultraviolet light), whose energy is greater than the energy bandgap of the host or the excited states if activator ions are present. The excited electrons later will return to the ground state, accompanied by the emission of photons. The energy difference between PL

emission and absorption is called the Stokes shift [13]. The PL emission spectrum is obtained by drawing the the intensity of light emitted from the sample against wavelength when excited by an appropriate source of excitation for continuous energy.

2.3.2. Cathodoluminescence (CL)

CL is the emission of light generated when the material is bombarded with high energy electron beam irradiation. In fact, CL is the opposite process of the photoelectric effect in which electron emission occurs through photons irradiation. CL occurs when high energy electrons beam impacts on a substance that will promote the electrons from the valence band into the conduction band, leaving behind a hole. When an electron and a hole recombine, it is possible for a photon to be emitted. The energy may also be transferred non-radiatively to activators which can then emit light. The energy (colour) of the photon, and the probability that a photon and not a phonon will be emitted, depends on the material, its purity and its defect state [8]. The CL emission spectrum is obtained by drawing the intensity of light emitted from the sample against the wavelength while the sample is excited by the electron beam.

2.3.3. Other types of luminescence

Many other types of luminescence are possible, based on the source of energy converted to light: **bioluminescence** is the emission of light generated by a living organism such as a firefly; **chemiluminescence** is the emission of light results from a chemical or electrochemical reaction; **radioluminescence** is the emission of light occurs due to exposing materials to ionizing radiation like α, β or γ rays; **electroluminescence** is the emission of light produced when an electric current passes through a material; **crystalloluminescence** is the emission of light produced during crystallization; **thermoluminescence** is luminescence activated thermally after initial irradiation by other means such as α, β, γ, UV or X-rays; **mechanoluminescence** is the emission of light generated due to any mechanical impact on a solid; **sonoluminescence** is the emission of short bursts of light from imploding bubbles in a liquid produced by high frequency sound waves or phonons [14]; **Triboluminescence** is the emission of light produced when the bonds of a substance are broken when crushed, scratched or rubbed; **Fractoluminescence** is the emission of light produced when bonds in certain crystals are broken by fractures and **Piezoluminescence** is the emission of light generated due to the action of pressure on certain solids [15].

2.4. Bismuth

Usually, the rare-earth ions (e.g. Eu, Pr, Yb) are used as activators for luminescent materials because of their intra-configurational 4f transitions [16]. However, the main group metal ions such as Bi^{3+}, Pb^{2+}, Sb^{3+} and Tl^{+} might also be useful luminescence centres [17]. Bismuth is a chemical element with symbol (Bi) and atomic number 83. Bismuth is situated in group 15 of the periodic table of elements and it is the heaviest element in this group with an atomic weight of 208.98 amu. Bi atoms have an electronic configuration [Xe] $4f^{14}5d^{10}6s^{2}p^{3}$. Elemental bismuth may occur naturally, although its oxides and sulphides form important commercial ores. Bi is non-radioactive as well as non-toxic [18]. The melting point and boiling point of Bi are 271 °C and 1564 °C, respectively. Bi has a large number of valence states (e.g. +3, +2, +1, 0, -2) in different host structures [19]. The Bi^{3+} trivalent state is usually the most stable valence state in most host materials [20]. Normally, the emission bands of Bi^{3+} are located in the ultraviolet, blue, green, or even red wavelength regions with differences in host materials. For instance, $YBO_3:Bi^{3+}$ [21] and $Y_3Al_{5x}Ga_xO_{12}:Bi^{3+}$ [22] display UV emission, $La_2O_3:Bi^{3+}$ [23] and La_2O_2S:Bi [24] show blue emission, $Ba_3Sc_4O_9:Bi^{3+}$ [25] and $YVO_4:Bi^{3+}$ [26] present green emission, $ScVO_4:Bi^{3+}$ [27] and $Y_2WO_6:Bi^{3+}$ [28] show red emission. The optical characteristic of Bi^{3+} ions have been investigated in various host structures [29]. They have an electronic ground state $^1S_0$ in the $6s^2$ configuration and the excited $6s^16p^1$ configuration consists of four energy level states, namely a triplet $^3P_0$, $^3P_1$, $^3P_2$ and a singlet $^1P_1$. The transitions from $^1S_0 \rightarrow {}^3P_0$ and $^1S_0 \rightarrow {}^3P_2$ are forbidden, while the transition from $^1S_0 \rightarrow {}^1P_1$ is allowed. The transition from $^1S_0$ to $^3P_1$ becomes allowed due to mixing of the $^1P_1$ and $^3P_1$ levels by spin orbit coupling [29]. Bi ions doped phosphor materials display wonderful optical characteristics because of the large number of valence states and strong interaction with the surrounding host structure. That is because of the outer electron orbitals of Bi ions are not shielded from the surrounding environment [30]. For example, Bi^{3+} ions activated with phosphor materials give emission in the near ultraviolet and blue region as well as green regions. Bi^{2+} ions emit orange-red light. The Bi^{+} ion or Bi^{0} gives broadband near-infrared emission in the range from 1000 to 1600 nm. The Bi_5^{3+} cluster gives broadband near to mid infrared in the range from 1000 to 3000 nm [31]. In all cases, the emission regions of these ions varied in different host materials [29]. In this research study, the main focus of investigations is the spectroscopic property of Bi^{3+} as a dopant in phosphor materials.

2.5. Lanthanum oxyhalides

The activated lanthanide oxyhalides LnOX (Ln = Y, La; X = F, Cl, Br) have been extensively studied because of their use as X-ray intensifying phosphors and also have potential applications in fluoroscopic screens, cathode ray tubes and lamps. Generally, the hygroscopic nature of the lanthanide oxyhalides decreases with increasing the ionic size of lanthanide atoms (i.e., the smaller the lanthanide, the, greater the hygroscopic nature of the substance) [32]. Lanthanum oxyhalides LaOX (X = Cl, Br, and F) have found much interest from researchers because of their excellent and unique magnetic, optical, electrical, and luminescent characteristics [33]. Lanthanum oxyhalide compounds doped by cerium have been reported to be potential oxygen-dominated phosphors. In the process of converting X-rays into visible light, these compounds are considered to be superior due to their high conversion efficiency, and are popularly called X-ray image converters [32]. In addition, lanthanum-based crystals are preferred to other compounds due to their high detection efficiency.

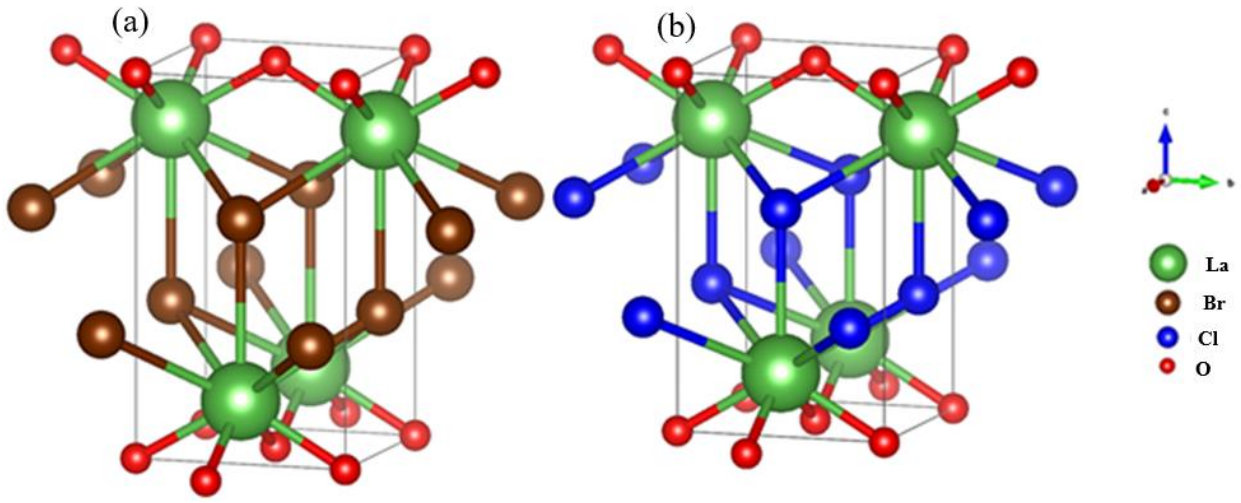

Figure 2.5: The unit cell of (a) LaOBr (COD number 9009169) and (b) LaOCl (COD number 1539093).

The LaOX (X = Cl, Br) hosts have wide band gaps, about 5.8 eV for LaOBr and 6 eV for LaOCl [34]. Both compounds belong to the tetragonal PbFCl-type crystal structure with space group *P*4/*nmm* (No. 129) [35]. Their crystal structures (Figure 2.5) were modelled with Vesta software [36] using the CIF files obtained from the Crystallography Open Database (COD) [37]. In both

structures the La^{3+} ions with C_{4v} site symmetry are bonded with four oxygen atoms (La-O) with the same bond length and five halide atoms having two distinct La-X bond lengths [38].

Most often rare earth ions are added as activators, e.g. phosphors based on LaOCl and LaOBr have been created by doping with Nd^{3+} and Yb^{3+} [39], Eu^{3+} [40] and Sm^{3+} [41]. However, the metal ions which are located in the main group on the periodic table, like Tl^{+}, Pb^{2+}, Bi^{3+} and Sb^{3+}, may also be useful activators for luminescence [42]. Sb^{3+} doping of LaOCl was reported by van Steensel and Blasse [43], while Wolfert and Blasse reported the luminescence properties of Bi^{3+} doped LaOCl [44] and LaOBr [45] several decades ago, observing two emission peaks in the ultraviolet and visible regions.

Lanthanum oxyfluoride (LaOF) has attracted much research interest because of its high chemical stability, low phonon energy, high refractive and high transparency in the NIR and UV-Vis regions [46]. Lanthanum oxyfluoride has been synthesised by different methods, such as thermal decomposition of lanthanum (III) carbonate fluoride ($LaFCO_3$) in air [47], solid-state reaction between ammonium fluoride (NH_4F) and lanthanum oxide (La_2O_3) or lanthanum (III) fluoride (LaF_3) and lanthanum oxide [48, 49], ball milling and calcination of a mixture of La_2O_3 and polytetrafluoroethylene [50], annealing of LaF_3 in air [51], sol–gel method [52], decomposition of lanthanum(III) trifluoroacetate in boiling oleylamine [53].

Lanthanum oxyfluoride has various stoichiometries and structures [54, 55], particularly at high temperatures, LaOF creates a fluorite-type crystal structure, in which lanthanum ions create a face-cantered cubic order and the fluoride and oxide ions occupy the tetrahedral interstitial sites, while at room temperature LaOF has either a rhombohedral or tetragonal crystal structure [56], depending on the chemical composition and/or anion ordering. In the tetragonal crystal structure the space group is *P*4/*nmm* (No. 129) and its structure is shown in figure 2.6 (a). Each La^{3+} ion with C_{4v} site symmetry is bonded with four oxygen atoms (La-O) with the same bond length and five halide atoms having two distinct La-F bond lengths. Figure 2.7 compares the tetragonal structures of LaOF with LaOX (x = Cl, Br). The environment of the La^{3+} ion is different despite the same C_{4v} site symmetry in both cases. In LaOCl there is a Cl^{-} ion directly below each La^{3+} ion along the direction of the four-fold rotation axis and the Cl^{-} anions form double layers, whereas in LaOF the F^{-} ions are relatively rotated so as to be directly below the O^{2-} ions and form only single

layers. In the rhombohedral crystal structure figure 2.6 (b), the space group is $R\bar{3}m$. Each La^{3+} ion has C_{3v} symmetry and is coordinated with four oxygen ions and four fluorine ions [57].

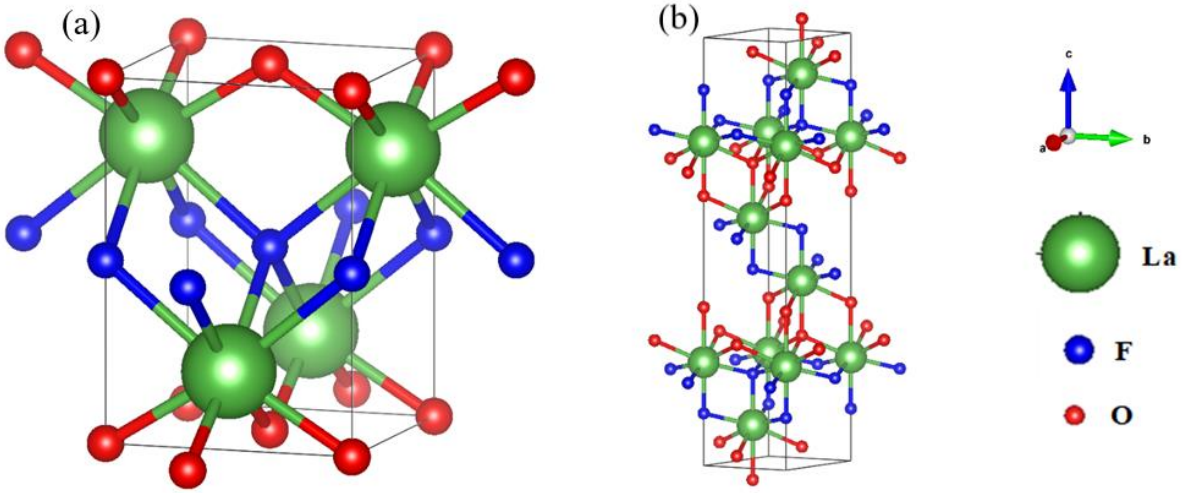

Figure 2.6: The unit cells of LaOF (a) Tetragonal (b) Rhombohedral crystal structure, drawn with the Vesta software [36].

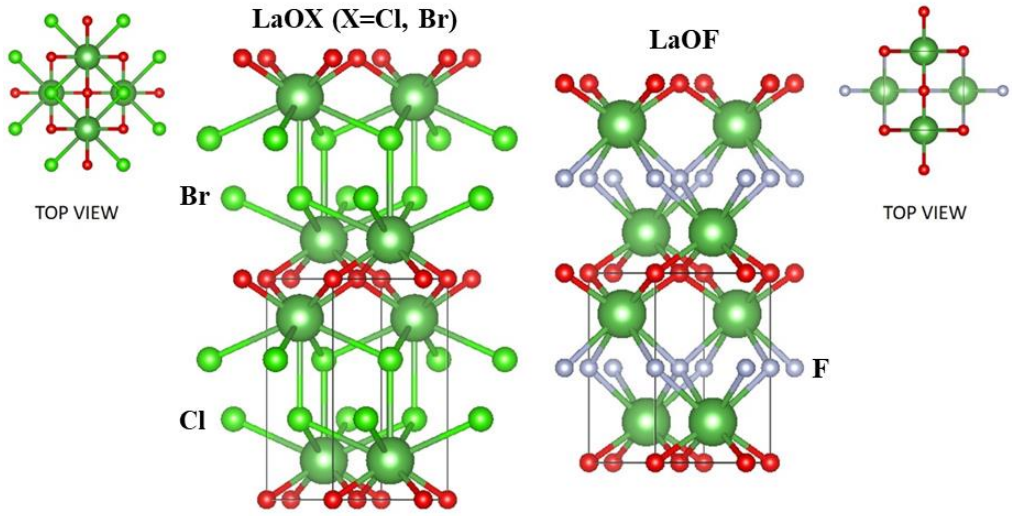

Figure 2.7: Comparison of the tetragonal structure of LaOF with LaOX (X = Cl, Br).

2.6. $LaGaO_3$ and $LaYO_3$

Lanthanide metal oxides have been widely studied because of their applications in optical electronics, radio electronics, nuclear and laser engineering, instrumentation, mechanical engineering, metallurgy, chemical industry and medicine [58]. Alloying La_2O_3 with Y_2O_3 and Ga_2O_3 have many applications in devices that people use every day such as DVDs, computer memory, rechargeable batteries, catalytic converters, cell phones, magnets, and fluorescent lamps [59].

Lanthanum oxide or lanthanum gallate ($LaGaO_3$) has attracted attention due to its potential use as a substrate for solid oxide fuel cells and as host lattice for phosphor applications [60]. $LaGaO_3$ has been assessed as a host material doped with various rare earth ions such as Sm^{3+}, Ln^{3+}, Dy^{3+}, Eu^{3+} and Tb^{3+} [61]. Bi^{3+} doping of $LaGaO_3$ was reported by Jacquier *et al*. [62], while Srivastava [63] reported the thermal quenching of Bi^{3+} luminescence in $LaGaO_3$ and explained the energy transfer mechanism between Bi^{3+} ions to host lattice-quenching centres.

Lanthanum gallate ($LaGaO_3$) belong to the orthorhombic type of structure with *Pbnm* space group [64]. This is a distorted perovskite structure. The crystal structure (Figure 2.8) was modelled with Vesta software [36] using the CIF files obtained from the Crystallography Open Database [37]. In the $LaGaO_3$ structure, the La^{3+} cations are bonded with eight oxygen atoms (La-O) with the same bond length and the Ga^{3+} cations are bonded with six oxygen (Ga-O) with the same bond length. The site symmetry of the Ga^{3+} site is C_i [65]. Figure 2.9 shows the phase diagram of the La_2O_3-Ga_2O_3 system from 200–1300 °C taken from [66].

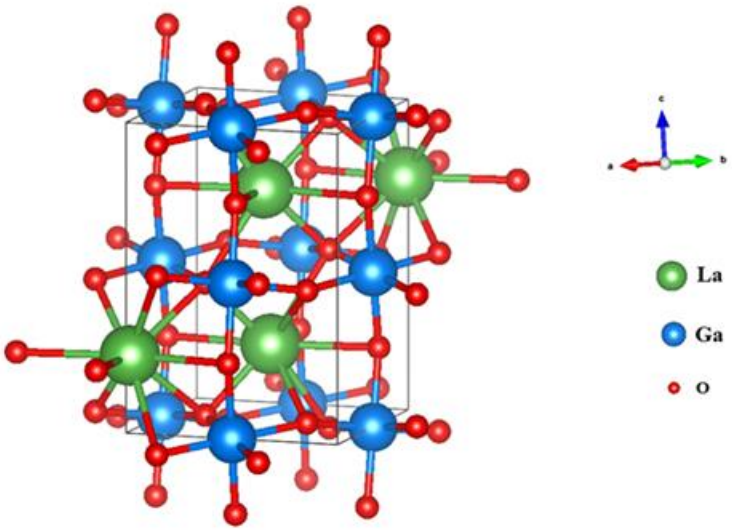

Figure 2.8: The unit cell of $LaGaO_3$ drawn with the Vesta software.

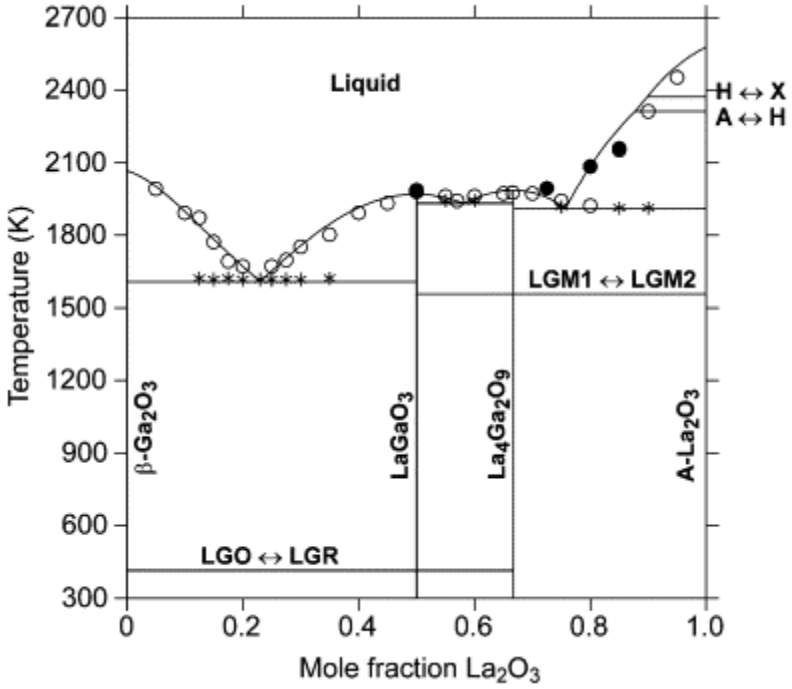

Figure 2.9. Phase diagram of the La_2O_3-Ga_2O_3 system from 300–2700 °C [66].

The structure and optical properties of lanthanum yttrium oxide ($LaYO_3$) have been studied in the past for optical applications [67]. At low temperatures, $LaYO_3$ has an orthorhombic structure,

while at high temperatures $LaYO_3$ has a monoclinic crystal structure [68]. Figure 2.10 shows the orthorhombic perovskite crystal structure of the $LaYO_3$ with space group *Pna*2_1 [69]. The crystal structure was modelled with Vesta software [36] using a CIF file obtained from the Crystallography Open Database [37]. The orthorhombic crystal cell of the $LaYO_3$ composed of a network of LaO_8 polyhedra linked to distorted YO_6 octahedra. The bond distances of La-O and Y-O range from 2.368–2.809 Å and 2.227–2.2851 Å, respectively [70]. $LaYO_3$ has been assessed as a phosphor host material activated with rare-earth ions (Eu^{3+}, Sm^{3+} and Tb^{3+}) and post-transition metal ions (Bi^{3+} and Pb^{2+}) [70]. Figure 2.11 shows the phase diagram of the La_2O_3–Y_2O_3 system from 1000–2600 °C as reported in [71].

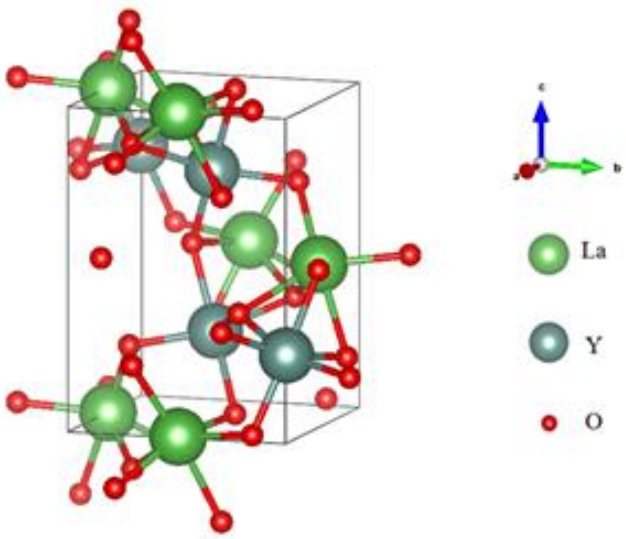

Figure 2.10: The unit cell of $LaYO_3$ drawn with the Vesta software (COD number: 1521869).

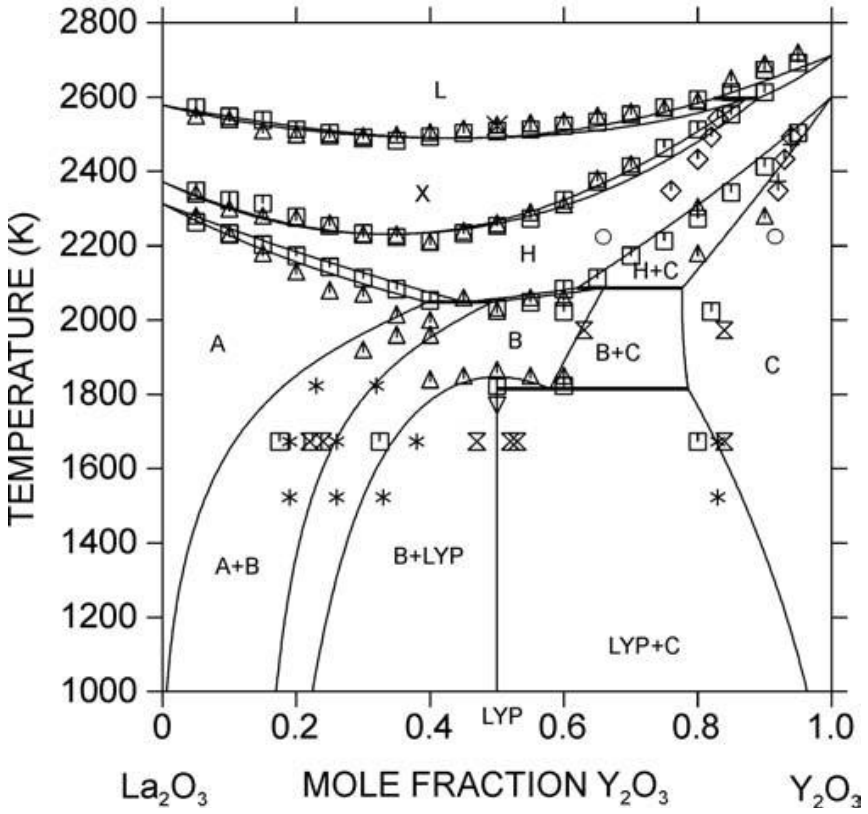

Figure 2.11: Calculated phase diagram of the La_2O_3–Y_2O_3 system from 1000–2600 °C. The phase name abbreviations: L – liquid, X – high temperature cubic phase, H – high temperature hexagonal phase, B – monoclinic phase, A – low temperature hexagonal phase, LYP – $LaYO_3$ perovskite [71].

2.7. Applications of phosphors

Phosphor materials have been widely used in various technological applications such as back lights for liquid crystal devices (LCD), light emitting diodes (LEDs), plasma display panels (PDP), infrared detectors (upconversion phosphor), phosphorescent paints (persistent phosphors), scintillators (detectors of X-ray and ionizing radiation), X-ray image intensifiers for photographic film as well as storage phosphors in filmless radiography, display devices and lighting sources [72, 73]. Some of these applications are shown in figure 2.12. The main applications are in fluorescent lamps and emissive displays. In addition, several X-ray detector systems are based on phosphor materials as well [74]. Among these applications, white light emitting diodes (LEDs) are an important potential application of phosphors.

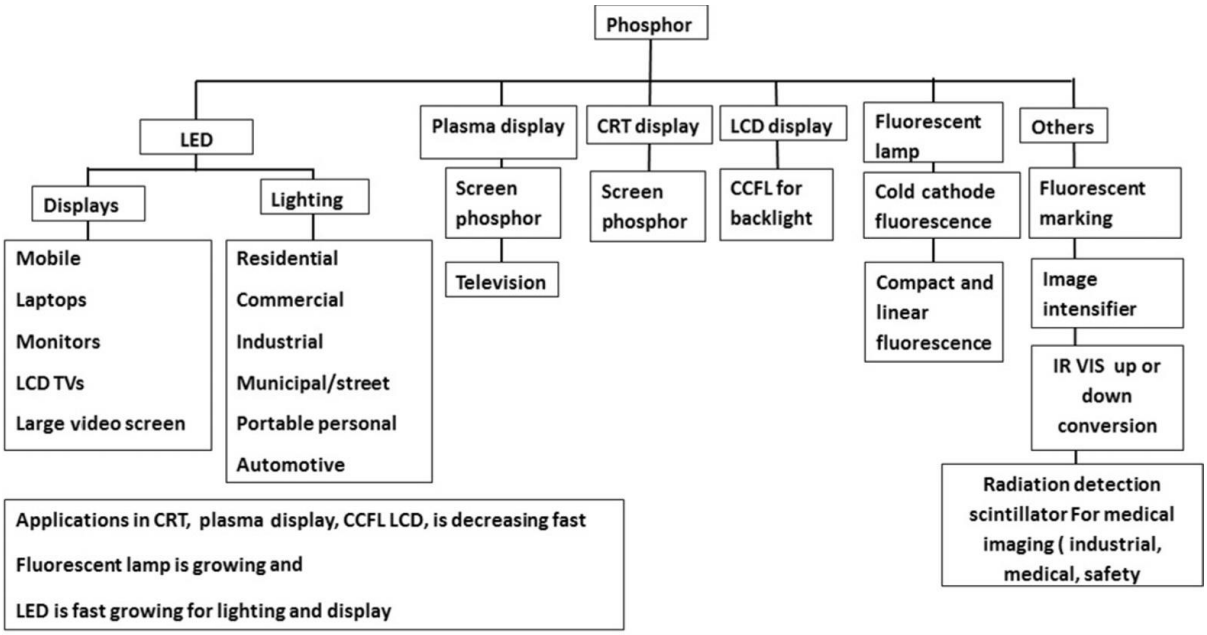

Figure 2.12: The application range of luminescent materials in different applications [75].

There are three main technological methods available to produce white light from LEDs, namely:

1. Combining several LED emitters with distinct colours such as the three primary colours, namely red, green and blue (RGB) incorporated into a single device to create white light [76, 77].
2. Use of a single near ultraviolet (n-UV) LED chip are to excite red, green, and blue phosphors for creating white light.
3. Use of a blue LED chip to excite a single yellow phosphor or mixed green and red phosphors to produce white light [78].

Since the emission wavelength of Bi^{3+} ions is dependent on the host and varies from UV to blue and longer wavelengths, each of these possibilities may be feasible with Bi-doped phosphors.

Figure 2.13: Various kinds of LED bulbs [79].

2.8. References

1. V. Đorđević, Ž. Antić, M.G. Nikolić, M.D. Dramićanin. The Concentration Quenching of Photoluminescence in Eu^{3+}-Doped La_2O_3. *Journal of Research in Physics* 37 (2013) 47–54. doi: 10.2478/jrp-2013-0005

2. G. Blasse, B.C. Grabmaier. Luminescent Materials. Springer-Verlag, Berlin Heidelberg (1994). ISBN: 978-3-540-58019-5, 978-3-642-79017-1. doi: 10.1007/978-3-642-79017-1

3. John A. DeLuca. An introduction to luminescence in inorganic solids. *Journal of Chemical Education* 57 (1980) 541–545. doi: 10.1021/ed057p541

4. S.R. Rotman. Wide-Gap Luminescent Materials: Theory and Application. Kluwer Academic, Dordrecht (1997). ISBN 978-1-4615-4100-4

5. D. H. Sliney. What is light? The visible spectrum and beyond. *Eye* (2016) 1–8. doi: 10.1038/eye.2015.252

6. What is Light: [Online]. Available from https://andor.oxinst.com/learning/view/article/what-is-light [Accessed 22 August 2021].

7. Wout van Bommel. Incandescence. *Encyclopedia of Color Science and Technology*, (2013) 1-2. doi: 10.1007/978-3-642-27851-8_149-2

8. K.V.R. Murthy, Hardev Singh Virk. Luminescence Phenomena: An Introduction. *Defect and Diffusion Forum* 347 (2013) 1–34. doi: 10.4028/www.scientific.net/DDF.347.1

9. Dan MacIsaac, Gary Kanner, and Graydon Anderson. Basic physics of the incandescent lamp (lightbulb). *The Physics Teacher* 37 (1999) 520–525. doi: 10.1119/1.880392

10. Incandescence: [Online]. Available from http://www.webexhibits.org/causesofcolor/3.html [Accessed 23 August 2021].

11. Incandescence: [Online]. Available from https://alchetron.com/Incandescence#incandescence-75816315-2d73-453b-ad82-2f87fd5a310-resize-750.jpeg [Accessed 23 August 2021].

12. Photoluminescence [Online]. Available from https://www.renishaw.com/en/photoluminescence-explained--25809 [Accessed 25 August 2021].

13. A. Edgar. Luminescent Materials. In: Kasap S., Capper P. (eds) Springer Handbook of Electronic and Photonic Materials. Springer Handbooks. Springer, Cham. (2017) doi: 10.1007/978-3-319-48933-9_38

14. Ashiq Hussain Khalid, Konstantinos Kontis. Thermographic Phosphors for High Temperature Measurements: Principles, Current State of the Art and Recent Applications. *Sensors* 8 (2008) 5673–5744. doi: 10.3390/s8095673

15. M.-M. Biggs, Synthesis, characterization and luminescent mechanism of ZnS:Mn^{2+} nanophosphor, M.Sc. thesis, University of the Free State (2009).

16. Qiangbing Guo, Beibei Xu, Dezhi Tan, Juechen Wang, Shuhong Zheng, Wei Jiang, Jianrong Qiu, Shifeng Zhou. Regulation of Structure Rigidity for Improvement of the Thermal Stability of Near-Infrared Luminescence in Bi-Doped Borate Glasses. *Optics Express* 21 (2013) 27835–27840. doi: 10.1364/OE.21.027835

17. G. Blasse, A. Bril. Investigations on Bi^{3+} Activated Phosphors. *The Journal of Chemical Physics* 48 (1968) 217–222. doi: 10.1063/1.1667905

18. Ram Mohan. Green Bismuth. *Nature* 2 (2010) 336 (1 page). doi: 10.1038/nchem.609

19. A. Yousif, R. M. Jafer, S. Som, M.M. Duvenhage, E. Coetsee, H.C. Swart. Ultra-

Broadband Luminescent from a Bi Doped CaO Matrix. *RSC Advances* 5 (2015) 54115–54122. doi: 10.1039/c5ra09246a

20. H.C. Swart, R.E. Kroon. (INVITED) Ultraviolet and visible luminescence from bismuth doped materials. *Optical Materials: X* 2 (2019) 100025. doi: 10.1016/j.omx.2019.100025

21. L. Chen, H. Zheng, J. Cheng, P. Song, G. Yang, G. Zhang and C. Wu. Site-selective luminescence of Bi^{3+} in the YBO_3 host under vacuum ultraviolet excitation at low temperature. *J. Lumin.* 128 12 (2008) 2027–2030. doi: 10.1016/j.jlumin.2008.07.007

22. A. Yousif, V. Kumar, H. A. A. Seed Ahmed, S. Som, L. L. Noto, O. M. Ntwaeaborwa and H. C. Swart. Effect of Ga^{3+} Doping on the Photoluminescence Properties of Y_3Al_5-xGa_xO_{12}:Bi^{3+} Phosphor. ECS J. Solid State Sci. Technol. 3 (2014) R222–R227. doi: 10.1149/2.0021412jss

23. B.M. Jaffar, HC. Swart, H.A.A. Seed Ahmed, A. Yousif, R.E. Kroon. Luminescence properties of Bi doped La_2O_3 powder phosphor. *Journal of Luminescence* 209 (2019) 217–224. doi: 10.1016/j.jlumin.2019.01.044

24. B.M. Jaffar, HC. Swart, H.A.A. Seed Ahmed, A. Yousif, R.E. Kroon. Optical properties and stability of Bi doped La_2O_2S. *Optical Materials* 95 (2019) 109260. doi: 10.1016/j.optmat.2019.109260

25. Y. Wang, J. Ding, and Y. Wang, Preparation and photoluminescence properties with the site-selected excitations of Bi^{3+} -activated $Ba_3Sc_4O_9$ phosphors. *J. Am. Ceram. Soc.* 100 (2017) 2612–2620. doi: 10.1111/jace.14789

26. E. Cavalli, F. Angiuli, F. Mezzadri, M. Trevisani, M. Bettinelli, P. Boutinaud and M. G. Brik. Tunable luminescence of Bi^{3+}-doped $YPxV_{1-x}O_4(0 \leq x \leq 1)$. *J. Phys. Condens. Matter.* 26 (2014) 385503. doi: 10.1088/0953-8984/26/38/385503

27. F. Kang X. Yang, M. Peng, L. Wondraczek, Z. Ma, Q. Zhang and J. Qiu. Red Photoluminescence from Bi^{3+} and the Influence of the Oxygen-Vacancy Perturbation in $ScVO_4$: A Combined Experimental and Theoretical Study. *J. Phys. Chem. C.* 118 (2014) 7515–7522. doi: 10.1021/jp4081965

28. G. Blasse and A. Bril, Investigations on Bi^{3+}-activated phosphors. *J. Chem. Phys.* 48 (1968) 217– 222. doi: 10.1063/1.1667905

29. Roy H.P. Awater, Pieter Dorenbos. The Bi^{3+} 6s and 6p Electron Binding Energies in Relation to the Chemical Environment of Inorganic Compounds. *Journal of Luminescence* 184 (2017) 221–231. doi: 10.1016/j.jlumin.2016.12.021

30. W.A.I. Tabaza, H.C. Swart, R.E. Kroon. Optical properties of Bi and energy transfer from Bi to Tb in $MgAl_2O_4$ phosphor. *Journal of Luminescence* 148 (2014) 192-197. doi: 10.1016/j.jlumin.2013.12.018

31. Renping Cao, Fangteng Zhang, Chenxing Liao, Jianrong Qiu. Yellow-to-Orange Emission from Bi^{2+}-doped RF_2 (R = Ca and Sr) Phosphors. *Optics Express* 21 (2013) 15728. doi: 10.1016/10.1364/OE.21.015728

32. G. Shwetha, V. Kanchana, N. Yedukondalu and G.Vaitheeswaran. Ab initio study of scintillating lanthanide oxyhalide host materials. *Materials Research Express* 2 (2015) 105901. doi: 10.1088/2053-1591/2/10/105901

33. U. Rambabu, A. Mathur, S. Buddhudu. Fluorescence spectra of Eu^{+3} and Tb^{+3}-doped lanthanide oxychloride powder phosphors. *Materials Chemistry and Physics* 61 (1999) 156-162. doi: 10.1016/s0254-0584(99)00122-4

34. S. I. Golovkova, A. M. Gurvich, T. I. Savikhlna, D. Starick, T. A. Birman, G. Herzog, R. V. Katomina, *et al.* Luminescence properties of lanthanum oxyhalides activated with terbium. *Journal of Applied Spectroscopy 35* (1981) 1208–1212. doi: 10.1007/bf00624115

35. Kenneth R. Kort and Sarbajit Banerjee. Shape-controlled synthesis of well-defined matlockite LnOCl (Ln: La, Ce, Gd, Dy) nanocrystals by a novel non-hydrolytic approach. *Journal of Inorganic Chemistry* 50 (2011) 5539–5544. doi: 10.1021/ic200114s

36. Koichi Momma and Fujio Izumi. VESTA 3 for Three-Dimensional Visualization of Crystal, Volumetric and Morphology Data. *Journal of Applied Crystallography* 44 (2011) 1272–1276. doi: 10.1107/S0021889811038970

37. A. Vaitkus, A. Merkys and S. Gražulis. Validation of the Crystallography Open Database using the Crystallographic Information Framework. *Journal of Applied Crystallography 54* (2021) 661-672. doi: 10.1107/S1600576720016532

38. Jorma Hölsä, Kari Koski, Sari Makkonen, Eija Säilynoja, Hanna Rahiala. X-ray powder diffraction and vibrational spectroscopic investigation of the $LaO(Cl_{1-x}Br_x)$ solid solutions. *Journal of Alloys and Compounds* 249 (1997) 217–220. doi: 10.1016/s0925-8388(96)02632-1

39. Guan. M, Mei. L. F, Huang. Z. H, Yang. C. X, Guo. Q. F, Xia. Z. G. Synthesis and near-infrared luminescence properties of $LaOCl:Nd^{3+}/Yb^{3+}$. *Journal of Infrared Physics and Technology* 60 (2013) 98-102. doi: 10.1016/j.infrared.2013.03.014

40. Lee. S. S, Park. H. I, Joh. C. H, Byeon. S. H. Morphology-dependent photoluminescence

property of red-emitting LnOCl:Eu (Ln = La and Gd). *Journal of Solid State Chemistry* 180 (2007) 3529–3534. doi: 10.1016/j.jssc.2007.10.020

41. Rambabu. U, Reddy. K. R, Annapurna. K, Balaji. T, Satyanarayana. J. V, S. Buddhudu. Fluorescence spectra of Sm^{3+}-doped lanthanide oxychloride powder phosphors. *Materials Letters* 27 (1996) 59–63. doi: 10.1016/0167-577x(96)80002-4

42. G. Blasse, A. Bril. Investigations on Bi^{3+} Activated Phosphors. *Journal of Chemical Physics* 48 (1968) 217–222. doi: 10.1063/1.1667905

43. L. I. Van Steensel and G. Blasse. The luminescence of Sb^{3+} in LaOCl. *Journal of Alloys and Compounds* 232 (1996) 60-62. doi: 10.1016/0925-8388(95)02017-9

44. A. Wolfert and G. Blasse. Luminescence of the Bi^{3+} ion in compounds LnOCl (Ln = La, Y, Gd). *Materials Research Bulletin* 19 (1984) 67–75. doi: 10.1016/0025-5408(84)90011-4

45. Wolfert, A & Blasse, G. Luminescence of Bi^{3+}-activated LaOBr, a system with emission from different states. *Journal of Luminescence* 33 (1985) 213–226. doi: 10.1016/0022-2313(85)90019-5

46. Emille M. Rodrigues, Ernesto R. Souza, Jorge H. S. K. Monteiro, Rafael D. L. Gaspar, Italo O. Mazali and Fernando A. Sigoli. Non-stabilized europium-doped lanthanum oxyfluoride and fluoride nanoparticles well dispersed in thin silica films. *Journal of Materials Chemistry* 22 (2012) 24109–24123. doi: 10.1039/C2JM34901A

47. Oliver Janka and Thomas Schleid. Facile Synthesis of Bastnaesite-Type $LaF[CO_3]$ and Its Thermal Decomposition to LaOF for Bulk and Eu^{3+}-Doped Samples. *European Journal of Inorganic Chemistry* 3 (2009) 357–362. doi: 10.1002/ejic.200800931

48. J. Hölsä. Effect of non-stoichiometry on the luminescence properties of lanthanum oxyfluoride. *Acta Chemica Scandinavica* 45 (1991) 583-587

49. C.T. Au, Y.Q. Zhang, H. He, S.Y. Lai, C.F. Ng. The characterization of $BaCO_3$-modified LaOF catalysts for the OCM reaction. *Journal of Catalysis* 167 (1997) 354-363. doi: 10.1006/jcat.1997.1577

50. J. Lee, Q. Zhang, F. Saito. Synthesis of nano-sized lanthanum oxyfluoride powders by mechanochemical processing. *Journal of Alloys and Compounds* 348 (2003) 214-219. doi: 10.1016/S0925-8388(02)00837-X

51. X. Zhang, D. Gao, L. Li. Down- and up-conversion luminescence of Tm^{3+}/Ho^{3+} codoped LaOF nanoparticles. *Journal of Applied Physics* 107 (2010)123528. doi: 10.1063/1.3436569

52. Grzyb Tomasz and Lis Stefan. Structural and Spectroscopic Properties of LaOF:Eu^{3+} Nanocrystals Prepared by the Sol–Gel Pechini Method. *Inorganic Chemistry* 50 (2011) 8112–8120. doi: 10.1021/ic2005453

53. Ya-Ping Du, Ya-Wen Zhang, Ling-Dong Sun, and Chun-Hua Yan. Luminescent Monodisperse Nanocrystals of Lanthanide Oxyfluorides Synthesized from Trifluoroacetate Precursors in High-Boiling Solvents. *Journal of Physical Chemistry C* 112 (2008) 405–415. doi: 10.1021/jp076717r

54. Davide Barreca, Elza Bontempi, Laura E. Depero, Cinzia Maragno, Eugenio Tondello and Paolo Zanola. Structural Characterization of Nanocrystalline Lanthanum Oxyfluoride Films Obtained by Chemical Vapor Deposition. *Journal of Nanoscience and Nanotechnology* 7 (2007) 2741–2747. doi: 10.1166/jnn.2007.606

55. A. K. Tyagi. Role of size of rare earth ion in the homogeneity range of REF_3–RE_2O_3 (RE = La, Nd, Y) systems. *Materials science letters* 14 (1995) 1502–1504. doi: 10.1007/bf00633143

56. J. W. Fergus. Crystal structure of lanthanum oxyfluoride. *Materials Science Letters* 16 (1997) 267–269. doi: 10.1023/A:1018584614532

57. Enjie He, Hairong Zheng, Zhenglong Zhang, Xisheng Zhang, Liangmin Xu, Zhenxing Fu, and Yu Lei. Influence of Crystal Structure on the Fluorescence Emission of Eu^{3+}: LaOF Nanocrystals. *Journal of Nanoscience and Nanotechnology* 10 (2010) 1908–1912. doi: 10.1166/jnn.2010.2057

58. O. V. Chudinovych, S. F. Korichev and E. R. Andrievskaya, Interaction of Yttrium, Lanthanum, and Samarium Oxides at 1600°C. *Powder Metallurgy and Metal Ceramics* 58 (2020) 599–607. doi: 10.1007/s11106-020-00113-0

59. Georgios Charalampides, Konstantinos I. Vatalis, Baklavaridis Apostoplos, Benetis Ploutarch-Nikolas. Rare Earth Elements: Industrial Applications and Economic Dependency of Europe. *Procedia Economics and Finance 24* (2015) 126–135. doi: 10.1016/S2212-5671(15)00630-9

60. T. Samuel, Ch. Satya Kamal, Srikanth Ravipati, Babajide Patrick Ajayi, V. Veeraiah , V. Sudarsan, K. Ramachandra Rao. High purity green photoluminescence emission from Tb^{3+}, Bi^{3+} co-doped $LaGaO_3$ nanophosphors. *Optical Materials* 69 (2017) 230–237. doi: 10.1016/j.optmat.2017.04.037

61. Xiaoming Liu and Jun Lin. $LaGaO_3$:A (A = Sm^{3+} and/or Tb^{3+}) as promising phosphors for

field emission displays. *Journal of Materials Chemistry* 18 (2008) 221–228. doi: 10.1039/b709929k

62. B. Jacquier, G. Boulon, G. Sallavuard, F. Gaume-Mahn. Bi^{3+} center in a lanthanum gallate phosphor. *Journal of solid state chemistry* 4 (1972) 374–378. doi: 10.1016/0022-4596(72)90152-1

63. Alok M. Srivastava. Luminescence of Bi^{3+} in LaGaO3. *Materials Research Bulletin* 34 (1999) 1391–1396. doi: 10.1016/s0025-5408(99)00149-x

64. W. Marti, P. Fischer, F. Altorfer, H. J. Scheel and M. Tadin. Crystal structures and phase transitions of orthorhombic and rhombohedral $RGaO_3$ (R=La, Pr, Nd) investigated by neutron powder diffraction. *Journal of Physics: Condensed Matter* 6 (1994) 127–135. doi: 10.1088/0953-8984/6/1/014

65. A.M. Srivastava, S.J. Camardello, M.G. Brik. (2016). Luminescence of Mn^{4+} in the orthorhombic perovskite, LaGaO3. *Journal of Luminescence* 183 (2017) 437–441. doi: 10.1016/j.jlumin.2016.11.015

66. M. Zinkevich, S. Geupel, F. Aldinger, A. Durygin, S. K. Saxena, M. Yang, Z.-K. Liu. Phase diagram and thermodynamics of the La2O3–Ga2O3 system revisited. *Journal of Physics and Chemistry of Solids* 67 (2006) 1901–1907. doi: 10.1016/j.jpcs.2006.03.012

67. U. Shirwadkar, W. H. Rhodes, C. Brecher, G. Baldoni, Y. Wang, M. McClish, T. Gupta, J. Glodo, and K. Shah. Scintillation properties of lanthanum yttrium oxide ceramic for gamma-ray detection. *2014 IEEE Nuclear Science Symposium and Medical Imaging Conference (NSS/MIC)* (2014)1-4. doi: 10.1109/NSSMIC.2014.7431228

68. Osamu Yamaguchi, Hidenao Kawabata, Hiroyuki Hashimoto, Kiyoshi Shimizu. New Modification of $LaYO_3$. *Journal of the American Ceramic Society* 70 (1987) 131-132. doi: 10.1111/j.1151-2916.1987.tb05669.x

69. E. Ruiz-Trejo, M.S. Islam, J.A. Kilner. Atomistic simulation of defects and ion migration in $LaYO_3$. *Solid State Ionics* 123 (1999) 121–129. doi: 10.1016/s0167-2738(99)00092-2

70. D. R. Taikar, Sumedha Tamboli and S. J. Dhoble. Synthesis and photoluminescence properties of red, green and blue emitting $LaYO_3$:M (M = Eu^{3+}, Tb^{3+}, Sm^{3+},Bi^{3+}, Pb^{2+}) phosphors. *Optik* 142 (2017) 183-190. doi: 10.1016/j.ijleo.2017.05.095

71. 71- O. Fabrichnaya, M. J. Kriegel, J. Seidel, G. Savinykh, L. P. Ogorodova, I. A. Kiseleva, H. J. Seifert. Calorimetric investigation of the $La_2Zr_2O_7$, $Nd_2Zr_2O_7$, $Sm_2Zr_2O_7$ and $LaYO_3$

compounds and CALPHAD assessment of the La_2O_3–Y_2O_3 system. *Thermochimica Acta* 526 (2011). 50–57. doi: 10.1016/j.tca.2011.08.021

72. William M. Yen, Shigeo Shionoya, Hajime Yamamoto. Phosphor Handbook. 2nd Edition. CRC Press, Boca Raton (2007). ISBN: 0-8493-3564-7

73. Arunachalam Lakshmanan (editor). Luminescence and display phosphors: phenomena and applications. Nova science publishers, Inc, (2008), New York. ISBN: 978-1-60456-018-3.

74. C. R. Ronda, T. Jüstel, H. Nikol. Rare Earth Phosphors: Fundamentals and Applications. *Journal of Alloys and Compounds* 275–277 (1998) 669–676. doi: 10.1016/S0925-8388(98)00416-2

75. G. Balachandran. Extraction of Rare Earths for Advanced Applications. *Treatise on Process Metallurgy* 3 (2014) 1291-1340. doi: 10.1016/B978-0-08-096988-6.09983-1

76. C. Michael Bourget. An Introduction to Light-emitting Diodes. *HortScience 43* (2008) 1944–1946. doi: 10.21273/HORTSCI.43.7.1944

77. FengWang, Xiao-KeLiu, FengGao. Advanced Nanomaterials for Solar Cells and Light-Emitting Diodes || *Fundamentals of Solar Cells and Light-Emitting Diodes* (2019) 1-35. doi: 10.1016/B978-0-12-813647-8.00001-1

78. Z. Wu, Z. Xia, Phosphors for white LEDs. *Nitride Semiconductor Light-Emitting Diodes (LEDs)* (2018)123–208. doi: 10.1016/b978-0-08-101942-9.00005-8

79. G. B. Nair, S. J. Dhoble. Fundamentals of LEDs. *The Fundamentals and Applications of Light-Emitting Diodes* (2021) 35–57. doi: 10.1016/b978-0-12-819605-2.00002-1

Chapter three

Preparation methods of phosphors

3.1. Introduction

In recent years phosphor preparation methods have been improved, which can control the size and shape of particles. Phosphor materials have been prepared by different methods, such as solid-state reactions [1], combustion synthesis [2, 3], sol-gel processing [4], precipitation [5], mechanochemical grinding [6] liquid-phase method [7] and hydrothermal synthesis [8], etc.

Usually, the solid-state reaction method is used to prepare phosphor materials. In this method, extensive mechanical mixing and high temperature annealing for a long period of time are required [9]. Solid-state reaction method has many advantages such as higher purity of outputs, good compositional control, widespread production, and solvent/surfactant-free processes.

The advantages of combustion synthesis are in its ability to produce well-crystallized, fine particle size powders rapidly without extensive high temperature annealing and mechanical separation steps. Grinding is often involved in the degradation of the intensity of the luminescent emission by creating surface defects that quench the emission [10].

Due to their advantages, the sol-gel combustion and solid-state synthesis have been used in this research study, and are discussed in further detail.

3.2. Sol-gel combustion method

The attraction of the sol-gel combustion synthesis is that it uses a unique combination of the chemical sol-gel process and combustion method which requires relatively simple equipment and produces samples in a short period of time [11]. Preparation of ceramic oxides using sol-gel combustion synthesis provides, in a single step, a product with high purity, good homogeneity, high surface area and low processing temperature [12]. Sol-gel combustion synthesis is based on the gelling and subsequent combustion of an aqueous solution containing a nitrate of the desired metals and an organic fuel (e.g. citric acid) and it yields a voluminous and fluffy product with a large surface area [13]. Glycine and urea are also appropriate fuels since they are amino acids and

can perform as a complexing agent of the metal ion and also act as fuel for the synthesis of oxide powders. This method can directly reach the final powders, or in some cases, a calcination is required [14].

In recent years, sol-gel process of ceramic has found much of interest because of its use to prepare materials with specific electronic, mechanical and optical properties due to the chemistry and microscopic structure of the solid that determines its characteristics. By this method the composition and structure at the molecular level can be controlled [14]. Reference [15] gives a brief, good description of the process. Figure 3.1 is a schematic diagram for the preparation of $LaGaO_3$:Bi powders by the citric acid sol-gel combustion process.

In the citric acid sol–gel combustion method, which is used in this research study to prepare $LaGaO_3$ and $LaYO_3$, the raw materials, which are usually a nitrate compound and a fuel (citric acid), are dissolved in water. The mixed solution is then heated to transform the sol into a high-viscosity gel. Increased gel temperature leads to an exothermic combustion process. After the combustion is complete, the resulting powder colour was brown, which indicates that it contains some remaining carbon because of the incomplete combustion of citric acid [16]. Heating the resulting brown powder at different temperatures between 800 °C and 1400 °C produced the final product (white powder), where the carbon impurity can be oxidized above 600 °C [16] and released as gaseous CO_2.

Sol-gel combustion process has several advantages such as, good control of stoichiometry, low-temperature and low cost process, high-quality nano/microcrystal and high purity product, production capability of multicomponent oxides with single phase and high surface area [10]. The exothermic reaction makes the product almost immediately and the product can be easily crushed and ground into a fine powder without the need for sophisticated equipment.

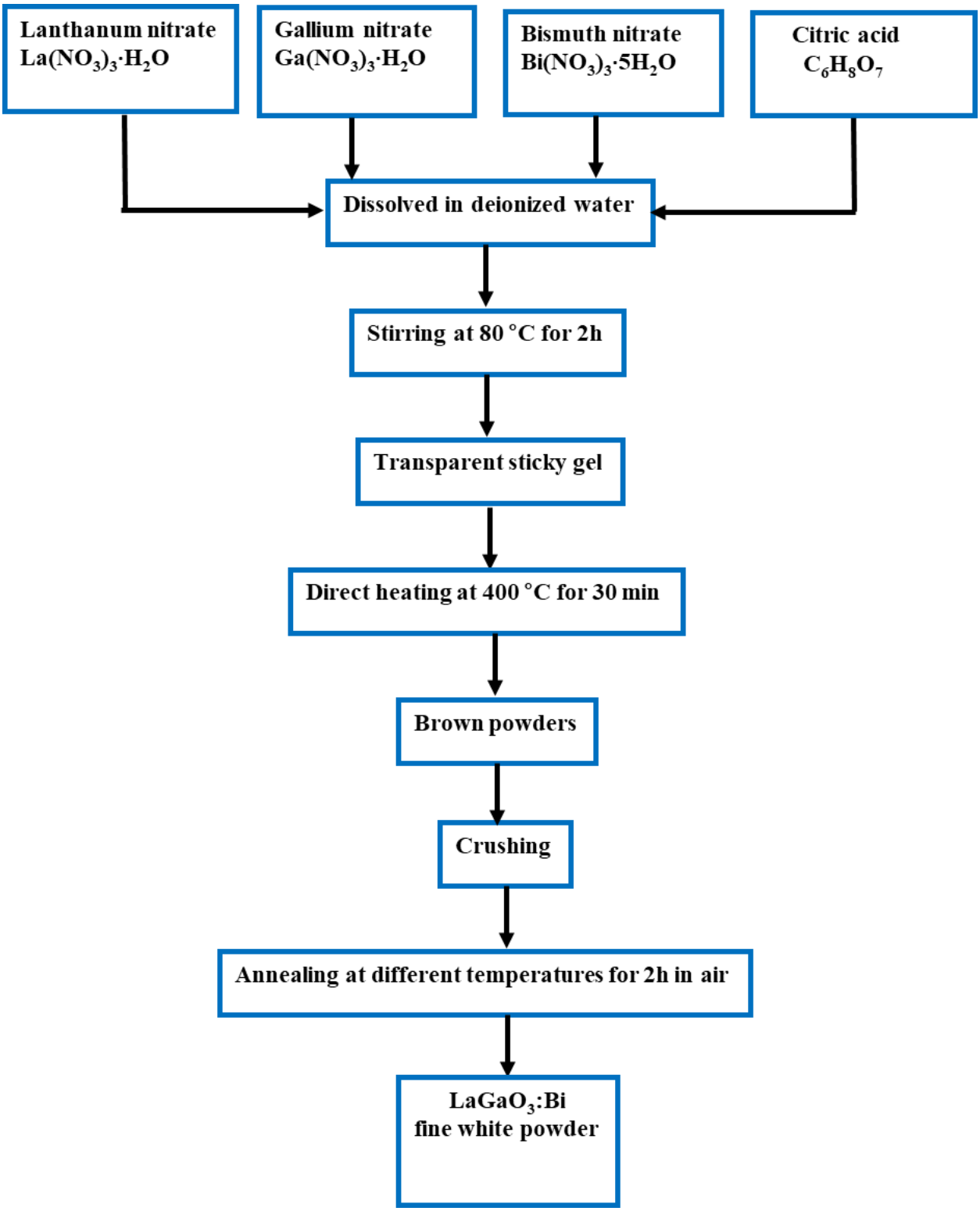

Figure 3.1: Schematic diagram for preparation of $LaGaO_3$:Bi powders by the citric acid sol-gel combustion method.

3.3. Solid-state reaction method

The solid-state reaction method or ceramic synthesis is a high-temperature synthesis method to prepare luminescent material. The solid state reaction method is widely employed to prepare complex oxides from a mixture of simple oxides, nitrates, carbonates, hydroxides, alkoxides, oxalates, and other metal salts. The interaction of solids with each other is not done naturally at room temperature, but samples must be heated to much higher temperatures until the reaction occurs at a suitable rate. There are several factors on which the feasibility and rate of the solid-state reaction depend, such as reaction conditions, structural characteristics of reactive materials, surface area and interaction of solids and change of free thermodynamic energy associated with interaction [17].

In the solid state reaction synthesis, which was utilized in this research study to synthesize LaOX (X = Cl, Br and F) phosphor powder, the raw materials were lanthanum oxide with high purity and ammonium chloride, ammonium bromide and ammonium fluoride which were used as a sources of chlorine, bromine and fluorine, respectively. The required quantities of raw chemicals were weighed, mixed and ground to a fine powder using an agate mortar and pestle. Sometimes, ethanol or acetone were used as a mixing medium to get a homogeneous mixture. The ground powder was transferred to alumina/porcelain crucibles and annealed at high temperature for a certain period of time, followed by dry grinding.

Figure 3.2: Schematic diagram for preparation of LaOCl:Bi powders by the solid state reaction synthesis.

3.4. Pulsed-laser deposition (PLD)

In 1965, Smith and Turner used a pulsed ruby laser to deposit a thin film in a vacuum atmosphere for the first time [18]. Four years later, thin films were produced from $SrTiO_3$ and $BaTiO_3$ powders by using pulsed laser evaporation [19]. Since then, PLD has been commonly used for the preparation of thin films of various metal oxides, complex metal oxides, insulators, semiconductors, polymer and biological materials, borides, carbides and nitrides [20]. PLD is a relatively new technique for depositing thin film using high-energy laser pulses to evaporate the surface of the material target inside a vacuum chamber and condensing the steam on the surface of the substrate to create a thin film layer with a thickness of up to a few micrometres [21]. The PLD technique has a high ability to control the formation of thin-film, morphology, composition, and growth process by adjusting the partial pressure of an ambient gas (e.g. oxygen). It can also be tuned by varying the substrate temperature, the energy of the depositing flux, and the relative and absolute arrival rates of atoms. Background gas and pressure can be varied as well, all of which effect the growth of the film. Background gas can be used to decrease the kinetic energy of the plume and to increase the number of chemical reactions between the plume and gas.

Most of the substances used in PLD have strong absorption in the ranges between 200 nm and 400 nm of laser wavelengths; which can easily achieve the energies required to convert a material into a plasma [22]. The process of forming a thin film in the PLD technique generally involves five basic stages (Figure 3.3):

1. Absorption of the laser by the target material.
2. Laser ablation of the target material and the formation of the plasma.
3. Plasma dynamics.
4. Deposition of the ablation material on the substrate.
5. Nucleation and growth of the required film.

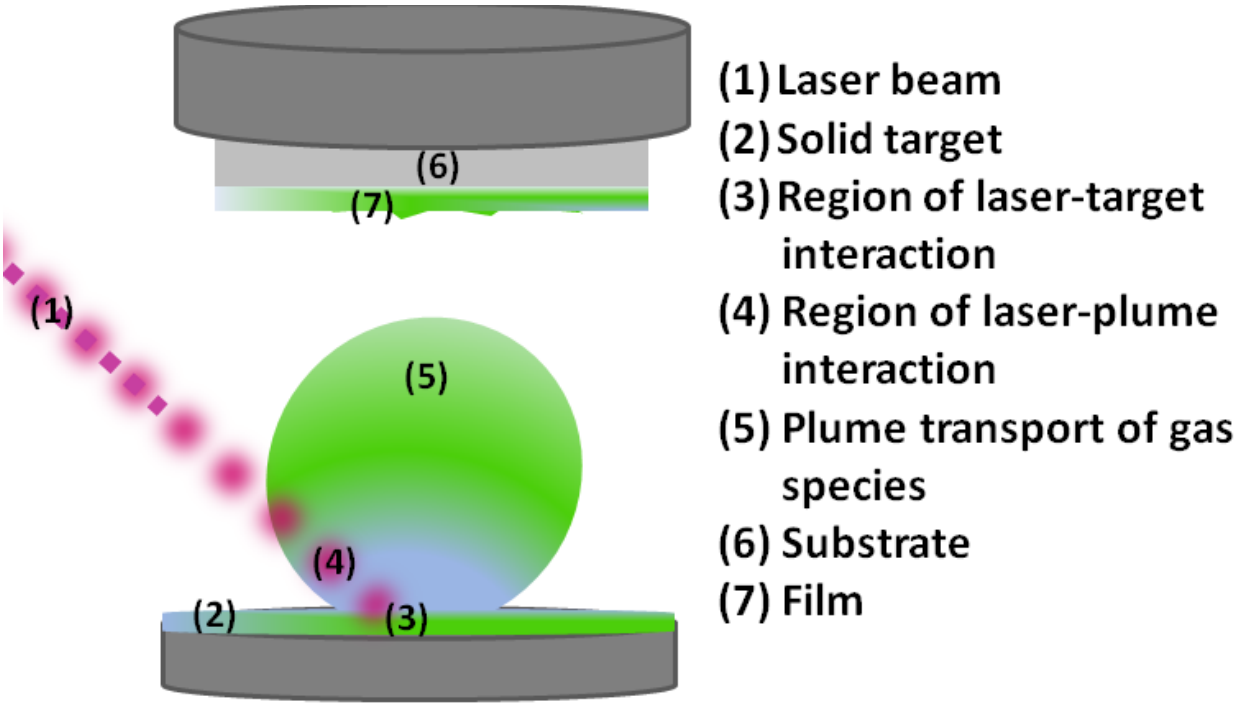

Figure 3.3: A schematic of the laser ablation process and its stages up to thin film formation [23]

The basic principles of PLD technique is quite simple, as shown schematically in figure 3.4. The high-power pulsed laser beam focused on the surface of a target material to vaporize, ionize and melt in either an ultrahigh vacuum chamber or in the presence of background gases (such as argon, oxygen and nitrogen) [24]. When the laser beam hits the surface of a target material, if the absorbed laser pulse has sufficient energy ablation will occur on the surface of the target. Ablation is the removal of the material from the surface of a target by ionization or vaporization processes [25]. After that, a plasma plume forms from the target surface. This plasma plume expands along a direction normal to the surface of the target. Then some of the evaporated plasma plume material is deposited on the substrate which is mounted in front of the target to create a thin film [26]. The laser beam is focused by a lens into a rotating target. The laser beam is incident on the target at an angle of 45°.

Argon fluoride (ArF) and krypton fluoride (KrF) excimer lasers with the wavelength of 193 and 248 nm, respectively, or Nd:YAG lasers are usually used as the deposition energy sources. The Nd:YAG laser is simple in maintenance and provides a compact system compared to an excimer lasers. The excimer lasers have high flexibility in the repetition rate, high pulse energy in the

ultraviolet range and high stability. The Nd:YAG 266 nm pulsed laser was used as the deposition sources in this research study to ablate the phosphor pellets in vacuum, argon and oxygen atmospheres. The laser energy (40 mJ/pulse), fluency and target-to-substrate distance fixed at 30 Hz, 1.7 J/cm^2 and 4.5 cm, respectively. The laser deposition time was 20 min and the substrate temperature was fixed at 300 °C. The deposition chamber was evacuated to a base pressure of 5x10^{-5} mbar.

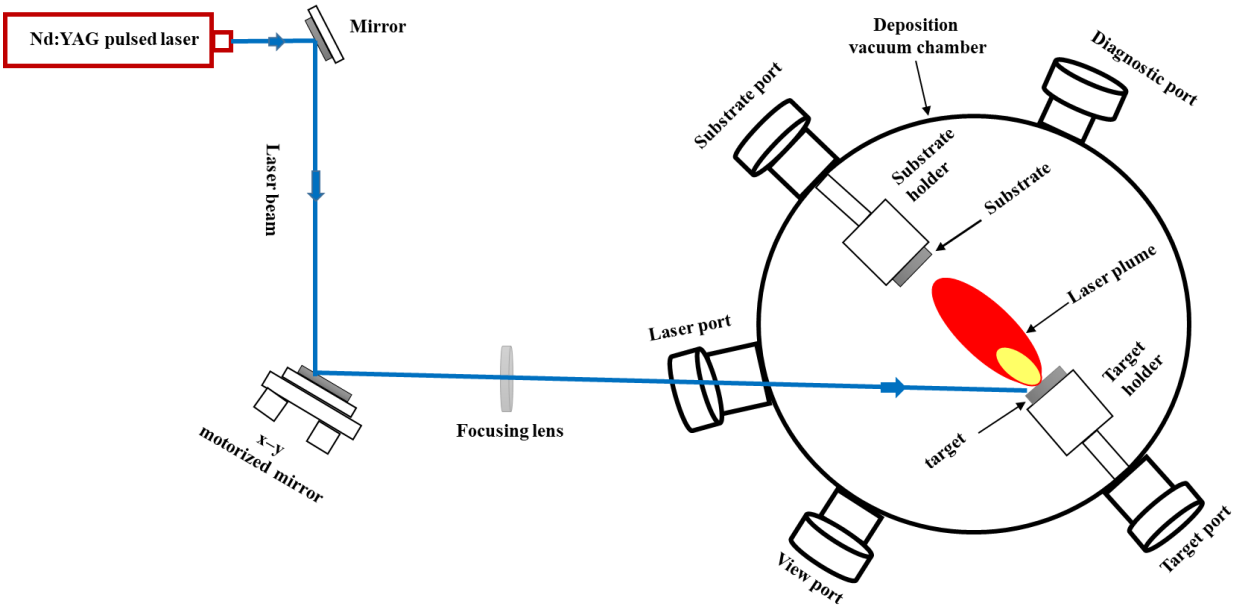

Figure 3.4: Schematic diagram of the PLD process [27].

3.4.1 Advantages of PLD

PLD system has some outstanding advantages compared to other systems used to prepare thin films deposition, like metalorganic vapour phase epitaxy (MOVPE), physical vapour deposition and chemical vapour deposition (CVD), magnetron sputtering, sol-gel and spray pyrolysis.

- PLD technology conceptually is a simple and flexible process in engineering design.
- The laser radiation evaporates the surface of the target and generally produces a film with the same composition as the target [28].

- PLD technique has a high ability to control the formation of thin-film, morphology, composition, and growth process by altering the partial pressure of gas like ambient oxygen pressure [21].
- The growth rate of the film can be controlled by varying the laser parameters, deposition time, the distance between the target and the substrate, etc. [28].
- PLD is inexpensive compared to some other techniques e.g. a single laser device can serve several vacuum systems and is able to produce multiple layers simply by switching between many different targets [29].
- A reliably and high-quality sample can be grown in less than an hour, so the method is fast [30].
- PLD is versatile. A very large range of substances can be prepared by PLD including metal oxides, complex metal oxides, insulators, semiconductors, polymer and biological materials, borides, carbides and nitrides. All that is needed is the desired composition target. It differs from other thin film deposition techniques such as (CVD) and (MBE) which require a different source of precursors for each component of the compound [20].

3.4.2. Disadvantages of PLD

Irregular particle size may occur on the surface of the film. This due to the presence of molten substance (up to ~ 10 μm) in the ablated substance [31]. There is a substantial splashing associated with the laser ablation itself, which produces large drops or molecules of the target material on the surface of the substrate, which is particularly dangerous because it will lead to the failure of the device, from the industrial perspective [32].

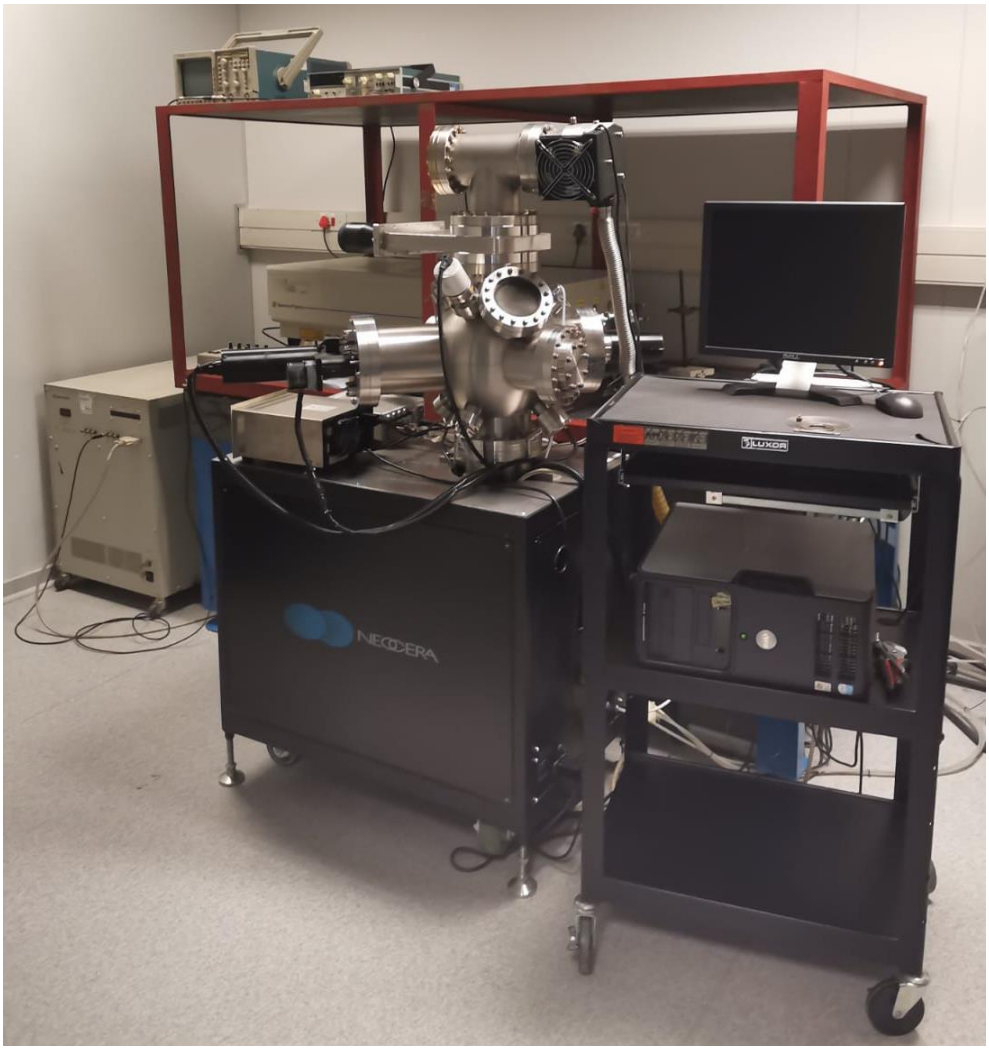

Figure 3.5: PLD technique at the University of the Free State at the Department of Physics.

3.5. References

1. Sangmoon Park, Cho, So-Hye. Spectral-converting study of $La_{1-m-n}Er_mYb_nOCl$ (m=0.001–0.2, n=0–0.1) phosphors. *Journal of Luminescence* 153 (2014) 90–95. doi: 10.1016/j.jlumin.2014.03.023
2. B.M. Jaffar, HC. Swart, H.A.A. Seed Ahmed, A. Yousif, R.E. Kroon. Luminescence properties of Bi doped La_2O_3 powder phosphor. *Journal of Luminescence* 209 (2019) 217–224. doi: 10.1016/j.jlumin.2019.01.044

3. Singanahally T. Aruna, Alexander S. Mukasyan. Combustion synthesis and nanomaterials. *Current Opinion in Solid State and Materials Science* 12 (2008) 44–50. doi: 10.1016/j.cossms.2008.12.002
4. A. Khorsand Zak; W.H. Abd. Majid; Majid Darroudi (2012). Facile synthesis and characterization of lanthanum (III) oxychloride nanoparticles using a natural polymeric matrix. *Materials Chemistry and Physics* 136 (2012) 705-709. doi: 10.1016/j.matchemphys.2012.07.045
5. H.V. Lee, J.C. Juan, Y.H. Taufiq-Yap. Preparation and application of binary acid–base CaO–La2O3 catalyst for biodiesel production. *Renewable Energy* 74 (2015) 124–132. doi: 10.1016/j.renene.2014.07.017
6. Jaeryeong Lee, Qiwu Zhang, Fumio Saito. Mechanochemical Synthesis of LaOX (X=Cl, Br) and Their Solid State Solutions. *Journal of Solid State Chemistry* 160 (2001) 469-473 doi: 10.1006/jssc.2001.9276
7. Sun Woog Kim, Kazuya Jyoko, Toshiyuki Masui, Nobuhito Imanaka. Green-emitting (La,M,Tb)OCl (M = Mg, Ca, and Sr) phosphors. *Optical Materials* 35 (2012) 280-284.doi: 10.1016/j.optmat.2012.08.022
8. Chunjie Wang, Yue Wang, Yongliang Cheng, Ling Zhu, Binglin Zou, Yu Zhao, Wenzhi Huang, Xizhi Fan, Zuhair Subhani Khan, Xueqiang Cao. Synthesis of nanocrystalline La_2O_3–Y_2O_3–ZrO_2 solid solutions by hydrothermal method: A crystal growth and structural study. *Journal of Crystal Growth* 335 (2011) 165–171. doi: 10.1016/j.jcrysgro.2011.09.026
9. Feliksas Ivanauskas, Aivaras Kareiva, Bogdanas Lapcun. On the modelling of solid state reactions.Synthesis of YAG. *Journal of Mathematical Chemistry* 37 (2005) 365–376. doi: 10.1007/s10910-004-1103-2
10. William M. Yen and Marvin J. Weber. Inorganic phosphors: compositions, preparation, and optical properties. CRC Press, Boca Raton (2004). ISBN 0-8493-1949-8
11. Chi-Hwan Han, Hak Soo Lee, and Sang Do Han. Synthesis of Nanocrystalline $TiO_2$by Sol-Gel Combustion Hybrid Method and Its Application to Dye Solar Cells. *Bulletin of the Korean Chemical Society* 29 (2008) 1495–1498. doi: 10.5012/bkcs.2008.29.8.1495
12. Yingchao Han, Shipu Li, Xinyu Wang, Xiaoming Chen. Synthesis and Sintering of Nanocrystalline Hydroxyapatite Powders by Gelatin-Based Precipitation Method. *Materials*

Research Bulletin 39 (2004) 25–32. doi: 10.1016/j.ceramint.2005.09.001

13. Lixin Song, Pingfan Du, Jie Xiong, Xiaona Fan, Yuxue Jiao. Preparation and Luminescence Properties of Terbium-Doped Lanthanum Oxide Nanofibers by Electrospinning. *Journal of Luminescence* 132 (2012) 171–174. doi: 10.1016/j.jlumin.2011.08.007
14. Jafar Baseri, Rahim Naghizadeh, Hamid Reza Rezaie, Farhad Golestanifard, Mohammad Golmohammad. A comparative study on citrate sol-gel and combustion synthesis methods of $CoAl_2O_4$ spinel. *International Journal of Applied Ceramic Technology* 17 (2020) 2709–2715. doi: 10.1111/ijac.13598
15. A. Khorsand Zak, M. Ebrahimizadeh Abrishami, W. H Abd Majid, Ramin Yousefi, S. M. Hosseini. Effects of Annealing Temperature on Some Structural and Optical Properties of ZnO Nanoparticles Prepared by a Modified Sol-Gel Combustion Method. *Ceramics International* 37 (2011) 393–398. doi: 10.1016/j.ceramint.2010.08.017
16. Karim Khan, Ayesha Khan Tareen, Sayed Elshahat, Ashish Yadav,Usman Khan, Minghui Yang, Luigi Bibbò and Zhengbiao Ouyang. Facile synthesis of a cationic-doped $[Ca_{24}Al_{28}O_{64}]^{4+}(4e^-)$ composite via a rapid citrate sol–gel method. *Dalton Transactions* 47 (2018) 3819-3830. doi: 10.1016/10.1039/c7dt04543c
17. Anthony. R. West. Solid state chemistry and its applications. 2nd edition. Wiley and Sons, (2005). ISBN 978-1-119-94294-8.
18. Howard M. Smith and A. F. Turner. Vacuum Deposited Thin Films Using a Ruby Laser. *Applied Optics* 4 (1965) 147-148. doi: 10.1364/AO.4.000147
19. Helmut Schwarz and H. A. Tourtellotte. Vacuum Deposition by High-Energy Laser with Emphasis on Barium Titanate Films. *Journal of Vacuum Science and Technology* 6 (1969) 373-378. doi: 10.1116/1.1492696
20. J. Orava. Chalcogenide Glasses || Deposition techniques for chalcogenide thin films. (2014) *265–309.* doi: 10.1533/9780857093561.1.265
21. Z. Liu. Shreir's Corrosion || Laser Applied Coatings. (2010) 2622–2635. doi: 10.1016/B978-044452787-5.00141-4
22. D. Bäuerle. Thin-Film Formation by Pulsed-Laser Deposition and Laser-Induced Evaporation. Laser Processing and Chemistry, (2011) 489–531. doi: 10.1007/978-3-642-17613-5_22
23. A. Yousif. Luminescent properties of $Y_3(Al, Ga)_5O_{12}$:Tb thin films. PhD thesis, University of the Free State (2014).

24. John Wiley and Sons, Pulsed laser deposition of thin films. Hoboken, New Jersey (2007). ISBN-13: 978-0-471-44709-2
25. Michael N. R. Ashfold, Frederik Claeyssens, Gareth M. Fuge and Simon J. Henley. Pulsed laser ablation and deposition of thin films. *Chemical Society Reviews* 33 (2004) 23–31. doi: 10.1039/B207644F
26. M. C. RAO. Pulsed laser deposition — ablation mechanism and applications. International Journal of Modern Physics: Conference Series 22 (2003) 355-360. doi: 10.1142/S2010194513010362
27. Omer Nur. Low Temperature Chemical Nanofabrication || Conventional nanofabrication methods. (2020) 49–86. doi: 10.1016/B978-0-12-813345-3.00003-4
28. T. Yoshitake, T. Hara and K. Nagayama. The influence of the repetition rate of laser pulses on the growth of diamond thin films by pulsed laser ablation of graphite. *Diamond and Related Materials* 12 (2003) 306–309. doi: 10.1016/S0925-9635(02)00333-3
29. R. Manoj. Characterisation of Transparent Conducting Thin Films Grown by Pulsed Laser Deposition and RF Magnetron Sputtering. Department of Physics Cochin University of Science and Technology Cochin – 682 022, Kerala, India, (2006).
30. A. Yousif, V. Kumar, H. A. A. Seed Ahmed, S. Som, L. L. Noto, O. M. Ntwaeaborwa and H. C. Swart. Effect of Ga^{3+} Doping on the Photoluminescence Properties of $Y_3Al_{5-x}Ga_xO_{12}:Bi^{3+}$ Phosphor. ECS J. Solid State Sci. Technol. 3(11) (2014) R222–R227. doi: 10.1149/2.0021412jss
31. S. N. Ogugua. Preparation and characterization of powders and pulsed laser deposited thin films of rare-earths doped oxyorthosilicates. PhD thesis, University of the Free State (2017).
32. Y. Hsiu. Structure and properties of transparent conductive ZnO films grown by pulsed laser deposition (PLD). MSc thesis, The University of Birmingham (2009).

Chapter four

Theory of characterization techniques

4.1. Introduction

This chapter presents a brief description of the various research techniques used to characterize the phosphor powders and thin films. These techniques include: **X-ray diffraction** (XRD) - to study the crystalline structure and the phase quality of the samples prepared and to determine the crystallite size; **Scanning electron microscopy** (SEM) - to study the surface morphology; **Energy dispersive spectroscopy** (EDS) - to study the chemical composition of the samples; **Ultraviolet–visible spectroscopy** (UV-vis) and **diffuse reflectance spectroscopy** (DRS) - to study the absorption wavelengths and determine the bandgap of the materials; **Photoluminescence spectroscopy** (PL) - to study the excitation, emission luminescence properties; and **Cathodoluminescence spectroscopy** (CL) - to study the light emission of phosphors when exposed to an electron beam.

4.2. X-ray diffraction (XRD)

X-rays were discovered in 1895 by Roentgen and are a form of electromagnetic radiation with wavelength ranging from 0.1 up to 10 nm, located in the range between ultraviolet rays and gamma rays. X-rays have a high ability to penetrate solid materials and give information about their internal crystalline composition. X-rays have unique features, which can be used well in imaging, scattering measurements and spectroscopy [1, 2].

The XRD technique was discovered by Von Laue in 1912. XRD can be used for identification of the degree of crystallinity, analysis of lattice parameters, phase identification and crystallite size determination. It can also be used to determine the crystalline structure of solid substances of powders, thin films, fibres, sheets metals, organics, ceramics, polymers and electronic materials [3]. The basic principles of this technique consists of the interaction between the incident X-ray radiation and the sample material. The diffractometer for XRD consists of three main elements: an X-ray source, a sample holder and an X-ray detector [4] as shown schematically in figure 4.1.

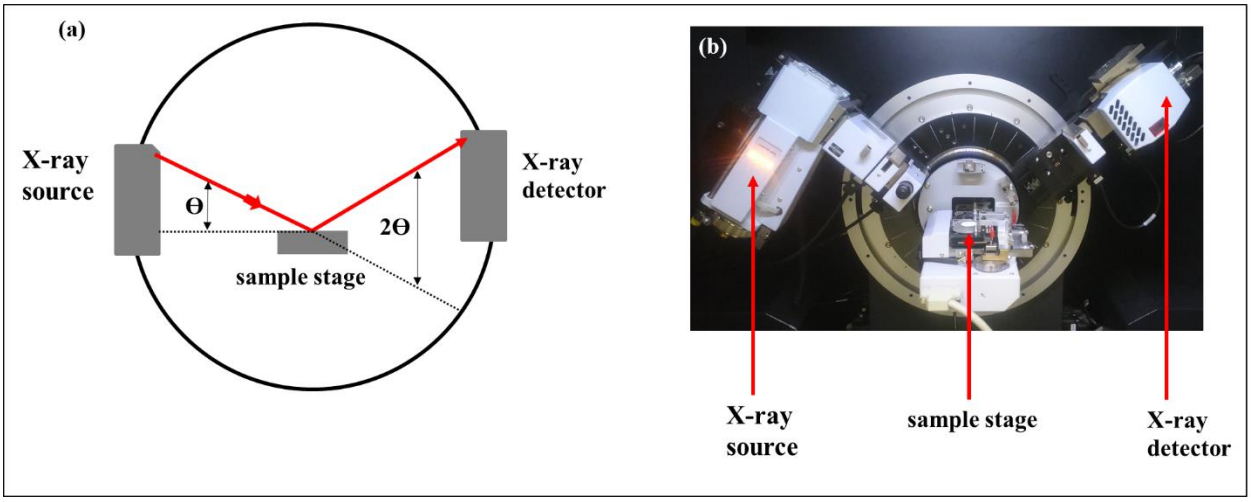

Figure 4.1: The X-ray diffractometer (a) diagrammatic representation (b) Photograph of a commercial system.

X-rays are usually produced either by synchrotron radiation or X-ray tubes. In an X-rays tube, which is the primary source of X-rays used in laboratory instruments, X-rays are generated by heating a tungsten filament to release electrons, which are accelerated towards a target anode. When the incident electrons interact with the electrons in the core-shell of the anode material, X-ray photons with energy characteristic of the anode substance are emitted. The characteristic spectrum consists of different components, e.g. Kα and Kβ are the most common components, with a specific characteristic wavelengths. The most common material used as a target is Cu. The wavelength (**λ**) of Cu Kα radiation is 0.15406 nm. A monochromator can be used to select a single wavelength from the source, or a nickel (Ni) β-filter can be used with Cu anode for this purpose. Ni can absorbs X-rays below 0.15 nm and can be used to filter the Kβ X-rays from Cu [4], as presented in figure 4.2.

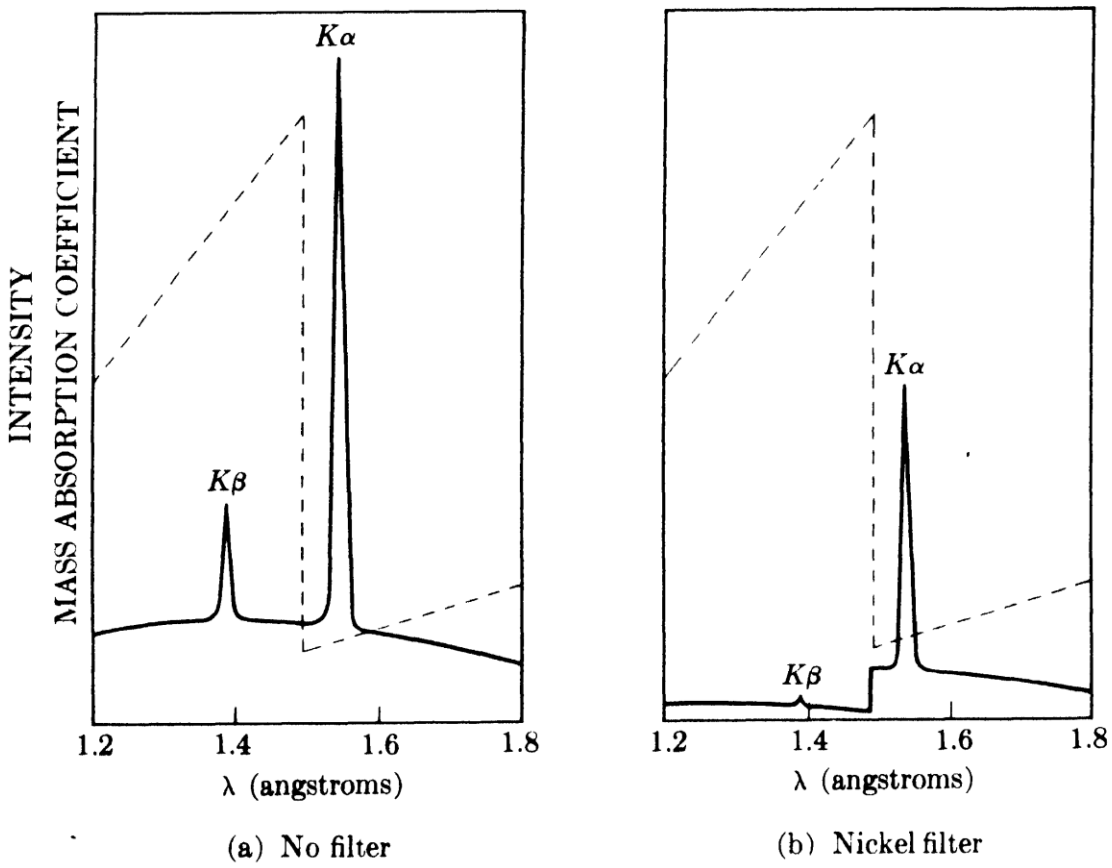

Figure 4.2: Copper X-ray radiation (a) before and (b) after passage through a nickel filter [5].

The interaction of incident X-rays with crystalline substance creates interference and some of the incident beams are diffracted constructively by the crystalline phases of the substance when the condition for Bragg's law is satisfied, as shown in figure 4.3. The parallel X-rays are projected onto crystal planes at an angle θ. The crystal planes diffract the rays and constructive interference occurs when the difference in the path is equal to a whole number of wavelengths. Bragg's law is given by:

$$n\lambda = 2d \sin\theta \quad \ldots\ldots\ldots\ldots\ldots\ldots\ldots\ldots\ldots\ldots (4.1)$$

where n is an integer that indicates the order of the reflection, θ is Bragg angle and d is the inter-planar distance. If the X-ray wavelength is known, the inter-planar distance can be obtained by measuring the Bragg angle [6].

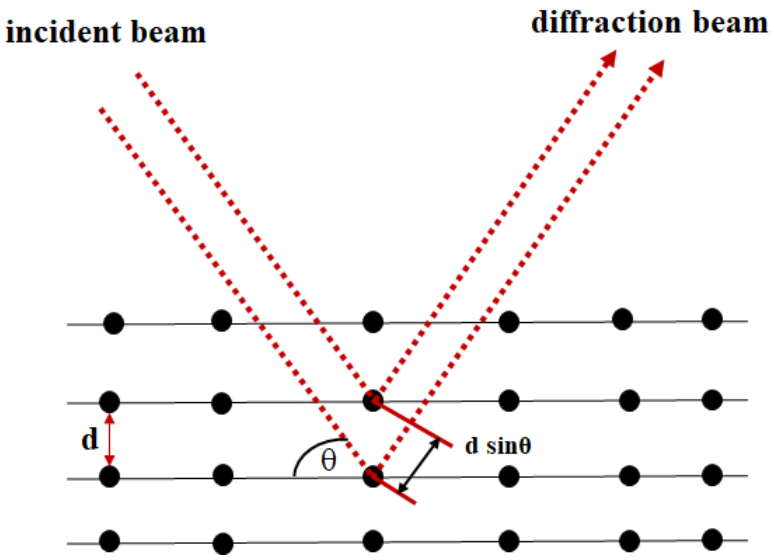

Figure 4.3: Schematic diagram showing the diffraction of X-rays from atoms and Bragg's law.

There is a relationship between Miller indexes (*hkl*) and lattice parameters for each reflection plane and the inter-planar distance (d_{hkl}). For instance, for cubic structures with a lattice parameter *a*, it can be formulated as [7].

$$d_{hkl} = \frac{a}{\sqrt{h^2+k^2+l^2}} \quad \ldots\ldots\ldots\ldots\ldots\ldots\ldots\ldots\ldots\ldots \quad (4.2)$$

The crystallite size, D, can be determined from the broadened peaks of the XRD spectra via using the Scherrer formula [8].

$$D = \frac{K\lambda}{\beta cos\theta} \quad \ldots\ldots\ldots\ldots\ldots\ldots\ldots\ldots\ldots\ldots\ldots\ldots \quad (4.3)$$

where λ is the X-ray wavelength, β is the full width at half maximum (FWHM) of a diffraction peak, θ is the Bragg angle and *K* is a constant related to crystallite shape, normally taken as 0.9 [6]. The value of β in 2θ axis of diffraction profile should be in radians. The θ can be in radians or degrees, since cosθ corresponds to the same number.

The average crystallite size and microstrain can be determined by using the Williamson-Hall equation:

$$\beta\cos\theta = \frac{K\lambda}{D} + 4\varepsilon \sin\theta \qquad (4.4)$$

where β is the 2θ full-width-at-half-maximum (in radians) for the diffraction peak at the angle θ, K is the shape factor (taken as 0.94), λ is the X-ray wavelength, D is the crystallite size and ε is the microstrain [9]. If a plot is drawn with 4sinθ along the x-axis and βcosθ along the y-axis, then the crystalline size can be estimated from the y-intercept and the strain ε from the slope of the line.

XRD patterns were collected at the department of Physics of the University of the Free State using a Bruker D8 Advance X-ray diffractometer equipped with a copper anode X-ray tube (figure 4.4). The system was operated using a 40 mA filament current and a generator voltage of 40 kV to accelerate the electrons. Moreover, a nickel filter was used to remove the Cu Kβ X-rays. Measurements were taken with a 2θ step size of 0.02°. It is important to load the samples at the same height, since otherwise small peak shifts may occur.

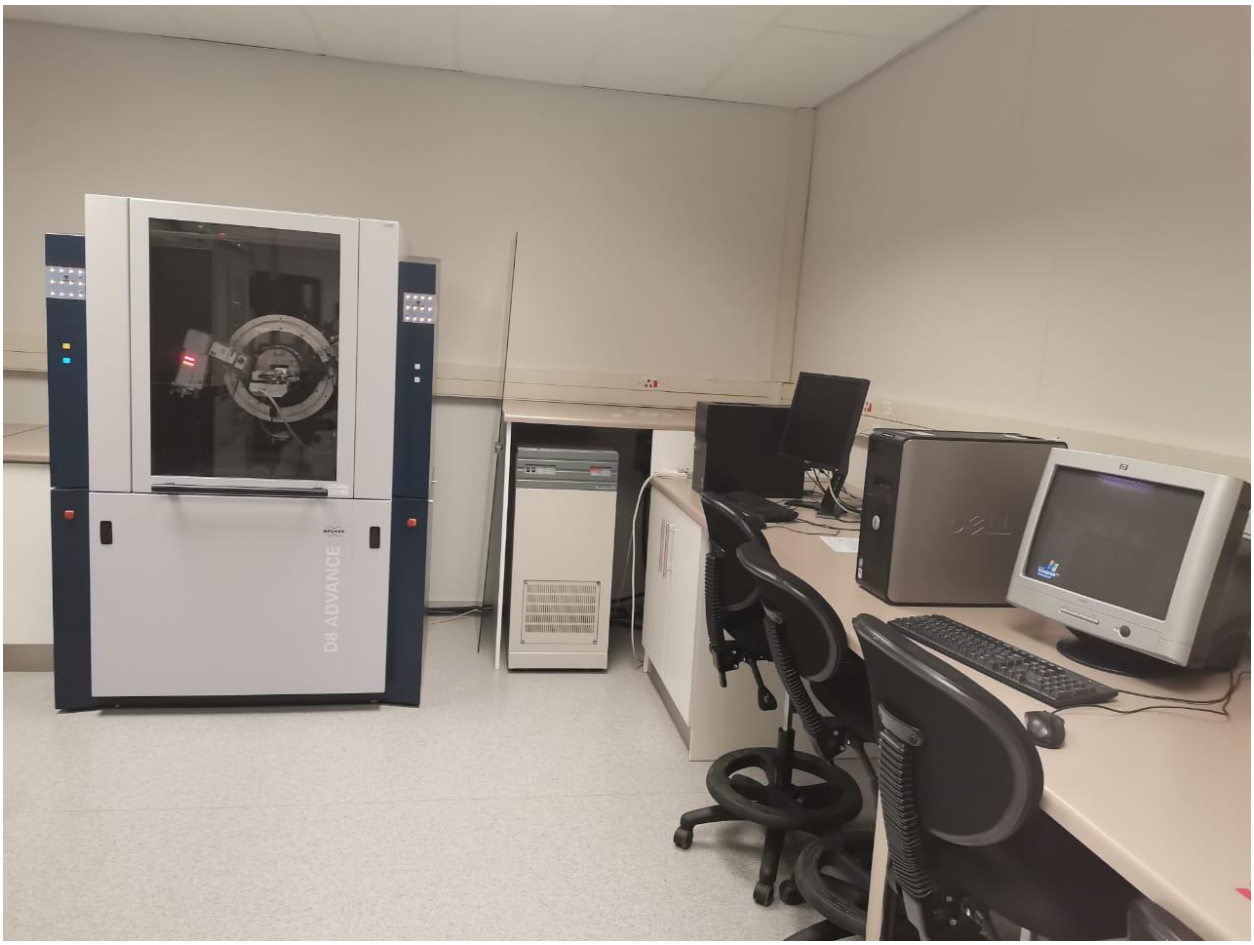

Figure 4.4: The Bruker D8 Advance X-ray diffractometer at the Department of Physics of the University of the Free State.

4.3. Scanning electron microscopy (SEM)

SEM is a technique widely used to analyse the microstructure and morphology of materials by using a focused beam of electrons to scan the surface of the substance and provide images of the topography and morphology of the sample [10]. Additional information about the elemental composition of the substance can also be provided if the system is equipped with an energy dispersive X-ray spectrometer (EDS), which will be described in the next section. The basic principle of the SEM technique depends on the interaction between an incident electron beam and a solid substance. During SEM measurements, the electron beam is generated from electron gun and then focused and accelerated towards the surface of the substance by electromagnetic lenses and is rastered by pairs of coils in the objective lens on the surface of the substance. Figure 4.5 displays a simple diagram of scanning electron microscopy. When the incident electrons interact

with the surface of the material, various types of electromagnetic radiation and electrons are generated from different depths including: secondary electrons, back-scattered electrons, characteristic X-rays, cathodoluminescence, Auger electrons, specimen current and transmitted electrons [11]. Figure 4.6 presents the main signals emitted as a result of electron beam interaction with the surface of the sample. The secondary electrons and backscattered electrons are the most important signals that are detected to produce SEM images. Secondary electrons are used principally for topographic contrast in the SEM (i.e., for the visualization of surface texture and roughness), while backscattered electrons are used for illustrating contrasts in compositions in multiphase samples (i.e. for rapid phase discrimination) [12].

The SEM measurements in this research study were done by using a JEOL JSM-7800F scanning electron microscope (figure 4.7) equipped with EDS. It provides extreme resolution of 0.8 nm at 15 kV and 1.2 nm at 1 kV and magnification from ×25 to ×1,000,000. A Schottky field-emission gun was used to produce the electrons [13]. The SEM image collection in this study was done with a 5 kV electron beam.

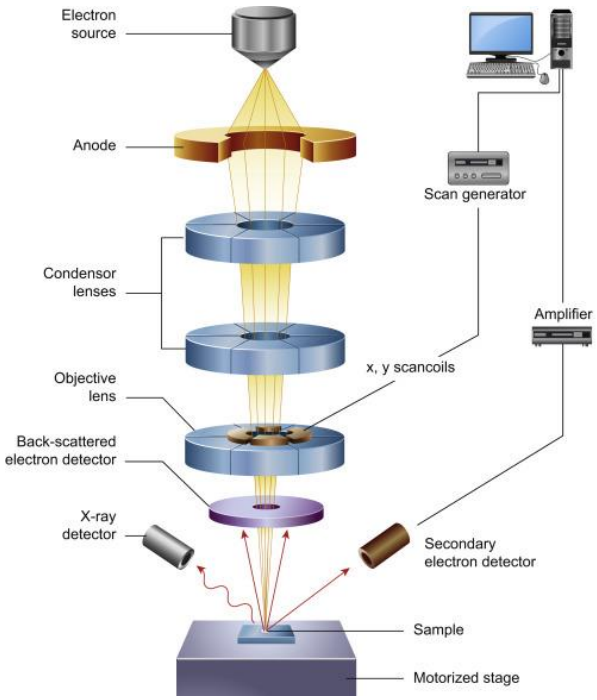

Figure 4.5: Schematic diagram of a typical SEM [14].

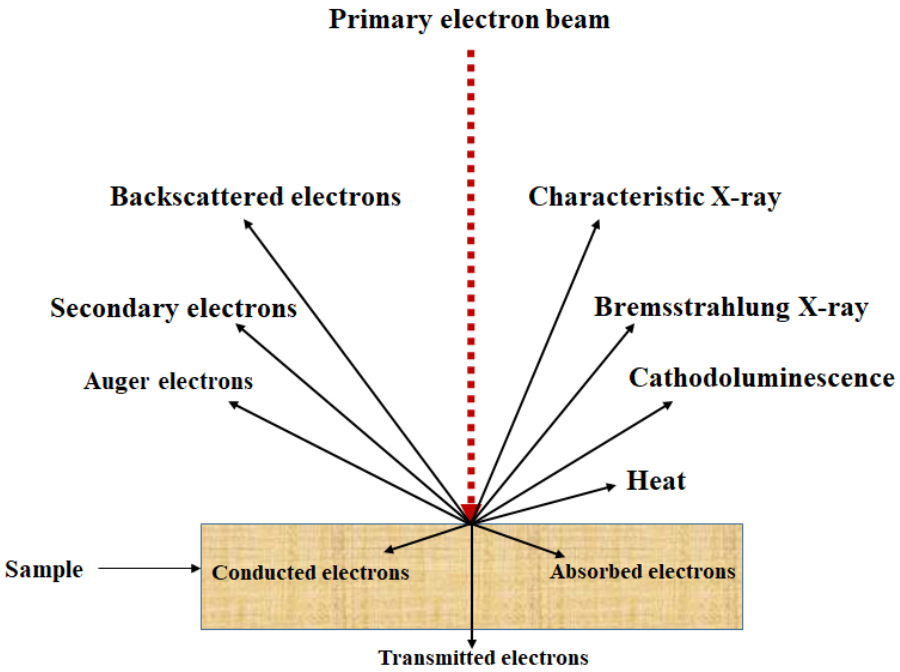

Figure 4.6: The signals produced from electron beam interaction with solid matter.

Figure 4.7: JEOL JSM-7800F system at the Centre for Microscopy at University of the Free State.

4.4. Energy dispersive X-ray spectroscopy (EDS)

EDS is an analytical technique used to analyse elements in a sample. It is also used in conjunction with scanning electron microscopy (SEM) to detect the X-rays emitted from the sample when it is bombarded by an electron beam to describe the elemental composition of the material under analysis. Features or phases as small as 1 μm can be analysed [15].

When the sample is bombarded by the SEM's electron beam, this beam interacts with the atoms inside the sample which become excited, resulting in the ejection of an electron from the inner shell of the sample atom and leaving a hole behind. The resulting holes are filled by electrons from a higher state, and a characteristic X-ray with specific energy related to the element of the atom is emitted to balance the energy difference.

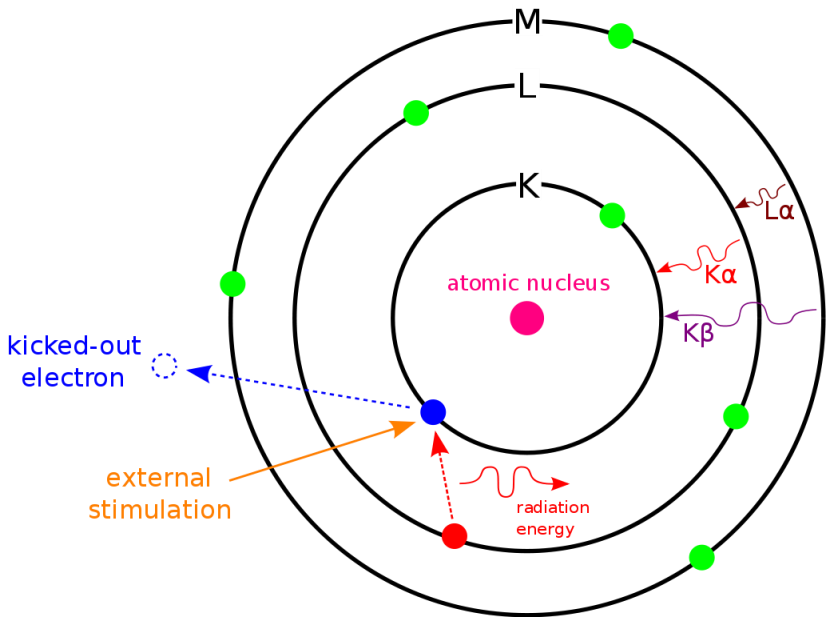

Figure 4.8: Schematic diagram of emitted characteristic X-rays in an atom [16].

The counts and energy of the emitted X-rays can be measured by using the EDS X-ray detector. When an incident X-ray hits the detector device, it makes a charge pulse that is proportional to the energy of the X-ray. The charge pulse is transformed to a voltage pulse by the sensitive preamplifier of the charge. The signal then will send to a multichannel analyser where the pulses are sorted by voltage. The energy (as specified from the voltage measurement) for each incident X-ray is sent to a computer for display and further evaluation of the data. The X-ray energy

spectrum against counts is assessed to determine the elemental composition of the sampled size [17].

In this study the chemical compositions of the phosphor powders and thin films were obtained using an X-Max^{N}80 detector from Oxford Instruments in the SEM as shown in Figure 4.7.

4.5. Ultraviolet-visible spectroscopy (UV-vis) and diffuse reflectance spectroscopy (DRS)

UV-vis is an optical spectroscopic technique that measures the intensity of light against the wavelength after passing through a sample or reflecting from a sample surface. The UV region ranges from 190 to 400 nm and the visible region from 400 to 800 nm [18]. The technique can provide both quantitative and qualitative information. Transmission measurements can be made for solid transparent samples or liquid samples, otherwise reflectance can be measured relative to a standard with an integrating sphere accessory. Figure 4.9 shows an illustrative diagram of a dual beam UV-visible spectrometer for liquid transmission measurements.

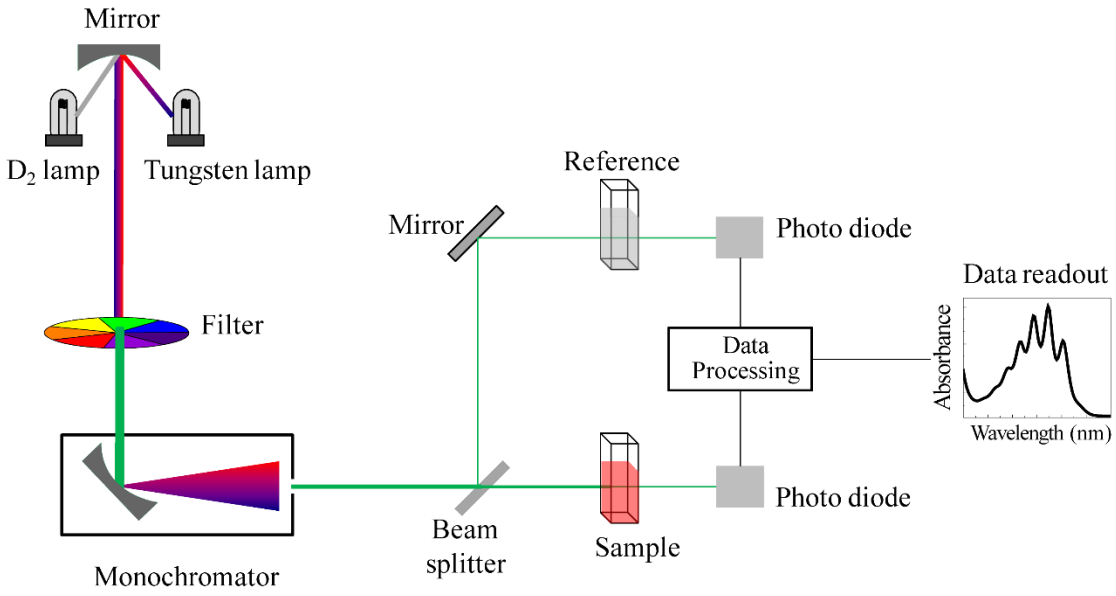

Figure 4.9: Schematic of UV-vis spectrophotometer [19].

In UV-vis the light source for UV measurements is usually a deuterium lamp and for visible measurements it is a tungsten-halogen lamp. The two lamps can cover the range of wavelengths of 200 – 800 nm. The wide range output from the light source is focused onto the diffraction grating to obtain a monochromatic beam, since the incoming light splits into its component colours of different wavelengths, like a prism but more efficiently [20].

For powder samples such as phosphor, the absorption and band gap values can be calculated by using DRS measurements, which is usually used to measure the reflected light from the powder samples. For a DRS measurement, the instrument must be equipped with an integrating sphere coated with a white standard to collect the light reflected by the standard and the sample [21]. During the DRS measurements, the light from the source is split into two beams: one directed to the detector as a reference and the second one directed to the sample. Some of the incident beam is absorbed by the sample and the second part will be diffused and reflected. The sample is positioned inside an integrating sphere that collects the diffusely scattered light by the sample. The collected light eventually reaches the detector, which compares the collected light from the source light to calculate the amount that has been absorbed. The Kubelka-Munk function

$$F(R_\infty) = \frac{(1-R_\infty)^2}{2R_\infty} \quad \ldots\ldots\ldots\ldots\ldots\ldots\ldots\ldots\ldots\ldots\ldots \text{(4.5)}$$

can be applied to convert the diffuse reflectance (R_∞) spectra to values $F(R_\infty)$ proportional to the absorption [22]. For direct band gap materials like LaOBr and LaOCl, a Tauc plot of $[F(R_\infty)h\nu]^{1/2}$ against $h\nu$ can then be used to calculate the optical band gap energies by fitting a linear region and extrapolating this to where it cuts the horizontal (energy) axis [23].

The Lambda 950 UV–vis spectrophotometer equipped with an integrating sphere that displays reflectance close to 100% reflectance in the wavelength range from near UV to the near infrared was used in this research study to obtain the diffuse reflectance spectra. The standard used was spectralon. Figure 4.10 presents the UV-vis spectrophotometer used in this project.

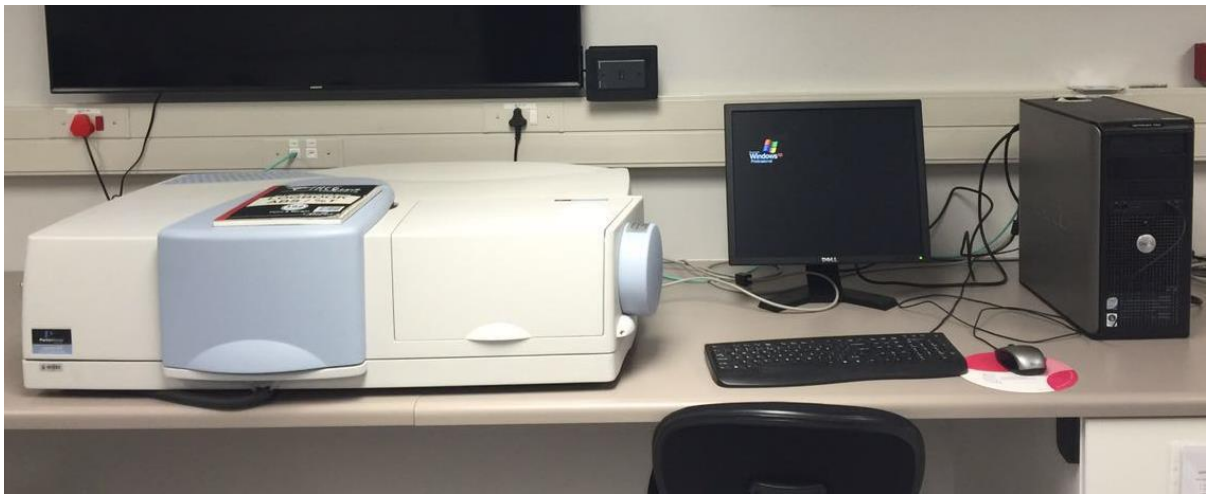

Figure 4.10: PerkinElmer Lambda 950 UV-vis-IR spectrometer at the Department of Physics, University of the Free State.

4.6. Photoluminescence (PL) spectroscopy

PL spectroscopy is a non-destructive analytical technique. In this technique, a substance is excited from its ground electronic state to one of its excited electronic states, usually by using a UV light or laser radiation. The luminescence is produced when the electrons return back to their normal electronic ground state level and this can be recorded as a plot of the intensity of emitted light against wavelength or energy [24]. The technique is usually used to record excitation and emission spectra as well as luminescence lifetimes.

In PL spectroscopy, the incident light is absorbed by a sample and imparts excess energy into the material in a process called *photo-excitation.* The photo-excitation causes the electron to jump from its electronic ground state to one of the various vibrational states in the excited electronic state. Non-radiative relaxation is accompanied with the emission of phonons, allowing the excited electron to lose energy until it reaches the lowest vibrational state of the excited electronic state [25]. When this electron returns to its initial state or to any luminescent centre from which the electron was excited, the excess energy may be released as emission of photon (called a radiative process) or it may return nonradiatively where the excess energy is transferred to another ion or defect, or used to excite phonons (heat). The released energy emitted as light (photoluminescence) corresponds to the energy difference between the two electron energy levels of the excited state

and the ground state involved in the transition. The quantity of the emitted light is related to the relative contribution of the radiative process. Figure 4.11 presents a schematic diagram of the PL technique is presented as visualized with the Jablonski diagram.

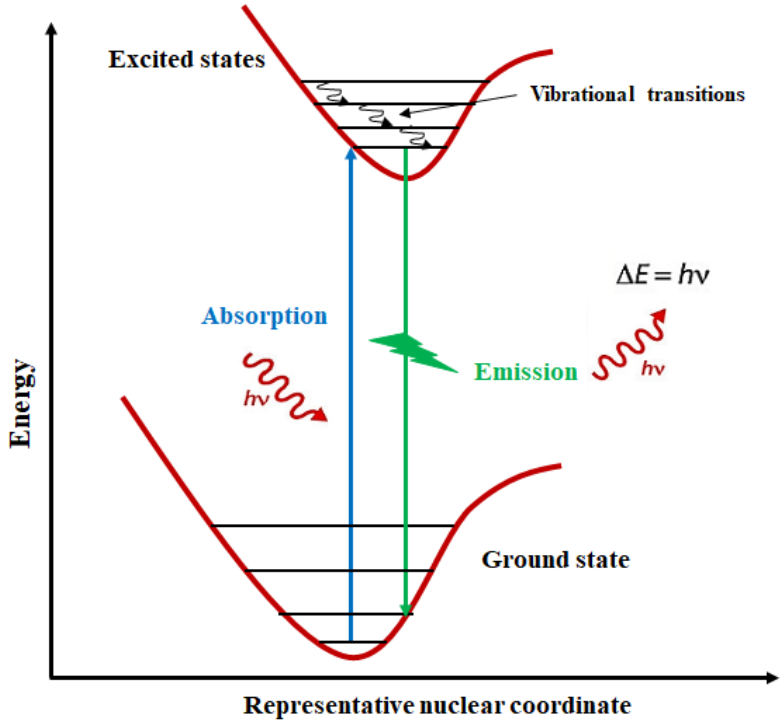

Figure 4.11: Schematic energy diagram presenting the excitation and emission involved in the photoluminescence process.

The emitted light, in almost all cases, has less energy relative to the original light from the energy source. Hence, PL spectra always possess a wavelength range that is longer than the wavelength of the excitation source [24], with the difference referred to as the Stokes shift. Figure 4.12 is a schematic diagram of the basic components of a PL spectrophotometer. This consists of the sample exposed to the light for excitation, a monochromator used to select excitation wavelength, and a detector used to observe the luminescence through another monochromator. Usually the angle between the detection of the excitation light and the detector is 90° to prevent the scattered light reaching the detector and a long-pass filter can also be placed between the sample and emission monochromator to block scattered excitation light. The emission spectrum is obtained when the excitation wavelength is kept fixed and the system scans through different wavelengths of emitted

radiation [26], while the inverse process gives an excitation curve. The International Commission for Illumination (CIE) coordinates of the emitted light was calculated using the GoCIE software [27]. The software uses the photoluminescence emission spectrum to calculate the CIE chromaticity coordinates of the phosphor materials. This software also illustrates the position of the coordinates in the chromaticity diagram and the expected colour of the phosphor. As presented in Figure 4.13, the vertexes of the triangle are the CIE coordinates of the three primary colours of red, green, and blue. The CIE coordinate of the white light is centred in the middle area an equal-energy point of (0.33, 0.33) [28].

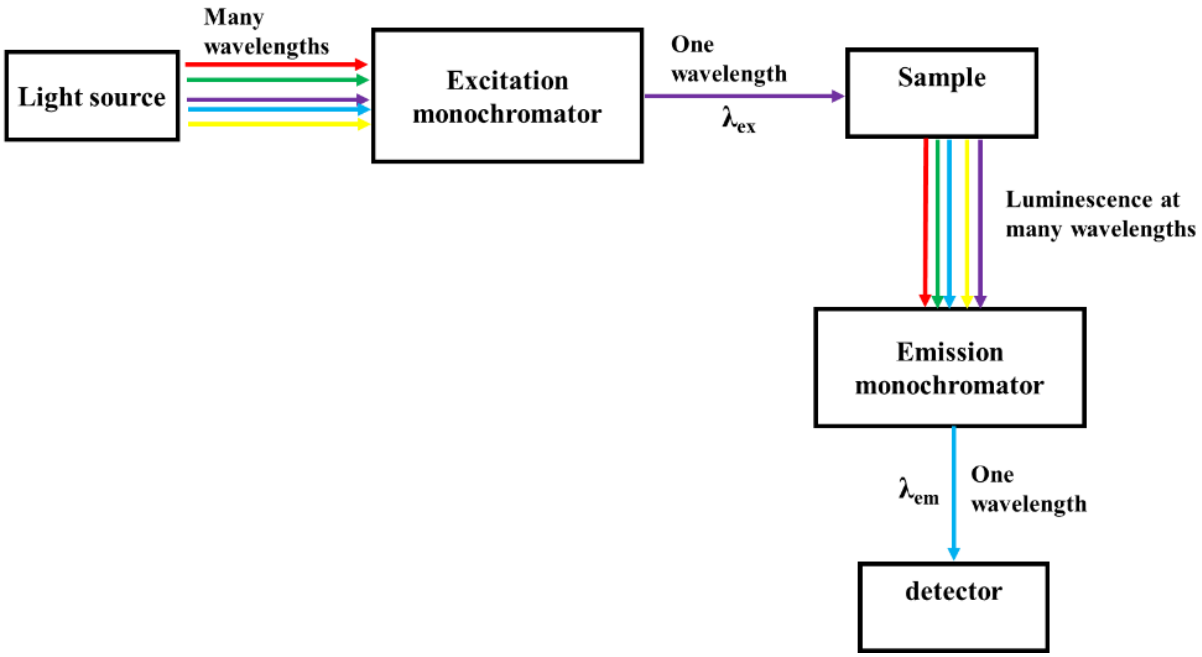

Figure 4.12: Schematic illustration of the basic components of a spectrophotometer.

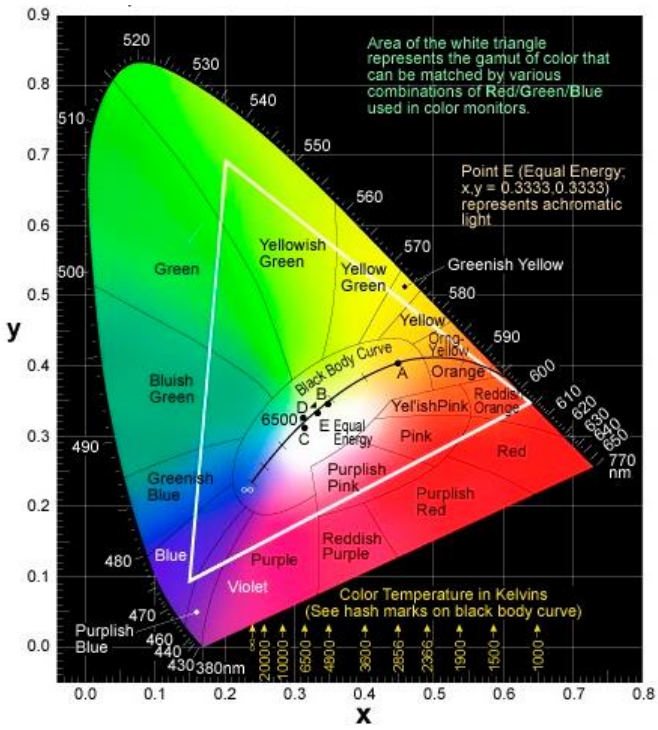

Figure 4.13: Diagram of the (CIE) chromaticity [28].

The photoluminescence properties of the powders and thin films in this study were measured by using an FS5 spectrometer with a continuous 150 W xenon lamp (figure 4.14 (a)) and an FLS980 spectrometer with a continuous 450 W xenon lamp (figure 4.14 (b)) both from Edinburgh Instruments and a He-Cd laser system with excitation wavelength equal to 325 nm and power of 26 mW (figure 4.14 (c)).

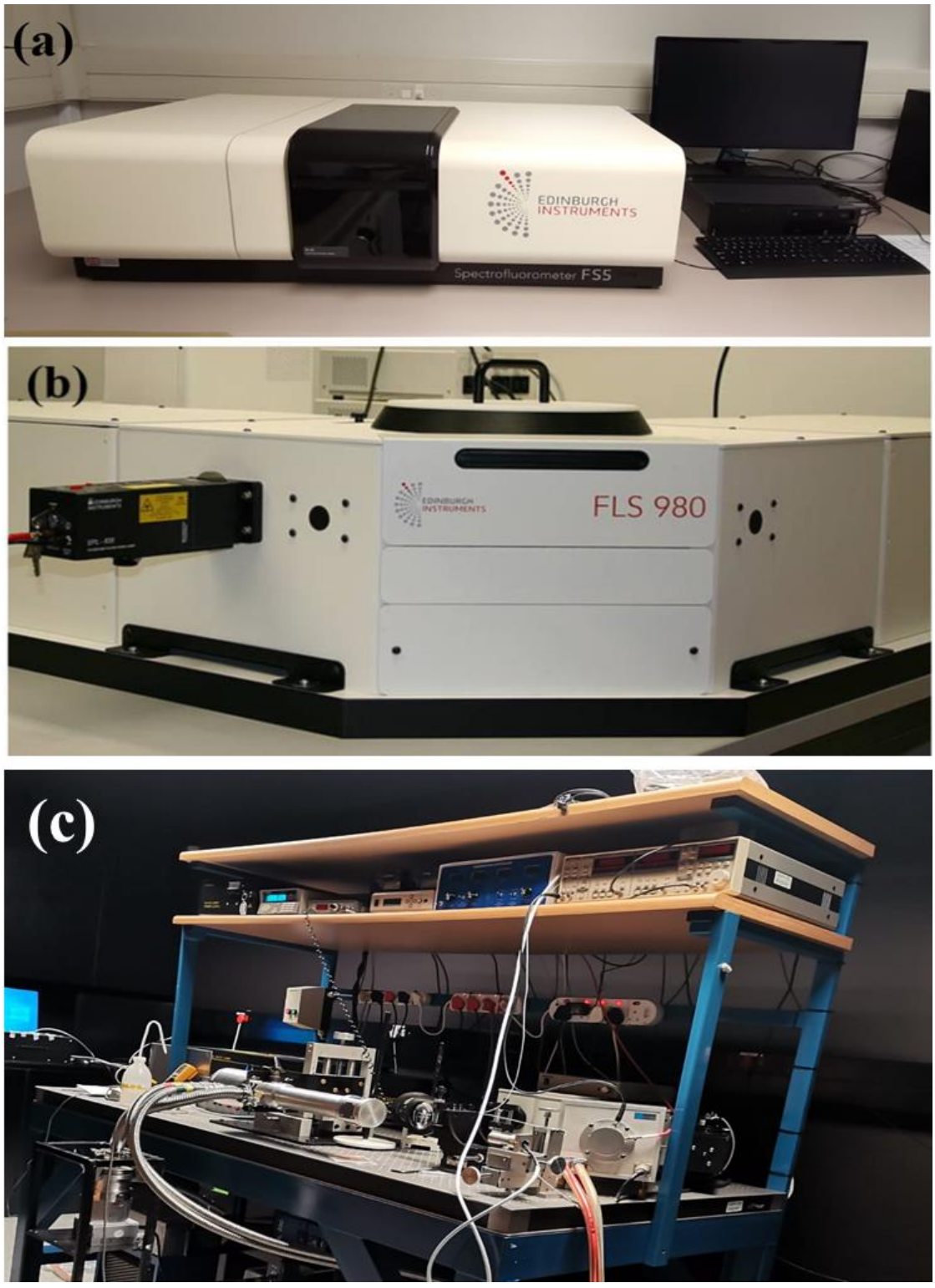

Figure 4.14: (a) FS5 spectrometer (b) FLS980 fluorescence spectrometer (c) PL system with 325 nm He-Cd laser, at the Department of Physics, University of the Free State.

4.7. Cathodoluminescence (CL) spectroscopy

Several substances display the CL phenomenon, which is the emission of photons (light) from a sample when excited by the high-energy electron beam. This includes semiconductors, many minerals and some organic compounds. The energy of the emitted photons in CL is typically 0.3 to 6 eV, covering the range of wavelengths from the UV to the near-infrared [29]. CL is the opposite of the photoelectric effect in which electron emission is occurred by irradiation with photons. CL is similar to PL but using electrons to excite the sample instead of photons. The screen of a television cathode ray tube (CRT) monitor is the most common example of the CL process [30].

CL emission occurs when a sample is bombarded by high-energy electron radiation. Energy from the incident electron is absorbed by the substances causing the electrons to be excited and move from the ground state (valence band) to the higher electronic state (conduction band), leaving a hole in the valence band. When this electron returns to its valence band (direct band to band recombination) or other luminescent centres (activator ions or structural defects), energy may be released in form of photons (light). The energy of the photon and the probability that a photon will be emitted or not depend on the substance, its purity and its defect state. Any non-metallic substance or semiconductors can be examined in this case. In terms of band structure, classical semiconductors, insulators, ceramics, gemstones, minerals, and glasses can be treated as well. Figure 4.15 displays the process causing cathodoluminescence emission.

In this research study, the CL measurements were carried out by using a Gatan MonoCL4 accessory fitted to SEM in a vacuum of ~10^{-5} Torr and electron energy of 5 keV.

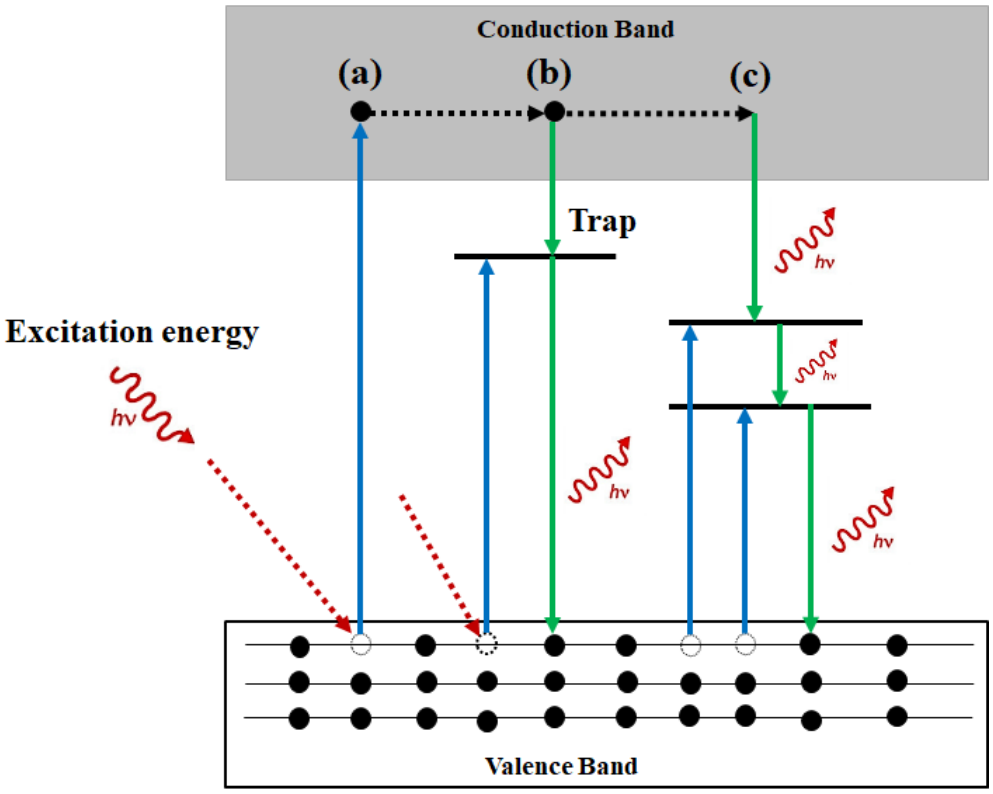

Figure 4.15: CL mechanisms due to the recombination processes in insulators or semiconductors: (a) recombination by direct band-to-band transition, (b) structural defects states in the forbidden gap and (c) the impurity energy levels [31].

4.8. X-ray photoelectron spectroscopy (XPS)

XPS, also referred to as electron spectroscopy for chemical analysis (ESCA), is a surface-sensitive quantitative spectroscopic technique commonly used to examine the chemical composition of the surface of the substance. XPS provides a total elemental analysis, except for hydrogen and helium because of their extremely low photoelectron cross sections and the fact that XPS is optimized to analyse core electrons. Furthermore, XPS provides a quantitative elemental analysis of the top 1-20 nm of solid surface. Information about chemical bonding and molecular orientation can also be provided [32]. Figure 4.16 shows schematically the XPS method, which is based on Einstein's classic explanation of the photoelectric effect. The major components of an XPS spectrometer are an X-ray source, electron energy analyser for the photoelectrons, electron detector and an efficient pumping system for the high vacuum requirement. As presented in figure 4.17, when a material

surface is bombarded by an X-ray photon having energy *hν* (where *h* is Planck's constant and *ν* is the frequency), this may be absorbed by an electron from a core level which is therefore ejected from the atom. The emitted electron should overcome the binding energy (BE) of the orbital in which it was located in the atom before leaving the surface of the material. The amount of remaining incident radiation energy determines the kinetic energy (KE) of the ejected electron. Thus the binding energy of the electron can be identified from the energy of the incident radiation and the kinetic energy of the electron, the binding energy determines the existing elements and the oxidation status of those elements. The energy of the electron emitted is measured by using a semi spherical electron analyzer. The KE of the ejected electron is given by

$$\mathrm{KE} = h\nu - \mathrm{BE} - \Phi \quad \ldots\ldots\ldots\ldots\ldots\ldots \quad (4.6)$$

where Φ is the spectrometer work function. XPS is considered as a surface sensitive analytical technique. Due to the very short path of the photoelectrons excited from the material, only the electrons that are generated from the top few atomic layers of the surface can reach the detector. Monochromatic X-rays are used as excitation sources. The most commonly used X-ray sources are Mg Kα, and Al Kα [33]. X-ray photoelectron spectroscopy must be performed under ultrahigh vacuum conditions (better than $1x10^{-8}$ Torr) in order to prevent scattering of photoelectrons and to minimize contamination of the sample surface.

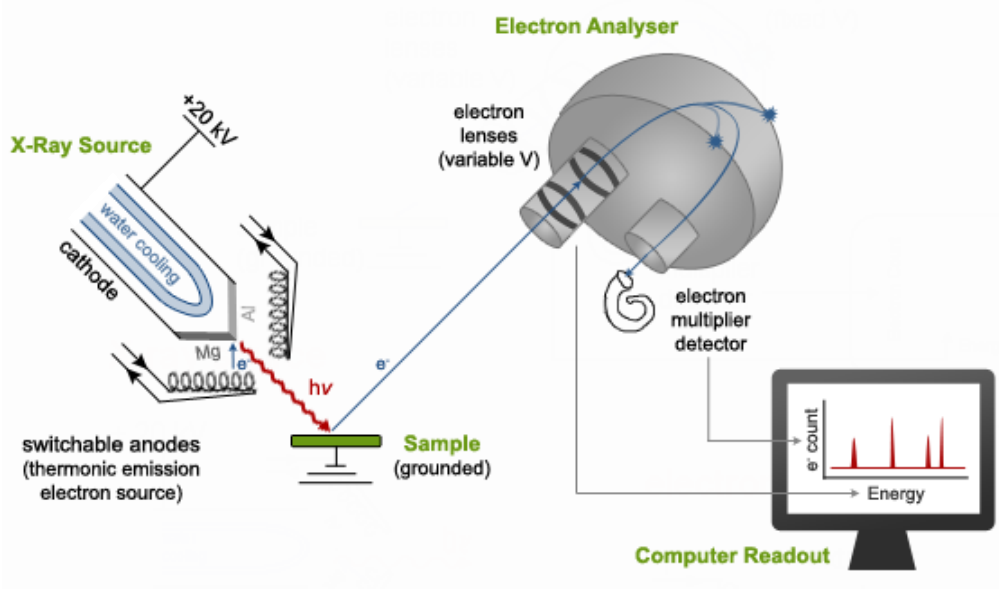

Figure 4.16: Schematic diagram of an XPS system [34].

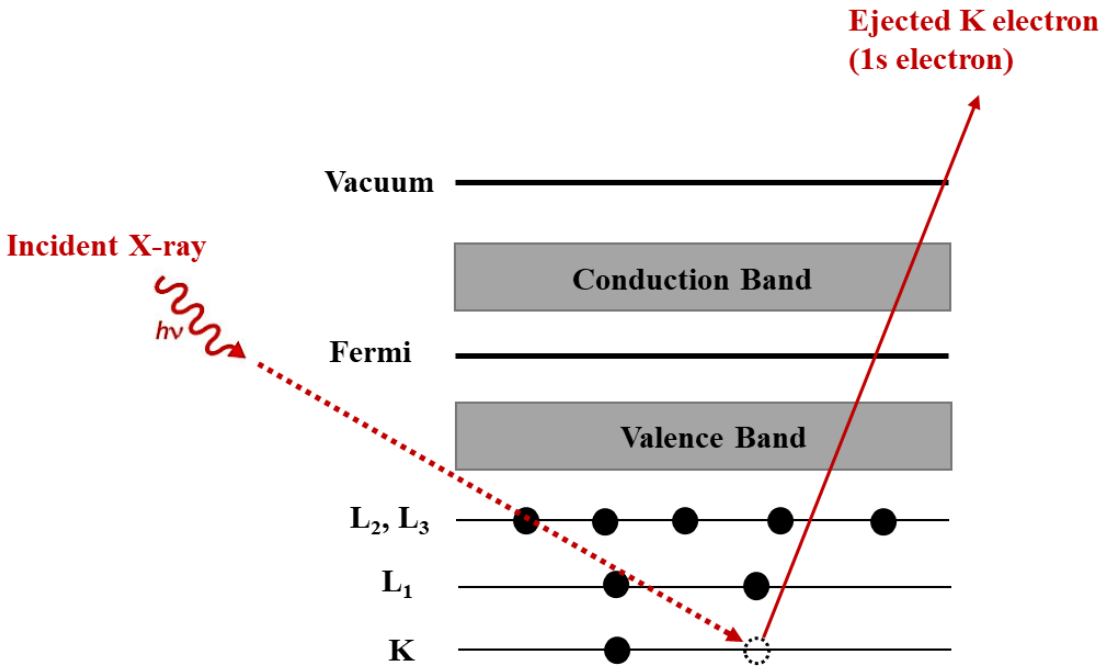

Figure 4.17: Schematic diagram of the XPS process, showing photoionization of an atom by the ejection of a 1s electron.

4.8.1. Advantages and Disadvantages of XPS [35]

XPS has advantages such as

- Nondestructive
- Surface sensitive (10-200 Å)
- Elemental sensitivity (typically parts per 1000)
- All elements can be detected (except H and He)
- Quantitative
- Chemical bonding information

However, XPS also has some disadvantages such as

- Large analysis area (several mm^2)
- Expensive ($200,000-$500,000/ instrument, $50-$500/ sample)
- High vacuum required(10^{-8} to 10^{-11} Torr)
- Slow (many hours per sample)
- Charging and energy referencing can be a challenge
- Low resolution (0.1-1.0 eV)

The XPS measurements in this study were performed on a PHI 5000 Versaprobe-scanning ESCA microprobe shown in figure 4.18. The XPS surveys were done with a 100 μm diameter monochromatic Al Kα X-ray beam generated by a 25 W, 15 kV electron beam. The sputtering was done with 2 kV, 2 μA 1×1 mm raster-Ar ion gun of sputtering rate of about 14 nm/min. For high resolution spectra the pass energy was generally set to 11 eV, giving an analyser resolution of less than or equal to 0.5 eV. Multipack version 9 software was utilized to analyse the spectra to identify the chemical compounds and their electronic states using Gaussian fits.

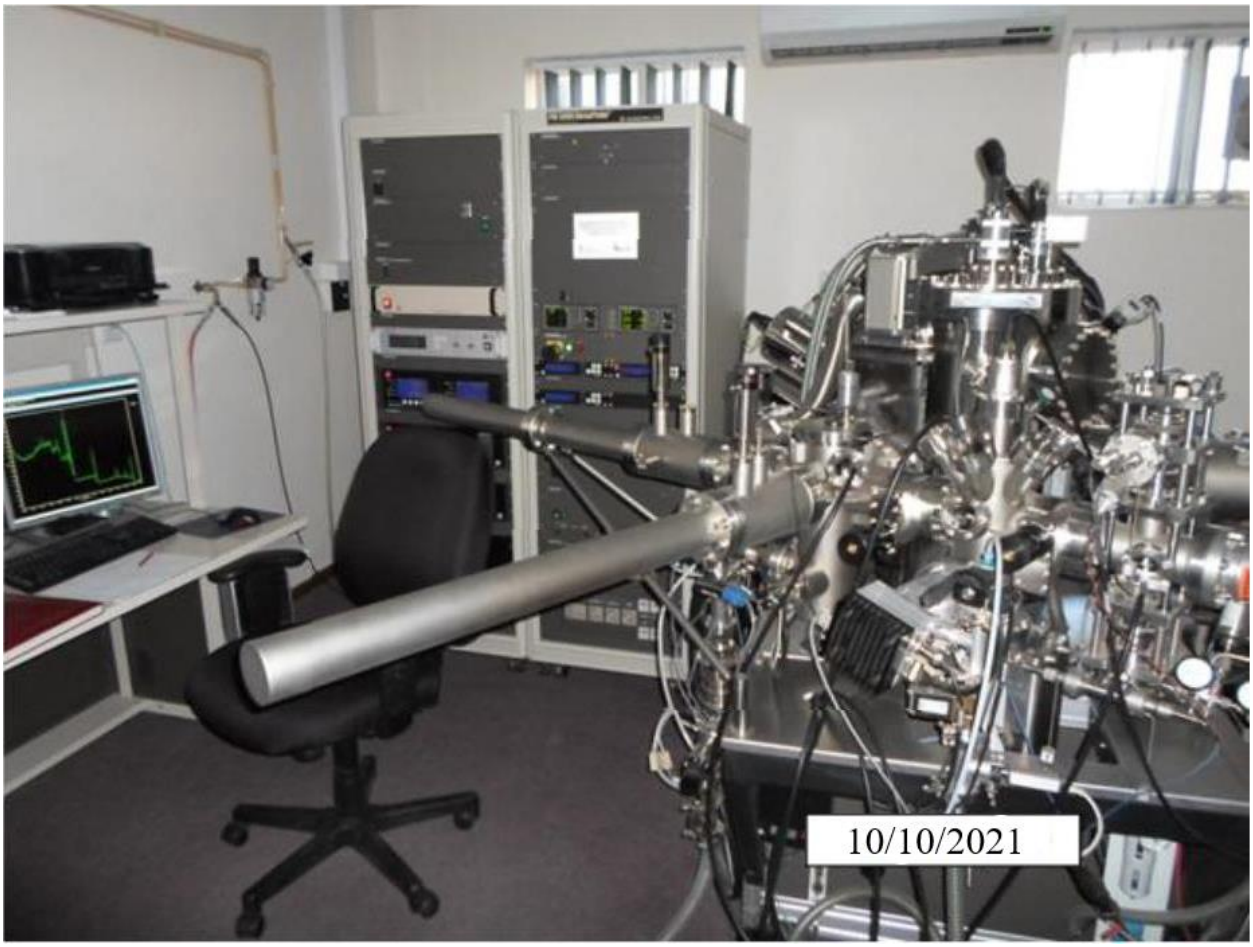

Figure 4.18: PHI 5000 Versaprobe XPS system at the Department of Physics, University of the Free State.

4.9. References

1. Jens Als-Nielsen, Des McMorrow. Elements of Modern X-ray Physics. 2nd Edition. John Wiley & Sons, London (2011). ISBN 978-0-470-97395-0

2. Victor I. Mikla, Victor V. Mikla (2014). Medical Imaging Technology || Advances in Imaging from the First X-Ray Images. (2014) 1–22. doi: 10.1016/B978-0-12-417021-6.00001-0

3. B. D. Cullity, Element of x-ray direction, Addison-Wesley Publishing Company, Inc. 2nd Edition. Canada (1978) 77-73950. ISBN: 0-201-01174-3

4. Andrei A. Bunaciu, Elena gabriela Udriştioiu, Hassan Y. Aboul-Enein. X-Ray Diffraction: Instrumentation and Applications. *Critical Reviews in Analytical Chemistry* 45 (2015) 289–99.

doi: 10.1080/10408347.2014.949616

5. B.D. Cullity. Elements of x-ray diffraction. Addison-Wesley Publishing Company, Reading (1956).

6. Ahmad Monshi, Mohammad Reza Foroughi, Mohammad Reza Monshi. Modified Scherrer Equation to Estimate More Accurately Nano-Crystallite Size Using XRD. *World Journal of Nano Science and Engineering* 2 (2012) 154–160. doi: 10.4236/wjnse.2012.23020

7. Vinod Kumar, H.C. Swart, S. Som, Vijay Kumar, A. Yousif, Anurag Pandey, S.K.K. Shaat, O.M. Ntwaeaborwa. The Role of Growth Atmosphere on the Structural and Optical Quality of Defect Free ZnO Films for Strong Ultraviolet Emission. *Laser Physics* 24 (2014) 105704. doi: 10.1088/1054-660X/24/10/105704

8. R.E. (Ted) Kroon. Nanoscience and the Scherrer equation versus the 'Scherrer–Gottingen equation'. *South African Journal of Science* 109(5/6) (2013) Art. #a0019 (2 pages). doi: 10.1590/sajs.2013/a0019

9. VD Mote, Y Purushotham and BN Dole. Williamson-Hall analysis in estimation of lattice strain in nanometer-sized ZnO particles. Journal of Theoretical and Applied Physics, 6 (2012) 1–8. doi: 10.1186/2251-7235-6-6

10. V. Meynen, P. Cool, E.F. Vansant. Verified Syntheses of Mesoporous Materials. *Microporous and Mesoporous Materials* 125 (2009) 170–223. doi: 10.1016/j.micromeso.2009.03.046

11. Marcelo de Assumpção Pereira-da-Silva, Fabio A. Ferri. Nanocharacterization Techniques || Scanning Electron Microscopy, (2017)1–35. doi: 10.1016/B978-0-323-49778-7.00001-1

12. Weilie Zhou, Zhong Lin Wang. Scanning Microscopy for Nanotechnology. Techniques and Applications. Springer Science+Business Media, New York (2006). ISBN-13: 978-0- 387-33325-0

13. JSM-7800F catalogue. [Online]. Available from https://sestar.irb.hr/images/instrumenti/documents/99.pdf (Accessed 12 December 2021).

14. SEM technique: [online]. Available from https://www.tekportal.net/scanning-electron-microscope/ (Accessed 19 September 2021).

15. I.M. Watt, The principles and practice of electron microscopy. 2nd Edition. Cambridge University Press, Cambridge (1997). ISBN: 0521435919

16. Hrishikesh Das. Characterization of defects and evaluation of material quality of low temperature epitaxial growth. Mississippi State University, 2010.

17. Kenneth P. Severin. Energy Dispersive Spectrometry of Common Rock Forming Minerals. Kluwer Academic Publishers, London (2004). ISBN 1-4020-2840-7

18. Muhammad Sajid Hamid Akash, Kanwal Rehman (2020) Ultraviolet-Visible (UV-VIS) Spectroscopy. In: Essentials of Pharmaceutical Analysis. Springer, Singapore. ISBN 978-981-15-1546-0. doi: 10.1007/978-981-15-1547-7

19. UV-Vis spectroscopy: [online]. Available from https://orgspectroscopyint.blogspot.com/p/basics-of-uv-visible-spectroscopy.html (Accessed 21 September 2021).

20. UV-Vis spectrophotometer: [online]. Available from https://edu.rsc.org/download?ac=12904 (Accessed 21 September 2021).

21. H.A.A. Seed Ahmed, *Luminescence from lanthanide ions and the effect of co-doping in silica and other hosts*, PhD thesis, University of the Free State, Bloemfontein, South Africa, 2012.

22. Rosendo López, Ricardo Gómez. Band-Gap Energy Estimation from Diffuse Reflectance Measurements on Sol-Gel and Commercial TiO_2: A Comparative Study. *Journal of Sol-Gel Science and Technology* 61 (2012) 1-7. doi: 10.1007/s10971-011-2582-9

23. Aman Pandey, Gunisha Jain, Divya Vyas, Silvia Irusta, Sudhanshu Sharma. Nonreducible, Basic La_2O_3 to Reducible, Acidic $La_{2-x}Sb_xO_3$ with Significant Oxygen Storage Capacity, Lower Band Gap, and Effect on the Catalytic Activity. *Journal of Physical Chemistry C* 121 (2017) 481-489. doi: 10.1021/acs.jpcc.6b10821

24. Sally Eaton-Magana, Christopher M. Breeding. An Introduction to Photoluminescence Spectroscopy for Diamond and Its Applications in Gemology. *Gems & Gemology* (2016) 1–17. doi: 10.5741/GEMS.52.1.2

25. J. García Solé, and L. E. Bausá, and D. Jaque. An introduction to the optical spectroscopy of inorganic solids. John Wiley & Sons, Chichester (2005). ISBN 0-470-86886-4

26. Daniel C. Harris. Quantitative Chemical Analysis. 7th Edition. W. H. Freeman and Company, New York (2007) p. 394. ISBN: 0-7167-7041-5

27. GoCIE V2, K. R. Justin Thomas, Department of chemistry, Indian Institute of Technology Rookee, India, 2009. http://faculty.iitr.ac.in/~krjt8fcy/gocie.html

28. L. Zhang, X.-L. Li, D. Luo, P. Xiao, W. Xiao, Y. Song, Q. Ang, B. Liu. Strategies to Achieve High-Performance White Organic Light-Emitting Diodes. *Materials* 10 (2017). 1378. doi: 10.3390/ma10121378

29. Cathodoluminescence: [online]. Available from https://en.wikipedia.org/wiki/Cathodoluminescence (Accessed 23 September 2021).

30. K.V.R. Murthy, Hardev Singh Virk. Luminescence Phenomena: An Introduction. *Defect and Diffusion Forum* 347 (2013) 1–34. doi: 10.4028/www.scientific.net/DDF.347.1

31. Roushdey Salh. Defect Related Luminescence in Silicon Dioxide Network: A Review. Chapter 8 in: Sukamar Basu (Editor) *Crystalline Silicon - Properties and Uses* (2011) 135–172. doi: 10.5772/22607

32. Terrance E. Conners, Sujit Banerjee. Surface Analysis of paper. Boca Raton, New York (1995) 232. ISBN: 0-8493-8992-5

33. Krishna M. Pamidimukkala. X-Ray Photoelectron Spectroscopy, Paper Surface Analysis By. *Encyclopedia of Analytical Chemistry* (2006) 1–17. doi: 10.1002/9780470027318.a2207

34. XPS process: [online]. Available from http://faculty.chem.queensu.ca/people/faculty/horton/research.html (Accessed 10 October 2021).

35. Andrade J.D. (1985) X-ray Photoelectron Spectroscopy (XPS). In: Andrade J.D. (eds) Surface and Interfacial Aspects of Biomedical Polymers. Springer, Boston, MA. doi: 10.1007/978-1-4684-8610-0_5

Chapter five

Comparative study of the photoluminescence and cathodoluminescence of Bi doped LaOCl and LaOBr phosphor powders

5.1. Introduction

Phosphor materials have many applications in modern technology such as light sources (fluorescent tubes and white light emitting diodes), X-ray detectors and intensifying screens, optoelectronic devices, displays and scintillators [1]. Lanthanum oxyhalide compounds, like LaOCl and LaOBr, have attracted some research interest because of their excellent electrical, magnetic, optical and luminescence properties [2]. These LaOX (X = Cl, Br) hosts have wide band gaps, about 5.8 eV for LaOBr and 6 eV for LaOCl [3]. Both compounds belong to the tetragonal PbFCl-type crystal structure with space group *P*4/*nmm* (No. 129) [4]. Their crystal structures (Figure 5. 1) were modelled with Vesta software [5] using the CIF files obtained from the Crystallography Open Database (COD) [6]. In both structures the La^{3+} ions with C_{4v} site symmetry are bonded with four oxygen atoms (La-O) with the same bond length and five halide atoms having two distinct La-Cl or La-Br bond lengths [7].

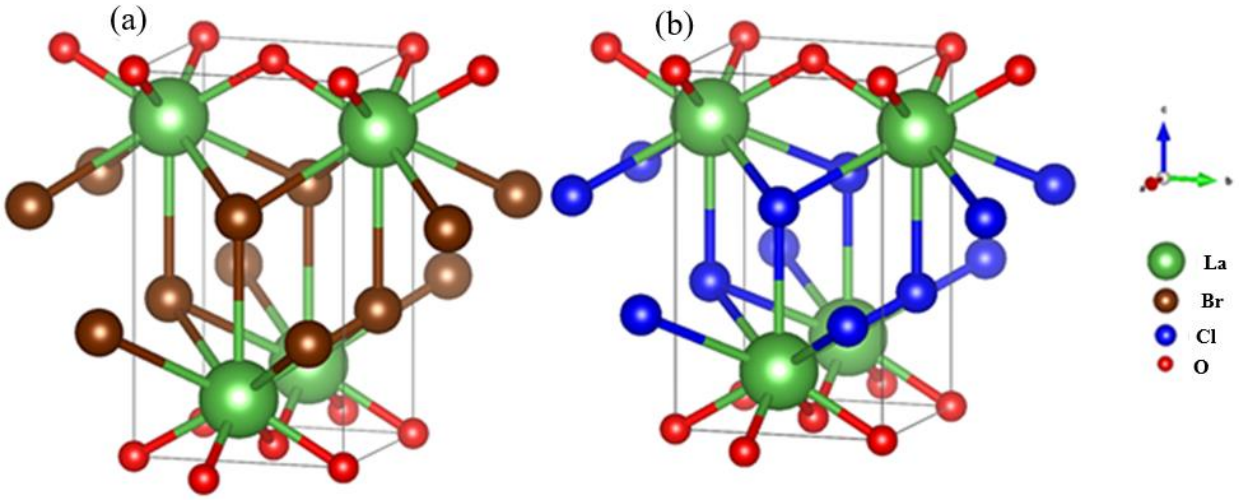

Figure 5. 1: The unit cell of (a) LaOBr (COD ID: 9009169) and (b) LaOCl (COD ID: 1539093).

Most often rare earth ions are added as activators, e.g. phosphors based on LaOCl and LaOBr have been created by doping with Nd^{3+} and Yb^{3+} [8], Eu^{3+} [9] and Sm^{3+} [10]. However, the metal ions

which are located in the main group on the periodic table, like Tl^{+}, Pb^{2+}, Bi^{3+} and Sb^{3+}, may also be useful activators for luminescence [11]. Sb^{3+} doping of LaOCl was reported by van Steensel and Blasse [12], while Wolfert and Blasse reported the luminescence properties of Bi^{3+} doped LaOCl [13] and LaOBr [14] several decades ago, observing two emission peaks in the ultraviolet and visible regions. Phosphor materials doped with Bi ions display interesting and variable luminescence characteristics because of the strong interaction of Bi ions with the surrounding host lattice (since the outer electron orbitals of Bi ions are not shielded from the surrounding environment [15], unlike in the case of the 4f electrons of rare earth ions) and due to the large number of possible Bi ion valence states. Luminescent materials doped with Bi^{3+} ions generally emit in the near ultraviolet and blue regions. The optical characteristics of Bi^{3+} ions have been investigated in various host structures [16]. They have an electronic ground state $^1S_0$ in the $6s^2$ configuration and the excited $6s^16p^1$ configuration consists of four energy level states, namely a triplet $^3P_0$, $^3P_1$, $^3P_2$ and a singlet $^1P_1$. The transitions from $^1S_0 \rightarrow {}^3P_0$ and $^1S_0 \rightarrow {}^3P_2$ are forbidden, while the transition from $^1S_0 \rightarrow {}^1P_1$ is allowed. The transition from $^1S_0$ to $^3P_1$ becomes allowed due to mixing of the $^1P_1$ and $^3P_1$ levels by spin orbit coupling [16].

For any phosphor to be used in an application, its stability under a particular application environment is an important consideration. In our previous work the host lanthanum oxide (La_2O_3) was found to be unstable and converted to the lanthanum hydroxide ($La(OH)_3$) after several days when exposed to the atmosphere [17]. Therefore Bi^{3+} activated LaOCl and LaOBr phosphor powders, having partial replacement of the oxygen anions with halide anions, were synthesised and investigated. The photoluminescence (PL) intensities were optimized by varying the Bi doping concentration and the annealing temperature. This work presents the PL excitation and emission spectra of LaOCl:Bi^{3+} and LaOBr:Bi^{3+} phosphor powders prepared by the solid state reaction method and their luminescence properties and stability were compared.

5.2. Experimental

Powder samples of lanthanum oxyhalide (LaOX, X = Cl, Br) were prepared via the solid-state reaction method. According to the reaction

$$La_2O_3 + 2NH_4X \rightarrow 2LaOX + 2NH_3 + H_2O \qquad (5.1)$$

the molar ratio of the La_2O_3 to NH_4X should be 1:2, but 25% excess NH_4X was used during synthesis. Before weighing, the La_2O_3 was annealed at 800 °C for 4 h in air to make sure it had not converted to $La(OH)_3$. To synthesize LaOCl, 1.1077 g of La_2O_3 (99.999%, Sigma Aldrich) and 0.4546 g NH_4Cl (99.999%, Sigma-Aldrich) were mixed in 10 ml of ethanol, while to synthesize LaOBr the NH_4Cl was replaced by 0.8324 g of NH_4Br (99.999%, Sigma-Aldrich). The mixture was ground thoroughly in an agate mortar with a pestle for 1 h. This mixed powder was transferred to a porcelain crucible and annealed at a temperature between 700 °C and 1200 °C for 5 h in air. The activator Bi^{3+} is expected to substitute La^{3+} ions since they have the same valence and similar ionic radii [18], therefore to dope samples a suitable small quantity of La_2O_3 was replaced by an equal molar quantity of Bi_2O_3 (99.999%, Sigma Aldrich).

The crystal structures were assessed using X-ray diffraction (XRD) measurements made with a Bruker D8 Advance diffractometer. To produce the Cu Kα characteristic X-rays used, an electron beam of current 40 mA was accelerated through 40 kV. The samples were examined using a JEOL JSM-7800F scanning electron microscope (SEM) and the elemental composition was assessed by means of its energy dispersive X-ray spectroscopy (EDS) attachment (X-Max^{N}80 detector) by Oxford Instruments. Diffuse reflectance spectra were recorded using a Lambda 950 UV-vis spectrophotometer from PerkinElmer with integrating sphere accessory. The PL properties of the powders were measured at room temperature using an FS5 spectrometer from Edinburgh Instruments, while the cathodoluminescence (CL) was measured using a Gatan MonoCL4 accessory fitted to SEM in a vacuum of ~10^{-5} Torr and electron energy of 5 keV. The PL degradation data were collected with an HR4000CG-UV-NIR CCD spectrometer using Spectrasuite software while the phosphor powder was excited by a 254 nm emitting fluorescent tube. The chemical state of the sample surfaces were analysed using X-ray photoelectron spectroscopy (XPS) before and after degradation using a PHI 5000 Versaprobe system. The spectra were obtained by using a monochromatic Al Kα X-ray beam (1486.6 eV) generated by a 25 W, 15 kV electron beam. The binding energy scale was shifted so that the C 1s peak of adventitious C occurred at 284.5 eV to compensate for possible charging. Spectra were deconvoluted and fitted using MULTIPACK software v.8.2.

5.3. Results and discussion

5.3.1. Structure, morphology and chemical composition

Figure 5.2 shows XRD patterns of undoped LaOX (X = Cl and Br) powder samples annealed at various temperatures between 700 and 1200 °C, together with reference data for LaOBr (JCPDS card no. 471676) and LaOCl (JCPDS card no. 080477) both belonging to the tetragonal PbFCl-type crystal structure with space group $P4/nmm$ (No. 129). For LaOBr, Figure 5.2(a), annealing in the lower temperature range from 700 °C up to 900 °C caused the formation of a pure LaOBr phase, while annealing at 1000 °C and 1100 °C produced some La_2O_3 and annealing at the highest temperature used (1200 °C) converted the LaOBr completely to La_2O_3 (JCPDS no. 050602). Therefore 900 °C was identified as the optimum temperature for annealing LaOBr samples. For LaOCl, Figure 5.2(b), annealing at temperatures from 700 °C up to 1100 °C produced the pure LaOCl phase while annealing at 1200 °C caused the formation of some La_2O_3. This showed that the LaOCl is more resistant to high temperature decomposition than LaOBr. The same temperature chosen to anneal the LaOBr samples (i.e. 900 °C) was also used to anneal the LaOCl samples. The XRD patterns of undoped and doped LaOX (0.7 mol% Bi) samples annealed at 900 °C are compared in Figure 5.3. No additional diffraction peaks were detected after doping, indicating that the Bi^{3+} ions were successfully inserted in the LaOX host structure.

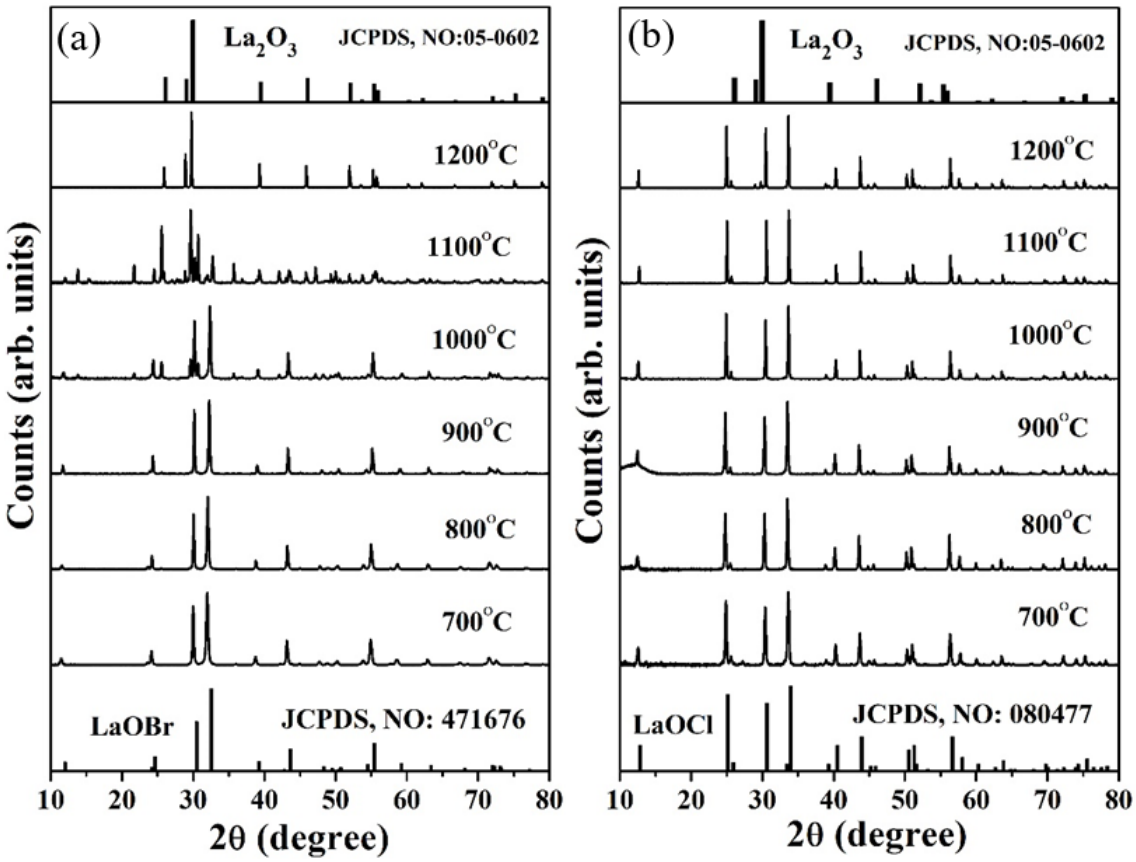

Figure 5.2: XRD patterns of (a) LaOBr and (b) LaOCl phosphor powders annealed at different temperatures.

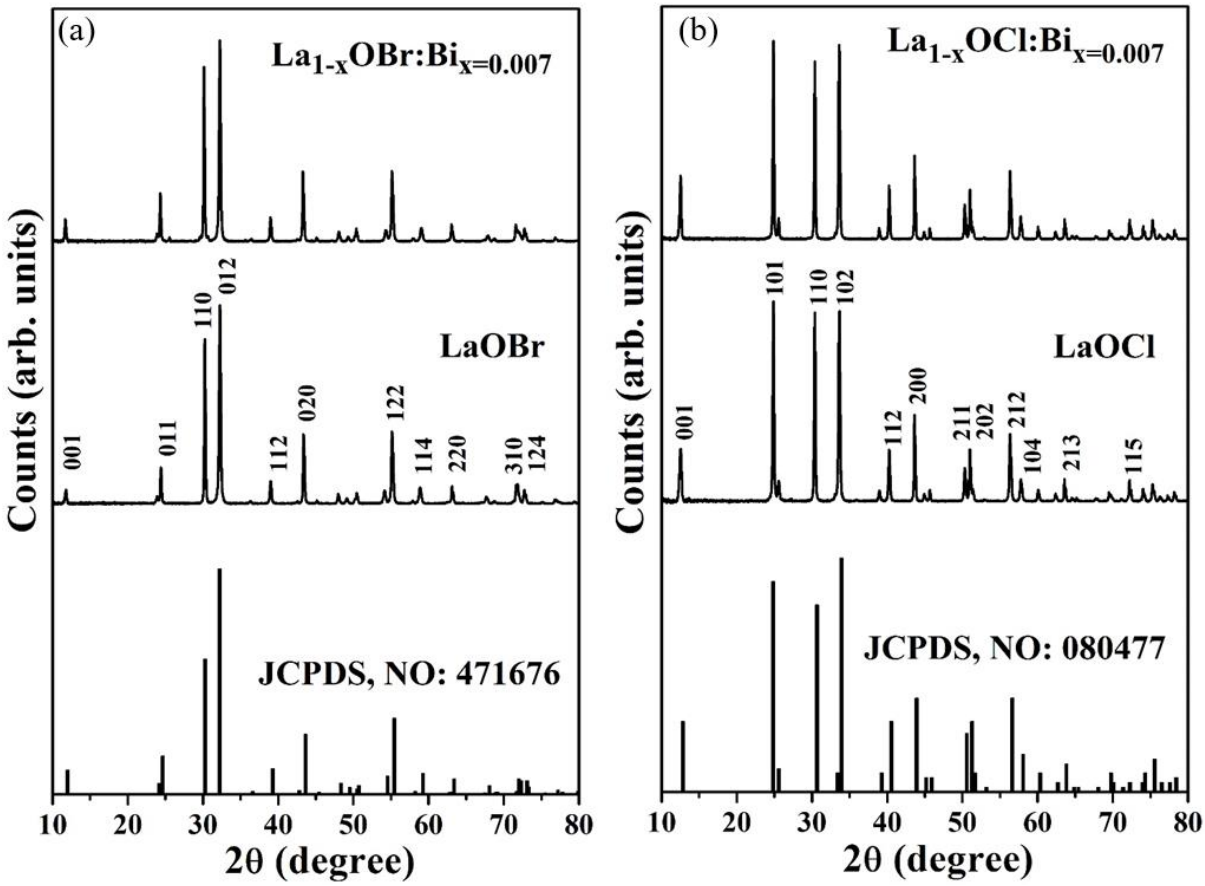

Figure 5.3: XRD patterns of (a) $La_{1-x}OBr:Bi_x$ and (b) $La_{1-x}OCl:Bi_x$ powders (x = 0 and 0.007) together with information from JCPDS card #471676 for LaOBr and #080477 for LaOCl.

Figure 5.4 presents the Williamson–Hall plots for the $La_{1-x}OBr:Bi_x$ and $La_{1-x}OCl:Bi_x$ (x = 0 and 0.007) samples. The average crystallite size and microstrain were determined by using the equation

$$\beta \cos\theta = \frac{K\lambda}{D} + 4\varepsilon \sin\theta \qquad (5.2)$$

where β is the 2θ full-width-at-half-maximum (in radians) for the diffraction peak at the angle θ, K is the shape factor (taken as 0.94), λ is the X-ray wavelength, D is the crystallite size and ε is the microstrain [15]. The crystallite size of the LaOBr pure host estimated by using the intercept of the Williamson–Hall linear fit was 31 nm, while for the doped sample (x = 0.007) it was 26 nm. The plots for the LaOBr pure host and doped samples had slopes representing the microstrains of 1.1 ± 0.3 % and 1.2 ± 0.3 %, respectively, so a significant difference could not be determined. For

the LaOCl pure host the crystallite size was 25 nm and that of the doped sample (x = 0.007) was 24 nm. The plots for the LaOCl pure host and doped samples had slopes of 0.2 ± 0.2 % and 0.3 ± 0.2 %, respectively, which are much smaller than for the LaOBr.

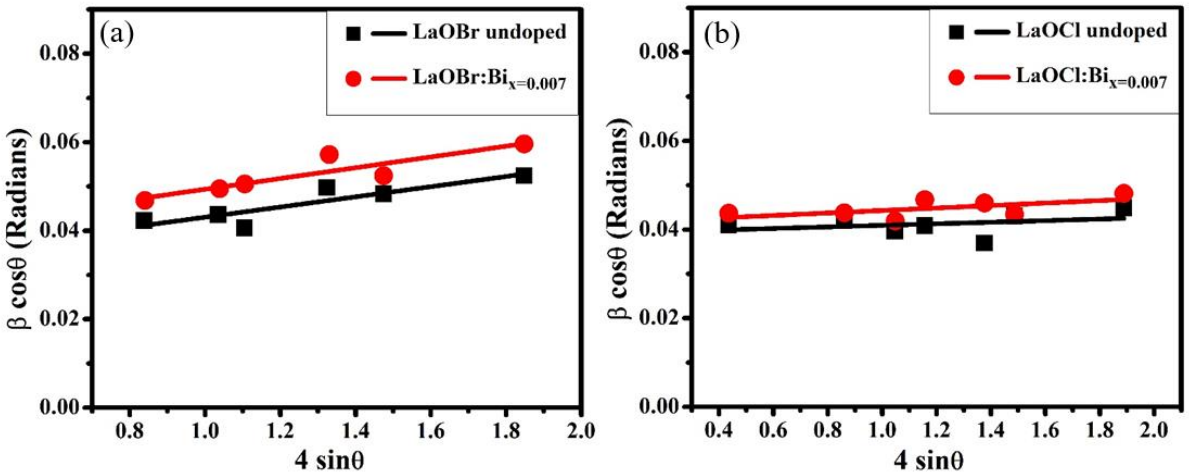

Figure 5.4: Williamson–Hall plots for (a) $La_{1-x}OBr:Bi_x$ and (b) $La_{1-x}OCl:Bi_x$ powders (x = 0 and 0.007).

Figure 5.5 shows SEM images of $La_{1-x}OCl:Bi_x$ (left) and $La_{1-x}OBr:Bi_x$ (right) phosphor powders annealed at 900 °C for various doping concentrations. The images show that the particles appear to be randomly oriented flat thin plates, with diameters which are close to 100 nm or larger. This significantly exceeds to the crystallite size obtained from XRD (~20-30 nm), which suggests that each particle consists of several grains. The flat growth of the particles may be as a result of the layered crystal structure (Figure 5.1). It is noted that the crystallites of rare earth oxybromides are small and very brittle due to the easy cleavage along the *ab*-plane [19], which suggests that the thin dimension is perpendicular to the elemental layers in the structure.

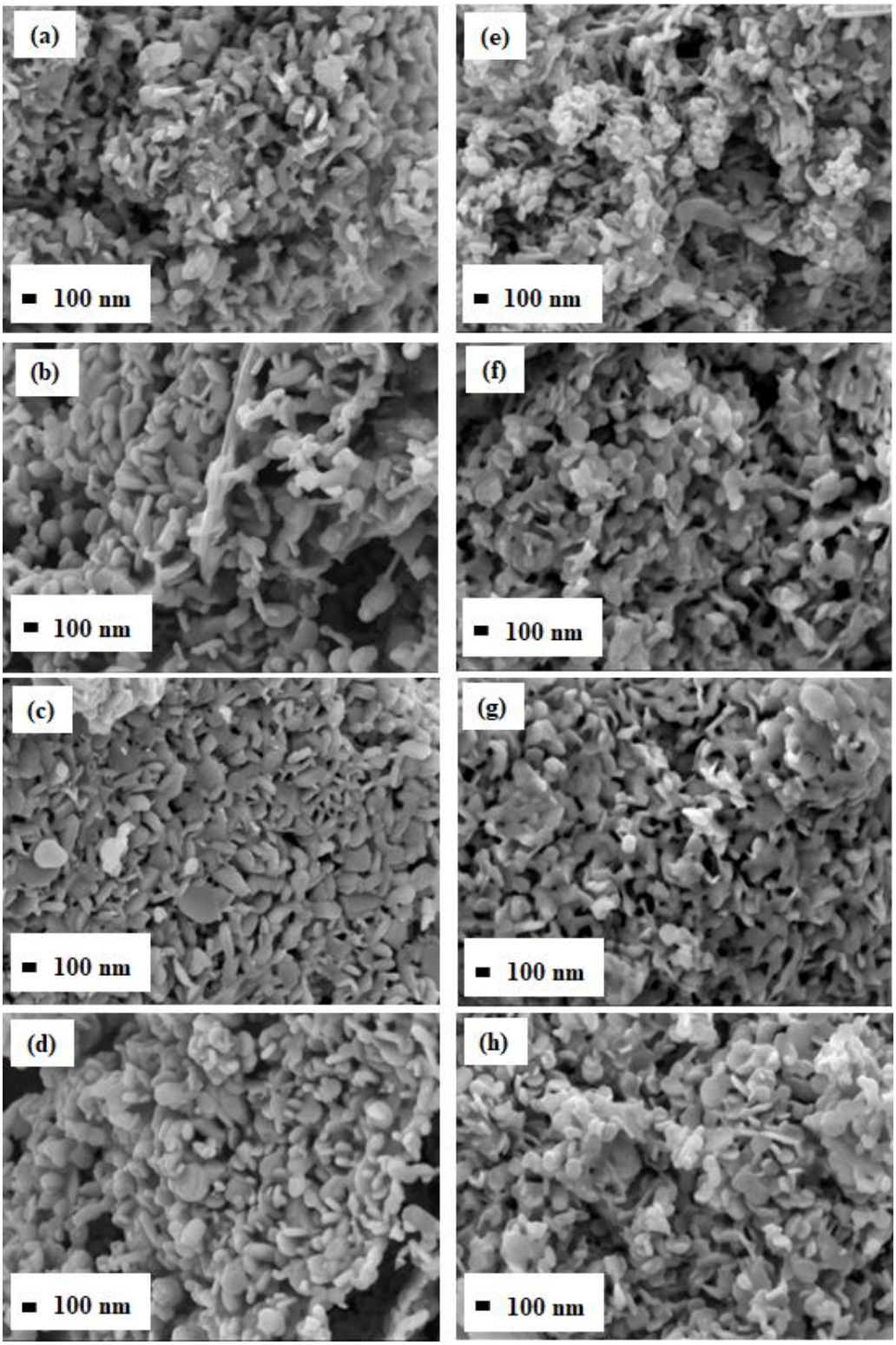

Figure 5.5: SEM images of $La_{1-x}OCl:Bi_x$ (left) and $La_{1-x}OBr:Bi_x$ (right) phosphor powders annealed at 900 °C: (a, e) x = 0, (b, f) x = 0.003, (c, g) x = 0.007, and (d, h) x = 0.01.

The EDS spectra of the undoped LaOBr and LaOCl samples (figure 5.6(a, c)) confirmed the presence of all the expected host elements (La, O, and Br or Cl), together with a small quantity of C that probably originated from the carbon tape that was used to mount the samples. The presence of Ir is due to coating the samples with this metal to improve conductivity and prevent charging in the SEM. The EDS spectra from the doped samples (figure 5.6(b, d)) were similar to the host samples. Although Bi X-rays of energy 2.419 keV may be expected at the energy indicated by the position of the blue lines in Figure 5.6(b, d), this was not observed in either sample, probably due to the low Bi concentration in even the sample with maximum doping (x = 0.01) considered in this study. For the $La_{1-x}OCl:Bi_x$ the expected Bi peak position also overlaps with the low energy side of the Cl peak which would make detecting it challenging.

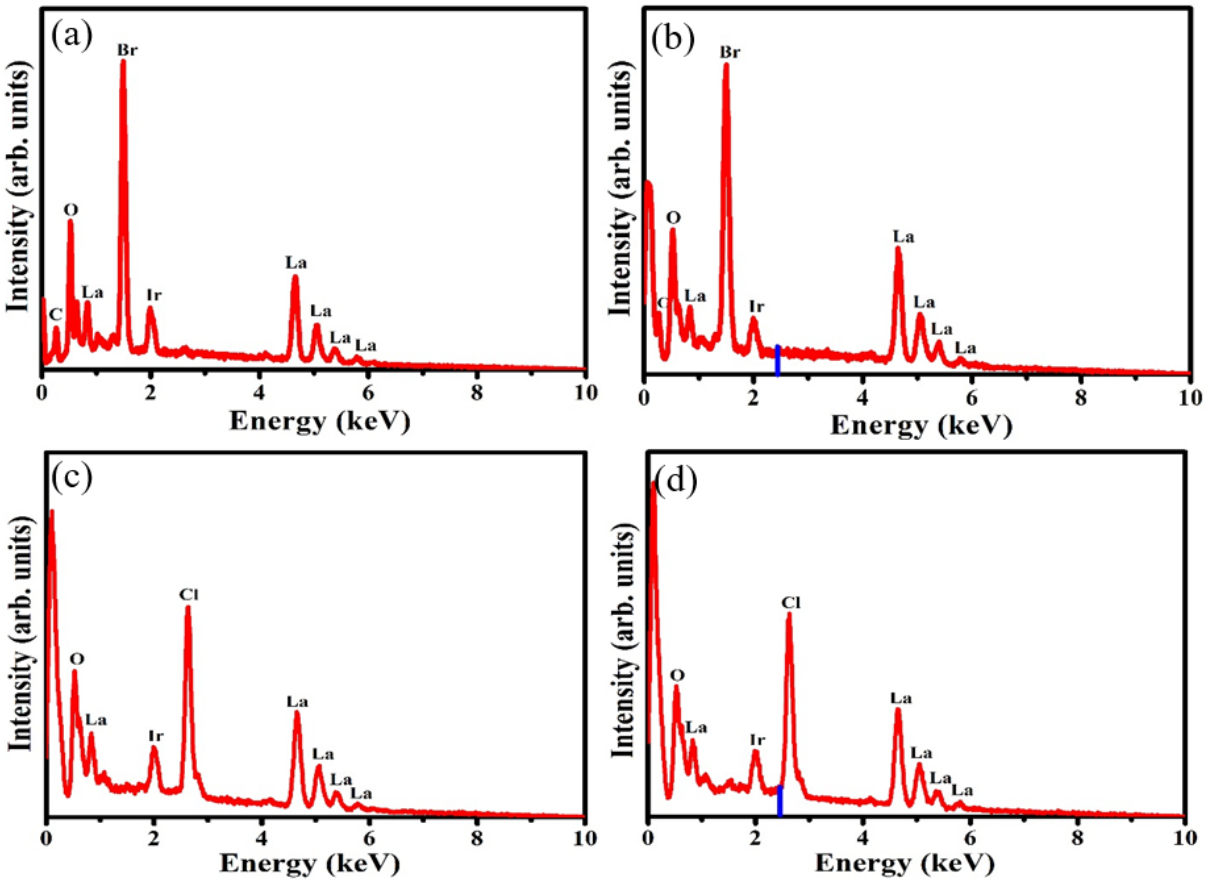

Figure 5.6: EDS spectra of (a) LaOBr and (b) $La_{1-x}OBr:Bi_{x=0.01}$ (c) LaOCl (d) $La_{1-x}OCl:Bi_{x=0.01}$ phosphor powders annealed at 900 °C.

5.3.2. Diffuse reflectance spectra

Diffuse reflectance spectroscopy was used to study the absorption properties of the LaOX (X = Br and Cl) undoped host lattices and the effects of the Bi dopant when inserted in the LaOX host lattices, as presented in Figure 5.7(a, b). The reflectance spectra of $La_{1-x}OBr:Bi_x$ samples (figure 5.7(a)) show two absorption bands, located at around 255 nm and 308 nm. The reflectance spectra of the $La_{1-x}OCl:Bi_x$ samples (figure 5.7(b)) also presented two absorption bands, centred at around 247 nm and 300 nm. The absorption increases with increasing Bi concentration. Based on PL excitation spectra to be presented later (figure 5.8), the absorption bands at shorter wavelengths centred at around 255 nm and 247 nm correspond to the absorption of Bi^{3+} ions, while the longer wavelength absorption bands at around 308 nm and 300 nm may correspond to Bi-induced defects or Bi-clusters. To calculate the band gap energy of LaOX host lattices, the Kubelka-Munk function $F(R) = \frac{(1-R)^2}{2R}$ was applied to convert the undoped host diffuse reflectance spectra to values proportional to the absorption [20]. For direct band gap materials like LaOBr and LaOCl, a Tauc plot of $[F(R_\infty)h\nu]^{1/2}$ against $h\nu$ can be used to calculate the optical band gap energies by fitting a linear region and extrapolating this to where it cuts the horizontal (energy) axis [21]. Such plots are presented in Figure 5.7(c, d) for the LaOBr and LaOCl, from which the band gap energies were estimated to be 5.38 eV and 5.76 eV, respectively. Donghyeon *et al.* [22] studied the diffuse reflectance spectra of LaOCl and LaOBr and found the bandgap energies to be 5.53 eV and 5.35 eV, respectively. Shweth *et al.* [23] calculated the band gap energies of LaOCl and LaOBr to be 5.76 eV and 5.30 eV, respectively, which are in better agreement with our results.

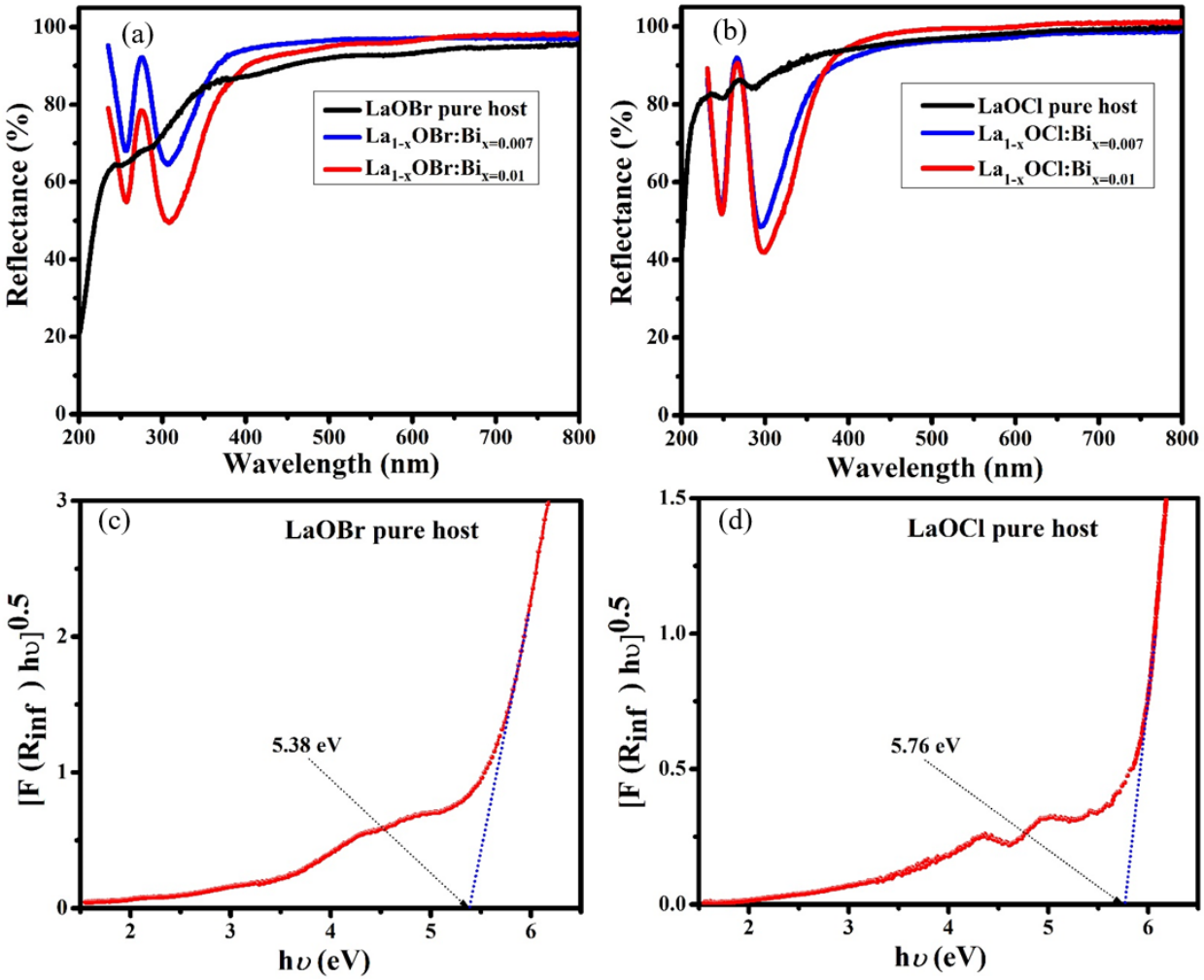

Figure 5.7: (a, b) Diffuse reflectance spectra of $La_{1-x}OBr:Bi_x$ and $La_{1-x}OCl:Bi_x$ pure hosts and activated samples. (c, d) A Tauc plot to determine the direct band gap energy for LaOCl and LaOBr pure hosts.

5.3.3. Photoluminescence

Figure 5.8(a, c) display the PL excitation and emission spectra of LaOCl and LaOBr doped with different Bi concentrations annealed at 900 °C, while Figure 5.8(b, d) present similar data for samples annealed at different temperatures for a fixed doping concentration (x = 0.007). The position of the excitation and emission bands from the Bi^{3+} ions depend on the host material. Two excitation peaks are centred at 235 nm and 266 nm for LaOCl:Bi and at 235 nm and 273 nm for LaOBr:Bi. Blasse and Bril [11] found similar excitation peaks for LaOCl:Bi and attributed the lower energy (longer wavelength) excitation peak to $^1S_0 \rightarrow {}^3P_1$ transitions (A band) of the Bi^{3+}

dopant ions and the shorter wavelength (higher energy) excitation peak to the $^1S_0 \rightarrow {}^1P_1$ transitions (C band). To better understand the origin of such excitation peaks, Wang *et al.* [24] established an empirical relationship between the energies of the A band ($^1S_0 \rightarrow {}^3P_1$) and C band ($^1S_0 \rightarrow {}^1P_1$), namely $E_C = 3.236 + 2.290(E_A - 2.972)^{0.856}$ for values in eV. If the A band excitation transitions for LaOCl:Bi and LaOBr:Bi occur at 266 nm (4.66 eV) and 273 nm (4.54 eV), then the corresponding C band energies are predicted at 6.82 eV (182 nm) and 6.60 eV (188 nm), respectively. These values are far from the observed higher energy excitation peak at 235 nm, indicating that they do not correspond to the C band transitions.

Alternatively, the metal-to-metal charge transfer (MMCT) energy between the Bi^{3+} ions at the La^{3+} cations of the host can be estimated using E_{MMCT} = 55 000 - 45 500χ/d (in cm^{-1}) [25], where χ is the electronegativity of the host cations and d is the distance between the Bi^{3+} and host cations (in Å), which can be obtained from $d = d_{host} + \frac{1}{2}(r\,(Bi^{3+}) - r\,(La^{3+}))$ where d_{host} is the distance between La^{3+} ions in the host. By using χ = 1.3 from previous work [26], r (Bi^{3+}) = 1.03 Å and r (La^{3+}) = 1.032 Å [27], as well as d_{LaOCl} = 4.109 Å and d_{LaOBr} = 4.145 Å (figure 5.1), the MMCT excitation for LaOCl:Bi and LaOBr:Bi can be expected at 40 600 cm^{-1} and 40 700 cm^{-1}, i.e. with negligible difference and both corresponding to ~245 nm. The observed higher energy excitation bands both occur at 235 nm, which are therefore attributed to MMCT transitions rather than to the C band as in early work [11]. For comparison, in our previous work [26] the MMCT between the Bi^{3+} ions at the La^{3+} cation of the La_2O_3 host was established to be 250 nm.

The emission (figure 5.8) consisted of two peaks, a strong one in the UV and a weak band in the visible range. Since it was not easy to directly judge the positions of the less intense, longer wavelength peaks accurately, Gaussian fitting (figure 5.9) was used. Fitted peaks were found at 344 nm (3.60 eV) and 450 nm (2.75 eV) for LaOCl:Bi and at 358 nm (3.46 eV) and 450 nm (2.75 eV) for LaOBr:Bi. Here the emission peaks centred at 344 nm and 358 nm were attributed to the $^3P_1 \rightarrow {}^1S_0$ transition of the Bi^{3+} ions in LaOCl and LaOBr. For comparison, La_2O_3:Bi has a broad blue emission located at 462 nm which was attributed to the transitions from the $^3P_1$ to the $^1S_0$ level [26]. Wolfert and Blasse [13, 14] observed two emission peaks in LaOCl:Bi and LaOBr:Bi, one in the UV region and the second in the visible region. They attributed the first to isolated Bi^{3+} ions and the second to BiOCl-rich or BiOBr-rich phases. Similarly, Van Steensel and Blasse [12]

ascribed the low energy peak in LaOCl:Sb^{3+} to an antimony-rich oxychloride phase. Therefore the weak, longer wavelength emission observed in the visible region near 450 nm in this study is attributed to clustering of Bi ions.

Figure 5.10(a, c) shows the maximum PL intensity of the shorter wavelength UV emission bands as a function of Bi doping concentration of $La_{1-x}OCl:Bi_x$ and $La_{1-x}OBr:Bi_x$, respectively: the maximum emission occurs for x = 0.007 for both. The PL intensity decreased above that concentration, due to concentration quenching. The PL emission intensity as a function of annealing temperature for $La_{1-x}OCl:Bi_{x=0.007}$ and $La_{1-x}OBr:Bi_{x=0.007}$ is shown in Figure 5.10(b, d). Data for LaOBr:Bi is only given between 700 °C and 900 °C since higher temperature annealing resulted in the formation of La_2O_3. Annealing at 900 °C gave the highest intensity while maintaining the pure phase and is considered optimal. For the $La_{1-x}OCl:Bi_x$ samples, which were more resistant to high temperature annealing, the PL emission intensity increased to its maximum for annealing at 900 °C and decreased gradually for higher temperatures.

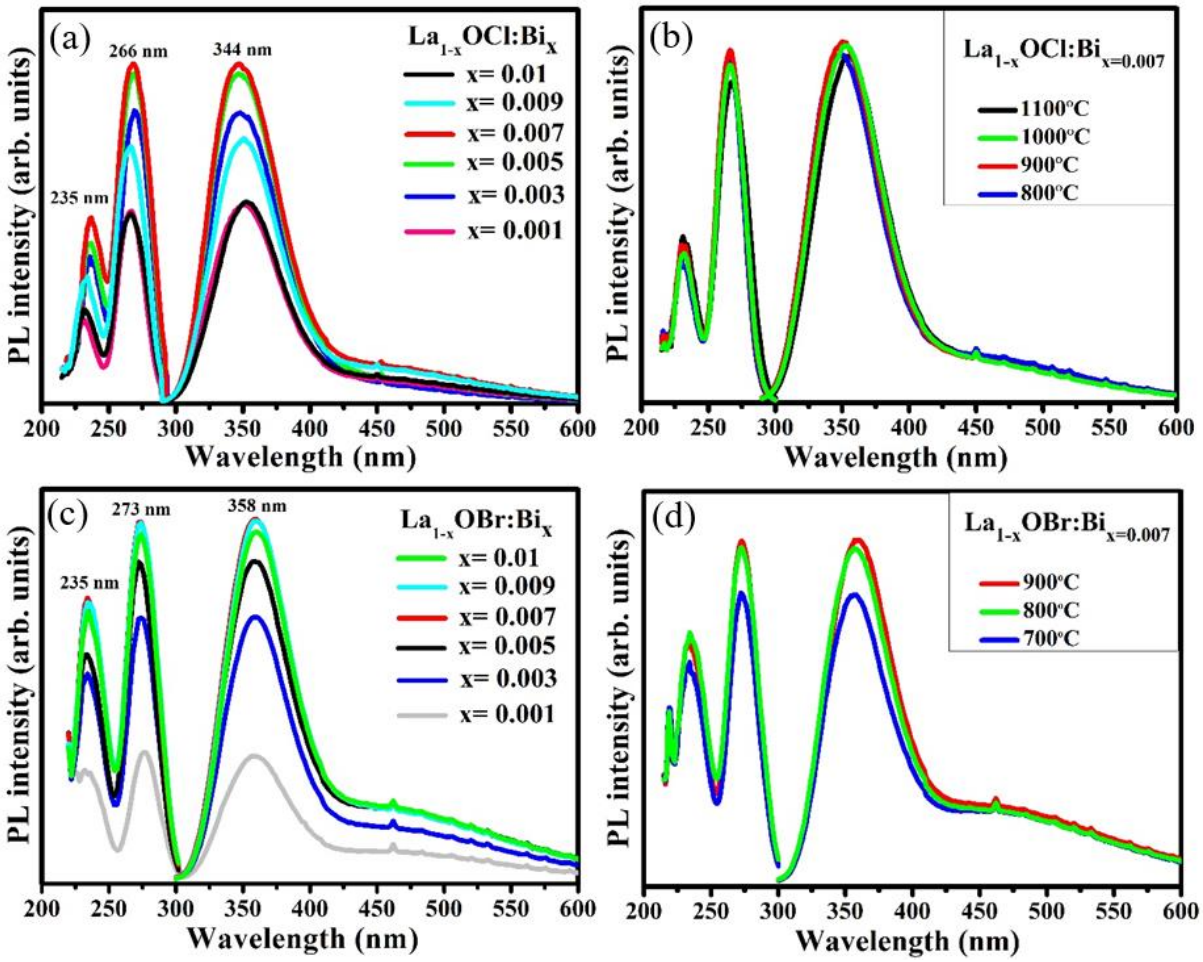

Figure 5.8: (a) Excitation and emission spectra of $La_{1-x}OCl:Bi_x$ doped with different Bi concentrations, annealed at 900 °C. (b) Excitation and emission spectra of $La_{1-x}OCl:Bi_{x=0.007}$ annealed at different temperatures. (c) Excitation and emission spectra of $La_{1-x}OBr:Bi_x$ doped with different Bi concentrations, annealed at 900 °C. (d) Excitation and emission spectra of $La_{1-x}OBr:Bi_{x=0.007}$ annealed at different temperatures.

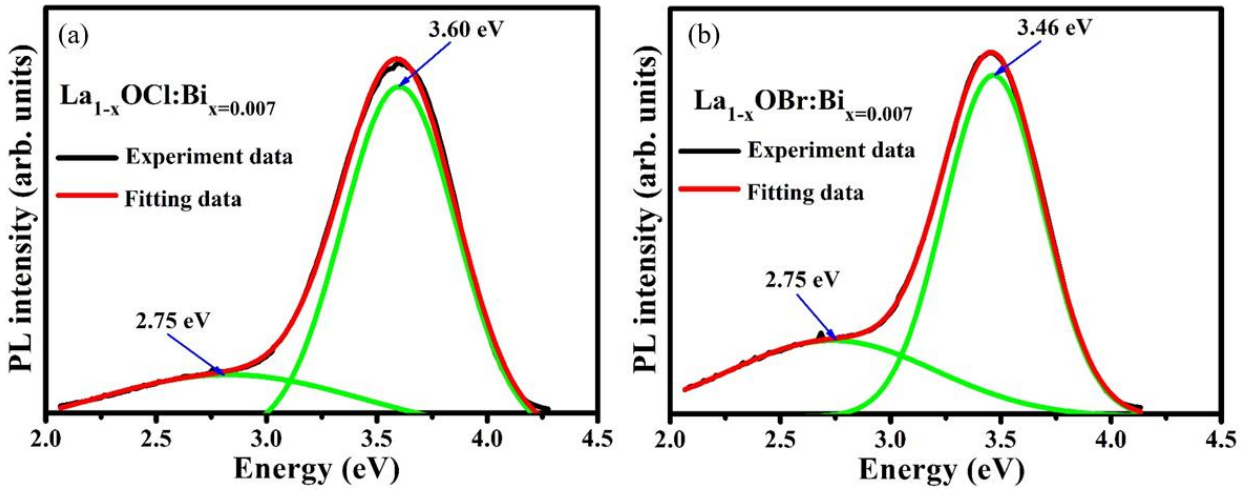

Figure 5.9: Gaussian fitting of the emission bands of (a) $La_{1-x}OCl:Bi_{x=0.007}$, excited by 4.66 eV (b) $La_{1-x}OBr:Bi_{x=0.007}$, excited by 4.54 eV.

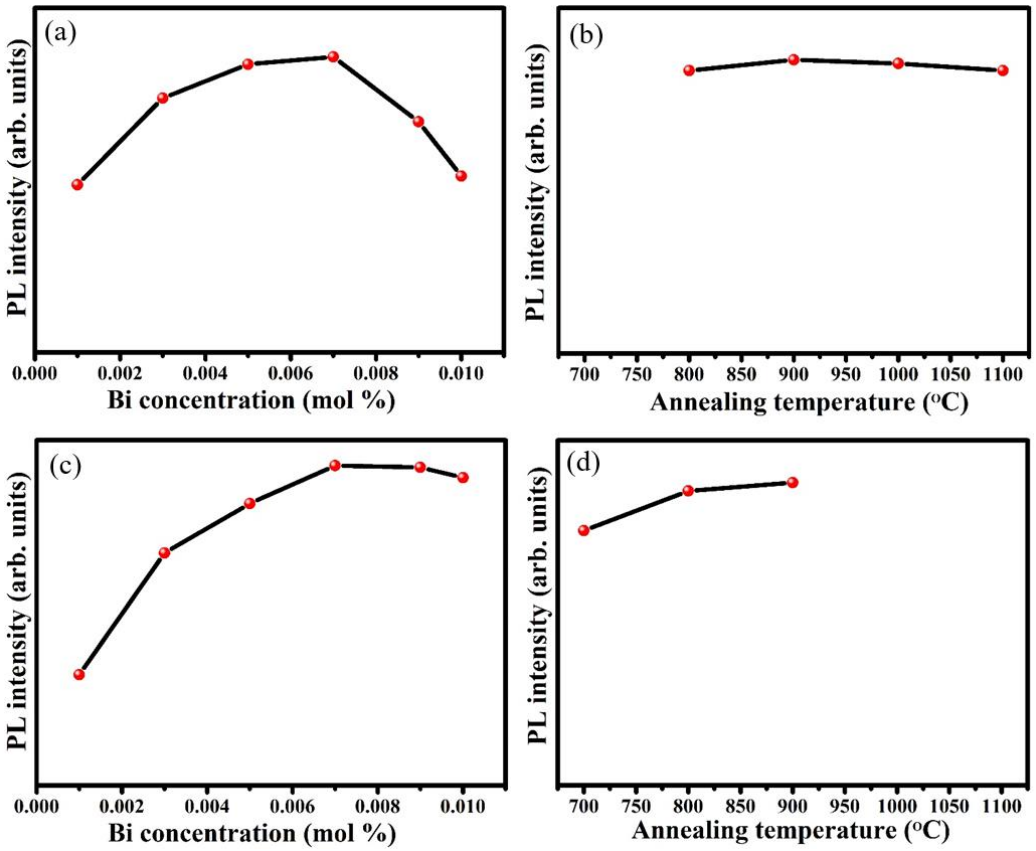

Figure 5.10: Emission peak intensity as a function of (a) Bi concentration and (b) annealing temperature of LaOCl:Bi, as well as emission peak intensity as a function of (c) Bi concentration and (d) annealing temperature of LaOBr:Bi.

Figure 5.11 compares the intensities of the excitation and emission spectra of $La_{1-x}OCl:Bi_{x=0.007}$ powder phosphor directly with $La_{1-x}OBr:Bi_{x=0.007}$, both annealed at 900 °C. The emission spectrum of the LaOCl:Bi was stronger and broader than the corresponding emission spectrum of LaOBr:Bi. The PL emission spectrum of LaOBr:Bi is centred at 358 nm, significantly red-shifted in comparison to the PL emission of LaOCl:Bi which is centred at 344 nm. The luminescence from the LaOBr:Bi sample was less intense compared to the LaOCl:Bi sample prepared under the same conditions with equal doping.

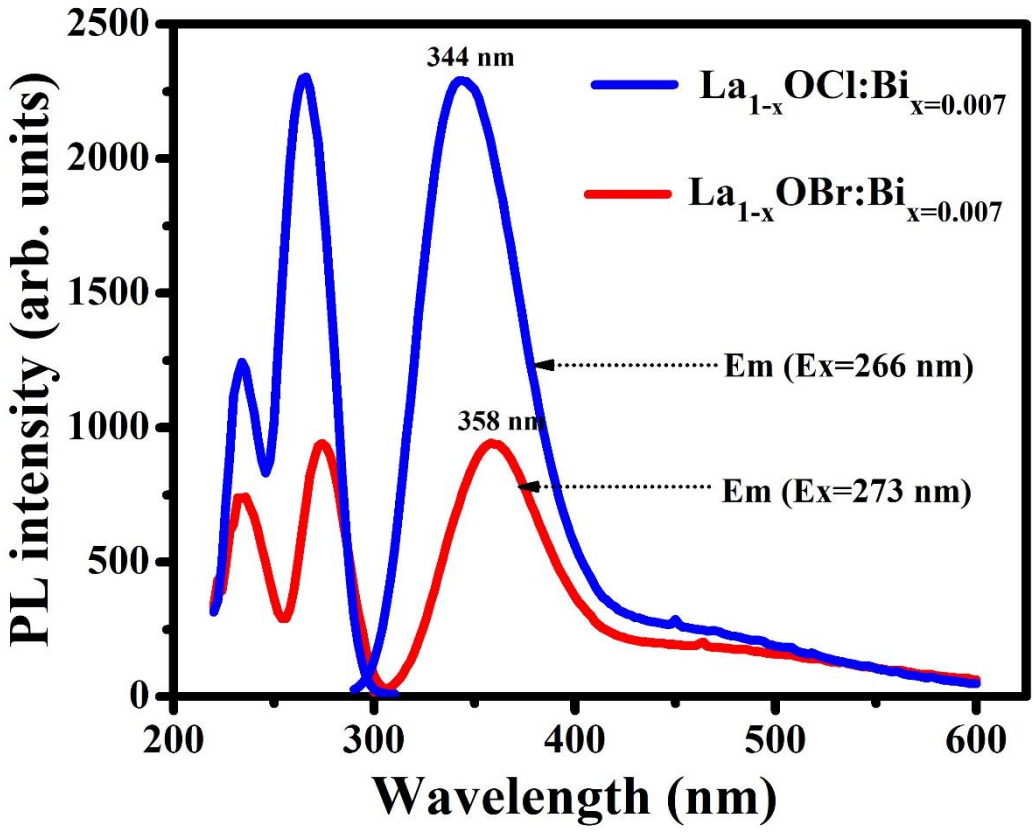

Figure 5.11: PL excitation and emission spectra of $La_{1-x}OBr:Bi_{x=0.007}$ and $La_{1-x}OCl:Bi_{x=0.007}$, annealed at 900 °C.

5.3.4. Cathodoluminescence

Figure 5.12 compares the PL and CL emission spectra of the (a) $La_{1-x}OCl:Bi_{x=0.007}$ and (b) $La_{1-x}OBr:Bi_{x=0.007}$ phosphor powders. The PL emission was excited by 266 nm for $La_{1-x}OCl:Bi_{x=0.007}$

and 273 nm for $La_{1-x}OBr:Bi_{x=0.007}$, while the CL emission was measured in a vacuum of the order of 10^{-5} – 10^{-6} Torr and electron energy of 5 keV. The PL and CL emission spectra have been normalized because the intensities measured from the two systems cannot be directly compared. In Figure 5.12(a) the PL emission spectrum of $La_{1-x}OCl:Bi_{x=0.007}$ is centred at 344 nm, slightly blue-shifted in comparison to the CL emission spectrum which is centred at 354 nm. The difference between CL and PL might be due to the large energy difference of the incident electrons (5 keV) compared to the excitation photons (4.66 eV) and hence the different mechanisms for the excitation. In our previous work [28] we also reported a red-shift for CL emission compared to PL for La_2O_3:Bi and La_2O_2S:Bi. No shift was observed in the position of the peaks between the CL and PL for the $La_{1-x}OBr:Bi_{x=0.007}$ as presented in Figure 5.12(b). A future study carefully examining the possible small emission shifts of Bi doped compounds for PL and CL may give further insight. The CL and PL emission spectra of LaOX:Bi (X = Cl and Br) phosphors had approximately the same broadness.

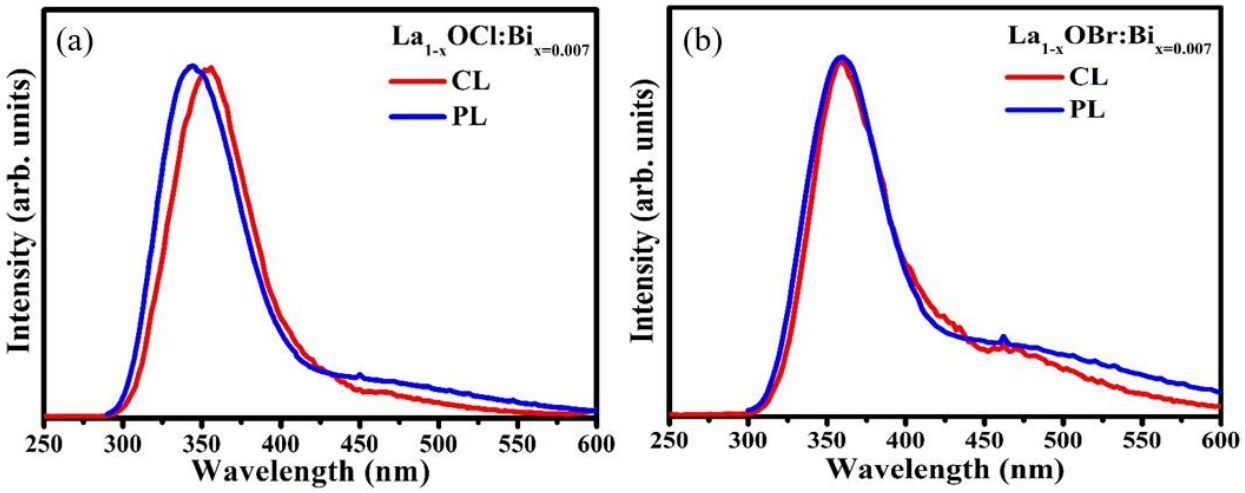

Figure 5.12: Normalized CL and PL emission spectra of (a) $La_{1-x}OCl:Bi_{x=0.007}$ (b) $La_{1-x}OBr:Bi_{x=0.007}$.

Figure 5.13 shows the CL emission spectra for (a) $La_{1-x}OCl:Bi_x$ and (b) $La_{1-x}OBr:Bi_x$ samples for different doping concentrations. For LaOCl:Bi the CL emission intensity decreased with increasing Bi concentrations, while the opposite trend occurred for LaOCl. In neither case was the maximum CL intensity obtained for the same doping concentration which was found to be optimal for PL emission intensity. This emphasizes that the luminescence properties observed for

phosphors in PL studies cannot necessarily be expected to also be applicable when excited by other mechanisms. The different trends observed for the CL emission intensity with Bi doping concentration was unexpected. Although a simple explanation cannot be offered at this time, it might be related to the different stabilities of the hosts or Bi diffusion during high energy excitation.

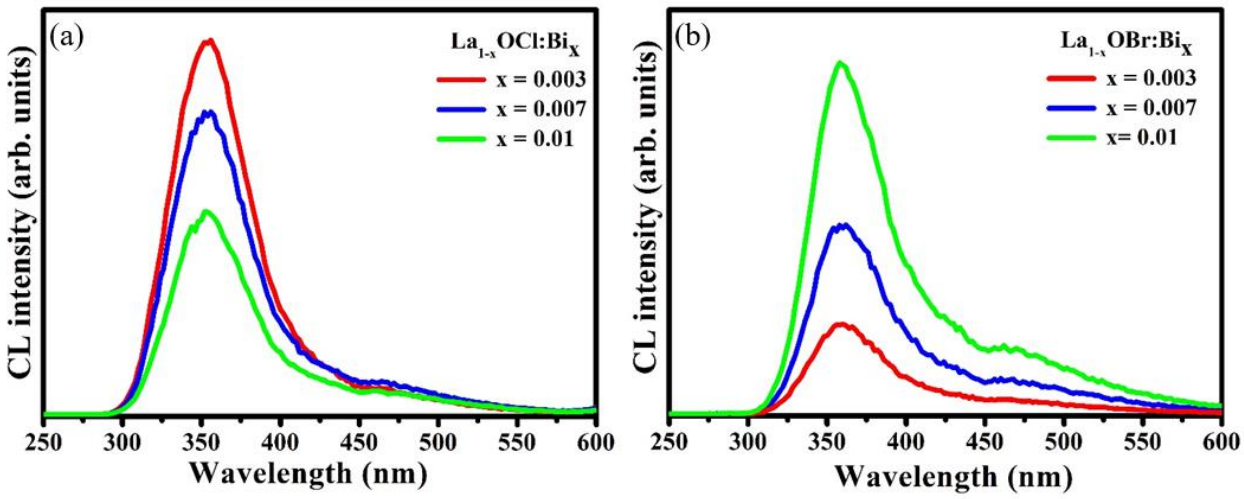

Figure 5.13: CL emission spectra of (a) $La_{1-x}OCl:Bi_x$ and (b) $La_{1-x}OBr:Bi_x$, doped with different Bi concentrations, annealed at 900 °C.

5.3.5. Stability of the phosphors and PL degradation under UV light

Figure 5.14(a, c) compares the XRD patterns of the $La_{1-x}OCl:Bi_{x=0.007}$ and $La_{1-x}OBr:Bi_{x=0.007}$ powder phosphors when freshly prepared and after 8 months of storage exposed to the atmosphere. The XRD patterns of both compounds changed over time. However, the bromide had a bigger change compared to the chloride and was therefore less stable. The LaOX (X = Cl and Br) powders phosphor are therefore unstable when exposed to the atmosphere for several months. It has previously been reported that LaOBr suffers from poor stability in moist environments [29] and while it is significantly less stable than LaOCl, the chloride-based host also degrades over time when stored. The new XRD peaks do not match La_2O_3 or $La(OH)_3$ and the degradation products have not been identified. Figure 5.14(b, d) present the corresponding PL emission spectra. It was observed that the PL emission decreased for both samples after storage, but the effect was much

stronger in the less stable bromide for which the luminescence intensity decreased to only about 30% of the initial value and shifted slightly to shorter wavelength.

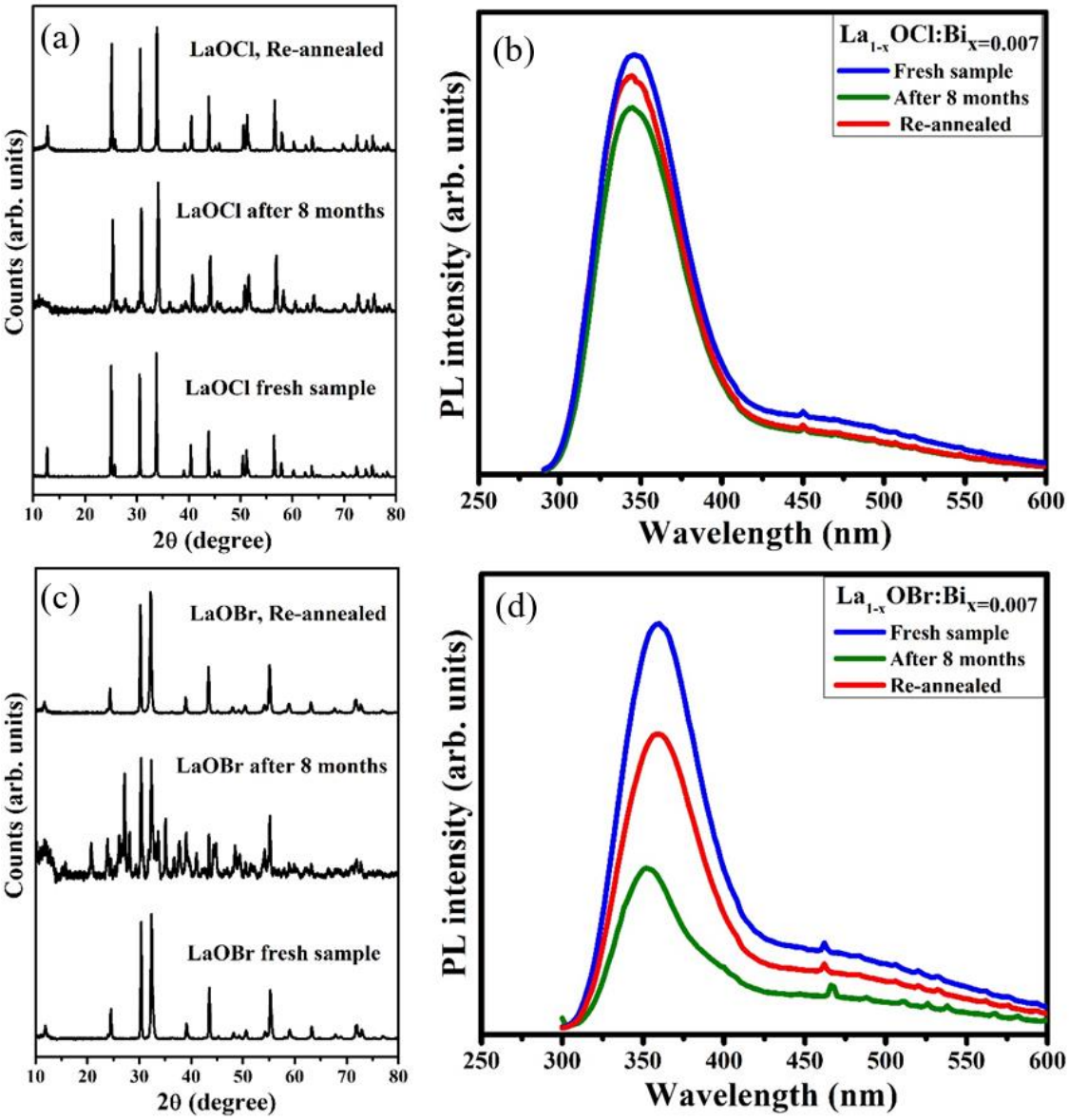

Figure 5.14: (a, c) XRD patterns of freshly prepared $La_{1-x}OCl:Bi_{x=0.007}$ and $La_{1-x}OBr:Bi_{x=0.007}$ powders initially and after 8 months, when exposed to the atmosphere and re-annealed samples. (b, d) PL emission spectra of freshly prepared $La_{1-x}OCl:Bi_{x=0.007}$ and $La_{1-x}OBr:Bi_{x=0.007}$ powders initially and after 8 months and re-annealed samples.

When the samples were re-annealed at 900 °C in air for 5 h, the XRD data suggested that the host structures reverted completely back to LaOCl and LaOBr. While the PL emission intensity for re-annealed LaOCl:Bi returned to almost its original level, the strong increase in the emission from re-annealed LaOBr:Bi was insufficient to return it to having emission comparable to a fresh sample. This may be due to some residual defects which act as quenching sites remain despite the phase purity suggested by the XRD results. Alternatively, this may be caused by segregation of Bi ions to non-luminescent metallic Bi nanoparticles during annealing and therefore a decrease in the Bi^{3+} concentration.

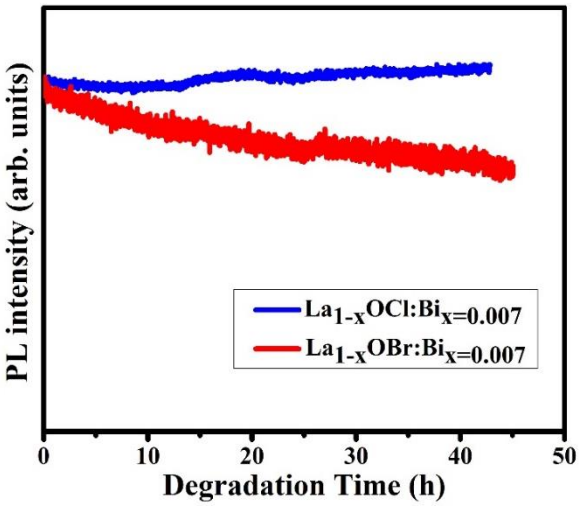

Figure 5.15: PL degradation curves of $La_{1-x}OCl:Bi_{x=0.007}$ and $La_{1-x}OBr:Bi_{x=0.007}$ exposed to 254 nm UV radiation at room temperature.

Long term storage therefore established that the LaOCl:Bi was not completely stable, while the LaOBr:Bi was significantly unstable. To further investigate the stability of the phosphors, their degradation under a 254 nm UV light which could simultaneously serve as a PL excitation source was tested. Figure 5.15 presents the degradation curves of the PL emission peak intensities for $La_{1-x}OCl:Bi_{x=0.007}$ and $La_{1-x}OBr:Bi_{x=0.007}$ at room temperature for 48 h. To ensure that possible long term changes in the excitation lamp intensity did not affect the results, the reflected signal was also monitored and used for reference. For $La_{1-x}OCl:Bi_{x=0.007}$, the PL intensity was fairly constant, while in the case of $La_{1-x}OBr:Bi_{x=0.007}$ the PL intensity continuously decreased. This shows that exposure to UV light significantly accelerated the degradation of the bromide host. XPS was used to

compare the surface chemical states of samples having undergone UV light exposure with un-exposed samples. The binding energy of the small C 1s peak attributed to surface hydrocarbons on the surface [30] is not shown, but was universally adjusted to 284.5 eV to compensate for charging.

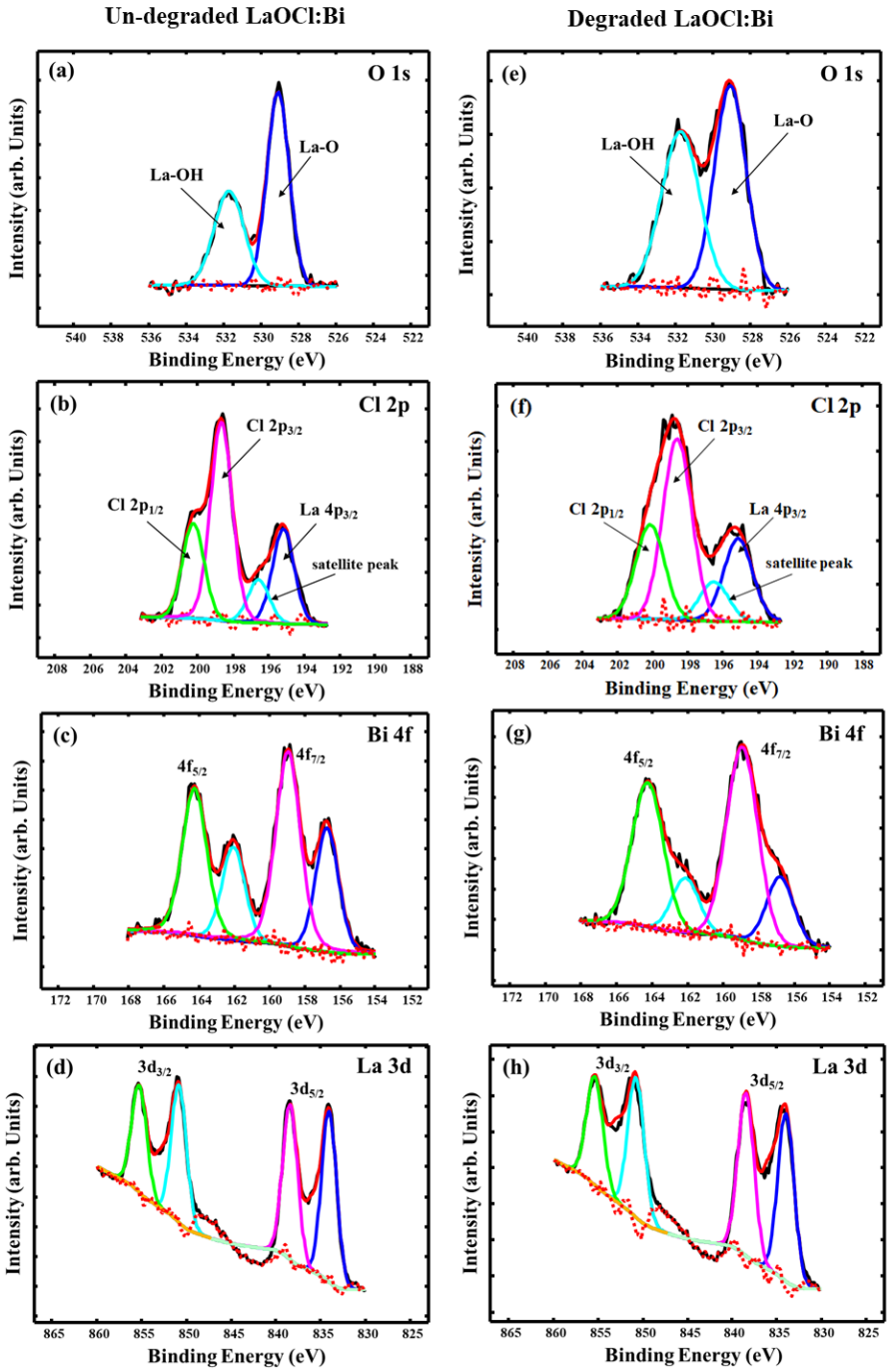

Figure 5.16: XPS data for un-degraded $La_{1-x}OCl:Bi_{x=0.007}$ in the binding energy regions of (a) O 1s (b) Cl 2p (c) Bi 4f (d) La 3d, with corresponding data for a degraded sample (e to h).

Figure 5.16(a, e) display the O 1s high-resolution XPS spectra for the un-exposed and exposed $La_{1-x}OCl:Bi_{x=0.007}$, respectively. Both spectra can be deconvoluted into two peaks, located at 529.1 for O in LaOCl and at 531.7 eV for O associated with hydroxyl (OH) groups [31]. The relative intensity of the second peak was greater for the UV-exposed sample (figure 5.16(e)), which indicates that the exposure of the sample to the 254 nm UV radiation increased the proportion of hydroxide and full-width-at-half-maximum (FWHM) of the peaks in the sample, even though the intensity of the PL emission was not reduced. The Cl 2p region shown in Figure 5.16(b, f) can be deconvoluted into two peaks located at 198.6 eV and 200.2 eV which were attributed to spin-orbit splitting into the $2p_{3/2}$ and $2p_{1/2}$ peaks, respectively [32]. The binding energy ranges for Cl 2p and La $4p_{3/2}$ peaks overlap, therefore two additional peaks were also fitted in the Cl 2p binding energy range which corresponded to the La $4p_{3/2}$ peak at 195.1 eV and a satellite peak at 196.5 eV [30]. Please note that the $4p_{1/2}$ La peak (213 eV) is outside the measured range and not shown. However, the FWHM of the peaks has increased for the sample exposed to the UV radiation. Despite the low Bi doping concentration (x = 0.007), XPS data for the Bi 4f peak was clear and is shown in Figure 5.16(c, g). Each spectrum consists of two pairs of spin-orbit split peaks having a separation of 5.3 eV, with the lower binding energy ($4f_{7/2}$) components at 156.8 eV and 158.9 eV. The lower binding energy corresponds to Bi^0 atoms, while the higher binding energy corresponds to Bi^{3+} ions which are expected to substitute La^{3+} ions in the host. The presence of the Bi^0 (metallic) was the result of Bi^{3+} segregation on the surface of the sample and its reduction to Bi^0 [33]. The FWHM of peaks has increased and the intensity of the peaks corresponding to Bi^0 atoms was less for the UV-exposed sample. The XPS spectrum of the La 3d binding energy region shown in Figure 5.16(d, h) is complex due to a variety of fitting challenges discussed in our previous work on La_2O_3 [17]. For the purpose of comparison here, we made a simple fit with Shirley background and two pairs of spin-orbit split peaks, having $3d_{5/2}$ components at 834.1 eV for the main peak and 838.4 eV for the satellite peak [34], while the $3d_{3/2}$ components are located at 16.8 eV higher energies. The FWHM of peaks has increased for the UV-exposed sample.

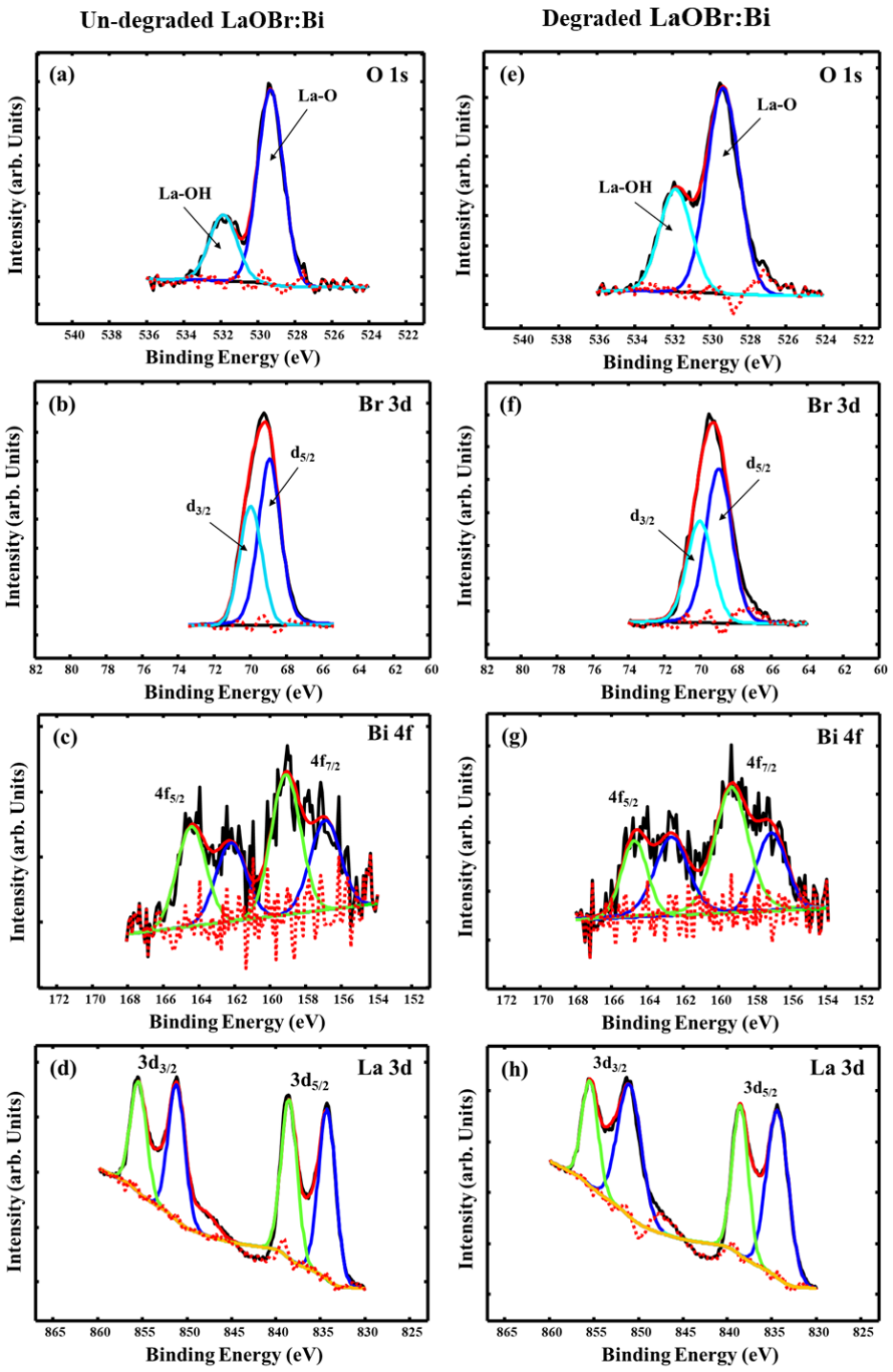

Figure 5.17: High resolution XPS peaks deconvolution of $La_{1-x}OBr:Bi_{x=0.007}$ (a) O 1s (b) Br 3d (c) Bi 4f (d) La 3d for un-degraded. Similar peaks are presented from (e to h) for $La_{1-x}OBr:Bi_{x=0.007}$ degraded sample.

Figure 5.17(a, e) show O 1s high-resolution XPS spectra for the un-exposed and exposed $La_{1-x}OBr:Bi_{x=0.007}$, respectively. The origin of the peaks is similar to that in LaOCl:Bi. The relative intensity of the second peak was greater for the UV-exposed sample (figure 5.17(e)), which indicates that the exposure of the sample to the 254 nm UV radiation increased the proportion of hydroxide as well as the FWHM of the peaks in the sample. The Br 3d region presented in Figure 5.17(b, f) can be deconvoluted into two main peaks centred at 68.9 eV and 70.0 eV which were attributed to the spin orbit splitting into the $3d_{3/2}$ and $3d_{5/2}$ peaks, respectively [32, 35]. The FWHM of the peaks has increased for the sample exposed to the UV radiation. The Bi 4f region is presented in Figure 5.17(c, g) and the spectra consist of two pairs of spin-orbit split peaks having separation of 5.3 eV, with the lower binding energy ($4f_{7/2}$) components at 156.8 eV and 159.1 eV. The origin of the peaks is similar to that in LaOCl:Bi, although the intensity is low as apparent from the poor signal-to-noise ratio and showing that the concentration of Bi on the surface is lower compared to the case of LaOCl:Bi. The presence of the Bi^0 (metallic) was the result of Bi^{3+} segregation on the surface of the sample and its reduction to Bi^0 [33]. The intensity of the peaks has slightly decreased for the UV-exposed sample. For the La 3d region shown in Figure 5.17(d, h) the spectra can be deconvoluted into two pairs of spin-orbit split peaks having a separation of 16.8 eV, the $3d_{5/2}$ components at 834.2 eV for the main peak and 838.5 eV for the satellite peak. The origin of the peaks is similar to that in LaOCl:Bi. Although the UV-exposed samples show some small differences compared to the un-exposed samples, e.g. an increase in the O peak related to hydroxide and a slight broadening of the anion peaks which may be due to a greater disorder, these changes are similar for both LaOCl:Br and LaOBr:Bi and therefore do not provide a clear picture explaining why the LaOBr:Bi exhibits degradation while the LaOCl:Bi does not under UV radiation. This suggests that changes may occur in the bulk and may possibly be related to the creation of point defects which act as non-radiative recombination centres in the LaOBr:Bi which has a lower bandgap.

5.4. Conclusion

Bi doped LaOCl and LaOBr were successfully synthesized by the solid state reaction method. XRD data confirmed that both LaOCl and LaOBr phases belong to the tetragonal crystal structure.

SEM images showed that the particles were aggregated and had irregular plate-like shapes. The reflectance spectra showed two absorption bands, located at 255 nm and 308 nm for LaOBr:Bi and 247 nm and 300 nm for LaOCl:Bi. The absorption bands at shorter wavelengths centred at around 255 nm and 247 nm correspond to the $^1S_0 \rightarrow {}^3P_1$ absorption of Bi^{3+} ions, while the longer wavelength absorption bands at around 308 nm and 300 nm may result from Bi-induced defects or Bi-clusters. The band gap energies were estimated to be 5.38 eV for LaOBr and 5.76 eV for LaOCl. The ultraviolet emission peaks were assigned to the $^3P_1 \rightarrow {}^1S_0$ transition of the Bi^{3+} ions, while additional relatively weak emissions in the visible range were attributed to Bi clustering. The PL emission intensity of LaOCl:Bi was about double that of LaOBr:Bi powder phosphor. LaOCl:Bi was found to be slightly unstable when exposed to the atmosphere for several months, while LaOBr:Bi was significantly less stable. The long term degradation was accompanied by a change in XRD patterns. The LaOBr:Bi phosphor was also found to degrade rapidly under 254 nm ultraviolet excitation, while LaOCl:Bi did not degrade under the same conditions. XPS data of the UV-exposed LaOCl:Bi and LaOBr:Bi showed an increase in the concentration of hydroxide on the surface of both the samples and broadening of the peaks associated with the anions. Since only the luminescence of the LaOBr:Bi degraded during UV-exposure, while the LaOCl:Bi did not, the similar changes in XPS results for both samples may indicate that the degradation is not due to a surface reaction, but may be due to non-radiative defects forming more easily in the bulk of LaOBr which has a smaller bandgap than LaOCl.

5.5. References

1. N. Dhananjaya, C. Shivakumara, Rohit Saraf, Sukanti Behera, H. Nagabhushana. Comparative study of Eu^{3+} activated LnOCl (Ln= La and Gd) phosphors and their Judd-Ofelt analysis. *Journal of Rare Earths 33* (2015) 946-953. doi: 10.1016/S1002-0721(14)60510-X
2. U. Rambabu, A. Mathur, S. Buddhudu. Fluorescence spectra of Eu^{3+} and Tb^{3+}-doped lanthanide oxychloride powder phosphors. *Materials Chemistry and Physics* 61 (1999) 156-162. doi: 10.1016/s0254-0584(99)00122-4

3. S. I. Golovkova, A. M. Gurvich, T. I. Savikhlna, D. Starick, T. A. Birman, G. Herzog, R. V. Katomina, *et al.* Luminescence properties of lanthanum oxyhalides activated with terbium. *Journal of Applied Spectroscopy 35* (1981) 1208-1212. doi: 10.1007/bf00624115
4. Kenneth R. Kort, Sarbajit Banerjee. Shape-controlled synthesis of well-defined matlockite LnOCl (Ln: La, Ce, Gd, Dy) nanocrystals by a novel non-hydrolytic approach. *Journal of Inorganic Chemistry* 50 (2011) 5539-5544. doi: 10.1021/ic200114s
5. Koichi Momma, Fujio Izumi. VESTA 3 for Three-Dimensional Visualization of Crystal, Volumetric and Morphology Data. *Journal of Applied Crystallography* 44 (2011) 1272-1276. doi: 10.1107/S0021889811038970
6. A. Vaitkus, A. Merkys, S. Gražulis. Validation of the Crystallography Open Database using the Crystallographic Information Framework. *Journal of Applied Crystallography*, *54* (2021) 661-672. doi: 10.1107/S1600576720016532
7. Jorma Hölsä, Kari Koski, Sari Makkonen, Eija Säilynoja, Hanna Rahiala. X-ray powder diffraction and vibrational spectroscopic investigation of the $LaO(Cl_{1-x}Br_x)$ solid solutions. *Journal of Alloys and Compounds* 249 (1997) 217-220. doi: 10.1016/s0925-8388(96)02632-1
8. M. Guan, L. Mei, Z. Huang, C. Yang, Q. Guo, Z. Xia. Synthesis and near-infrared luminescence properties of $LaOCl:Nd^{3+}/Yb^{3+}$. *Journal of Infrared Physics and Technology* 60 (2013) 98-102. doi: 10.1016/j.infrared.2013.03.014
9. S.S. Lee, H.I. Park, C.H. Joh, S.H. Byeon. Morphology-dependent photoluminescence property of red-emitting LnOCl:Eu (Ln = La and Gd). *Journal of Solid State Chemistry* 180 (2007) 3529–3534. doi: 10.1016/j.jssc.2007.10.020
10. U. Rambabu, K. Rajamohan Reddy, K. Annapurna, T. Balaji, J.V. Satyanarayana, S. Buddhudu. Fluorescence spectra of Sm^{3+}-doped lanthanide oxychloride powder phosphors. *Journal of Materials Letters* 27 (1996) 59-63. doi: 10.1016/0167-577x(96)80002-4
11. G. Blasse, A. Bril. Investigations on Bi^{3+} Activated Phosphors. *Journal of Chemical Physics* 48 (1968) 217-222. doi: 10.1063/1.1667905
12. L. I. Van Steensel, G. Blasse. The luminescence of Sb^{3+} in LaOCl. *Journal of Alloys and Compounds* 232 (1996) 60-62. doi: 10.1016/0925-8388(95)02017-9

13. A. Wolfert, G. Blasse. Luminescence of the Bi^{3+} ion in compounds LnOCl (Ln = La, Y, Gd). *Materials Research Bulletin* 19 (1984) 67–75. doi: 10.1016/0025-5408(84)90011-4
14. A. Wolfert, G. Blasse. Luminescence of Bi^{3+}-activated LaOBr, a system with emission from different states. *Journal of Luminescence* 33 (1985) 213-226. doi: 10.1016/0022-2313(85)90019-5
15. W.A.I. Tabaza, H.C. Swart, R.E. Kroon. Optical properties of Bi and energy transfer from Bi to Tb in $MgAl_2O_4$ phosphor. *Journal of Luminescence* 148 (2014) 192-197. doi: 10.1016/j.jlumin.2013.12.018
16. Roy H.P. Awater, Pieter Dorenbos. The Bi^{3+} 6s and 6p Electron Binding Energies in Relation to the Chemical Environment of Inorganic Compounds. *Journal of Luminescence* 184 (2017) 221–231. doi: 10.1016/j.jlumin.2016.12.021
17. B.M. Jaffar, H.C. Swart, H.A.A. Seed Ahmed, A. Yousif, R.E. Kroon, Stability of Bi doped La_2O_3 powder phosphor and PMMA composites. *Journal of Physics and Chemistry of Solids* 131 (2019) 156-163. doi: 10.1016/j.jpcs.2019.04.004
18. R.D. Shannon. Revised Effective Ionic Radii and Systematic Studies of Interatomic Distances in Halides and Chalcogenides. *Journal of Acta Crystallographica Section A* 32 (1976) 751-767. doi: 10.1107/S0567739476001551
19. Jorma Hölsä, Mika Lastusaari, Janne Niittykoskiac, Regino Sàez Puche. Interplay between crystal structure and magnetic susceptibility of tetragonal ROBr. *Physical Chemistry Chemical Physics* 4 (2002) 3091-3097. doi: 10.1039/b110745n
20. Rosendo López, Ricardo Gómez. Band-Gap Energy Estimation from Diffuse Reflectance Measurements on Sol-Gel and Commercial TiO_2: A Comparative Study. *Journal of Sol-Gel Science and Technology* 61 (2012) 1-7. doi: 10.1007/s10971-011-2582-9
21. Aman Pandey, Gunisha Jain, Divya Vyas, Silvia Irusta, Sudhanshu Sharma. Nonreducible, Basic La_2O_3 to Reducible, Acidic $La_{2-x}Sb_xO_3$ with Significant Oxygen Storage Capacity, Lower Band Gap, and Effect on the Catalytic Activity. *Journal of Physical Chemistry C* 121 (2017) 481-489. doi: 10.1021/acs.jpcc.6b10821
22. Donghyeon Kim, Sangha Park, Sungyun Kim, Seong-Gu Kang, Jung-Chul Park. Blue-Emitting Eu^{2+}-Activated LaOX (X = Cl, Br, and I) Materials: Crystal Field Effect. *Journal of Inorganic Chemistry* 53 (2014) 11966-11973. doi: 10.1021/ic5015576

23. G Shwetha,V Kanchana,N Yedukondalu, G Vaitheeswaran. Ab initio study of scintillating lanthanide oxyhalide host materials. *Materials Research Express* 2 (2015) 105901. doi: 10.1088/2053-1591/2/10/105901
24. Lili Wang, Qiang Sun, Qingzhi Liu, Jinsheng Shi. Investigation and Application of Quantitative Relationship between sp Energy Levels of Bi^{3+}ion and Host Lattice. *Journal of Solid State Chemistry* 191 (2012) 142-46. doi: 10.1016/j.jssc.2012.03.015
25. Philippe Boutinaud. Revisiting the Spectroscopy of the Bi^{3+} Ion in Oxide Compounds. *Inorganic Chemistry* 52 (2013) 6028-6038. doi: 10.1021/ic400382k
26. B.M. Jaffar, H.C. Swart, H.A.A. Seed Ahmed, A. Yousif, R.E. Kroon. Luminescence properties of Bi doped La_2O_3 powder phosphor. *Journal of Luminescence* 209 (2019) 217-224. doi: 10.1016/j.jlumin.2019.01.044
27. R.D. Shannon. Revised Effective Ionic Radii and Systematic Studies of Interatomie Distances in Halides and Chaleogenides. *Acta Crystallographica Section A* 32 (1976) 751-767. doi: 10.1107/S0567739476001551
28. B.M. Jaffar, HC. Swart, H.A.A. Seed Ahmed, A. Yousif, R.E. Kroon. Cathodoluminescence degradation of Bi doped La_2O_3 and La_2O_2S phosphor powders. *Physica B: Condensed Matter* 574 (2019) 411659. doi: 10.1016/j.physb.2019.411659
29. C. R. Ronda, H. Bechtel, U. Kynast, T. Welker. The degradation behavior of LaOBr:Tb under cathode-ray excitation. *Journal of Applied Physics* 75 (1994) 4636-4641. doi: 10.1063/1.355913
30. M.F. Sunding, K. Hadidi, S. Diplas, O.M. Løvvik, T.E. Norby, A.E. Gunnæs. XPS Characterisation of in Situ Treated Lanthanum Oxide and Hydroxide Using Tailored Charge Referencing and Peak Fitting Procedures. *Journal of Electron Spectroscopy and Related Phenomena* 184 (2011) 399-400. doi: 10.1016/j.elspec.2011.04.002
31. Jerry Pui Ho Li, Xiaohong Zhou, Yaoqi Pang, Liang Zhu, Evgeny I. Vovk, Linna Cong, Alexander P. van Bavel, Shenggang Li and Yong Yang. Understanding of binding energy calibration in XPS of lanthanum oxide by in situ treatment. *Physical Chemistry Chemical Physics* 21 (2019) 22351-22358. doi: 10.1039/c9cp04187g
32. Kuang-Hsu Wu, Da-Wei Wang, Qingcong Zeng, Yang Li, Ian R. Gentle. Solution phase synthesis of halogenated graphene and the electrocatalytic activity for oxygen reduction

reaction. *Chinese Journal of Catalysis* 35 (2014) 884-890. doi: 10.1016/S1872-2067(14)60108-X

33. N. A. M. Saeed, E. Coetsee, R. E. Kroon, M. Bettinelli, H. C. Swart. Photoluminescence of Bi^{3+} doped in YOF phosphor as an activator. *Optical Materials* 119 (2021) 111291. doi: 10.1016/j.optmat.2021.111291
34. Suresh Reddy Sanivarapu, John Berchmans Lawrence, and Gosipathala Sreedhar. Role of Surface Oxygen Vacancies and Lanthanide Contraction Phenomenon of $Ln(OH)_3$ (Ln = La, Pr, and Nd) in Sulfide-Mediated Photoelectrochemical Water Splitting. *ACS Omega* 3 (2018) 6267-6278. doi: 10.1021/acsomega.8b00429
35. Kangli Liu,a Xiaochao Zhang, Changming Zhang, Guangmin Ren, Zhanfeng Zheng, Zhiping Lv and Caimei Fan. Enhanced photocatalytic reduction of CO_2 to CO over BiOBr assisted by phenolic resin-based activated carbon spheres. *RSC Advances* 9 (2019) 14391-14399. doi: 10.1039/c9ra01329f

Chapter six

Luminescence properties of Bi doped LaOF phosphor powder

6.1. Introduction

The luminescence characteristics of Bi^{3+} ions have been studied in many different host lattices [1] and exhibited wonderful optical characteristics because of their strong interaction with the surrounding host lattice [2]. Bi^{3+} ions have $^1S_0$ ground state in the $6s^2$ configuration and four excited energy levels in the $6s^16p^1$ configuration, namely a triplet $^3P_0$, $^3P_1$, $^3P_2$ and a singlet $^1P_1$. The transitions from $^1S_0 \rightarrow {}^3P_0$ and $^1S_0 \rightarrow {}^3P_2$ are forbidden, while the transition from $^1S_0 \rightarrow {}^1P_1$ is allowed. The transition from $^1S_0$ to $^3P_1$ becomes allowed due to mixing of the $^1P_1$ and $^3P_1$ levels by spin orbit coupling [1]. Phosphor materials activated with Bi^{3+} ions generally emit in the near-ultraviolet or blue regions, so hosts such as lanthanum oxyfluoride (LaOF) that are conducive to Bi^{3+} emission at longer wavelengths are less common and therefore of particular interest.

LaOF has potential as a phosphor host material because of its high chemical stability, low phonon energy, high refractive index and high transparency in the near infrared, visible and ultraviolet regions [3]. LaOF has been synthesized by different techniques such as the thermal decomposition of lanthanum (III) carbonate fluoride ($LaFCO_3$) in air [4], the solid-state reactions between ammonium fluoride (NH_4F) and lanthanum oxide (La_2O_3) or lanthanum(III) fluoride (LaF_3) and La_2O_3 [5, 6], ball milling and the calcination of a mixture of polytetrafluoroethylene and La_2O_3 [7], annealing of LaF_3 in air [8], the sol–gel method [9] and the decomposition of lanthanum (III) trifluoroacetate in boiling oleylamine [10].

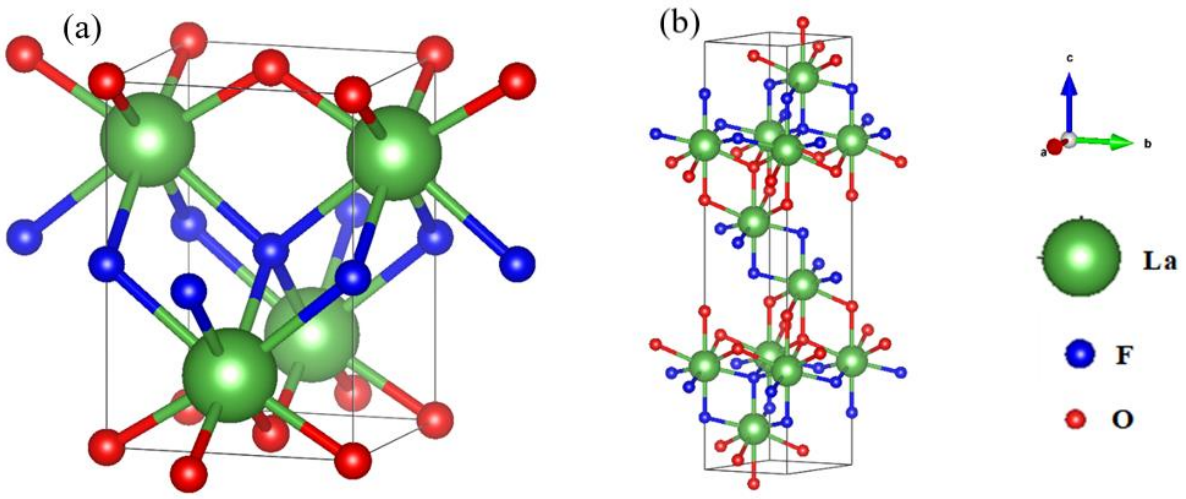

Figure 6.1: The unit cells of LaOF. (a) Tetragonal crystal structure (COD number: 7037053) and (b) Rhombohedral crystal structure (COD number: 9009071).

LaOF has various stoichiometries and structures [11, 12]. At high temperatures LaOF has a cubic fluorite-type structure, while at room temperatures LaOF has either a rhombohedral or tetragonal crystal structure [13] depending on the chemical composition and/or anion ordering. If the fluorine ratio relative to oxygen is excessive in the compound, the ordering occurs along the [001] direction resulting in a tetragonal distortion, but if the compound contains excess oxygen the ordering occurs along the [111] direction resulting in a rhombohedral lattice [14]. Both tetragonal and a rhombohedral crystal structures were modelled with Vesta software [15] using the CIF files obtained from the Crystallography Open Database (COD) [16]. In the tetragonal crystal structure the space group is *P*4/*nmm* (no. 129) and its structure is shown in figure 6.1(a). Each La^{3+} ion with C_{4v} site symmetry and is coordinated with four oxygen ions (La-O) with the same bond length and four fluoride ions (La-F) having the same bond lengths [17, 18]. This structure is different to the other lanthanum oxyhalides LaOX (X = Cl, Br). Although the structures have the same space group, the F^- ions are smaller than the Cl^- or Br^- ions and do not form double layers and the orientation of the La-X bonds relative to the La-O bonds when viewed along the Z axis is rotated 45 degrees. In the rhombohedral crystal structure, shown in Figure 6.1(b), the space group is $R\bar{3}m$ (no. 166). Each La^{3+} ion has C_{3v} symmetry and is coordinated with four oxygen ions and four fluorine ions [9, 17], with one of each type of anion lying along the three-fold rotation axis.

LaOF has been used as phosphor host doped with Er^{3+} and Yb^{3+} [18], as well as Bi^{3+} and Eu^{3+} [19]. In this work the photoluminescence (PL) excitation and emission spectra of LaOF:Bi^{3+} phosphor powders prepared by the solid state reaction method were investigated and discussed. The PL intensity was optimized by varying the Bi doping concentration and the annealing temperature. The stability of the optimized LaOF:Bi^{3+} phosphor when exposed to UV radiation was also assessed.

6.2. Experimental

Powder samples of lanthanum oxyfluoride (LaOF) were synthesized using the solid-state reaction method. According to the reaction

$$La_2O_3 + 2NH_4F \rightarrow 2LaOF + 2NH_3 + H_2O \qquad (6.1)$$

the molar ratio of the La_2O_3 to NH_4F should be 1:2, but 25% excess of ammonium fluoride was used during synthesis. Before weighing, the La_2O_3 was annealed at 800 °C for 4 h in air to make sure it had not converted to $La(OH)_3$. To synthesize LaOF, 1.3032 g of La_2O_3 (99.999%, Sigma Aldrich) and 0.3704 g NH_4F (99.999%, Sigma-Aldrich) were mixed in 10 ml of ethanol. The mixture was ground thoroughly in an agate mortar with a pestle for 1 h. This mixed powder was transferred to a porcelain crucible and annealed at a temperature between 700 °C and 1100 °C for 5 h in air. The Bi dopant is expected to substitute La^{3+} ions since they have the same valence and similar ionic radii [20], therefore to dope samples a suitable small quantity of La_2O_3 was replaced by an equal molar quantity of Bi_2O_3 (99.999%, Sigma Aldrich).

The crystal structures were assessed using X-ray diffraction (XRD) measurements made with a Bruker D8 Advance diffractometer with Cu Kα X-rays created by an electron beam of current 40 mA accelerated through 40 kV. The samples were examined using a JEOL JSM-7800F scanning electron microscope (SEM) and the elemental composition was assessed by means of energy dispersive X-ray spectroscopy (EDS) with an Oxford Instruments X-Max^{N}80 detector. The photoluminescence (PL) properties of the powders were measured at room temperature using an

FS5 spectrometer from Edinburgh Instruments. The International Commission for Illumination (CIE) coordinates of the emitted light was calculated using the GoCIE software [21]. The PL degradation data were collected with an HR4000CG-UV-NIR CCD spectrometer using Spectrasuite software while the phosphor powder was excited by a 254 nm emitting fluorescent tube. The chemical state of the sample surfaces were analysed using X-ray photoelectron spectroscopy (XPS) before and after degradation using a PHI 5000 Versaprobe system. The spectra were obtained by using a monochromatic Al Kα X-ray beam (1486.6 eV) generated by a 25 W, 15 kV electron beam. The binding energy scale was shifted so that the C 1s peak of adventitious C occurred at 284.5 eV to compensate for possible charging. Spectra were deconvoluted and fitted using MULTIPAK software v.8.2.

6.3. Results and discussion

6.3.1. Structure, morphology and chemical composition analysis

Figure 6.2(a) presents XRD patterns of undoped LaOF powder samples annealed at different temperatures between 700 and 1100 °C, together with reference data for different phases of LaOF (JCPDS cards no. 0050470 and no. 0060281). Annealing in the lower temperature range from 700 °C up to 1000 °C caused the formation of a pure tetragonal LaOF phase, while annealing at the highest temperature used (1100 °C) produced two XRD diffraction peaks, 006 and 018, which are characteristic of the rhombohedral structure. The tetragonal phase is more likely with excess fluorine and the rhombohedral phase with excess oxygen [13, 14]. Since the samples were synthesized with excess fluorine the tetragonal phase may be expected, while the conversion to the rhombohedral phase for high temperature annealing in air shows the loss of fluorine and its replacement by excess oxygen under such conditions. The annealing temperature of 1000 °C was identified as the optimum temperature for annealing the LaOF samples based on later PL measurements.

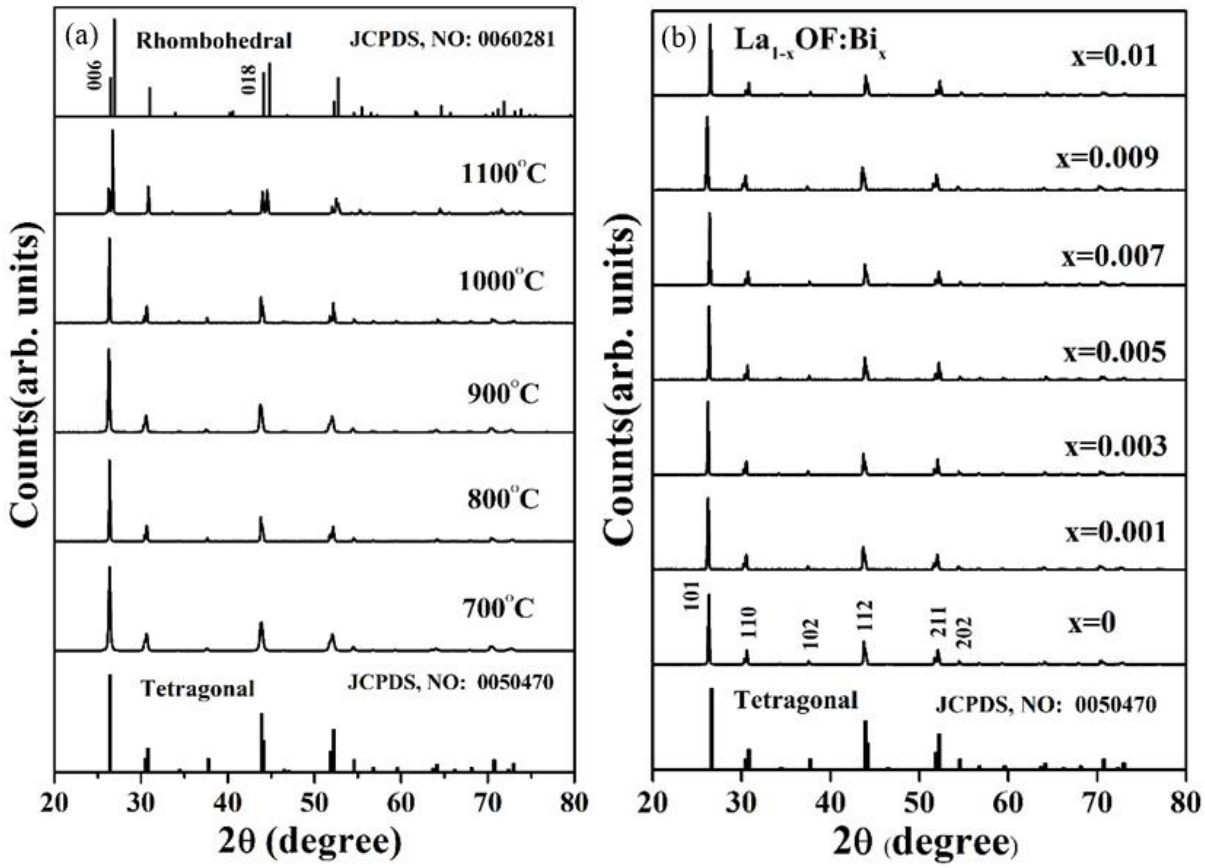

Figure 6.2: XRD patterns of LaOF phosphor powders (a) annealed at different temperatures (b) doped with different Bi concentrations and annealed at 1000 °C, together with information from JCPDS cards no. 0050470 and 0060281.

Table 6.1: Crystallite sizes calculated from the Scherrer equation.

Bi concentration (x)	Crystallite size (nm)
0	60
0.001	62
0.003	64
0.005	62
0.007	62
0.009	63
0.01	64

Figure 6.2(b) shows the XRD patterns of $La_{1-x}OF:Bi_x$ (x = 0, 0.001, 0.003, 0.005, 0.007, 0.009 and 0.01) phosphor powder samples annealed at 1000 °C. The addition of Bi did not result in a change of the tetragonal LaOF phase. The crystallite size *D* was determined from the full-width

at half-maximum β of the main 101 diffraction peak using the Scherrer formula [22], $D = \frac{0.9\lambda}{\beta\cos\theta}$ where λ is the X-ray wavelength and θ is the Bragg angle. The other diffraction peaks are overlapping double peaks, so it is hard to determine their broadening and hence they are not suitable for analysis using the Scherrer equation. The results are summarized in Table 6.1 and show that the doping had little influence of the crystallite size of the pure host (~60 nm).

Figure 6.3 shows SEM images of the $La_{1-x}OF:Bi_x$ phosphor powders doped with various Bi concentrations, annealed at 1000 °C. The images show that the shape of the particles of the LaOF pure host is similar to the doped samples, which means that the addition of the Bi did not affect the morphology of the particles. The EDS spectrum of the LaOF pure host sample confirmed the presence of all the host elements (La, O, and F) as expected, together with a small quantity of C that probably originated from the carbon tape that was used to mount the samples and adventitious C due to the atmosphere and handling. The presence of Ir is due to coating the samples with this metal to improve conductivity and prevent charging in the SEM. The EDS spectrum of the sample doped with high Bi concentration (x = 0.01) is similar to the LaOF pure host sample except for the additional very small peak near 2.5 keV attributed to the Bi dopant. No other elements were detected in the samples, indicating that the $La_{1-x}OF:Bi_x$ phosphors were pure.

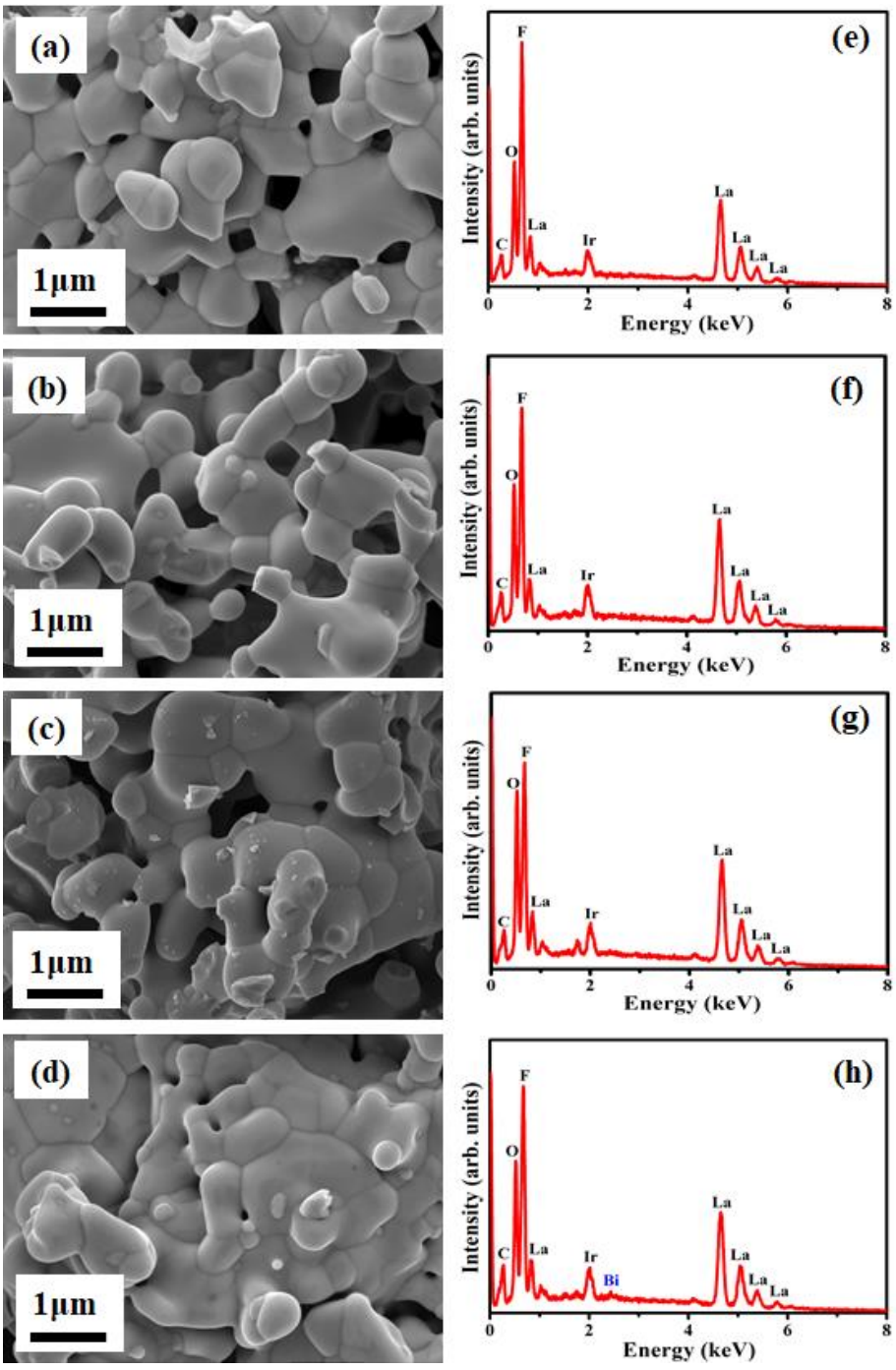

Figure 6.3: SEM images (left) and EDS spectra (right) for $La_{1-x}OF:Bi_x$ phosphor powders annealed at 1000 °C (a, e) x = 0, (b, f) x = 0.003, (c, g) x = 0.005 and (d, h) x = 0.01.

Figure 6.4 shows the EDS spectra of the $La_{1-x}OF:Bi_{x=0.005}$ phosphor powders annealed at various temperatures, with quantification of the host elements shown as insets. Figure 6.4(f) illustrates

that the ratio of the fluorine decreased with increasing annealing temperatures, while the ratio of oxygen increased. This explains why the tetragonal structure converted to the rhombohedral structure when the annealing temperature was very high (i.e. 1100 °C).

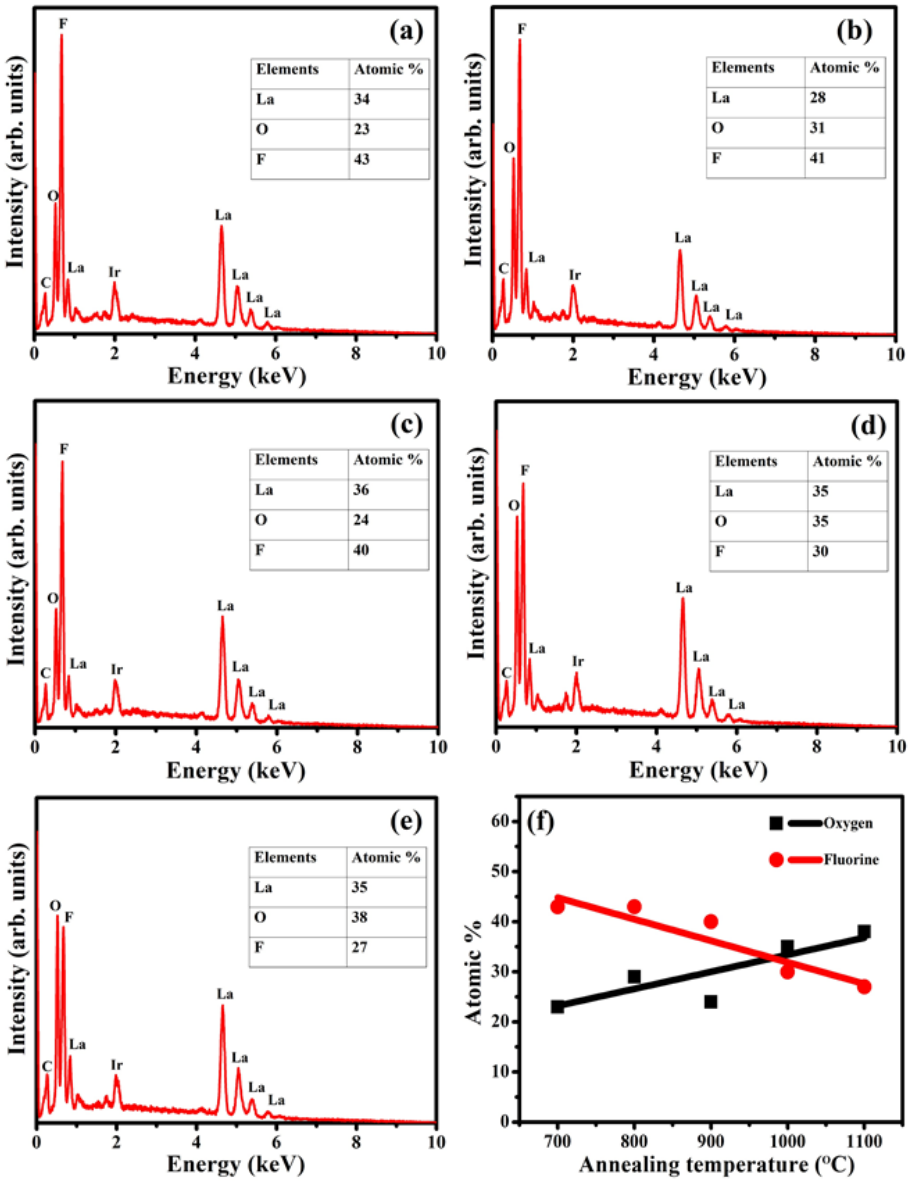

Figure 6.4: EDS spectra of $La_{1-x}OF:Bi_{x=0.005}$ phosphor powders annealed at various temperatures (a) 700 °C, (b) 800 °C, (c) 900 °C, (d) 1000 °C, and (e) 1100 °C. (f) Atomic % of O and F as a function of annealing temperature.

6.3.2. Diffuse reflectance spectra

The absorption properties of the LaOF pure host material and the effects of the Bi dopant when inserted in the host lattice were studied by using diffuse reflectance spectroscopy, as shown in figure 6.5. The reflectance spectrum of $La_{1-x}OF:Bi_{x=0.005}$ sample annealed at 1000 °C (blue line) shows two absorption bands, located at around 245 nm and 290 nm. The absorption band at the shorter wavelength (245 nm) is attributed to the absorption of Bi^{3+} ions, while the absorption band at the longer wavelength at around 290 nm may correspond to Bi-induced defects or Bi-clusters. The pure host shows high reflectance over the entire measured range, with only weak absorption below 350 nm which is not strong enough to correspond to band-to-band host absorption, but may be from defects or impurities. This implies that the band gap is large, greater than the upper limit for our instrument capable of measuring to 200 nm (~6.2 eV). Suresh *et al.* [23] studied the diffuse reflectance spectra of LaOF:Sm^{3+} and found the band gap energy of a LaOF pure host to be 4.08 eV. Xiangyu Yan *et al.* [24] determined the band gap energy of LaOF to be 5.56 eV. These other researchers who obtained lower band gaps may have interpreted defect or impurity absorption as host absorption or the differences in band gap values may be due to the different preparation methods which influence the particle size, morphology and defects.

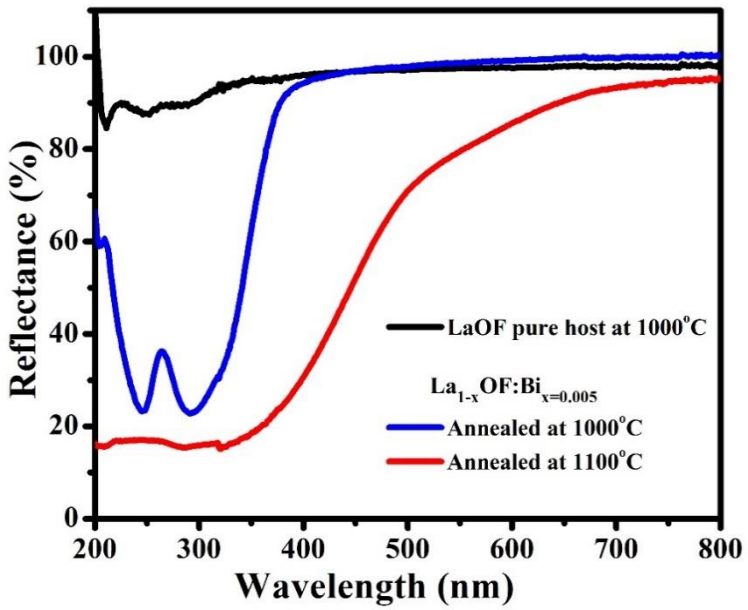

Figure 6.5: Diffuse reflectance spectra of LaOF pure host and $La_{1-x}OF:Bi_{x=0.005}$ annealed at 1000 °C and 1100 °C, respectively.

The reflectance of $La_{1-x}OF:Bi_{x=0.005}$ annealed at 1100 °C (red line) is also shown in figure 6.5 and differs greatly from the sample annealed at 1000 °C, having much broader absorption starting already in the visible range and extending through the UV. This difference is attributed to the phase change of the LaOF host when annealed at 1100 °C, which also results in quenching of the luminescence to be presented next.

6.3.3. Photoluminescence analysis

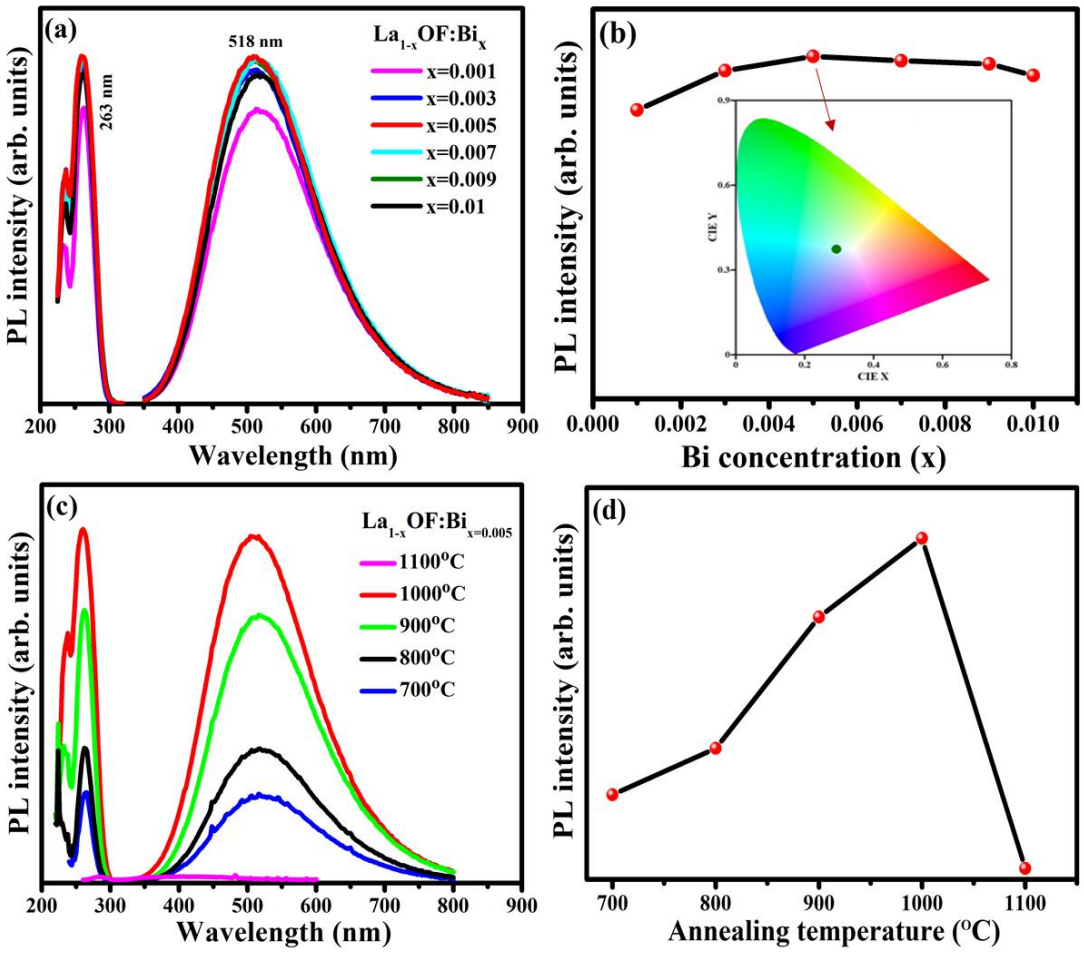

Figure 6.6: (a) Excitation and emission spectra of $La_{1-x}OF:Bi_x$ doped with various Bi concentrations, annealed at 1000 °C. (b) Emission peak intensity as a function of Bi concentration. The inset shows the CIE diagram with colour coordinates of the sample x = 0.005. (c) Excitation and emission spectra of $La_{1-x}OF:Bi_{x=0.005}$ annealed at various temperatures. (d) Emission peak intensity as a function of the annealing temperature.

Figure 6.6(a) presents the PL excitation and emission spectra of $La_{1-x}OF:Bi_x$ doped with various Bi concentrations annealed at 1000 °C. A broad white emission band centred at 518 nm was observed when excited at 263 nm. The excitation and emission were attributed to the $^1S_0 \leftrightarrow {}^3P_1$ transition of Bi^{3+} ions, matching the assignment of Yang and Park [19] who studied the PL of $La_{0.99}O_{0.65}F_{1.7}$:Bi. Figure 6.6(b) shows the PL emission intensity as a function of Bi doping concentration, with the maximum occurring for x = 0.005. The luminescence intensity decreased at higher concentrations due to concentration quenching. The quenching occurs because of migration of energy between the activators and may occur for low dopant fractions from 0.001 to 0.01 [25] due to strong interaction between the Bi^{3+} ions. The inset shows the chromaticity coordinates X = 0.30 and Y = 0.38 of the $La_{1-x}OF:Bi_{x=0.005}$ powder phosphor determined using the GoCIE software [21].

Figure 6.6(c) shows the PL spectra for samples annealed at different temperatures, while Figure 6.6(d) shows the emission peak intensity as a function of the annealing temperature. The luminescence intensity increased with increasing annealing temperature up to 1000 °C, while the luminescence of the sample annealed at 1100 °C was negligible in comparison. Annealing at 1100 °C produced the rhombohedral phase of LaOF rather than the tetragonal phase obtained at lower temperatures, so the effect is clearly associated with the host crystal phase.

Although there is no obvious reason why the rhombohedral phase should not be conducive to efficient luminescence of Bi^{3+} ions, it is possible that defects in the F-deficient rhombohedral phase act as non-radiative recombination centres. To further explore the reason for the quenching of luminescence after annealing above 1000 °C, XPS measurements of the host samples annealed at 1000 °C and 1100 °C were compared.

Figure 6.7 presents the high resolution XPS spectra of the La 3d, O 1s and F 1s binding energy regions of the undoped LaOF host material after sputter cleaning. The La 3d binding energy region contains two pairs of spin-orbit split peaks, having their lower binding energy $3d_{5/2}$ components near 834 eV for the main peak and 838 eV for a satellite peak [26]. The F 1s spectrum exhibited a single peak near 685 eV [27], while the O 1s spectrum near 530 eV is more complex. The main O

1s peak due to the lattice oxygen of LaOF has additional bands on the higher binding energy side related to defects and contamination that result in the broad asymmetrical structure. Fitting and deconvolution of these spectra were not performed because they did not show strong differences despite the change in crystal phase as revealed by XRD. Note that more details and deconvolution of the components of the O 1s peak will be discussed later in Figure 6.12 in the context of the degraded samples.

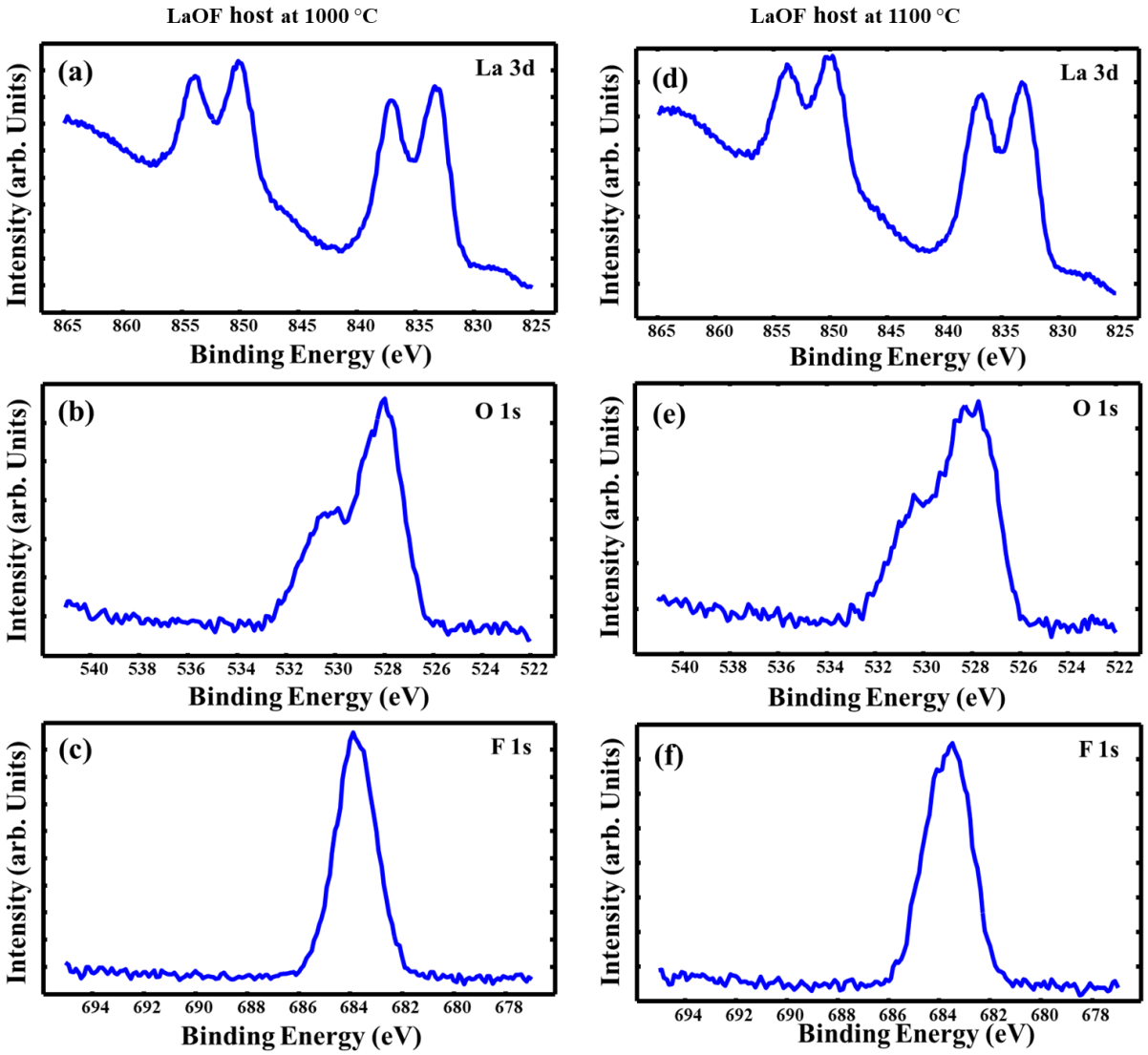

Figure 6.7: XPS spectra for LaOF host annealed at 1000 °C in the binding energy regions of (a) La 3d, (b) O 1s (c) F 1s. Similar spectra are shown in (d, e, f) for the LaOF host annealed at 1100 °C.

Figure 6.8 shows the XPS high-resolution spectra of the Bi 4f binding energy region for the doped $La_{1-x}OF:Bi_x$ samples annealed at 1000 °C and 1100 °C. The data corresponds to two different doping concentrations (x = 0.005 and x = 0.01) and spectra are given both before (red line) and after (blue line) sputter cleaning the surface. Note that the vertical scale of each part is different and, for the weakest signal in Figure 6.8(a) before sputtering, the additional peak near 169 eV is due to a small amount of sulphate (S) contamination [28]. Predictably, the Bi signal from the samples with higher doping concentration (x = 0.01) is much stronger. However, it should be noted that for the lower doped sample (x = 0.005) the Bi signal is significantly higher for the sample annealed at 1100 °C than 1000 °C, even after it is reduced by sputter cleaning.

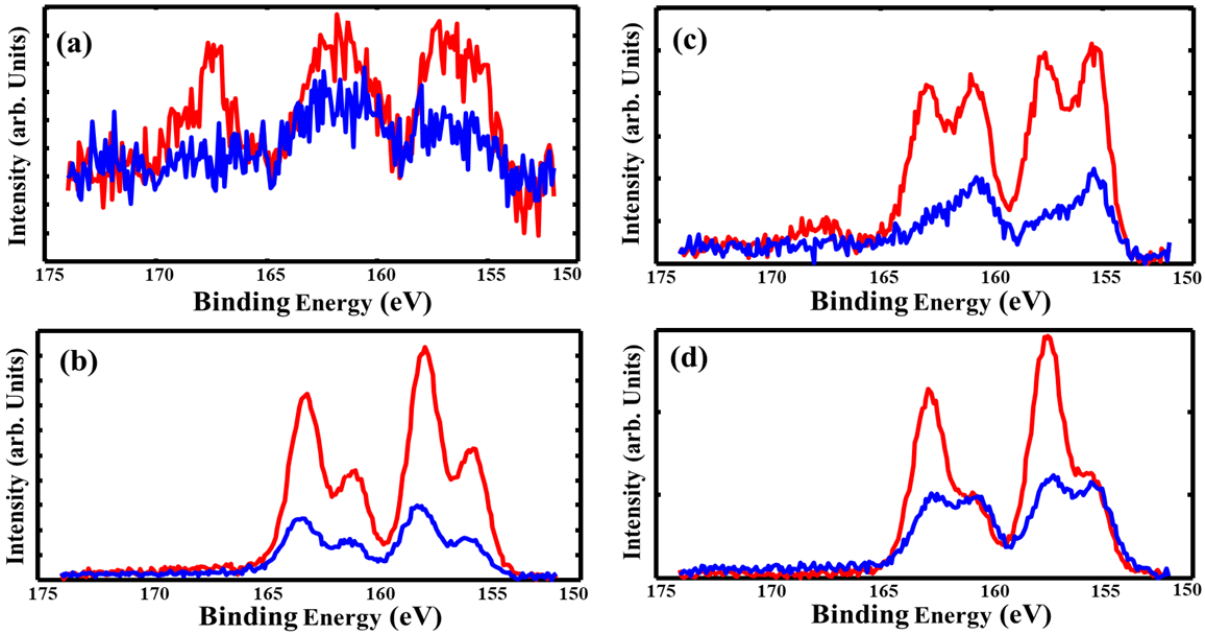

Figure 6.8: High-resolution XPS spectra of Bi 4f in $La_{1-x}OF:Bi_x$ annealed at 1000 °C with (a) x= 0.005 and (b) x = 0.01. Similar spectra are shown in (c, d) for samples annealed at 1100 °C. The red and blue lines are data before and after sputter cleaning the surface, respectively.

Each Bi spectrum consists of two spin-orbit pairs having separation of 5.3 eV, with the lower $4f_{7/2}$ binding energy components near 156.7 eV and 158.6 eV. The smaller of these two binding energies corresponds to metallic Bi, which is the result of Bi^{3+} segregation to the surface of the sample and its reduction to Bi^0 [29]. The higher binding energy corresponds to Bi^{3+} ions substituting La^{3+} ions

in the LaOF host, although Bi_2O_3 due to oxidation of metallic Bi on the surface is also likely to contribute. The XPS results reveal much enhanced Bi segregation to the surface at the higher annealing temperature, with stronger signals and improved signal-to-noise ratio. Jafer *et al.* [30] studied the effect of heating temperature on Y_2O_3 doped Bi phosphor powders and attributed the increase of the XPS peak counts of the Bi 4f peak to the segregation effects of the dopant to the particle surface. This segregation may be further enhanced due to the instability related to the phase change from the tetragonal to the rhombohedral structure. The dramatic decrease in the luminescence of the sample annealed at 1100° is therefore attributed primarily to a significant reduction in the Bi^{3+} ion concentration in the bulk material due to its segregation to the surface, where it can exist as metallic Bi or oxidize to form Bi_2O_3.

6.3.4. Stability of LaOF:Bi and PL degradation under UV irradiation

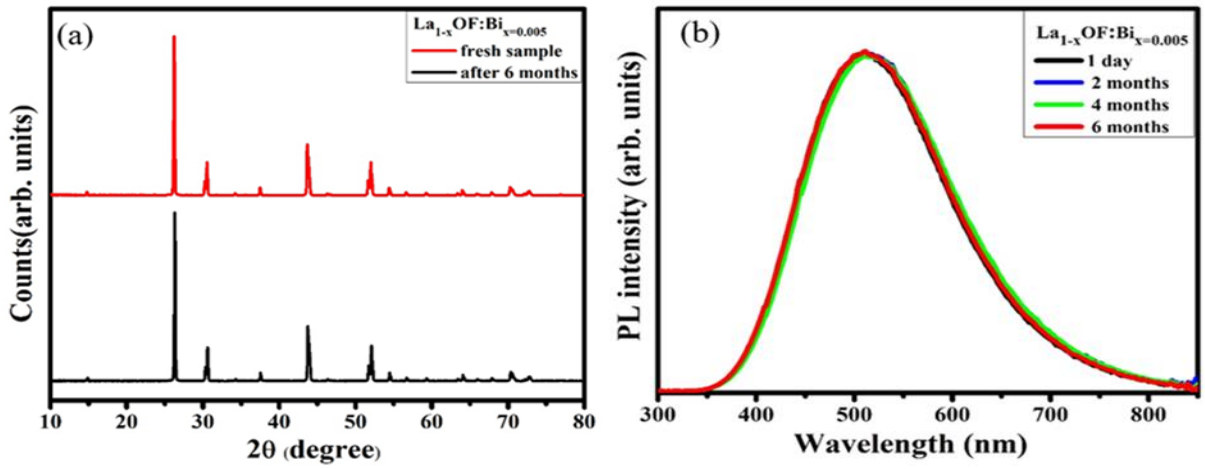

Figure 6.9: (a) XRD patterns of freshly prepared $La_{1-x}OF:Bi_{x=0.005}$ powders initially and after 6 months, when exposed to the atmosphere. (b) PL emission spectra of $La_{1-x}OF:Bi_{x=0.005}$ excited at 263 nm exposed to the atmosphere for 6 months.

Figure 6.9(a) shows the XRD patterns of the freshly prepared $La_{1-x}OF:Bi_{x=0.005}$ phosphor powder and after 6 months of storage exposed to the atmosphere. The XRD patterns of the phosphor did not change over this time. Figure 6.9(b) shows that the PL emission spectra for the samples after storage are similar to the freshly prepared sample. This shows that the chemical structure and

optical properties of the $La_{1-x}OF:Bi_{x=0.005}$ phosphor powder were stable when exposed to the atmosphere for several months. For comparison, the LaOX (X = Cl, Br) doped Bi were found to be unstable when stored for several months.

Figure 6.10 illustrates degradation of the PL emission intensity of the $La_{1-x}OF:Bi_{x=0.005}$ powder sample over time when exposed to a 254 nm UV source (which also served as the PL excitation source). The emission decreased slowly but continuously when the sample was exposed to the UV light at room temperature for ~42 h. XPS measurements were made to investigate the degradation and Figure 6.11 compares the XPS high resolution spectra of samples before (left) and after (right) exposure to the 254 nm excitation source for ~42 h, for different binding energy regions associated with the C 1s (contamination), La 3d, O 1s, F 1s and Bi 4f electrons. Spectra measured before (red) and after (blue) sputter cleaning are presented. As expected, the main C 1s peak, attributed to hydrocarbons on the surface [31], decreased substantially after the sputter cleaning. The small C peak located at around 290 eV is due to the C in carbonates [32]. The XPS spectra of the La 3d shown in Figure 6.11(b and g) and the F 1s spectrum shown in Figure 6.11(c, h) are similar to what was already discussed in Figure 7 and are enhanced after sputter cleaning due to the removal over surface contamination to which the XPS technique is very sensitive.

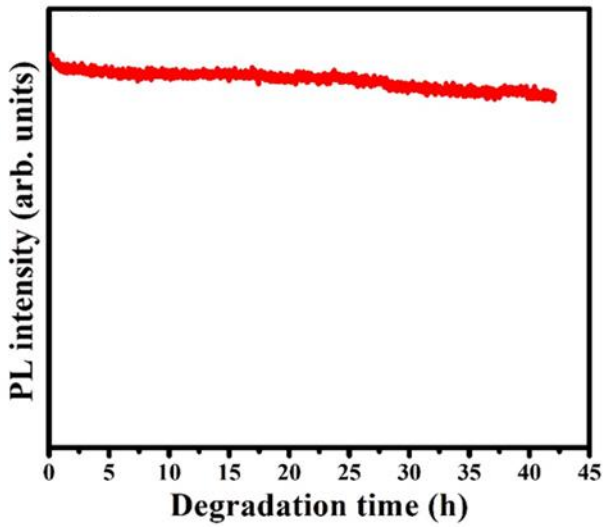

Figure 6.10: PL degradation curve of $La_{1-x}OF:Bi_{x=0.005}$ exposed to 254 nm UV radiation at room temperature.

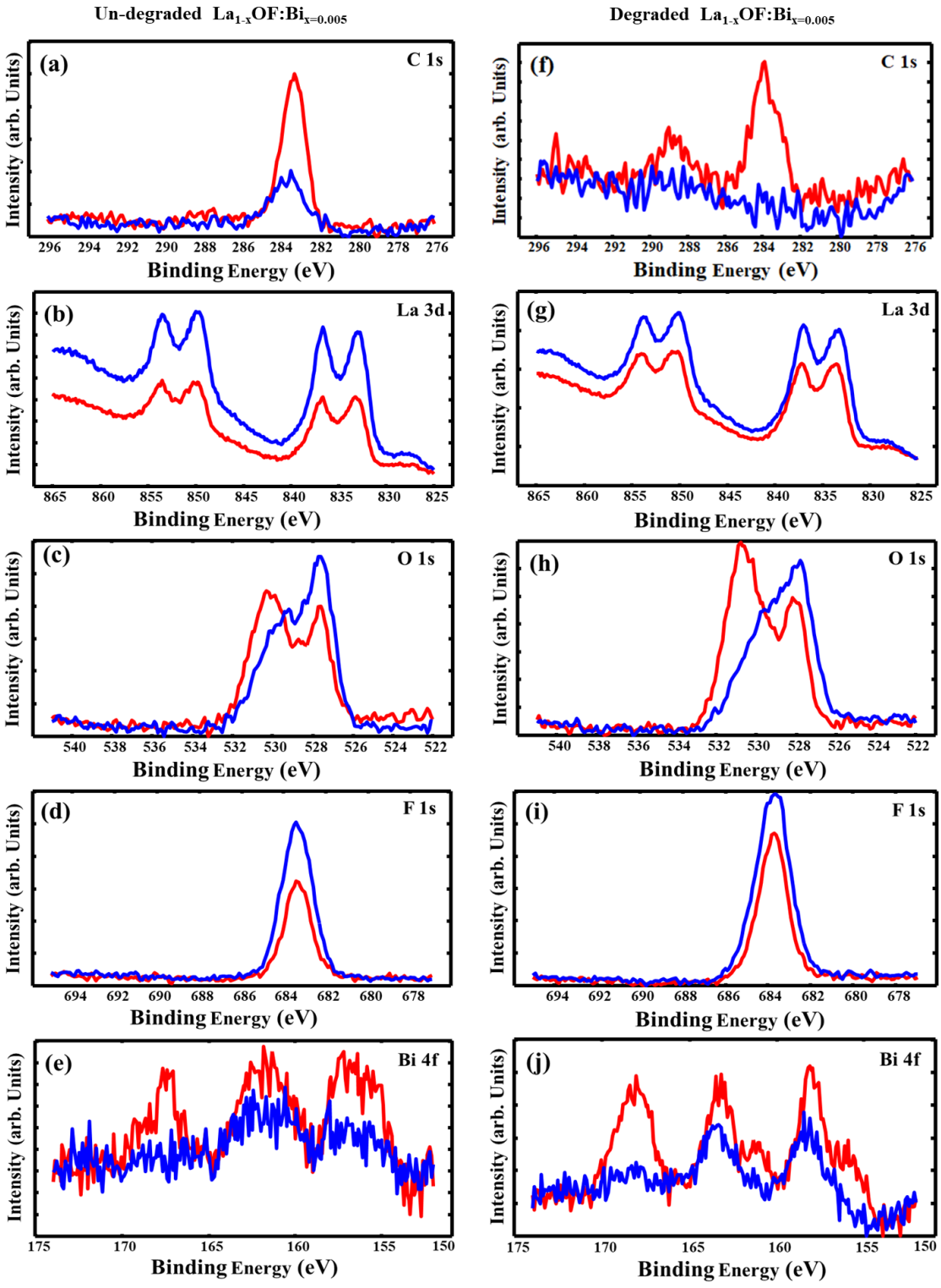

Figure 6.11: XPS spectra for un-degraded $La_{1-x}OF:Bi_{x=0.005}$ in the binding energy regions of (a) C 1s, (b) La 3d, (c) O 1s (d) F 1s, (e) Bi 4f, with corresponding spectra for the degraded sample (f to j). The red and blue curves are the measurements before and after sputter cleaning, respectively.

Figure 6.11(c, h) show the O 1s XPS high-resolution spectra for the original and degraded $La_{1-x}OF:Bi_{x=0.005}$, respectively. Deconvolution of the O 1s spectra into the different peaks for the sputter cleaned sample is shown in Figure 6.12(a, c), which are composed of three peaks. The peak centred at 528.8 eV is related to crystal lattice oxygen in the LaOF network, while the peak at 530.5 eV is due to O atoms in the vicinity of O vacancies in the structure [28, 33]. The third peak located at 531.9 eV can be ascribed to hydroxyl (OH) or carbonate groups [24, 27] which is due to contamination.

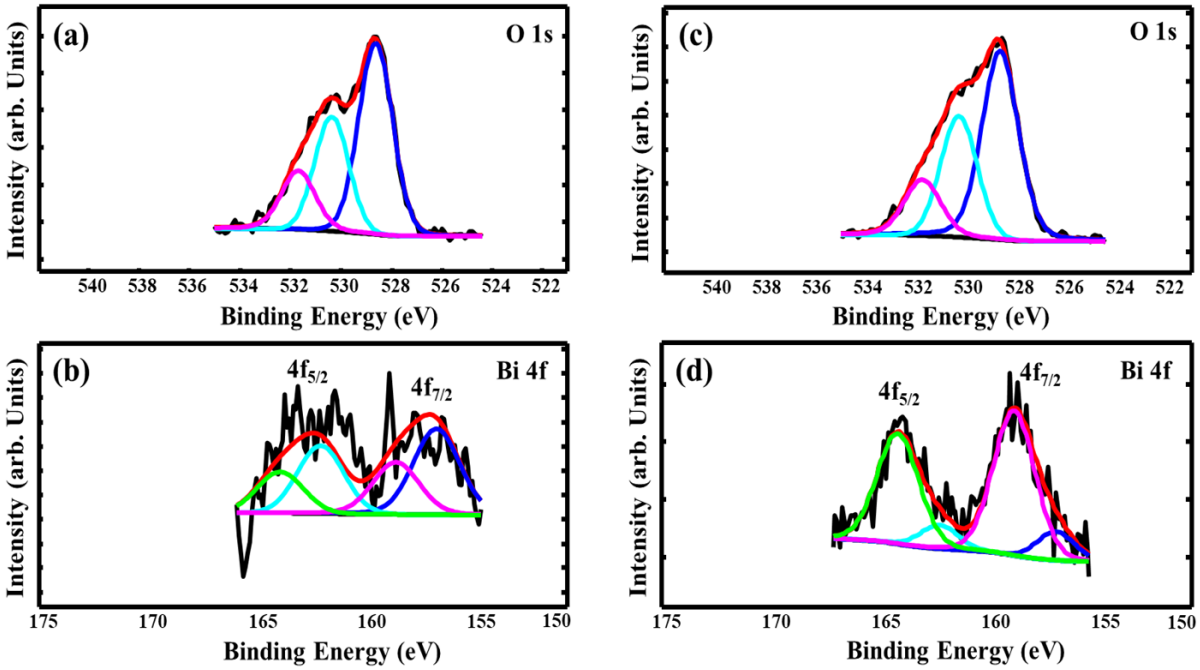

Figure 6.12: Deconvolution of the XPS spectra of $La_{1-x}OF:Bi_{x=0.005}$ in the binding energy regions of (a) O 1s (b) Bi 4f. Similar spectra are shown in (c, d) for the degraded sample.

Despite the low Bi doping concentration (x = 0.005), the XPS peaks in the spectra for the Bi 4f binding energy region are clear in Figure 6.11(e, j). They consist of two pairs of spin-orbit split peaks which have been interpreted earlier with reference to Figure 6.8. Each Bi spectrum consists of two spin-orbit pairs having separation of 5.3 eV, with the lower $4f_{7/2}$ binding energy components near 156.7 eV and 158.6 eV. As pointed out earlier, the smaller of these two binding energies

corresponds to metallic Bi, which is the result of Bi^{3+} segregation to the surface of the sample and its reduction to Bi^0 [29]. The higher binding energy corresponds to Bi^{3+} ions substituting La^{3+} ions in the LaOF host, although Bi_2O_3 due to oxidation of metallic Bi on the surface is also likely to contribute. The additional peak at ~169 eV is due to S which can be ascribed to sulphate [28] contamination from the environment and these peaks were effectively eliminated by sputter cleaning. The sputter cleaning also affected the intensity of the Bi peaks, although the general form was not drastically altered as was the case in Figure 6.8. Deconvolution of the Bi 4f spectra into the different peaks for the sputter cleaned sample is shown in Figure 6.12(b, d). It is observed that the XPS intensity of the Bi 4f peak for the degraded sample has increased, due to the Bi^{3+} segregation on the surface of the sample as a result of UV radiation. The relative size of the higher binding energy Bi^{3+} component for the degraded sample increased and is dominant, indicating that after Bi segregated to the surface it probably oxidized to form Bi_2O_3.

6.4. Conclusion

Lanthanum oxyfluoride doped Bi was successfully prepared via the solid-state reaction synthesis. The XRD patterns revealed that the phosphor powder crystallized in tetragonal and rhombohedral structures depending on the annealing temperature. The SEM images showed that the shape of the particles of the LaOF pure host is similar to the doped samples. The EDS spectra confirm that the ratios of the oxygen and fluorine changed by changing the annealing temperatures. A broad white emission centred at 518 nm was observed when excited at 263 nm, which was attributed to the $^3P_1 \rightarrow {}^1S_0$ transition of the Bi^{3+} ions. The emission intensity was measured as a function of Bi doping concentration, with the maximum occurring for x = 0.005. The LaOF:Bi phosphor powder was found to be degraded under 254 nm ultraviolet excitation, while it was found stable when exposed to the atmosphere for several months. XPS data confirmed that the annealing at 1100 °C and exposure of the sample to UV radiation result in segregation of the Bi^{3+} on the surface of the sample.

6.5. References

1. Roy H.P. Awater, Pieter Dorenbos. The Bi^{3+} 6s and 6p Electron Binding Energies in Relation to the Chemical Environment of Inorganic Compounds. *Journal of Luminescence* 184 (2017) 221–231. doi: 10.1016/j.jlumin.2016.12.021
2. W.A.I. Tabaza, H.C. Swart, R.E. Kroon. Optical properties of Bi and energy transfer from Bi to Tb in $MgAl_2O_4$ phosphor. *Journal of Luminescence* 148 (2014) 192-197. doi: 10.1016/j.jlumin.2013.12.018
3. Emille M. Rodrigues, Ernesto R. Souza, Jorge H. S. K. Monteiro, Rafael D. L. Gaspar, Italo O. Mazali and Fernando A. Sigoli. Non-stabilized europium-doped lanthanum oxyfluoride and fluoride nanoparticles well dispersed in thin silica films. *Journal of Materials Chemistry, 22* (2012) 24109–24123. doi: 10.1039/C2JM34901A
4. Oliver Janka and Thomas Schleid. Facile Synthesis of Bastnaesite-Type $LaF[CO_3]$ and its Thermal Decomposition to LaOF for Bulk and Eu^{3+}-Doped Samples. *European Journal of Inorganic Chemistry* 3 (2009) 357–362. doi: 10.1002/ejic.200800931
5. J. Hölsä. Effect of non-stoichiometry on the luminescence properties of lanthanum oxyfluoride. *Acta Chemica Scandinavica*, 45 (1991) 583-587. doi :10.3891/acta.chem.scand.45-0583
6. C.T. Au, Y.Q. Zhang, H. He, S.Y. Lai, C.F. Ng. The characterization of $BaCO_3$-modified LaOF catalysts for the OCM reaction. *Journal of Catalysis* 167 (1997) 354-363. doi: 10.1006/jcat.1997.1577
7. J. Lee, Q. Zhang, F. Saito. Synthesis of nano-sized lanthanum oxyfluoride powders by mechanochemical processing. *Journal of Alloys and Compounds* 348 (2003) 214-219. doi: 10.1016/S0925-8388(02)00837-X
8. X. Zhang, D. Gao, L. Li. Down- and up-conversion luminescence of Tm^{3+}/Ho^{3+} codoped LaOF nanoparticles. *Journal of Applied Physics* 107 (2010)123528. doi: 10.1063/1.3436569
9. Grzyb Tomasz and Lis Stefan. Structural and Spectroscopic Properties of LaOF:Eu^{3+} Nanocrystals Prepared by the Sol–Gel Pechini Method. *Inorganic Chemistry* 50 *(*2011*) 8112–8120.* doi: 10.1021/ic2005453
10. Ya-Ping Du, Ya-Wen Zhang, Ling-Dong Sun, and Chun-Hua Yan. Luminescent Monodisperse Nanocrystals of Lanthanide Oxyfluorides Synthesized from Trifluoroacetate Precursors in

High-Boiling Solvents. *Journal of Physical Chemistry C* 112 (2008) 405–415. doi: 10.1021/jp076717r

11. Davide Barreca, Elza Bontempi, Laura E. Depero, Cinzia Maragno, Eugenio Tondello and Paolo Zanola. Structural Characterization of Nanocrystalline Lanthanum Oxyfluoride Films Obtained by Chemical Vapor Deposition. *Journal of Nanoscience and Nanotechnology* 7 (2007) 2741–2747. doi: 10.1166/jnn.2007.606
12. A. K. Tyagi. Role of size of rare earth ion in the homogeneity range of REF_3–RE_2O_3 (RE = La, Nd, Y) systems. *Journal of Materials Science Letters* 14 (1995) 1502–1504. doi: 10.1007/bf00633143
13. J. W. Fergus. Crystal structure of lanthanum oxyfluoride. *Journal of Materials Science Letters* 16 (1997) 267–269. doi: 10.1023/A:1018584614532
14. W. H. Zachirasen. Crystal Chemical Studies of the 5f-Series of Elements. XIV. Oxyfluorides, XOF. Acta *Crystallographica* 4 (1951) 231–236. doi: 10.1107/s0365110x51000787
15. Koichi Momma, Fujio Izumi. VESTA 3 for Three-Dimensional Visualization of Crystal, Volumetric and Morphology Data. *Journal of Applied Crystallography* 44 (2011) 1272-1276. doi: 10.1107/S0021889811038970
16. A. Vaitkus, A. Merkys, S. Gražulis. Validation of the Crystallography Open Database using the Crystallographic Information Framework. *Journal of Applied Crystallography* *54* (2021) 661-672. doi: 10.1107/S1600576720016532
17. Enjie He, Hairong Zheng, Zhenglong Zhang, Xisheng Zhang, Liangmin Xu, Zhenxing Fu, and Yu Lei. Influence of Crystal Structure on the Fluorescence Emission of Eu^{3+}: LaOF Nanocrystals. *Journal of Nanoscience and Nanotechnology* 10 (2010) 1908–1912. doi: 10.1166/jnn.2010.2057
18. Wongi Noh and Sangmoon Park (2017). Synthesis and distinct up-converting behaviors of Er^{3+}, Yb^{3+} doped LaOF and $LaO_{0.65}F_{1.7}$ phosphors. *Optical Materials* 66 (2017) 589–594. doi: 10.1016/j.optmat.2017.02.057
19. Sungjun Yang and Sangmoon Park. Bi^{3+} and Eu^{3+} Activated Luminescent Behaviors in Non-Stoichiometric $LaO_{0.65}F_{1.7}$ Structure. *Materials* 13 (2020) 2326. doi: 10.3390/ma13102326
20. R.D. Shannon. Revised Effective Ionic Radii and Systematic Studies of Interatomic Distances in Halides and Chalcogenides. *Acta Crystallographica Section A* 32 (1976) 751–767. doi: 10.1107/S0567739476001551

21. GoCIE V2, K. R. Justin Thomas, Department of chemistry, Indian Institute of Technology Rookee, India, 2009. http://faculty.iitr.ac.in/~krjt8fcy/gocie.html
22. R.E. (Ted) Kroon. Nanoscience and the Scherrer equation versus the 'Scherrer–Gottingen equation'. *South African Journal of Science* 109(5/6) (2013) Art. #a0019 (2 pages). doi:10.1590/sajs.2013/a0019
23. C. Suresh, H. Nagabhushana, G.P. Darshan, R.B. Basavaraj, D. Kavyashree, S.C. Sharma, A. Arulmozhi, B. Daruka Prasad, H.J. Amith Yadav. Facile LaOF: Sm^{3+} based labeling agent and their applications in residue chemistry of latent fingerprint and cheiloscopy under UV–visible light. Arabian Journal of Chemistry 11 (2018) 460-482. doi: 10.1016/j.arabjc.2017.09.014
24. X. Yan, D. Dai, K. Ma, S. Zuo, W. Liu, X. Li, Chao Yao. Microwave hydrothermal synthesis of lanthanum oxyfluoride nanorods for photocatalytic nitrogen fixation: Effect of Pr doping. *Frontiers of Materials Science* 14 (2020) 43–51. doi: 10.1007/s11706-020-0488-6
25. D.L. Dexter, James H. Schulman. Theory of Concentration Quenching in Inorganic Phosphors. *The Journal of Chemical Physics* 22 (1954) 1063–1070. doi: 10.1063/1.1740265
26. Suresh Reddy Sanivarapu, John Berchmans Lawrence, and Gosipathala Sreedhar. Role of Surface Oxygen Vacancies and Lanthanide Contraction Phenomenon of $Ln(OH)_3$ (Ln = La, Pr, and Nd) in Sulfide-Mediated Photoelectrochemical Water Splitting. *American Chemical Society Omega* 3 (2018) 6267-6278. doi: 10.1021/acsomega.8b00429
27. D. Barreca, A. Gasparotto, C. Maragno, E. Tondello. Nanocrystalline Lanthanum Oxyfluoride Thin Films by XPS. *Surface Science Spectra* 11 (2004) 52–58. doi: 10.1116/11.20050401
28. J. Yang, Y. Liang, K. Li, G. Yang, Y. Zhu, S. Liu, W. Lei. New reaction pathway induced by the synergistic effects of Bi plasmon and La^{3+} doping for efficient visible light photocatalytic reaction on BiOCl. *Applied Surface Science* 458 (2018) 769–780. doi: 10.1016/j.apsusc.2018.07.051
29. N. A. M. Saeed, E. Coetsee, R. E. Kroon, M. Bettinelli, H. C. Swart. Photoluminescence of Bi^{3+} doped in YOF phosphor as an activator. *Optical Materials,* 119 (2021) 111291. doi: 10.1016/j.optmat.2021.111291
30. R.M. Jafer, H.C. Swart, A. Yousif, Vinod Kumar, E. Coetsee. The Effect of Annealing Temperature on the Luminescence Properties of Y_2O_3 phosphor Powders doped with a High Concentration of Bi^{3+}. *Journal of Luminescence* 180 (2016) 198–203. doi: 10.1016/j.jlumin.2016.08.042

31. M.F. Sunding, K. Hadidi, S. Diplas, O.M. Løvvik, T.E. Norby, A.E. Gunnæs. XPS Characterisation of in Situ Treated Lanthanum Oxide and Hydroxide Using Tailored Charge Referencing and Peak Fitting Procedures. *Journal of Electron Spectroscopy and Related Phenomena* 184 (2011) 399-400. doi: 10.1016/j.elspec.2011.04.002
32. John F. Moulder, William F. Stickle, Peter E. Sobol, Kenneth D. Bomben. Jill Chastain (Editor). Handbook of X-ray Photoelectron Spectroscopy. Revised Ed. Perkin Elmer Corporation, Eden Prairie, Minnetsoa, USA (1992). ISBN: 978-0-9627026-2-4
33. H.-L. Guo, Q. Zhu, X.-L. Wu, Y.-F. Jiang, X. Xie, A.-W. Xu, (2015). Oxygen deficient ZnO1−xnanosheets with high visible light photocatalytic activity. *Nanoscale* 7 (2015) 7216–7223. doi: 10.1039/c5nr00271k

Chapter seven

Bi doped LaOCl and LaOF thin films grown by pulsed laser deposition

7.1. Introduction

The activated lanthanide oxyhalides (LnOX: Ln = La, Y, Gd and X = Cl, F, Br) are of interest because of their use as X-ray intensifying phosphors and they also have potential applications in fluoroscopic screens, cathode ray tubes and lamps. In particular, lanthanum oxyhalides (LaOX) have found much interest from researchers because of their excellent and unique magnetic, optical, electrical and luminescent characteristics [1, 2]. Phosphor powders of LaOCl and LaOF doped with Bi have shown potential as stable phosphor materials. Although both these compounds have the same tetragonal PbFCl-type crystal structure with space group *P*4/*nmm* (No. 129) [3, 4], Figure 7. 1 shows that the environment of the La^{3+} ion is different despite the same C_{4v} site symmetry in both cases. In LaOCl there is a Cl^- ion directly below each La^{3+} ion along the direction of the four-fold rotation axis and the Cl^- anions form double layers, whereas in LaOF the F^- ions are relatively rotated so as to be directly below the O^{2-} ions and form only single layers.

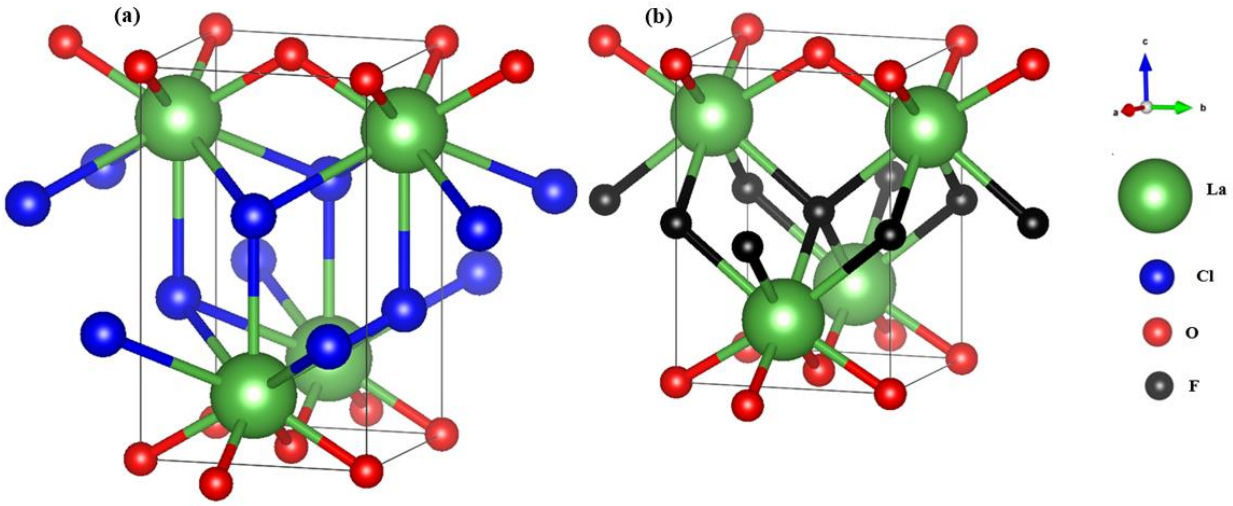

Figure 7.1: The unit cell of (a) LaOCl and (b) LaOF modelled with Vesta software [5] using CIF files obtained from the Crystallography Open Database [6], number 1539093 for LaOCl and number 7037053 for LaOF.

The luminescence properties of Bi^{3+} ions in a variety of host materials have been investigated widely [7]. The ground state of the Bi^{3+} ion is $^1S_0$, while the excited configuration consists of four energy levels, namely $^3P_0$, $^3P_1$, $^3P_2$ and $^1P_1$. The optical transition from $^1S_0$ to $^1P_1$ (C-band) is a spin allowed transition. The transition from $^1S_0$ to $^3P_1$ (A-band) is allowed because of the mixing of the $^1P_1$ and $^3P_1$ levels by spin-orbit coupling. The transition from $^1S_0$ to $^3P_2$ (B-band) is forbidden, but can be possible by coupling with unsymmetrical lattice vibrational modes. The transition from $^1S_0$ to $^3P_0$ is strongly forbidden [8]. Bi^{3+} ions substitute La^{3+} ions in doped samples (due to their similar ionic radii and equal valence) and the difference in environment has a strong effect on the Bi^{3+} luminescence. While LaOCl:Bi powder emits in the ultraviolet, the emission of LaOF:Bi powder is strongly red-shifted into the visible range with much greater Stokes shift.

Thin film phosphors have significant advantages compared to common powder forms, e.g. relatively large thermal stability, structural density, better coherence with the basic substrates and effective thermal dissipation for high energy operation [9]. Pulsed laser deposition (PLD) has been commonly used for the preparation of thin films of various metal oxides, complex metal oxides, insulators, semiconductors, polymer and biological materials, borides, carbides and nitrides [10]. PLD is a relatively new technique for depositing thin films using high energy laser pulses to evaporate the surface of the material target inside a vacuum chamber and condensing the vapour on the surface of a substrate to create a thin film layer with a thickness of up to a few micrometres [11]. The PLD technique has a high ability to control the formation of thin films, morphology, composition and growth process by varying the partial pressure of a gas in the deposition chamber and selecting the substrate temperature [12]. Thin films of LaOCl formed by evaporation of LaB_6 on NaCl [13] and sol-gel LaOF [14] have been studied some time ago. The aim of this work is to investigate the properties of LaOX (X = Cl, F) crystalline thin films doped with Bi prepared by using the PLD technique in a vacuum and different argon (Ar) pressures. Ar was selected since it is a non-reactive gas, rather than oxygen which may have unintentionally oxidized the oxyhalide materials during deposition. The influence of the pressure of the background Ar atmosphere on the structural and optical properties of the thin films was studied, while keeping other experimental parameters such as substrate temperature, target to substrate distance and deposition times constant.

7.2. Experimental

To create a target for the laser ablation, powder samples of $La_{1-x}OCl:Bi_x$ and $La_{1-x}OF:Bi_x$ were first prepared via the solid-state reaction method. For the oxychloride the optimum synthesis temperature was 900 °C with doping concentration x = 0.007, while for the oxyfluoride the corresponding values were 1000 °C and x = 0.005. These powders were pressed using a hydraulic press to make target pellets which were annealed at 900 °C for 8 h in air to remove all adventitious water containing species that may be present and then transferred to the chamber of the PLD system and positioned on a rotating target holder. Annealing of the target pellets was found to be vital to prevent them from breaking apart to emit a powder of the material inside the PLD deposition chamber under the action of the laser.

Si (100) substrates were cleaned in an ultrasonic bath using acetone, ethanol and finally using a distilled water bath consecutively for 15 min each. The cleaned substrates were then blown dry with nitrogen gas. The PLD system was pumped to a base pressure of 5×10^{-5} mbar (~ 0.04 mTorr) and a thin film was deposited under these conditions (referred to as 'vacuum'). Additional films were created in a similar way, except that the deposition chamber was pumped to base pressure and then back-filled with Ar to a pressure of 10, 20 or 40 mTorr. A frequency quadrupled Nd:YAG pulsed laser emitting at 266 nm was used to ablate the targets. The laser energy (40 mJ/pulse), fluency and target-to-substrate distance fixed at 30 Hz, 1.7 J/cm^2 and 4.5 cm, respectively. The deposition time was 20 min and the substrate temperature was fixed at 300 °C.

The crystal structures were assessed using X-ray diffraction (XRD) measurements made with a Bruker D8 Advance diffractometer. To produce the Cu Kα characteristic X-rays used, an electron beam of current 40 mA was accelerated through 40 kV. The samples were examined using a JEOL JSM-7800F scanning electron microscope (SEM) and the elemental composition was assessed by means of its energy dispersive X-ray spectroscopy (EDS) attachment (X-Max^{N}80 detector) by Oxford Instruments. The PL properties of the films were measured at room temperature using an FLS980 spectrometer from Edinburgh Instruments with a continuous 450 W xenon lamp.

7.3. Results and discussion

7.3.1. Structure, morphology and chemical composition analysis

Figure 7.2 shows the XRD patterns of (a) LaOCl:Bi and (b) LaOF:Bi thin films deposited in vacuum and different Ar pressures, together with the powders that were used to make the PLD targets. For the LaOCl:Bi shown in Figure 7.2(a) all peak positions matched well with the corresponding powder. The XRD signal from the LaOF:Bi thin films was comparatively weaker, as can be seen by the greater relative signal-to-noise ratio in Figure 7.2(b). The thin film of LaOF:Bi produced in vacuum displayed the three most intense peaks corresponding to the powder. For the other samples created in Ar environments, the diffraction peak at 26.7° dominated the XRD patterns, indicating some preferential orientation of the (101) plane. As the Ar gas pressure increased, the intensity of the 101 diffraction peak increased, suggesting an increase in the thicknesses of the films. The sample grown in 10 mTorr Ar also displayed several sharp additional diffraction peaks (marked with asterisks, *). These peaks were also found for a clean substrate having no deposited film and are due to the weak (forbidden) Si 200 peak near 33° and also some Si 400 peaks for weak X-rays of different wavelengths due to tungsten (W) contamination of the Cu anode [15].

The LaOF:Bi film deposited in 10 mTorr Ar showed the thinnest layer on the surface of the substrate, compared to the films deposited in 20 and 40 mTorr Ar as well as in vacuum. As a result of the poor coverage and gaps between the particles evident from the SEM images, the peaks related to Si in the structure for both the XRD pattern and EDS spectrum are more pronounced than for the other samples. While the Ar background gas can reduce the kinetic energy of the ablated particles in the plume before reaching the substrate, it is not clear why the thinnest layer was formed for the 10 mTorr Ar sample.

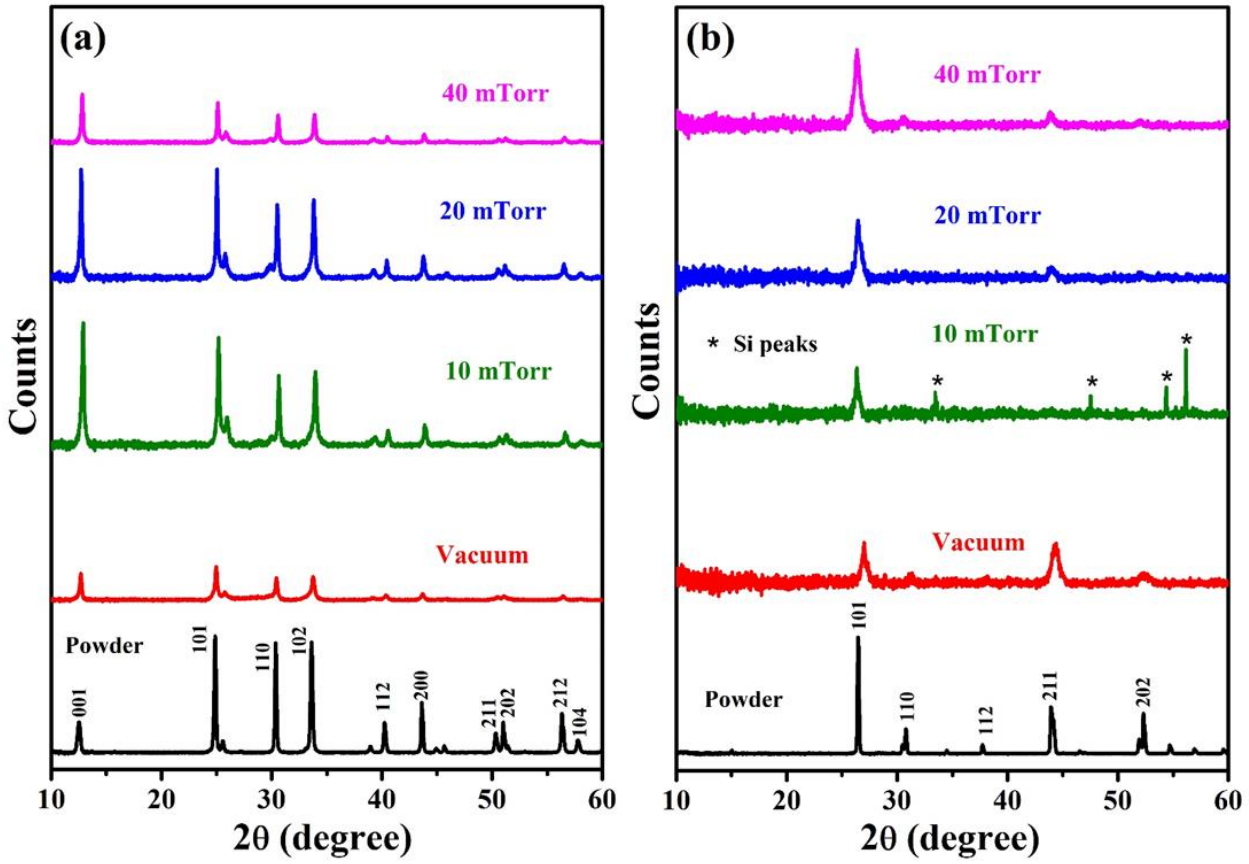

Figure 7.2: XRD patterns of (a) LaOCl:Bi and (b) LaOF:Bi thin films deposited in vacuum and different Ar pressures, together with the powders from which PLD target was made.

The average crystallite sizes for the LaOCl:Bi and LaOF:Bi thin films were determined using the Scherrer equation [16], $D = \frac{0.9\lambda}{\beta cos\theta}$, where λ is the X-ray wavelength and θ is the Bragg angle. The results are tabulated in Table 7.1 and show that the average crystallite size for the LaOCl:Bi for the film deposited in a vacuum is smaller than those deposited in different Ar pressures and the average crystallite size increased with increasing Ar pressure. The opposite trend was obtained for LaOF:Bi where the average crystallite size of the film deposited in a vacuum is greater than those deposited in different Ar pressures and decreased with increasing Ar pressure. This indicates that LaOCl and LaOF do not perform similarly during laser ablation and PLD. Both the lower atomic mass and higher chemical reactivity of F [18] compared to Cl may cause it to interact more strongly with the Ar background gas and thereby limit the amount to F reaching the substrate, which could account for the small crystallite size for LaOF:Bi and its decrease with Ar pressure.

Table 7.1: Crystallite sizes (nm) calculated from the Scherrer equation.

Film	Base pressure ~0.04 mTorr	Ar gas pressure		
		10 mTorr	20 mTorr	40 mTorr
LaOCl:Bi	27	32	34	36
LaOF:Bi	20	18	16	12

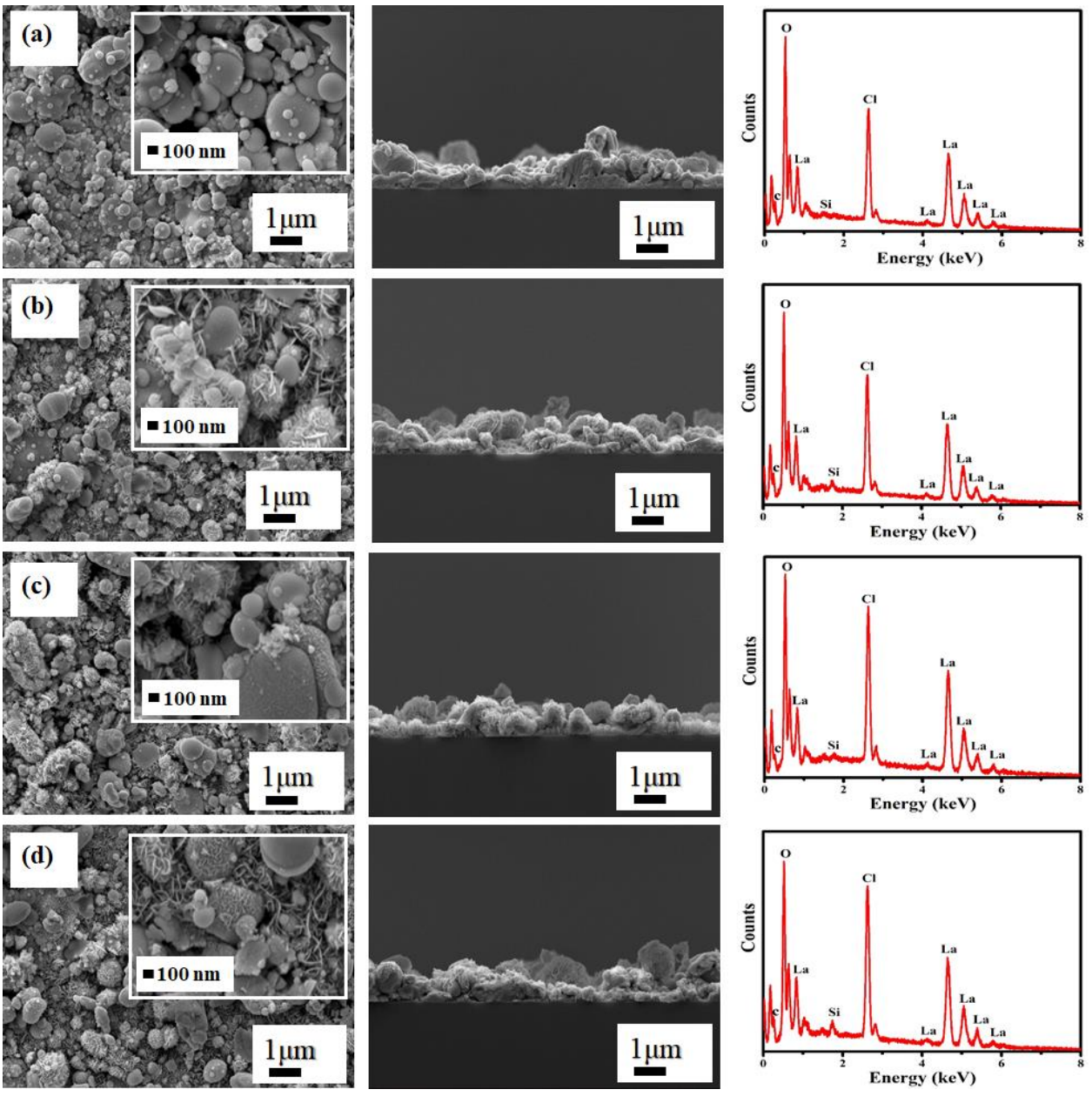

Figure 7.3: Plan view and cross sectional SEM images as well as EDS of LaOCl:Bi thin films deposited (a) in vacuum and with different Ar pressures of (b) 10, (c) 20 and (d) 40 mTorr.

Figure 7.3 presents the plan-view and cross-sectional SEM images and EDS spectra of the LaOCl:Bi thin films. The images show that the particles had different spherical sizes for the film deposited in a vacuum. The films deposited in different Ar pressures had particles of different spherical sizes as well as flower-like shapes with platelets. The cross-sectional images of the thin films were similar and clearly revealed the presence of spherical particles and flower-like shapes in the morphology. The EDS spectra of the films are similar to the powders, indicating good transfer of stoiciometry from the target to thin film during PLD. The presence of Si in the EDS spectra was due to the Si (100) substrate. Changing of Ar pressure did not effect on the chemical composition of the films.

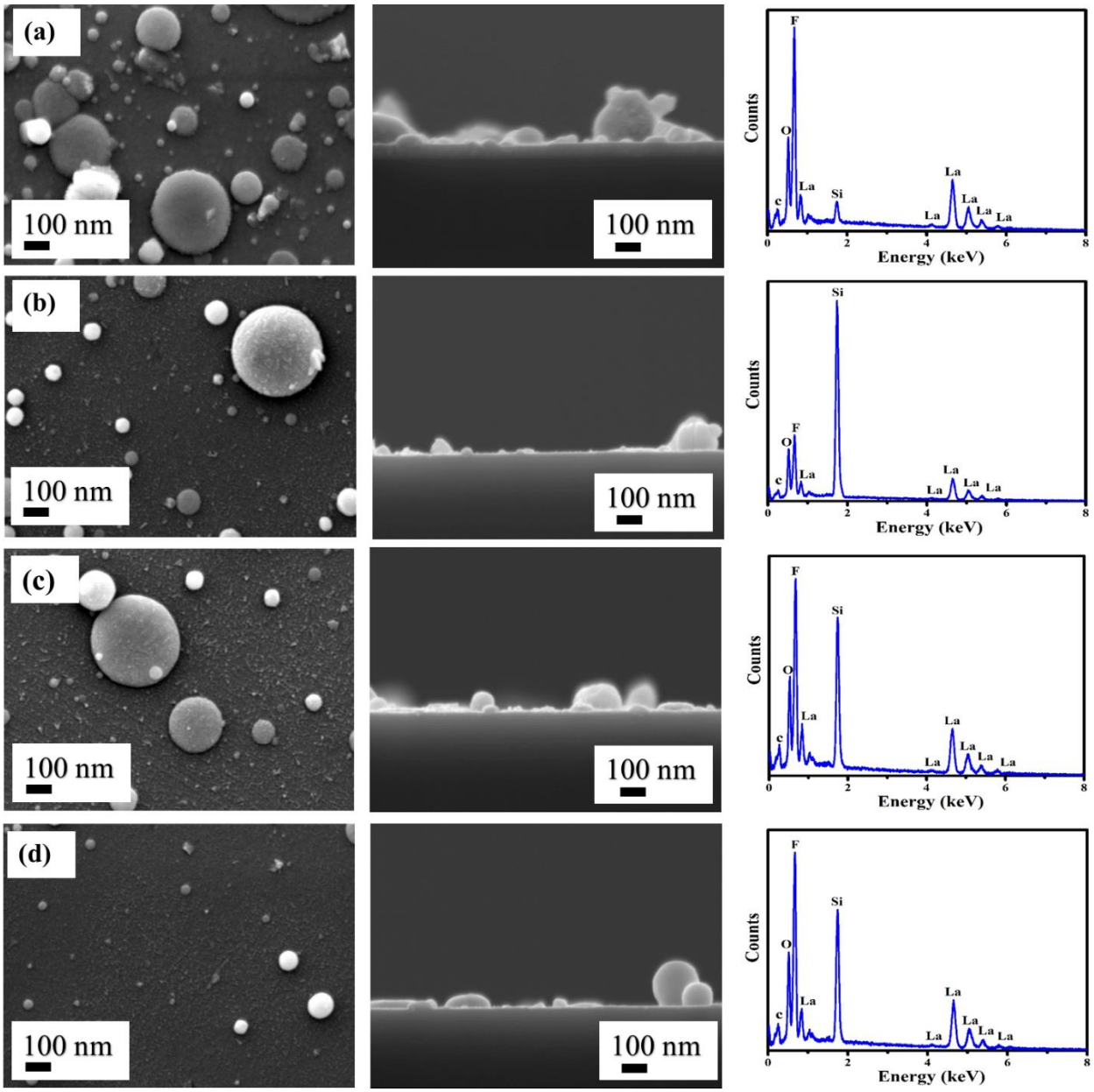

Figure 7.4: Plan view and cross sectional SEM images as well as EDS of LaOF:Bi thin films deposited (a) in vacuum and with different Ar pressures of (b) 10, (c) 20 and (d) 40 mTorr.

Figure 7.4 presents the plan-view and cross-sectional SEM images and EDS spectra of LaOF:Bi thin films. Note that the magnification is greater than in Figure 7.3 for LaOCl. Particles of spherical shape with distinct sizes were observed. The cross-sectional images were similar and confirmed the presence of spherical particles in the morphology. It is clear from the SEM images that the

films consisted of much less material than for the corresponding films of LaOCl. The EDS spectra of the films are similar to the powder, indicating that the stoiciometry is retained from the target to thin film during PLD. The EDS spectra of the thin films also show the Si peak from the substrate. This is much more prominent for the films of LaOF than for the films of LaOCl and the Si peak dominates the EDS spectrum of the LaOF film deposited at an Ar pressure of 10 mTorr, which also showed XRD peaks due to the Si substrate (figure 7.2(b)). The relative size of the Si EDS peak decreased for the LaOF films grown at higher Ar pressures of 20 and 40 mTorr, but these films still consist of very little material. The thickest LaOF film, which can be observed for the cross-sectional SEM image and has the smallest Si EDS peak, was created under vacuum PLD conditions. Therefore the presence of a background gas to reduce the kinetic energy of ablated material before reaching the substrate was not beneficial for the growth of LaOF films.

7.3.2. Photoluminescence analysis

Figure 7.5(a, b) display the PL excitation and emission spectra of the LaOCl:Bi and LaOF:Bi powder samples with emission bands at around 344 nm and at 518 nm under excitations of 266 nm and 263 nm, respectively. These excitation and emission peaks have been attributed to the transitions between the $^3P_1$ excited state and $^1S_0$ ground state of the Bi^{3+} ions. Figure 7.5(c, d) show the PL excitation and emission spectra of the thin films. While the form of the PL emission of the LaOCl and LaOF:Bi thin films matched that of the powders. The films deposited in vacuum for both compounds showed the lowest intensity. This is unexpected for the LaOF:Bi films since for this material the film grown in vacuum was the thickest. For the LaOCl:Bi thin films deposited in Ar the PL emission intensity increased with increasing Ar gas pressures, while the PL intensity for the LaOF:Bi thin films deposited in Ar increased with the increase of the Ar gas pressures up to 20 mTorr and then decreased with a further increase in Ar gas pressure. However, the emission of LaOF:Bi deposited in vacuum showed a shoulder peak at around 380 nm, which may originate from defect emission. This emission has been attributed to individual ionizing oxygen vacancies in LaOF, which results from the recombination of a photogenerated hole with an electron occupying an oxygen vacancy [18, 19]. The presence of a high concentration of such defects in the LaOF:Bi film formed in vacuum could increase non-radiative recombination pathways for excited Bi^{3+} ions and quench their luminescence.

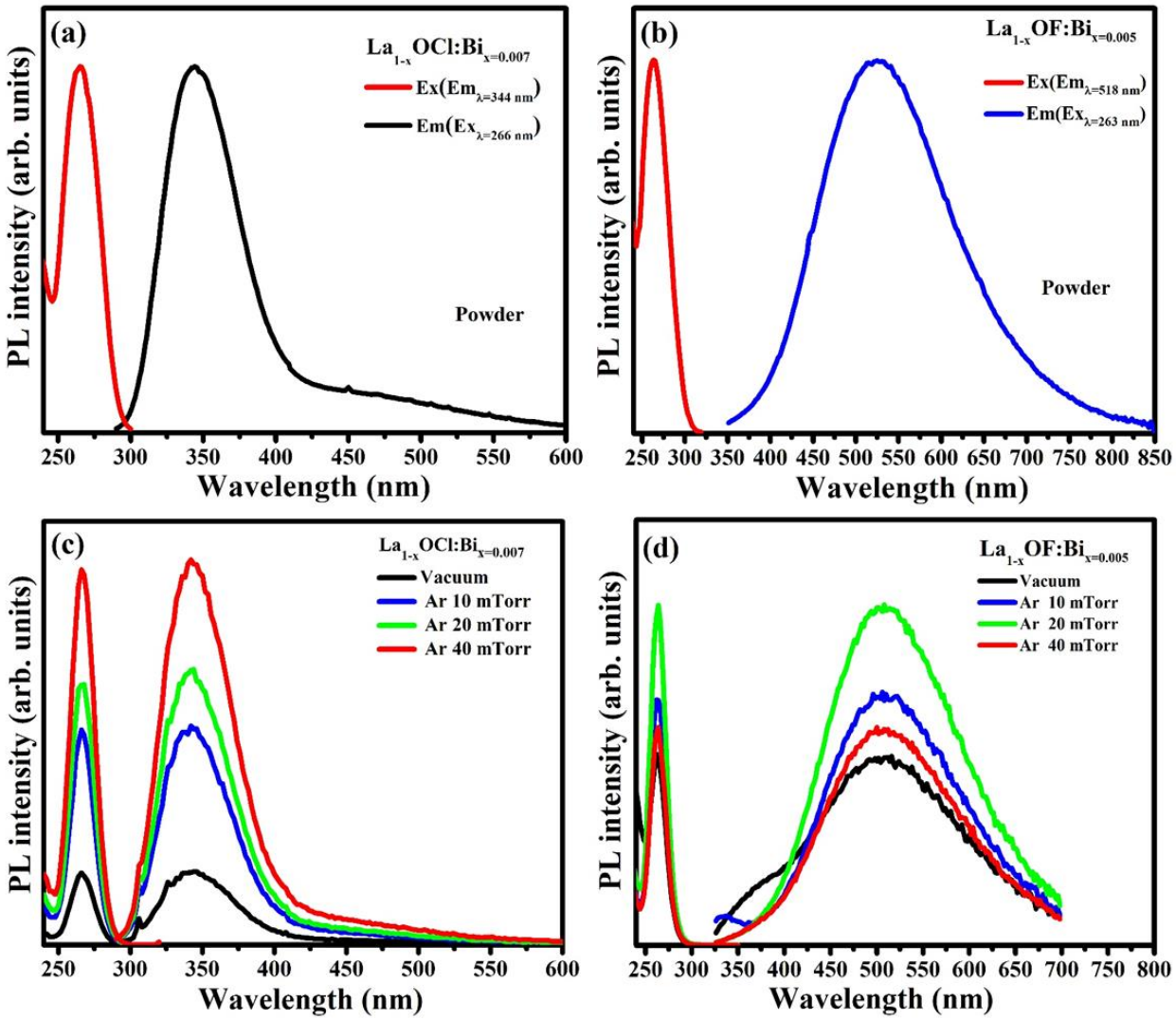

Figure 7.5: PL excitation and emission spectra of the $La_{1-x}OCl:Bi_{x=0.007}$ and $La_{1-x}OF:Bi_{x=0.005}$ (a, b) for the powders and (c, d) PLD thin films deposited in vacuum and different Ar pressures, respectively.

Figure 7.6(a) displays the PL emission spectra of the LaOCl:Bi and LaOF:Bi powder samples, which are compared in Figure 7.6(b) to the intensities and wavelengths of the emission for the best LaOCl:Bi and LaOF:Bi thin films, produced under Ar pressures of thin film 40 and 20 mTorr, respectively. The emission spectra of the LaOCl:Bi powder and film was narrow and at shorter wavelength than the corresponding emission spectra of LaOF:Bi. For both powder and films, the luminescence from the LaOF:Bi samples was less intense compared to the corresponding LaOCl:Bi samples.

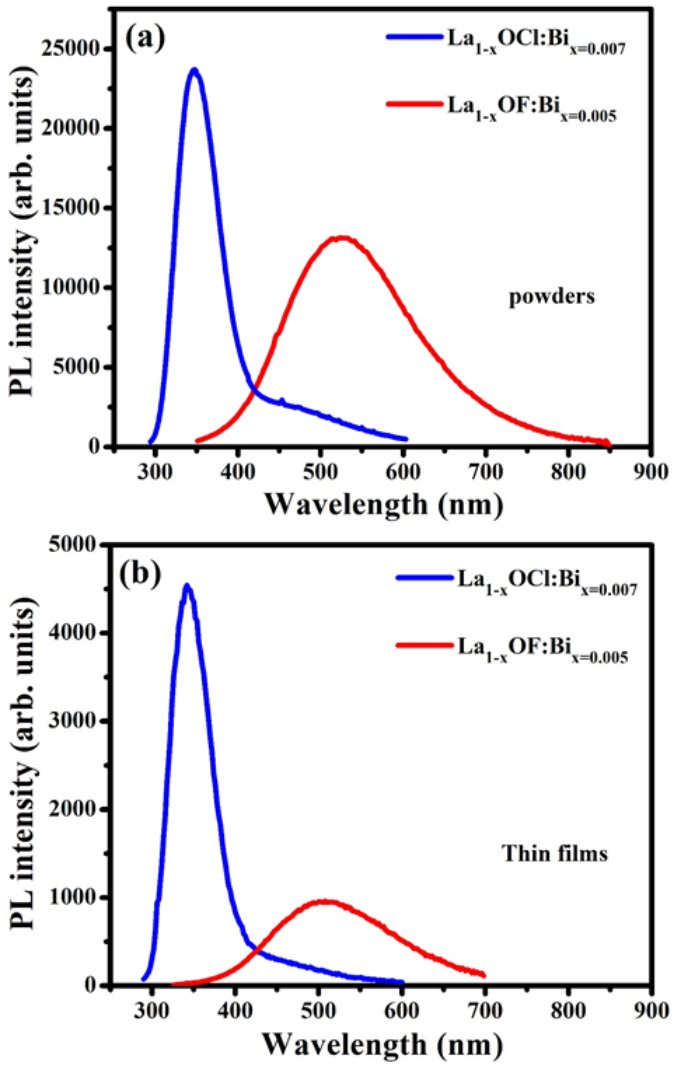

Figure 7.6: PL emission spectra of (a) LaOCl:Bi and LaOF:Bi powders, and (b) PLD thin films of each material exhibiting the strongest emission (i.e. produced with Ar pressures of 40 mTorr for LaOCl:Bi and 20 mTorr for LaOF:Bi).

While PLD worked well to produce thin films of LaOCl:Bi, the quality of the LaOF:Bi films which were created was less good. The layers were much thinner and less material was deposited. A reason for this may be the different bandgaps of LaOCl and LaOF. We determined the band gap of LaOCl powder to be 5.76 eV (~215 nm). The bandgap of LaOF was difficult to measure with our instrument, which only measures down to 200 nm, but is expected to be greater than that of LaOCl since the bandgap of LnOX increases as X varies from I to Br to Cl to F [20, 21]. In both

cases the bandgap of the materials is greater than the energy corresponding to the 266 nm PLD laser photons which will limit strong absorption. Since the bandgap of LaOF is bigger than that of LaOCl, it will absorb the PLD laser light even less effectively and therefore the laser pulse energy will be spread through a greater volume, so the material is less heated and not as much is ablated. This indicates that the PLD laser wavelength, relative to the bandgap of the target material, can have a strong influence on the quality of thin films produced by PLD.

7.4. Conclusion

Bi doped LaOCl and LaOF phosphor thin films were successfully synthesized by the PLD technique. XRD data confirmed that both LaOCl and LaOF phases belong to the tetragonal crystal structure. The SEM images of LaOCl show that the particles had different spherical sizes for the film deposited in a vacuum. The films deposited in different Ar pressures had particles of different spherical sizes as well as flower-like shapes with platelets. The SEM images of LaOF show that the particles had spherical shape with distinct sizes. The LaOF films consisted of much less material than for the corresponding films of LaOCl. The EDS spectra of the films are similar to the powder. Photoluminescence measurements revealed that the films exhibited emission around 344 nm for LaOCl:Bi and 518 nm for LaOF:Bi under excitations of 266 nm and 263 nm, respectively. These excitation and emission peaks have been attributed to the transitions between the $^3P_1$ excited state and $^1S_0$ ground state of the Bi^{3+} ions. For both powder and films, the luminescence from the LaOF:Bi samples was less intense compared to the corresponding LaOCl:Bi samples.

7.5. References

1. G. Shwetha, V. Kanchana, N. Yedukondalu and G.Vaitheeswaran. Ab initio study of scintillating lanthanide oxyhalide host materials. *Materials Research Express* 2 (2015) 105901. doi: 10.1088/2053-1591/2/10/105901
2. U. Rambabu, A. Mathur, S. Buddhudu. Fluorescence spectra of Eu^{+3} and Tb^{+3}-doped lanthanide oxychloride powder phosphors. *Materials Chemistry and Physics* 61 (1999) 156-162. doi: 10.1016/s0254-0584(99)00122-4
3. Kenneth R. Kort and Sarbajit Banerjee. Shape-controlled synthesis of well-defined matlockite LnOCl (Ln: La, Ce, Gd, Dy) nanocrystals by a novel non-hydrolytic approach. *Journal of*

Inorganic Chemistry 50 (2011) 5539–5544. doi: 10.1021/ic200114s

4. J. W. Fergus. Crystal structure of lanthanum oxyfluoride. *Journal of Materials Science Letters* 16 (1997) 267–269. doi: 10.1023/A:1018584614532
5. Koichi Momma and Fujio Izumi. VESTA 3 for Three-Dimensional Visualization of Crystal, Volumetric and Morphology Data. *Journal of Applied Crystallography* 44 (2011) 1272–1276. doi: 10.1107/S0021889811038970
6. A. Vaitkus, A. Merkys and S. Gražulis. Validation of the Crystallography Open Database using the Crystallographic Information Framework. *Journal of Applied Crystallography* 54 (2021) 661-672. doi: 10.1107/S1600576720016532
7. Roy H.P. Awater, Pieter Dorenbos. The Bi^{3+} 6s and 6p Electron Binding Energies in Relation to the Chemical Environment of Inorganic Compounds. *Journal of Luminescence* 184 (2017) 221–231. doi: 10.1016/j.jlumin.2016.12.021
8. A.M. Srivastava, S.J. Camardello. Concentration Dependence of the Bi^{3+} luminescence in $LnPO_4$ (Ln = Y^{3+}, Lu^{3+}). *Optical Materials* 39 (2015) 130–133. doi: 10.1016/j.optmat.2014.11.011
9. A. Yousif, H. C. Swart, O. M. Ntwaeaborwa and E. Coetsee. Conversion of $Y_3(Al,Ga)_5O_{12}:Tb^{3+}$ to $Y_2Si_2O_7:Tb^{3+}$ thin film by annealing at higher temperatures. *Applied Surface Science* 270 (2013) 331–339. doi: 10.1016/j.apsusc.2013.01.025
10. J. Orava. Chalcogenide Glasses. Deposition techniques for chalcogenide thin films. (2014) 265–309. doi: 10.1533/9780857093561.1.265
11. Z. Liu. Shreir's Corrosion. Laser Applied Coatings. (2010) 2622–2635. doi: 10.1016/B978-044452787-5.00141-4
12. R. M. Jafer, H. C. Swart, A. Yousif and E. Coetsee. The effect of different substrate temperatures on the structure and luminescence properties of $Y_2O_3:Bi^{3+}$ thin films. *Solid State Science* 53 (2016) 30–36. doi: 10.1016/j.solidstatesciences.2016.01.005
13. Shigeo Horiuchi and Chuhei Oshima. Growth of LaOCl crystalline films. *Journal of Crystal Growth* 23 (1974) 239-241. doi: 10.1016/0022-0248(74)90243-7
14. S. Fujihara, T. Kato, T. Kimura. Sol-gel synthesis and luminescent properties of oxyfluoride $LaOF:Eu^{3+}$ thin films. *Materials science letters* 20 (2001) 687– 689. doi: 10.1023/a:1010946621624

15. E. H. H. Hasabeldaim, O. M. Ntwaeaborwa, R. E. Kroon, E. Coetsee-Hugo, H. C. Swart. Pulsed laser deposition of a ZnO:Eu^{3+} thin film: study of the luminescence and surface state under electron beam irradiation. *Applied Surface Science* (2019) 144281. doi: 10.1016/j.apsusc.2019.144281
16. R.E. (Ted) Kroon. Nanoscience and the Scherrer equation versus the 'Scherrer–Gottingen equation'. *South African Journal of Science* 109(5/6) (2013) Art. #a0019 (2 pages). doi: 10.1590/sajs.2013/a0019
17. L. Levee, C. Calogero, E. Barbieri, S. Byrne, C. Donahue, M. Eisenberg, S. Hattenbacha, J. Lea, J.F. Capitania, J. Roithovác, D. Schröder. Formation of argon–boron bonds in the reactions of BFn+/2+ cations with neutral argon. International Journal of Mass Spectrometry 323-324 (2012) 2–7. doi: 10.1016/j.ijms.2012.05.006
18. Guguloth Ravi, Madderla Sarasija, Dasari Ayodhya, Lunavath Shanthi Kumari and Dongamanti Ashok. Facile synthesis, characterization and enhanced catalytic reduction of 4-nitrophenol using $NaBH_4$ by undoped and Sm^{3+}, Gd^{3+}, Hf^{3+} doped La_2O_3 nanoparticles. *Nano Convergence* 6 (2019) 1-9. doi: 10.1186/s40580-019-0181-6
19. Chenguo Hu, Hong Liu, Wenting Dong, Yiyi Zhang, Gang Bao, Changshi Lao, and Zhong L. Wang. $La(OH)_3$ and La_2O_3 Nanobelts—Synthesis and Physical Properties. *Advanced Materials* 19 (2007) 470–474. doi: 10.1002/adma.200601300
20. D. Kim, J. R. Jeong, Y. Jang, J.-S. Bae, I. Chung, R. Liang, J.-C. Park. Self-emitting blue and red EuOX (X = F, Cl, Br, I) materials: band structure, charge transfer energy, and emission energy. *Physical Chemistry Chemical Physics* 21 (2019) 1737-1747. doi: 10.1039/c8cp06470a
21. D. Kim, S. Park, S. Kim, S.-G. Kang, J.-C. Park. Blue-Emitting Eu^{2+}-Activated LaOX (X = Cl, Br, and I) Materials: Crystal Field Effect. *Inorganic Chemistry* 53 (2014) 11966–11973. doi: 10.1021/ic5015576

Chapter eight

Stability and photoluminescence of Bi doped $(La,Y)_2O_3$ phosphor powders

8.1. Introduction

The interest in post-transition metal ions such as Tl^+, Pb^{2+}, Bi^{3+} and Sb^{3+} has been increasing over the past decade because of their potential as low cost alternatives to the rare earth ions for luminescence applications, which can be used in high-energy physics, low pressure lamps, X-ray imaging devices and scintillation [1, 2, 3]. Bi^{3+} ion doped phosphor materials display useful tuneable optical characteristics because of the strong interaction with the surrounding host structure [4, 5]. The ground energy level of the Bi^{3+} ion is $^1S_0$, having a $6s^2$ outer electron configuration, whereas the excited state $6s^16p^1$ configuration consists of the four energy levels $^3P_0$, $^3P_1$, $^3P_2$ and $^1P_1$. The optical transition from $^1S_0$ to $^1P_1$ is allowed, but generally of high energy corresponding to the vacuum ultraviolet range. The transition from $^1S_0$ to $^3P_1$ becomes allowed through the mixing between $^1P_1$ and $^3P_1$ levels by spin orbit coupling and is generally responsible for luminescence, while the optical transitions from $^1S_0$ to $^3P_0$ and $^3P_2$ are spin forbidden [6].

The addition of relatively low proportions of La_2O_3 to Y_2O_3 as a sintering aid was pioneered by Rhodes *et al.* [7, 8, 9] in the 1980s and is still an area of research [10]. Y_2O_3 doped with Nd and mixed with varying amounts of La_2O_3 as a sintering aid was investigated as a means of producing transparent ceramics, although luminescence measurements were not reported [11]. $(La,Y)_2O_3$ materials with varying proportion and phases dictated by the annealing temperature were investigated for catalysis application [12]. $LaYO_3$ doped with Sr and having the orthorhombic perovskite structure is of interest as a high temperature proton conducting material for solid oxide fuel cells [13, 14]. $(La,Y)_2O_3$ was compared to yttrium garnet compounds for their suitability as hosts for Yb doped infrared lasers, although very few details of the material were provided [15]. $LaYO_3$ doped with Bi and Tb was investigated for application as near infrared reflectance pigments, but luminescence measurements were not included [16]. The photoluminescence of 1 mol% Bi doped $LaYO_3$ with an orthorhombic perovskite structure was measured by Taikar *et al.* [17], who found blue emission at 493 nm for excitation at 330 nm. For any phosphor to be used in an application, its stability under the particular application environment is an important

consideration. In previous work it was demonstrated that La_2O_3 doped with Bi is a potentially useful blue emitting phosphor emitting at 462 nm when excited at 308 nm [18]. The host, however, was converted to $La(OH)_3$ within a few days when exposed to the atmosphere [19] and must therefore be protected from air exposure. In contrast to La_2O_3, the host Y_2O_3 is stable and Bi doped Y_2O_3 has been investigated by several other researchers (e.g. see the review in [5]). Due to the two possible symmetry sites (C_2 and S_6) of Y in cubic Y_2O_3 which may be occupied by the Bi dopant, the luminescence of Y_2O_3:Bi is more complicated than that of La_2O_3:Bi (for which La has a single site with a C_{3v} symmetry) and multiple excitation wavelengths would generally be required to excite the Bi^{3+} ions in the different sites, while shifts in emission could occur when the excitation varied slightly. The stability of interlanthanide perovskites to withstand oxygen and carbon dioxide is positively reported [20], so that perovskite $LaYO_3$ with equal proportions of La and Y is not expected to degrade during storage in the atmosphere. The aim of this work was to investigate the mixed $(La,Y)_2O_3$:Bi phosphor system as a possible material that shows stability in the atmosphere and to investigate its structure and luminescence properties.

8.2. Experimental

Powder samples of $La_{2-y}Y_yO_3$ with varying cation proportion (y) were prepared via citric acid sol-gel combustion synthesis [21], in order to investigate their structure and gauge their stability when exposed to the atmosphere. The precursors were lanthanum nitrate ($La(NO_3)_3{\cdot}6H_2O$, 99.999%), yttrium nitrate ($Y(NO_3)_3{\cdot}6H_2O$, 99.999%) and citric acid ($C_6H_8O_7{\cdot}H_2O$, 99.5%), which was used as a fuel for combustion. The molar ratio of metal ions to citric acid was 1:2.

These were mixed with 40 ml of distilled water in a glass beaker. The reaction beaker was heated at 80 °C under vigorous stirring for 3 h, after which about 20 ml of gel remained. This was transferred to a porcelain crucible which was placed into a muffle furnace maintained at 250 °C for 30 min. The combustion reaction created white fumes and a white powder was formed as the product. This as-prepared powder was annealed for 2 h in air at different temperatures between 1000 °C and 1400 °C. To dope samples with Bi, an appropriate small amount of $La(NO_3)_3{\cdot}6H_2O$ was substituted by an equal amount of bismuth nitrate ($Bi(NO_3)_3.5H_2O$, 99.999%).

X-ray diffraction (XRD) measurements were performed in order to ascertain the crystal phase of the materials produced. A D8 Advance diffractometer from Bruker with Cu Kα X-rays (40 kV, 40

mA) was used. The samples were also examined using a JEOL JSM-7800F scanning electron microscope (SEM) and the elemental composition was assessed by means of its energy dispersive X-ray spectroscopy (EDS) attachment (X-Max^{N}80 detector) by Oxford Instruments. The photoluminescence (PL) properties of the powders were measured at room temperature using an FS5 spectrometer from Edinburgh Instruments. The International Commission for Illumination (CIE) coordinates of the emitted light was calculated using the GoCIE software [22].

8.3. Results and discussion

8.3.1. Structure and stability of undoped $(La,Y)_2O_3$

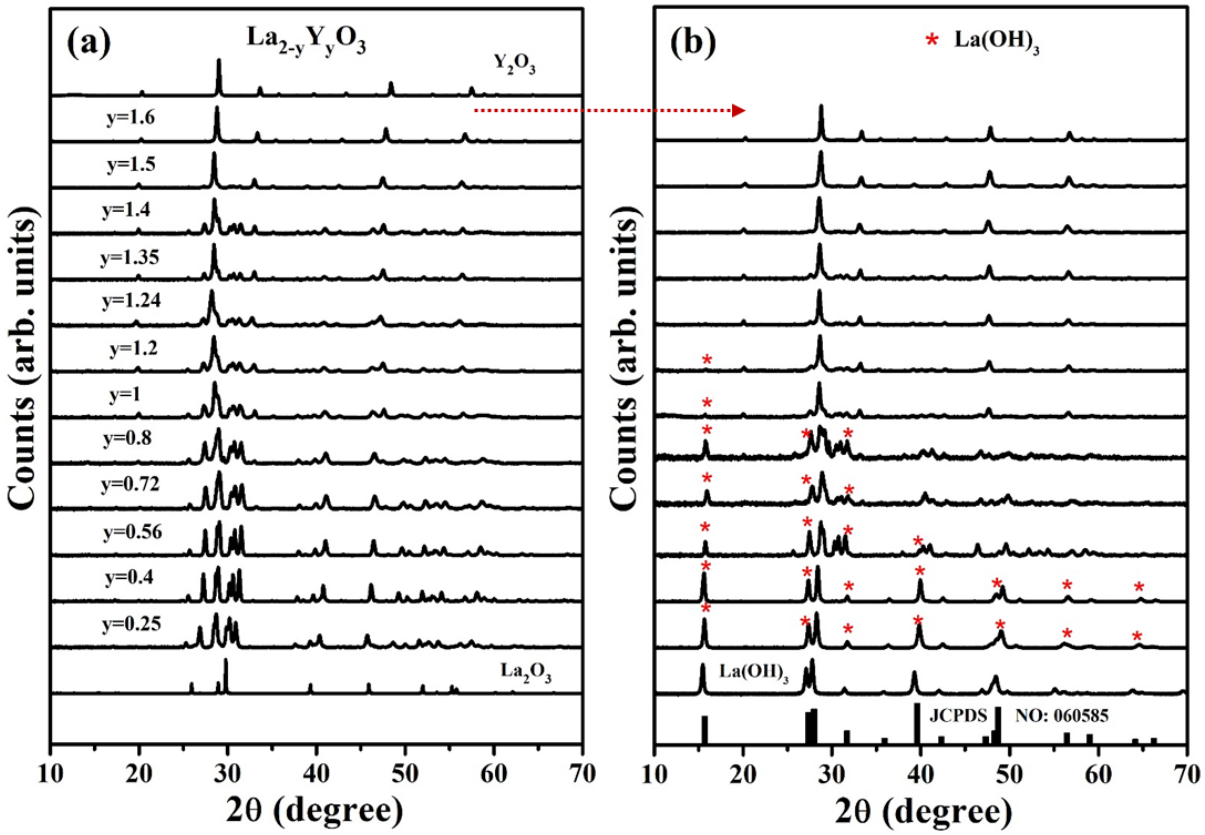

Figure 8.1: XRD patterns of $(La,Y)_2O_3$ phosphor powders with different La and Y ratios. (a) Freshly prepared samples. (b) After being exposed to the atmosphere for 4 months.

Figure 8.1(a) presents the XRD patterns obtained from freshly prepared $La_{2-y}Y_yO_3$ powder phosphors with varying proportion of La and Y, annealed at 1200 °C after combustion synthesis.

Besides at the extremes corresponding to y = 0 (La_2O_3) and y = 2 (Y_2O_3) for which the patterns matched well with the hexagonal and cubic phases expected of these materials. Most of the XRD patterns were complicated because of the possibilities of mixed phases as well as potential shifting of the lattice parameters of each phase with varying composition. The La_2O_3-Y_2O_3 pseudobinary phase diagram has been investigated and revised numerous times over the past sixty years. While early efforts were misleading, e.g. greatly retarded progress of the development of non-porous single phase Y_2O_3 doped with La as a sintering aid [23], improved diagrams were published in the mid-1970's [24, 25] which eliminated the proposed but erroneous stoichiometric phase $La_{1.5}Y_{0.5}O_3$. Progress up to 2005 was reviewed by Chen [26] and subsequently Fabrichnaya *et al.* have further modelled this pseudobinary phase diagram and published several refinements between 2006 and 2013 [27, 28, 29, 30].

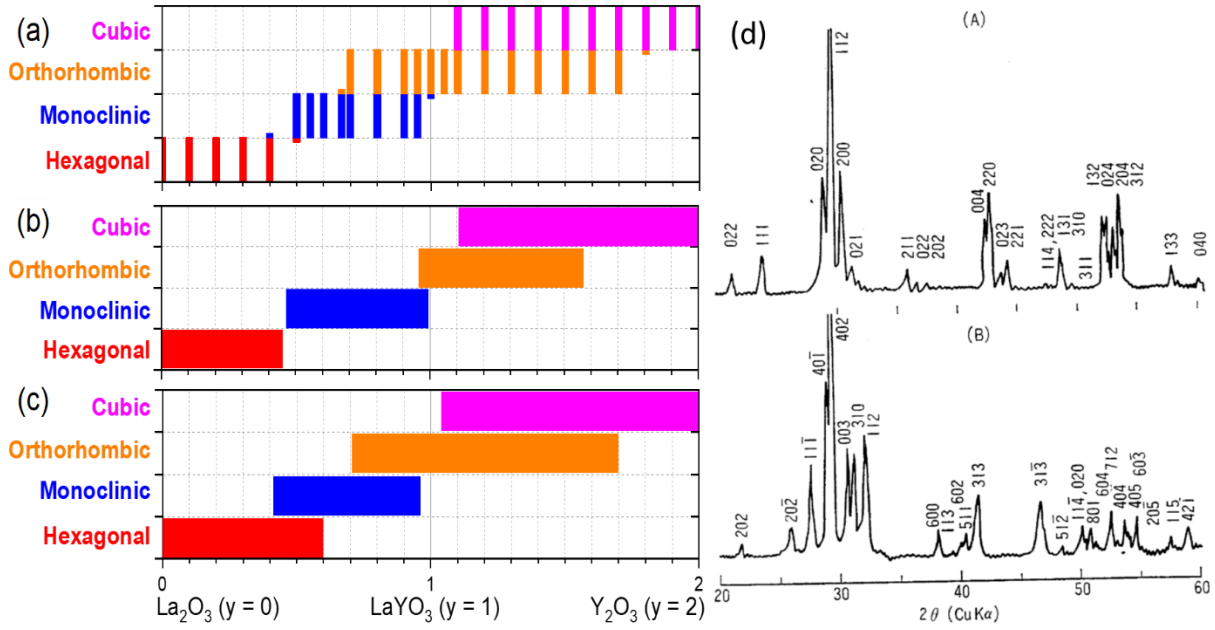

Figure 8.2: Reported phases of $La_{2-y}Y_yO_3$ as determined by XRD for material (a) cooled from 1300 °C based on data in Table 3 of Ref. [25] where the small fractions have been added to indicate instances where *very weak* XRD reflections were noted; (b) cooled from 1400 °C based on the description in Ref. [31]; and (c) at 1500 °C based on the description in Ref. [32]. Part (d) shows the experimental XRD patterns of A: orthorhombic and B: monoclinic $LaYO_3$, reproduced from [25] without alteration, © Journal of the Ceramic Society of Japan, under Creative Commons CC BY-ND 4.0 (https://creativecommons.org/licenses/by-nd/4.0/).

The La_2O_3-Y_2O_3 pseudobinary phase diagram shows that solid $La_{2-y}Y_yO_3$ exists in six distinct phases, designated by X, H, A, B, C and P. Of these X and H only occur at high temperature and are not retained even after rapid quenching, so they do not occur in samples at room temperature. The phases A, B and C correspond respectively to the well-known hexagonal, monoclinic and cubic phases of rare-earth oxides [33], with pure La_2O_3 having the hexagonal A structure and pure Y_2O_3 having the cubic C structure. The monoclinic B structure occurs for several rare-earth oxides with intermediate ionic radius and can also occur for the mixed oxide $La_{2-y}Y_yO_3$. Additionally, an orthorhombic (distorted perovskite) structure occurs when the proportions of La and Y are almost equal (y = 1) and $LaYO_3$ is classified as one of eleven known and recently reviewed interlanthanide perovskite materials [20]. Figure 8.2 shows the wide overlap of phases which have been reported as a function of composition in a number of studies. Some differences can be attributed to the different temperatures associated with the data, while generally the complexity of the system is exhibited. Figure 8.2(c) was derived from current work to extend the La_2O_3-Y_2O_3 pseudobinary phase diagram to the ternary La_2O_3-Y_2O_3-Nd_2O_3 system [32] and the phase ranges reported at 1500 °C suggests that two aspects of the 2013 pseudobinary phase diagram of Fabrichnaya *et al*. [30] may require further consideration: firstly, there is disagreement whether the orthorhombic perovskite phase $LaYO_3$ exists in a narrow composition range y = 0.96 – 1.04 or instead as a stoichiometric phase with y = 1; and secondly, the composition at the boundary of the hexagonal and hexagonal+monoclinic phase fields at 1500 °C (1773 K) is much lower in the phase diagram ($y \approx 0.24$) compared to the recently published data (y = 0.42).

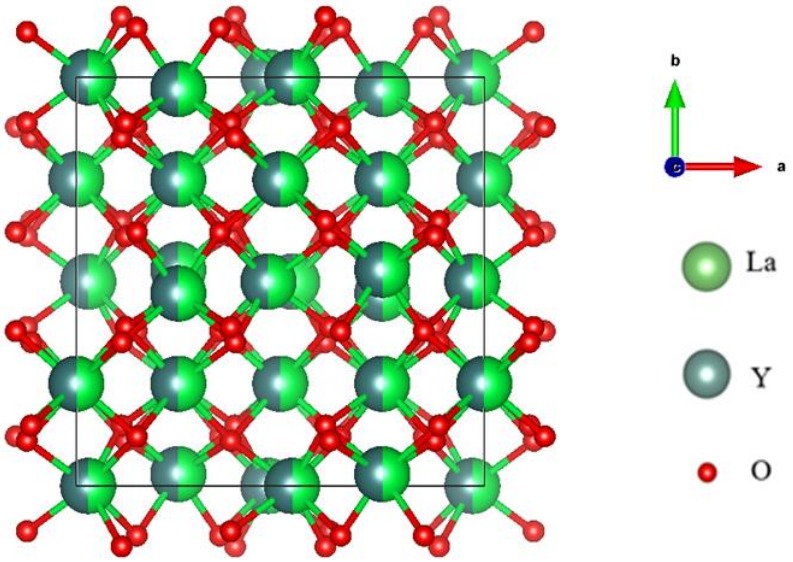

Figure 8.3: Cubic crystal structure of $LaYO_3$ drawn with the Vesta software [34].

An additional consideration is that nanomaterial of the $LaYO_3$ (y = 1) composition may unexpectedly crystallize in the cubic C phase, as first reported by Yamaguchi [35] and again rediscovered by Dordevic *et al.* who studied Sm [36] and Eu [37, 38] doped material. This metastable phase cannot be accommodated in the equilibrium phase diagram and undergoes a non-reversible change to the orthorhombic structure when annealed at 1210 - 1250 °C [35]. It is illustrated in Figure 8.3. To model the crystal structure, cubic structure of La_2O_3 was taken from [39] as a starting point. The lattice parameter adjusted to that given for $LaYO_3$ by Yamaguchi [35], namely a = 10.906 Å. Half of the La^{3+} ions need to be replaced by Y^{3+} ions. Since the 32 La^{3+} ions in the unit cell are distributed over two sites, namely 24 in the C_2 sites and 8 in the S_6 sites, there is no *a priori* manner to do this. Dordevic et al [37] modelled their XRD data for $LaYO_3$:Eu and gave refined structural parameters showing that the smaller number of centrosymmetric S_6 sites are favoured by La^{3+} ions. However, there is still a mixture of ions at both sites and their occupancy may have been affected by the strong Eu^{3+} doping concentration. For simplicity we created a model in which Y^{3+} replaces La^{3+} randomly over the two sites: therefore the occupancy of both of the La sites was halved and additional Y was added at the same sites with 50% occupancy.

With an increase of the Y content up to y = 0.8, mixed phases of the monoclinic and orthorhombic structure (see Figure 8.2(d)) were observed. Both orthorhombic and cubic structures were observed

when the concentration of Y increased from 1 up to 1.4. Pure phases of $LaYO_3$ cubic structure were observed when the proportion of Y increased to y = 1.5 and y = 1.6.

Figure 8.1(b) displays the XRD patterns for the same samples after being exposed to the atmosphere for 4 months during storage. By comparing the patterns with the standard for $La(OH)_3$ (JCPDS card #05-0685), mixed phases of the oxide and hydroxide were observed when $y \leq 1.2$, while at the higher concentrations $1.24 \leq y \leq 1.6$ the powders were found to be stable. This shows that in addition to the hexagonal phase of La_2O_3 being unstable in the atmosphere and forming a $La(OH)_3$, the monoclinic and orthorhombic phases of $La_{2-y}Y_yO_3$ were also susceptible to hydroxylation, i.e. La_2O_3 was not effectively stabilized by alloying with a small proportion of Y_2O_3. In this work $La_{0.5}Y_{1.5}O_3$ was therefore chosen to study further due to its high chemical stability. The PL was investigated and optimized by varying the Bi doping concentration and the annealing temperature.

8.3.2. Structure and morphology of Bi doped $La_{0.5}Y_{1.5}O_3$

Figure 8.4 shows the XRD patterns of $La_{0.5-x}Y_{1.5}O_3:Bi_x$ phosphor powder samples activated with different Bi concentrations (x = 0, 0.001, 0.003, 0.005, 0.007, 0.01 and 0.012) and annealed at 1200 °C for 2 h in air. Although Figure 2 suggests the probability of encountering a mixture of orthorhombic and cubic phases for the host alloy with composition y = 1.5, the experimentally observed crystal structure corresponded to a single phase cubic material (both for the doped material shown in Figure 8.4 and the pure host shown in Figure 8.1(a)). Since single phase cubic material can occur for nanomaterial with Y content as low as y = 1, i.e. $LaYO_3$ [35-38], although the present result was unexpected from data obtained in phase diagram studies, it is in line with other experimental observations. No other diffraction peaks were detected due to impurities, indicating that the Bi^{3+} ions were successfully inserted in the $La_{0.5}Y_{1.5}O_3$ host lattice. No shifting in the positions of the peaks was detected when the Bi concentration was increased.

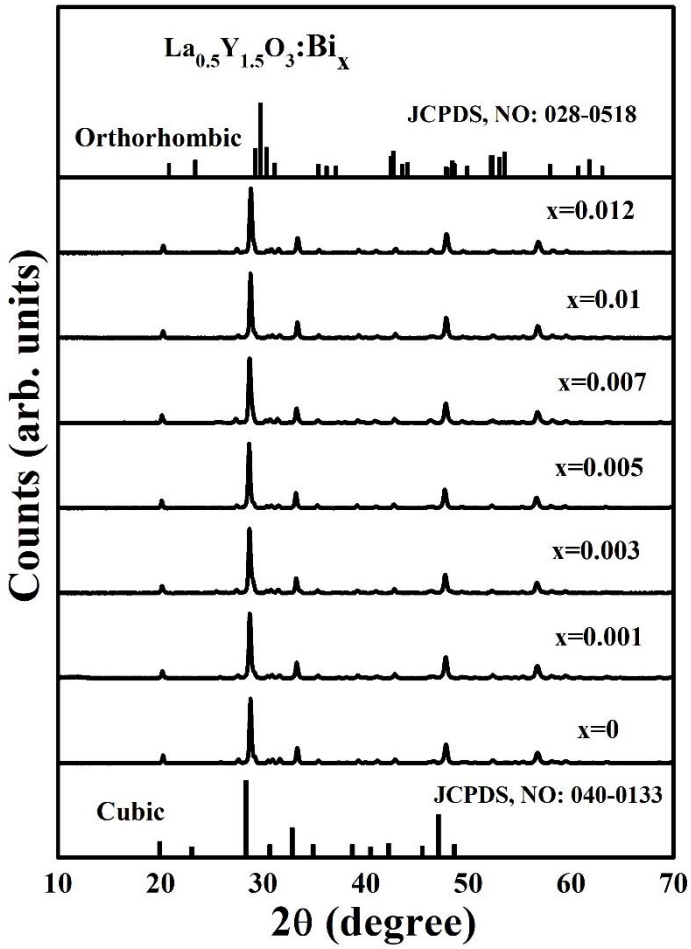

Figure 8.4: XRD patterns of $La_{0.5-x}Y_{1.5}O_3:Bi_x$ powders annealed at 1200 °C. The standards for different possible phases of $LaYO_3$ are shown on the top and bottom.

Figure 8.5 displays the SEM images for the $La_{0.5}Y_{1.5}O_3$ pure host phosphor powders and doped samples which were annealed at 1200 °C. Figure 8.5(a) is the SEM image for the $La_{0.5}Y_{1.5}O_3$ pure host. The shape of the particles was cubic. Figure 8.5(b, c and d) are the SEM images for the doped samples for which the shape of the particles changed from cubic to more round when Bi was inserted in the host structure.

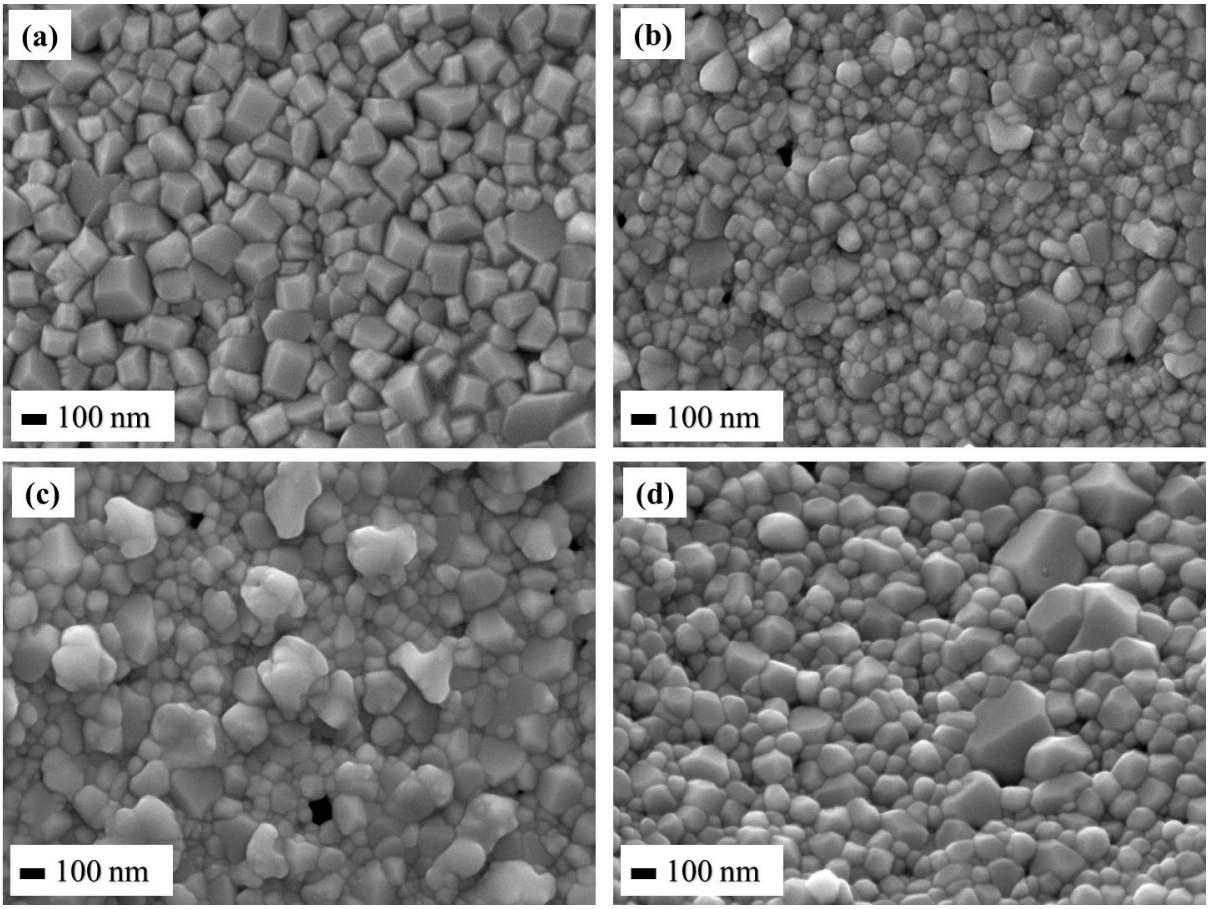

Figure 8.5: SEM images of the $La_{0.5}Y_{1.5}O_3:Bi_x$ phosphor powders annealed at 1200 °C (a) x = 0, (b) x = 0.003, (c) x = 0.005 and (d) x = 0.01.

Figure 8.6(a) shows the EDS spectrum of the $La_{0.5}Y_{1.5}O_3$ pure host sample. All the elements were detected in the sample as expected (La, Y, O), together with a very small quantity of C that probably coming from the citric acid precursor used in the sol-gel combustion synthesis, or possibly could result from the carbon tape that was used to mount the samples. Figure 8.6(b) shows the EDS spectrum for the $La_{0.5}Y_{1.5}O_3:Bi_{x=0.01}$ doped sample. The spectrum is similar to the undopd sample. Although Bi X-ray of energy 2.419 keV may be expected as indicated by the position of the blue line in Figure 8.6(b), this was not detected, probably due to the low Bi concentration in even the sample with maximum doping (x = 0.012) considered in this work. The EDS data show that the atomic percentages of the $La_{0.5}Y_{1.5}O_3$ pure host were La 9%, Y 23% and O 68%, while for the doped sample were La 11%, Y 26% and O 63%. The expected amounts in $La_{0.5}Y_{1.5}O_3$ are:

La 10%, Y 30% and O 60%. The results show that the La was as expected, while the Y a little lower and the O a little higher than expected.

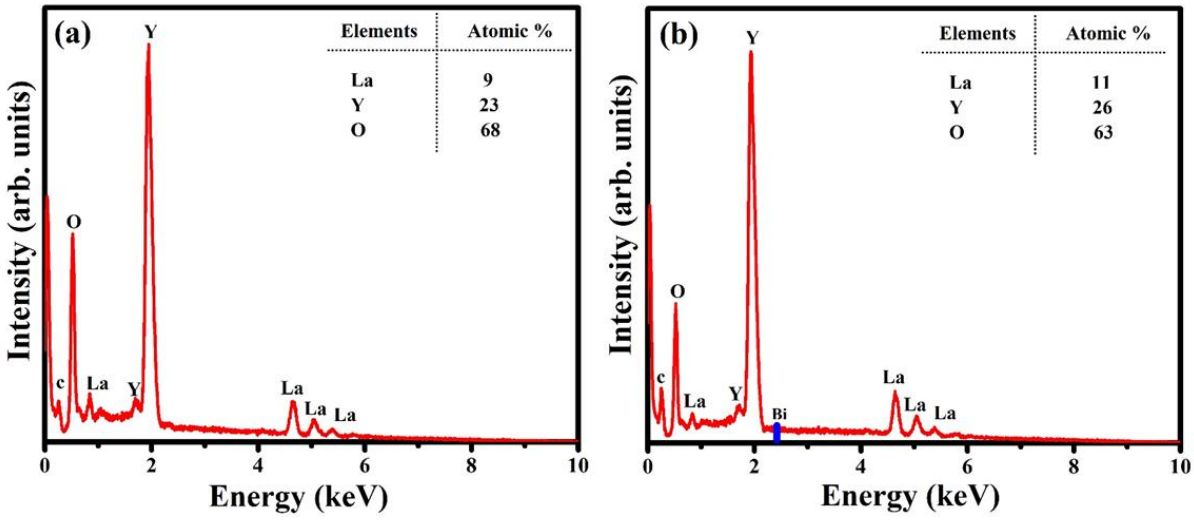

Figure 8.6: EDS spectra of (a) $La_{0.5}Y_{1.5}O_3$ pure host (b) $La_{0.5-x}Y_{1.5}O_3:Bi_{x=0.012}$ phosphor powders annealed at 1200 °C.

8.3.3. Photoluminescence analysis

Figure 8.7(a) shows the PL excitation and emission spectra for $La_{0.5-x}Y_{1.5}O_3:Bi_x$ phosphor powder doped with various Bi concentrations, annealed in air at 1200 °C for 2 h. The PL emission intensity as a function of Bi doping concentration is presented in Figure 8.7(b). Figure 8.7(c) presents the PL excitation and emission spectra of $La_{0.5-x}Y_{1.5}O_3:Bi_{x=0.005}$ annealed at different temperatures. Two emission peaks were observed centred at 425 nm and 529 nm when the phosphor was excited by 333 nm. The PL emission intensity increased with increasing Bi concentration until x = 0.005, then decreased above that concentration due to concentration quenching which occurred due to migration of energy between the dopants. Appreciable quenching may occur for low dopant concentrations of 0.001 to 0.012 mol% [40]. Figure 8.7(d) shows the PL emission intensity as a function of annealing temperature, for annealing in air between 1000 °C to 1400 °C. The intensity of emission increased with the increasing the heating temperature, reaching the maximum at a heating temperature 1200 °C and then decreased with a further increase in temperature. The

emission intensity might be expected to increase as the heating temperature was increased because of an improvement in the crystalline quality and removal of defects. Jafer *et al.* [41] studied the effect of heating temperature on Y_2O_3 doped Bi phosphor powders and attributed the increase of the emission intensity with heating temperature up to a maximum value to segregation effects of the dopant to the particle surface, while the quenching of the luminescence at higher heating temperatures was due to evaporation loss of the dopant from the surface of the sample.

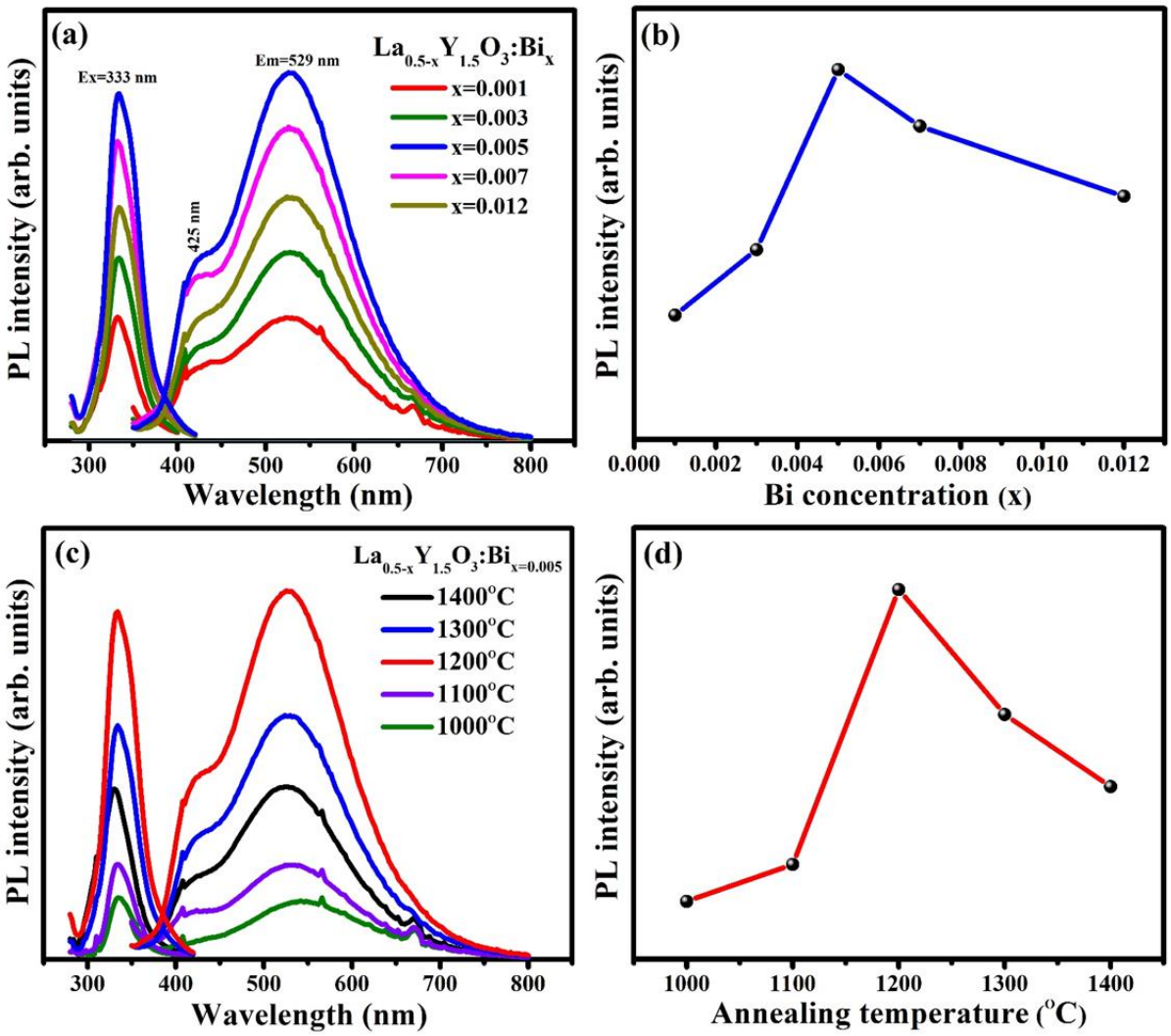

Figure 8.7: (a) Excitation and emission spectra of $La_{0.5-x}Y_{1.5}O_3:Bi_x$ doped with different Bi concentrations, annealed in air at 1200 °C. (b) Emission peak intensity as a function of Bi concentration (x). (c) Excitation and emission spectra of $La_{0.5-x}Y_{1.5}O_3:Bi_{x=0.005}$ annealed at different temperatures. (d) Emission peak intensity as a function of the annealing temperature.

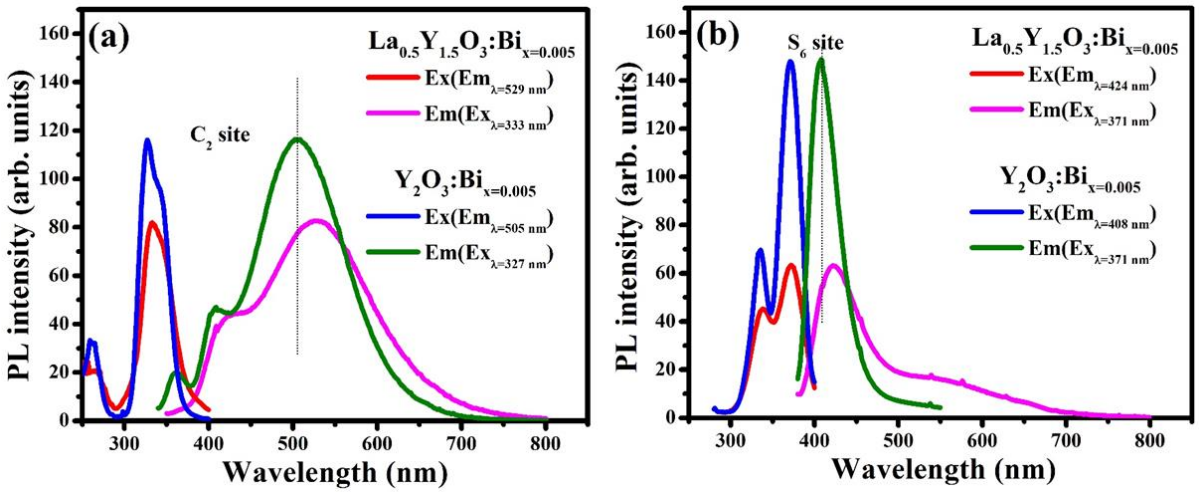

Figure 8.8: Excitation and emission spectra of $La_{0.5-x}Y_{1.5}O_3:Bi_{x=0.005}$ and $Y_{2-x}O_3:Bi_{x=0.005}$ related to Bi (a) in C_2 site and (b) in S_6 site.

Since the $La_{0.5}Y_{1.5}O_3$ in this study has the same cubic crystal structure as Y_2O_3, Figure 8.8 compares the PL excitation and emission spectra for $La_{0.5-x}Y_{1.5}O_3:Bi_{x=0.005}$ powder phosphor directly with $Y_{2-x}O_3:Bi_{x=0.005}$, both annealed in air for 2 h at 1200 °C. In these cubic structures the lanthanide ions have two sites, with point symmetry C_2 and S_6, that Bi^{3+} ions may substitute, giving rise to a double set of excitation-emission curves for the Bi^{3+} luminescence which is well known for Y_2O_3:Bi [5]. Figure 8.9(a) compares the materials for excitation of Bi^{3+} in the C_2 site. While this occurs for $Y_{2-x}O_3:Bi_{x=0.005}$ at 327 nm with emission at 505 nm, the excitation band of the $La_{0.5}Y_{1.5}O_3:Bi_{x=0.005}$ in at 333 nm with emission 529 nm. The Stokes shift for emission in the S_6 site is much smaller as shown in Figure 8.9(b). Both materials have the excitation maximum at 371 nm. The PL emission spectrum of $Y_2O_3:Bi_{x=0.005}$ is at 408 nm, while that of $La_{0.5}Y_{1.5}O_3:Bi_{x=0.005}$ occurs at a slightly longer wavelength of 424 nm. For comparison, Bi doped Gd_2O_3 has emission at 505 nm from the C_2 site and at 418 nm from the S_6 site [42]. La_2O_3:Bi has a broad blue emission located at 462 nm [18] which is therefore intermediate between the emission wavelengths of 529 nm and 424 nm obtained from $La_{0.5}Y_{1.5}O_3$:Bi in this work. The luminescence from the $La_{0.5}Y_{1.5}O_3:Bi_{x=0.005}$ sample was less intense compared to the $Y_{2-x}O_3:Bi_{x=0.005}$ sample for both sites. Therefore, unless the small differences in emission wavelength are useful, the unalloyed host Y_2O_3 which is also stable may be better suited for phosphor applications than $La_{0.5}Y_{1.5}O_3$. The decrease of emission intensity for the alloyed host compared to the pure host may be to mixing disorder and the associated strain that could enhance non-radiative recombinations.

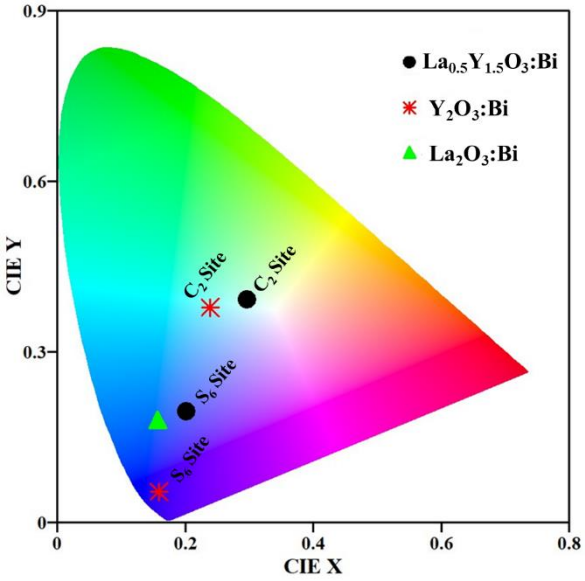

Figure 8.9: CIE coordinate diagram of $La_{0.5-x}Y_{1.5}O_3:Bi_{x=0.005}$, $Y_{2-x}O_3:Bi_{x=0.005}$ and $La_{2-x}O_3:Bi_{x=0.002}$ phosphor powders.

Figure 8.9 shows the chromaticity coordinates of $La_{0.5-x}Y_{1.5}O_3:Bi_{x=0.005}$, $Y_{2-x}O_3:Bi_{x=0.005}$ and $La_{2-x}O_3:Bi_{x=0.002}$ phosphor powders, annealed at 1200 C in air for 2h, The $La_{0.5-x}Y_{1.5}O_3:Bi_{x=0.005}$ and $Y_{2-x}O_3:Bi_{x=0.005}$ in C_2 site showed white colour and blue colour in S_6 site. The $La_{2-x}O_3:Bi_{x=0.002}$ shows blue colour located between S_6 and C_2 sites of $La_{0.5-x}Y_{1.5}O_3:Bi_{x=0.005}$ and $Y_{2-x}O_3:Bi_{x=0.005}$. The excitation wavelengths and chromaticity coordinates X and Y for all compounds are summarized in table 8.1.

Table 8.1: Excitation wavelengths and chromaticity coordinates.

Material		Excitation (nm)	X	Y
$La_{0.5-x}Y_{1.5}O_3:Bi_{x=0.005}$	S_6	371	0.20	0.20
	C_2	333	0.30	0.39
$Y_{2-x}O_3:Bi_{x=0.005}$	S_6	371	0.16	0.05
	C_2	327	0.24	0.38
$La_{2-x}O_3:Bi_{x=0.002}$		308	0.16	0.18

8.4. Conclusion

$La_{2-y}Y_yO_3$ was successfully synthesized via the citric acid sol-gel combustion method. Material with composition $La_{0.5}Y_{1.5}O_3$ was single phase with cubic crystal structure and was stable after being exposed to the atmosphere for four months. SEM images showed that the shape of particles changed from cubic to more round when Bi was doped in host structure. EDS of the $La_{0.5}Y_{1.5}O_3$ pure host and doped samples confirmed the presence of the host elements as expected, although the Bi dopant was not detected because of its low concentration. The PL of $La_{0.5-x}Y_{1.5}O_3:Bi_x$ excited at 333 nm consisted of a broad emission from 350 nm to 800 nm that consisted out of two peaks centred at 424 nm and 529 nm which has a maximum intensity for x = 0.005. This emission was attributed to Bi^{3+} ions in C_2 sites of the host. Bi^{3+} also occupied the S_6 sites for which blue emission at 424 nm was obtained for excitation at 371 nm. Although the luminescence from the $La_{0.5-x}Y_{1.5}O_3:Bi_{x=0.005}$ sample was less intense compared to $Y_{2-x}O_3:Bi_{x=0.005}$, there was a significant colour shift and the emission from Bi^{3+} ions at the S_6 site was close to that emitted by unstable La_2O_3:Bi .

8.5. References

1. Ziqiang Jiang, Xiaochen Yu, Xinghua Su, Zhihua Sun, Li Duan. Crystal structure and luminescence properties of Bi^{3+} activated $Ca_2Y_3Sb_3O_{14}$ phosphors in near UV region. *Journal of Alloys and Compounds* 637 (2015) 281–285. doi: 10.1016/j.jallcom.2015.02.209
2. V.Babin, K.Chernenko, L.Lipińska, E.Mihokova, M.Nikl, L.S.Schulman, T.Shalapska *et al*. Luminescence and excited state dynamics of Bi^{3+} centers in Y_2O_3. *Journal of Luminescence* 167 (2015) 268-277. doi: 10.1016/j.jlumin.2015.06.029
3. İlhan Pekgözlü, Ertuğrul Erdoğmuş, Soner Çubuk, Ali Sadi Başak. Synthesis and photoluminescence of $LiCaBO_3$: M (M: Pb^{2+} and Bi^{3+}) phosphor. *Journal of Luminescence* 132 (2012) 1394–1399. doi: 10.1016/j.jlumin.2012.01.001
4. Roy H.P. Awater, Pieter Dorenbos. The Bi^{3+} 6s and 6p Electron Binding Energies in Relation to the Chemical Environment of Inorganic Compounds. *Journal of Luminescence* 184 (2017) 221–231. doi: 10.1016/j.jlumin.2016.12.021
5. H. C. Swart, & R. E. Kroon. Ultraviolet and visible luminescence from bismuth doped materials. *Optical Materials: X* (2019) 100025. doi: 10.1016/j.omx.2019.100025

6. W.A.I. Tabaza, H.C. Swart, R.E. Kroon. Optical properties of Bi and energy transfer from Bi to Tb in $MgAl_2O_4$ phosphor. *Journal of Luminescence* 148 (2014) 192–197. doi: 10.1016/j.jlumin.2013.12.018
7. W. H. Rhodes. Controlled transient solid second-phase sintering of yttria. *Journal of the American Ceramic Society* 64 (1981) 13-19. doi: 10.1111/j.1151-2916.1981.tb09551.x
8. G. C. Wei, T. Emma, W. H. Rhodes, S. Horvath, M. Harmer. Analytical Microscopy Study of Phases and Fracture in Y_2O_3-La_2O_3 Alloys. *Journal of the American Ceramic Society* 71 (1988) 820–825. doi: 10.1111/j.1151-2916.1988.tb07529.x
9. W. H. Rhodes. Phase Chemistry in the Development of Transparent Polycrystalline Oxides. *Phase Diagrams in Advanced Ceramics* (1995) 1–41. doi: 10.1016/b978-012341834-0/50002-7
10. J. K. Thomas, C. T. Mathew, J. Koshy, S. Solomon. Influence of La^{3+} ion in the yttria matrix in improving the microhardness of infrared transparent nano $La_xY_{2-x}O_3$ sintered via hybrid heating. *Journal of Advanced Ceramics* 6 (2017) 240–250. doi: 10.1007/s40145-017-0235-3
11. J. M. Luo, L. P. Deng, J. L. Xu. Fabrication of $(Nd_{0.01}La_xY_{0.99-x})_2O_3$ Nanoparticles and Transparent Ceramics by Combustion Synthesis. *Journal of Nanoscience and Nanotechnology* 11 (2011) 9705–9708. doi: 10.1166/jnn.2011.5284
12. J. L. Rehspringer, P. Poix, A. Kaddouri, D. Andriamasinoro, A. Kiennemann. Methane activation over $La_{2x}Y_{2-2x}O_3$ ($0 \leqslant x \leqslant 1$) catalysts. *Catalysis Letters* 10 (1991) 111–120. doi: 10.1007/bf00764742
13. E. Ruiz-Trejo, M.S. Islam, J.A. Kilner. Atomistic simulation of defects and ion migration in $LaYO_3$. *Solid State Ionics* 123 (1999) 121–129. doi: 10.1016/s0167-2738(99)00092-2
14. N. Danilov, G. Vdovin, O. Reznitskikh, D. Medvedev, A. Tsiakaras, P. Demin. Physico-chemical characterization and transport features of proton-conducting Sr-doped $LaYO_3$ electrolyte ceramics. *Journal of the European Ceramic Society* 36 (2016) 2795–2800. doi: 10.1016/j.jeurceramsoc.2016.04.018
15. J. Ben-Xue, H. Tong-De, W. Yu-Song, L. Wen-Bin, P. Yu-Bai, F. Tao, Y. Qiu-Hong. Comparative spectroscopic investigation of Yb-doped YAG, YSAG and $YLaO_3$ transparent ceramics. *Chinese Physics B* 17 (2008) 3407–3411. doi: 10.1088/1674-1056/17/9/043

16. Y. Xiao, B. Huang, J. Chen, X. Sun. Novel Bi^{3+} doped and Bi^{3+} /Tb^{3+} co-doped $LaYO_3$ pigments with high near-infrared reflectances. *Journal of Alloys and Compounds* 762 (2018) 873–880. doi: 10.1016/j.jallcom.2018.05.233
17. D. R. Taikar, S. Tamboli, S. J. Dhoble. Synthesis and photoluminescence properties of red, green and blue emitting $LaYO_3$:M (M = Eu^{3+} , Tb^{3+} , Sm^{3+} ,Bi^{3+} , Pb^{2+}) phosphors. *Optik - International Journal for Light and Electron Optics* 142 (2017) 183–190. doi: 10.1016/j.ijleo.2017.05.095
18. B.M. Jaffar, HC. Swart, H.A.A. Seed Ahmed, A. Yousif, R.E. Kroon. Luminescence properties of Bi doped La_2O_3 powder phosphor. *Journal of Luminescence* 209 (2019) 217–224. doi: 10.1016/j.jlumin.2019.01.044
19. B.M. Jaffar, H.C. Swart, H.A.A. Seed Ahmed, A. Yousif, R.E. Kroon. Stability of Bi doped La_2O_3 powder phosphor and PMMA composites. *Journal of Physics and Chemistry of Solids* 131 (2019) 156-163. doi: 10.1016/j.jpcs.2019.04.004
20. C. Artini. Crystal chemistry, stability and properties of inter lanthanide perovskites: A review. *Journal of the European Ceramic Society* 37 (2017) 427–440. doi: 10.1016/j.jeurceramsoc.2016.08.041
21. Yousif, R. M. Jafer, S. Som, M.M. Duvenhage, E. Coetsee, H.C. Swart. Ultra-broadband luminescent from a Bi doped CaO matrix. *RSC Advances* 5 (2015) 54115–54122. doi: 10.1039/C5RA09246A
22. GoCIE V2, K. R. Justin Thomas, Department of chemistry, Indian Institute of Technology Rookee, India, 2009. http://faculty.iitr.ac.in/~krjt8fcy/gocie.html
23. Allen. M. Alper. Phase diagrams in advanced ceramics. Academic Press, San Diego, London New York (1995). ISBN: 0-12-341834-8
24. J. Coutures, M. Foex. Etude à haute température du diagramme d'equilibre du Système formé par le sesquioxyde de lanthane avec le sesquioxyde d'Yttrium. *Journal of Solid State Chemistry* 11 (1974) 294–300. doi: 10.1016/s0022-4596(74)80034-4
25. M. Mizuno, A. Rouanet, T. Yamada, T. Noguchi. Phase diagram of the system La_2O_3-Y_2O_3 at high temperatures. *Journal of the Ceramic Association, Japan* 84 (1976) 342–348. doi: 10.2109/jcersj1950.84.971_342

26. M. Chen, B. Hallstedt, L. J. Gauckler. CALPHAD modeling of the La_2O_3–Y_2O_3 system. *Computer Coupling of Phase Diagrams and Thermochemistry* 29 (2005) 103–113. doi: 10.1016/j.calphad.2005.06.006
27. O. Fabrichnaya, M. Zinkevich, F. Aldinger, Thermodynamic assessment of the systems La_2O_3–Al_2O_3 and La_2O_3–Y_2O_3, Int. *International journal of materials research* 97 (2006) 1495-1501. doi: 10.3139/146.101411
28. O. Fabrichnaya, G. Savinykh, G. Schreiber, M. Dopita, H. J. Seifert. Experimental investigation and thermodynamic modelling in the ZrO_2–La_2O_3–Y_2O_3 system. *Journal of Alloys and Compounds* 493 (2010) 263–271. doi: 10.1016/j.jallcom.2009.12.076
29. O. Fabrichnaya, M. J. Kriegel, J. Seidel, G. Savinykh, L. P. Ogorodova, I. A. Kiseleva, H. J. Seifert. Calorimetric investigation of the $La_2Zr_2O_7$, $Nd_2Zr_2O_7$, $Sm_2Zr_2O_7$ and $LaYO_3$ compounds and CALPHAD assessment of the La_2O_3–Y_2O_3 system. *Thermochimica Acta* 526 (2011) 50–57. doi: 10.1016/j.tca.2011.08.021
30. O. Fabrichnaya, G. Savinykh, G. Schreiber, H. J. Seifert. Phase relations in the ZrO_2–Nd_2O_3–Y_2O_3–Al_2O_3 system: Experimental study and thermodynamic modeling. *Journal of the European Ceramic Society* 32 (2012) 3171–3185. doi: 10.1016/j.jeurceramsoc.2012.04.034
31. M. Yoshimura, X.-Z. Rong. Various solid solutions in the systems Y_2O_3-R_2O_3 (R=La, Nd, and Sm) at high temperature. *Journal of Materials Science Letters* 16 (1997) 1961–1963. doi: 10.1023/a:1018559322304
32. O. V. Chudinovych, O. R. Andrievskaya, J. D. Bogatyryova, V. V. Kovylyaev, O. I. Bykov. Phase equilibria in the La_2O_3-Y_2O_3-Nd2O3 system at 1500 °C. *Journal of the European Ceramic Society* 41 (2021) 6606–6616. doi: 10.1016/j.jeurceramsoc.2021.06.017
33. G. Adachi, N. Imanaka. The Binary Rare Earth Oxides. *Chemical Reviews* 98 (1998) 1479–1514. doi: 10.1021/cr940055h
34. Koichi Momma, Fujio Izumi. VESTA 3 for Three-Dimensional Visualization of Crystal, Volumetric and Morphology Data. *Journal of Applied Crystallography* 44 (2011) 1272–1276. doi: 10.1107/S0021889811038970
35. Osamu Yamaguchi, Hidenao Kawabata, Hiroyuki Hashimoto, Kiyoshi Shimizu. New Modification of $LaYO_3$. *Journal of the American Ceramic Society* 70 (1987) 131-132. doi: 10.1111/j.1151-2916.1987.tb05669.x

36. V. Đorđević, M.G. Nikolić, Ž. Antić, M. Mitrić and M.D. Dramićanin. $LaYO_3:Sm^{3+}$ Nanocrystalline Phosphor: Preparation and Emission Properties. *Acta Physica Polonica A* 120 (2011) 303-305. doi: 10.12693/APhysPolA.120.303
37. V. Đorđević, M. G. Nikolić, B. Bartova, R. M. Krsmanović, Ž. Antić, M. D. Dramićanin. Eu^{3+}-doped $(Y_{0.5}La_{0.5})_2O_3$: new nanophosphor with the bixbyite cubic structure. *Journal of Nanoparticle Research* 15 (2012) 1322-1332. doi: 10.1007/s11051-012-1322-6
38. V. Đorđević, Ž. Antić, V. Lojpur, M. D. Dramićanin. Europium-doped nanocrystalline Y_2O_3–La_2O_3 solid solutions with bixbyite structure. *Journal of Physics and Chemistry of Solids* 75 (2014) 1152–1159. doi: 10.1016/j.jpcs.2014.05.009
39. K. Persson. Materials Data on La_2O_3 (SG:164) by Materials Project. (2014). doi: 10.17188/1194889
40. D.L. Dexter, James H. Schulman. Theory of Concentration Quenching in Inorganic Phosphors. *The Journal of Chemical Physics* 22 (1954) 1063–1070. doi: 10.1063/1.1740265
41. R.M. Jafer, H.C. Swart, A. Yousif, Vinod Kumar, E. Coetsee. The Effect of Annealing Temperature on the Luminescence Properties of Y_2O_3 phosphor Powders doped with a High Concentration of Bi^{3+}. *Journal of Luminescence* 180 (2016) 198–203. doi: 10.1016/j.jlumin.2016.08.042
42. M. H. M. Abdelrehman, R. E. Kroon, A. Yousif, H. A. A. Seed Ahmed, H. C. Swart. Photoluminescence, thermoluminescence, and cathodoluminescence of optimized cubic Gd_2O_3:Bi phosphor powder. *Journal of Vacuum Science & Technology A* 38 (2020) 063207. doi: 10.1116/6.0000567

Chapter nine

Alloying Bi doped La_2O_3 and Ga_2O_3 for stable phosphor powder and pulsed laser deposited thin films

9.1. Introduction

Bismuth (Bi) ions doped in phosphor materials display interesting and variable luminescence characteristics because of the strong interaction of Bi ions with the surrounding host lattice [1]. For any phosphor to be used in an application, its stability under a particular environment is an important consideration. In our previous work, the host lanthanum oxide (La_2O_3) was found to be unstable and converted to lanthanum hydroxide ($La(OH)_3$) after a few days when exposed to the air [2], making it unsuitable for photoluminescence (PL) applications unless the phosphor is protected from the atmosphere. With the goal to obtain similar luminescence as produced from La_2O_3 doped with Bi, but to improve the stability of the phosphor, we have previously alloyed La_2O_3 with the rare-earth oxide Y_2O_3. In the present work, we chose to investigate alloying with Ga_2O_3. Gallium (Ga) is a post-transition metal like Bi, but has a much smaller ionic radius. For VI coordination the ionic radius of Bi^{3+} is 0.103 nm and that for La^{3+} is 0.1032 nm. In comparison, Y^{3+} ions have radii of 0.090 nm, while for Ga^{3+} the ionic radius is only 0.062 nm [3]. Although Ga^{3+} is a trivalent ion like the others mentioned and therefore forms compounds with the same stoichiometry (e.g. Ga_2O_3), its electron configuration is $[Ar]3d^{10}$ which is optically inert and this makes it suitable for a phosphor host ion. This is in contrast to Bi^{3+} ions with configuration $[Xe]4f^{14}5d^{10}6s^2$, where the s^2 electrons make them optically active. Based on the relative sizes of the ionic radii, when Bi^{3+} is doped in $(La,Ga)_2O_3$ material the Bi^{3+} ions are expected to substitute La^{3+} ions rather than Ga^{3+} ions.

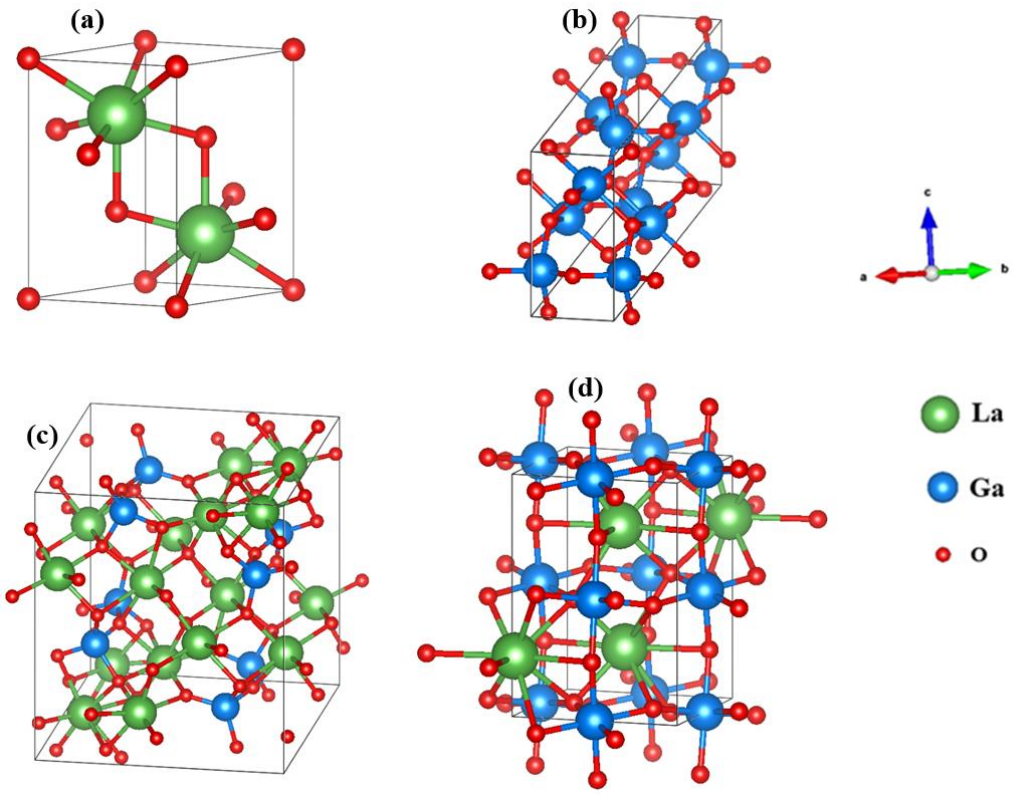

Figure 9.1: The unit cells of (a) La_2O_3 (b) β-Ga_2O_3 (COD ID: 2004987) (c) $La_4Ga_2O_9$ (COD ID: 2104432) and (d) $LaGaO_3$ (COD ID: 1526869). All crystal structures were modelled with Vesta software [4] using CIF files from the Crystallography Open Database [5] except for La_2O_3 [6].

La_2O_3 belongs to the trigonal crystal system with space group $P\bar{3}m1$ (No. 164) [7] and its unit cell is presented in Figure 9.1(a). Each La^{3+} ion has equivalent surroundings, with C_{3v} site symmetry and coordination number seven (three O^{2-} ions being slightly further than the other four) [8]. Ga_2O_3 has several various polymorphs, namely α, β, γ, δ and ε [9]. β-Ga_2O_3 is the most stable form under normal conditions and has monoclinic crystal structure with space group $C2/m$. The unit cell of β-Ga_2O_3 shown in Figure 9.1(b) consists of two inequivalent Ga sites (with tetrahedral and octahedral coordination) and three inequivalent O sites (two of which are three-fold coordinated and the other four-fold coordinated) [10]. The pseudobinary phase diagram for $La_{2-y}Ga_yO_3$ is given by Zinkevitch *et al.* [11] and contains two compounds with specific mixed cation stoichiometry, namely $La_4Ga_2O_9$ (y = 2/3) and $LaGaO_3$ (y = 1). The monoclinic crystal structure of $La_4Ga_2O_9$ with $P2_1/c$ space group [12, 13] is shown Figure 8.1(c), while $LaGaO_3$ has an orthorhombic crystal structure with *Pbnm* space group [14] as presented in Figure 9.1(d). This is a distorted perovskite

structure consisting of a three-dimensional sub-lattice of corner bonded GaO_6 octahedra and the La^{3+} ions are each bonded to twelve oxygen atoms [15]. Although it is common for minerals with the formula ABO_3 to take the perovskite structure, this is not always the case, e.g. when the cations are both large. This limits the known interlanthanide perovskites to only eleven known cases [16] of which six involve La paired with the smallest rare earths, namely Lu, Yb, Tm, Er, Ho and Y. Therefore $LaYO_3$ is on the limit of materials crystalizing in the perovskite structure. However, due to the small size of the Ga^{3+} ion, the compound $LaGaO_3$ is among the typical materials that exhibit the perovskite structure and this provides impetus to studying the $(La,Ga)_2O_3$ system in addition to our earlier effort with $(La,Y)_2O_3$.

$LaGaO_3$ has previously been assessed as a host material doped with various rare earth ions such as Yb^{3+} and Er^{3+} [15], Sm^{3+} and Tb^{3+} [17] to study the luminescence properties, colour rendering properties and superior stability under an electron beam. Bi^{3+} doping of $LaGaO_3$ was reported by Jacquier *et al.* [18] almost half a century ago, while Srivastava [19] reported the thermal quenching of Bi^{3+} luminescence in $LaGaO_3$ and explained the energy transfer mechanism between Bi^{3+} ions to host lattice-quenching centres. In this work La_2O_3 alloyed with varying proportions of Ga_2O_3 was investigated to assess its stability against degradation to a hydroxide by using X-ray diffraction. From this investigation it was decided to alloy La_2O_3 and Ga_2O_3 in equal proportions to form $LaGaO_3$ and study the luminescent properties of this material doped with Bi in powder and thin film form. Pulsed laser deposition (PLD) can transfer the material without changing its stoichiometry from the ablation target to a growing film [20]. $LaGaO_3$:Bi films were deposited on a Si substrate in vacuum and different oxygen atmospheres at a substrate temperature of 300 °C for 20 min. The luminescence properties, morphology and structure were assessed.

9.2. Experimental

9.2.1. Powder preparation

Powder samples were prepared via the citric acid sol-gel combustion synthesis. To prepare the pure host, $LaGaO_3$, 2.5980 g of lanthanum nitrate ($La(NO_3)_3 \cdot 6H_2O$, 99.999%), 2.6085 g of gallium nitrate ($Ga(NO_3)_3 \cdot H_2O$, 99.999%), 2.5216 g of citric acid monohydrate ($C_6H_8O_7 \cdot H_2O$, 99.5%) and 40 ml of distilled water were mixed in a glass beaker. The citric acid monohydrate functioned as

a fuel for combustion and the molar ratio of metal ions to citric acid monohydrate was 1:2. All chemicals were purchased from Sigma Aldrich. The reaction beaker was heated at 80 °C under vigorous stirring for 2 h, after which about 20 ml of gel remained. This was transferred to a porcelain crucible which was placed into a muffle furnace maintained at 250 °C for 30 min. The combustion reaction created white fumes and a white powder was formed as the product. This powder was annealed for 2 h in air at different temperatures between 900 °C and 1400 °C prior to characterisation. The proportion of La and Ga could easily be varied by changing the amounts of the precursor nitrates used. Since the Bi dopant was expected to be incorporated by replacement of La, for doped samples an appropriate amount of $La(NO_3)_3 \cdot 6H_2O$ was substituted by an equal amount of bismuth nitrate ($Bi(NO_3)_3.5H_2O$, 99.999%).

9.2.2. Thin film preparation

The thin films were created from $La_{1-x}GaO_3:Bi_{x=0.03}$ powder which was found to be the optimum doping concentration for maximum luminescence intensity. To make a target for laser ablation, 7 g of this powder phosphor was pressed without binders into a pellet ~1.5 cm in diameter by using a hydraulic press at a pressure of 75 tons for 2 h and then annealed at 900 °C for 8 h. Si (100) substrates were cleaned in an ultrasonic bath using acetone, ethanol and finally distilled water consecutively for 15 min each. The cleaned substrates were blown dry with nitrogen gas and loaded in the PLD chamber at a distance 4.5 cm from the target. The PLD chamber was evacuated to a base pressure of $5x10^{-5}$ mbar (i.e. 0.04 mTorr). The fourth harmonic of a Nd:YAG laser was used to ablate the target using 266 nm wavelength pulses of duration ~6 ns each having energy of 40 mJ at a rate of 30 Hz. From the estimated size of the focussed laser spot on the target, the energy density was 1.7 J/cm^2. The deposition time was 20 min and the Si substrate temperature was fixed at 300 °C. Samples prepared in this way are described as having been produced in vacuum. To prepare other thin films in an oxygen environment, after evacuation of the PLD chamber O_2 gas was back-filled to a pressure of either 10, 20 or 40 mTorr before ablation began. A background atmosphere of oxygen gas was chosen rather than a non-reactive gas since the material being ablated is already an oxide.

9.2.3. Characterization

The phase composition was characterized by X-ray diffraction (XRD) measurements using a Bruker D8 Advance diffractometer. The Cu Kα X-ray source was operated at an accelerating

voltage of 40 kV and a current of 40 mA and emitted characteristic X-rays with wavelength 0.154 nm. XRD patterns were measured with a step of 0.02° between $2\theta = 10°$ and 80° for the powders and $2\theta = 20°$ and 60° for the thin films. A JSM-7800F scanning electron microscope (SEM) was used to analyse the particle morphology. Inside the SEM the chemical composition was determined by energy dispersive X-ray spectroscopy (EDS) using an X-Max^{N}80 detector from Oxford Instruments. Diffuse reflectance spectra were recorded using a Lambda 950 UV-vis spectrophotometer from PerkinElmer with a spectralon integrating sphere accessory. The photoluminescence (PL) properties of the powders were measured at room temperature using an FS5 spectrometer from Edinburgh Instruments, while the PL spectra for the thin films were measured with a He-Cd laser PL system with a 325 nm excitation wavelength. The cathodoluminescence (CL) was measured using a Gatan MonoCL4 accessory fitted to SEM in a vacuum of ~10^{-5} Torr and electron energy of 5 keV.

9.3. Results and discussion

9.3.1. Structure and stability of La_2O_3 alloyed with Ga_2O_3

Figure 9.2(a) shows XRD patterns of freshly prepared powders with different proportions of La and Ga, i.e. $La_{2-y}Ga_yO_3$, annealed at 1000 °C, together with La_2O_3 and data from JCPDS card #371433 for $La_4Ga_2O_9$ on the bottom and data from JCPDS card #411103 for β-Ga_2O_3 and #241102 for $LaGaO_3$ on the top. With an increase of the Ga concentrations from y = 0.2 up to 0.3, mixed phases of La_2O_3 and $La_4Ga_2O_9$ were observed when compared the standards. For y = 0.4 and 0.53, the material exhibited the crystal structure of $La_4Ga_2O_9$, which are lower values than the theoretical value of y = 2/3 corresponding to this phase. With an increasing of the concentrations of Ga from y = 0.64 up to 0.88, mixed phases of the $La_4Ga_2O_9$ and the orthorhombic perovskite $LaGaO_3$ were observed. When y = 0.94 and 1, the material exhibited the crystal structure of $LaGaO_3$.

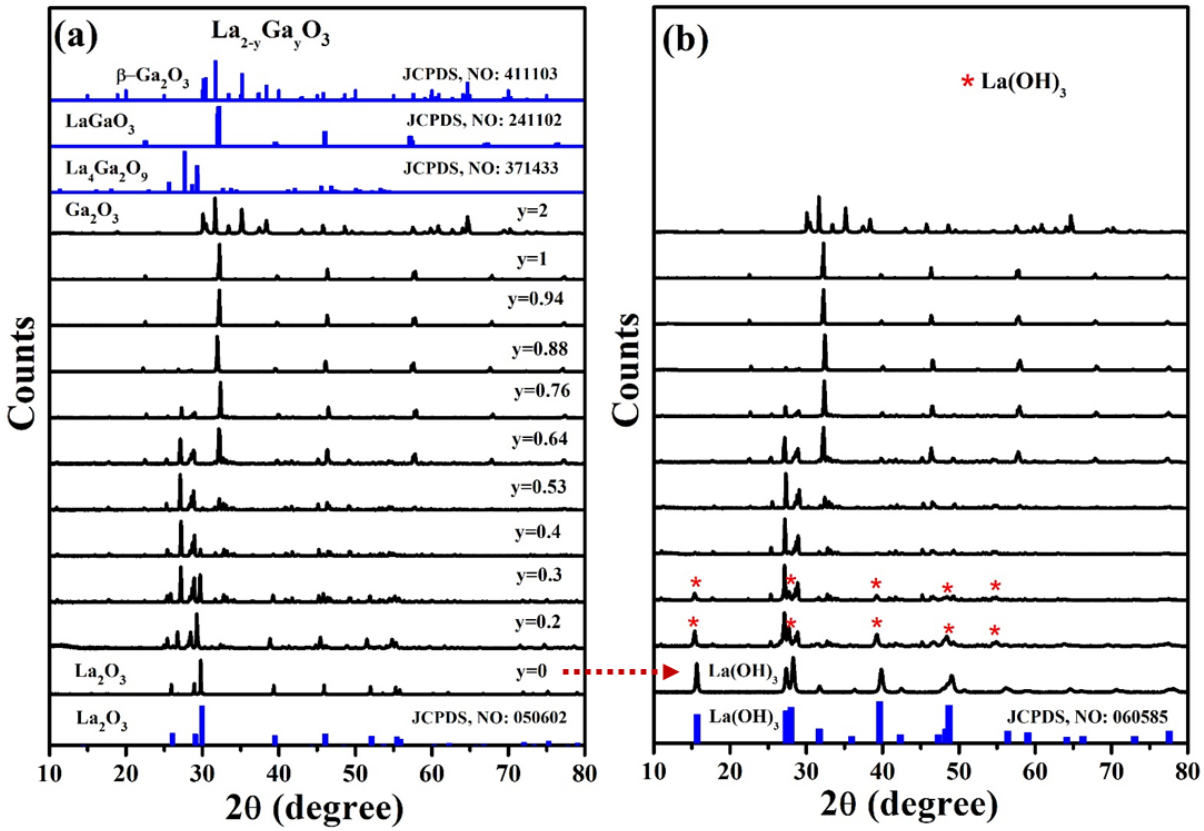

Figure 9.2: XRD patterns of $La_{2-y}Ga_yO_3$ phosphor powders doped with different proportions of La and Ga. (a) freshly prepared samples, with the standard for La_2O_3 below and the standards for $La_4Ga_2O_9$, $LaGaO_3$ and β-Ga_2O_3 above. (b) After being exposed to the atmosphere for 4 months. The standard for $La(OH)_3$ is shown at the bottom.

Figure 9.2(b) presents the XRD patterns of the samples exposed to the atmosphere for 4 months. By comparing the patterns with the standard for $La(OH)_3$ (JCPDS card #05-0685), mixed phases of the oxide and hydroxide were observed when the amount of Ga was y = 0.2 or 0.3. At higher concentrations of Ga from y = 0.4 up to 1, the powders were found to be stable under atmosphere.

9.3.2. Characterization of $LaGaO_3$:Bi phosphor powders

Figure 9.3(a) displays the XRD patterns of $La_{1-x}GaO_3:Bi_x$ powders doped with various Bi concentrations annealed at 1200 °C, together with information from JCPDS card #812304 for $LaGaO_3$. The structure corresponds to that of the orthorhombic $LaGaO_3$ (distorted perovskite)

discussed earlier and no additional diffraction peaks were detected after Bi doping. Also, no shifting of the peak positions was observed when the Bi concentration increased, confirming that the Bi^{3+} ions substituted for La^{3+} ions of very similar ionic radius. Figure 9.3(b) shows the XRD patterns of $La_{1-x}GaO_3:Bi_{x=0.003}$ annealed at different temperatures between 800 °C and 1400 °C. Annealing in the lower temperature range from 800 °C up to 900 °C produced mixed phases of La_2O_3 and β-Ga_2O_3, while annealing at higher temperatures from 1000 °C up to 1400 °C formed a single $LaGaO_3$ phase material.

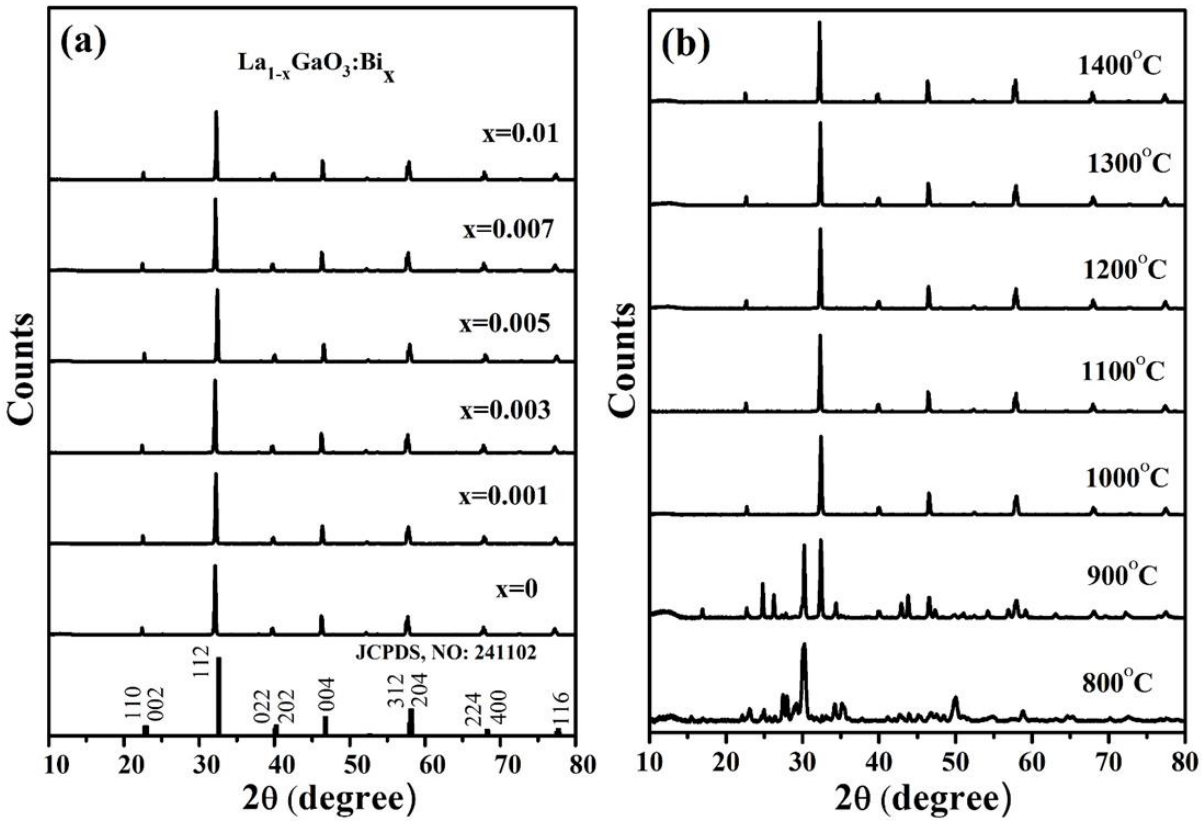

Figure 9.3: XRD patterns of (a) $La_{1-x}GaO_3:Bi_x$ powders phosphors doped with different Bi concentrations annealed at 1200 °C, together with information from JCPDS card #812304 for $LaGaO_3$. (b) $La_{1-x}GaO_3:Bi_{x=0.003}$ annealed at different temperatures.

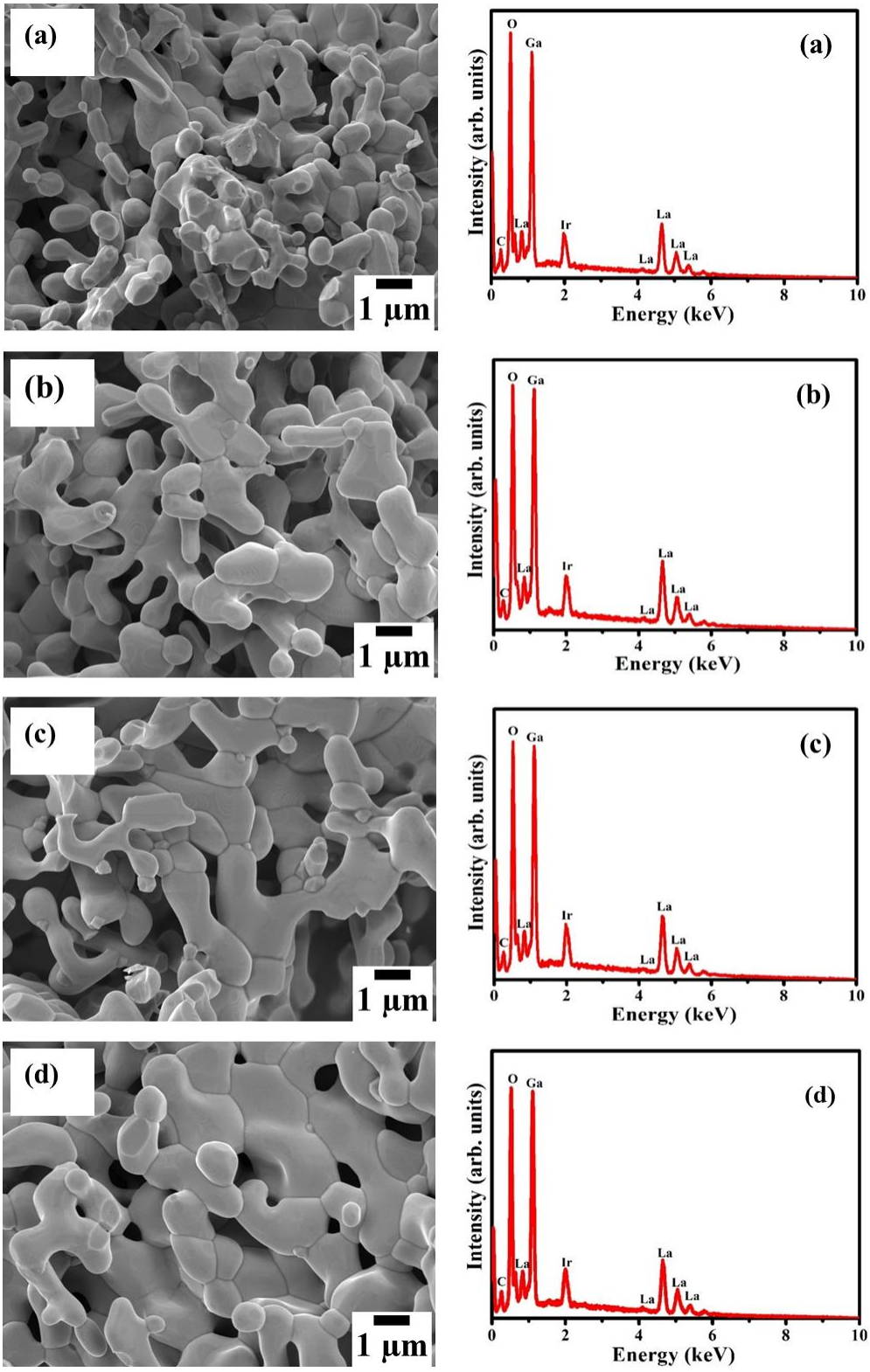

Figure 9.4: SEM images (left) and EDS spectra (right) for $La_{1-x}GaO_3:Bi_x$ phosphor powders annealed at 1200 °C (a) x = 0, (b) x = 0.003, (c) x = 0.005 and (d) x = 0.01.

Figure 9.4 presents the SEM images and EDS spectra of the $La_{1-x}GaO_3:Bi_x$ phosphor powders doped with different Bi concentrations, annealed at 1200 °C. The shape of the undoped particles was similar to that of the doped samples. The grain size increased when the Bi was inserted in the host structure. The addition of Bi has been reported to lower the activation energy for grain growth of LiZnTi ferrite ceramics, which therefore enhances grain growth [21]. The EDS spectrum of the $LaGaO_3$ pure host sample shows the peaks corresponding to La, Ga, and O, together with a very small quantity of C that probably originated from the citric acid precursor used in the sol-gel combustion synthesis, or possibly could result from the carbon tape that was used to mount the samples. The presence of Ir on the samples is due to coating with this metal to improve conductivity and prevent charging of the sample in the SEM. The EDS spectra of the $La_{1-x}GaO_3:Bi_x$ (x = 0.003, 0.005 and 0.01) samples were similar to the host sample and the Bi was not detected because of its low concentration. No other elements were detected in the samples, indicating that the $La_{1-x}GaO_3$:Bi phosphors were pure.

Figure 9.5 displays the SEM images of the $La_{1-x}GaO_3:Bi_{x=0.005}$ phosphor powders after being annealed at different temperatures. Figure 9.5(a) shows the sample annealed at 900 °C for which the small particles aggregated and had irregular shapes. When the annealing temperature was increased to 1100 °C, the particles were agglomerated to each other and nearly rounded. Annealing at a higher temperatures of 1200 °C and 1300 °C, shown in Figure 9.5(c, d), created a homogeneous microstructure with large elongated particles. Figure 9.5(e) presents the sample annealed at the highest temperature of 1400 °C, exhibiting a larger and rounder shape due to extensive grain growth.

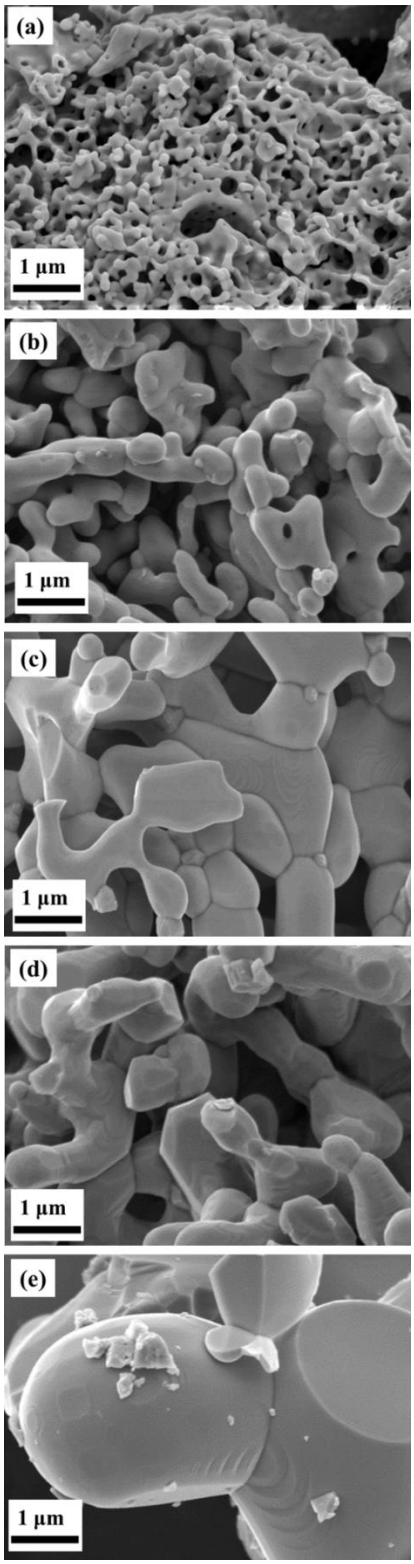

Figure 9.5: SEM images of the $La_{1-x}GaO_3:Bi_{x=0.005}$ phosphor powders annealed at different temperatures (a) 900 °C, (b) 1100 °C, (c) 1200 °C, (d) 1300 °C, and (e) 1400 °C.

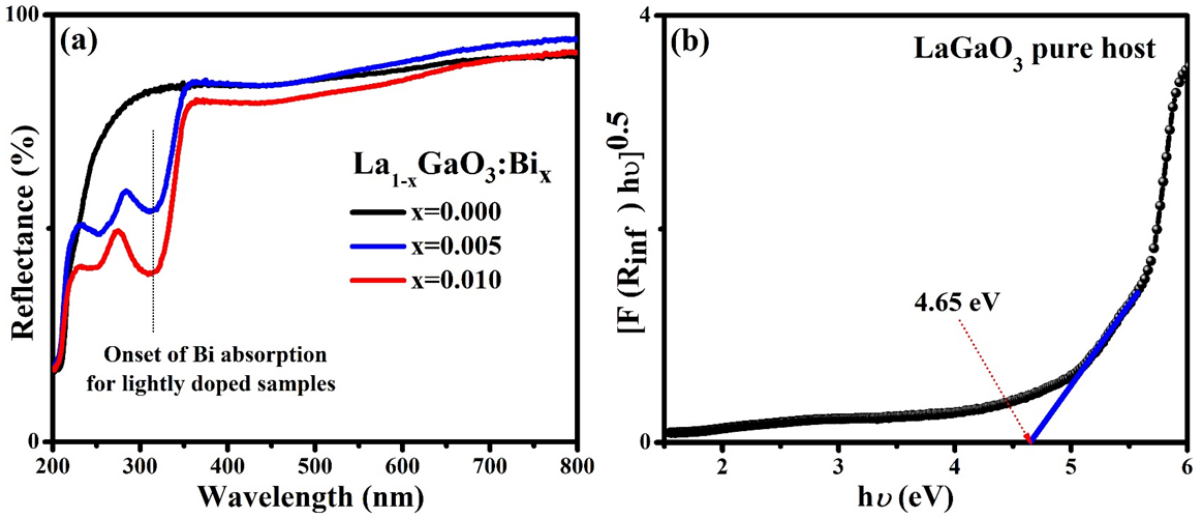

Figure 9.6: (a) Diffuse reflectance spectra of $LaGaO_3$ pure host and doped samples annealed at 1200 °C. (b) A Tauc plot to obtain the indirect optical band gap of undoped $LaGaO_3$.

Figure 9.6(a) presents the diffuse reflectance spectra of the $LaGaO_3$ pure host and $La_{1-x}GaO_3:Bi_x$ phosphor powders doped with different Bi concentrations, annealed at 1200 °C. The reflectance spectra of the doped powder samples showed three absorption bands centered at around 210 nm, 250 nm and 310 nm. The absorption band centered at 210 nm was also observed for the undoped sample and was attributed to absorption above the band gap. The absorption bands centered at 250 nm and 310 nm were only present in the doped samples and was therefore attributed to absorption by Bi^{3+} ions. To estimate the bandgap of the undoped host material, the Kubelka-Munk formula $F(R_\infty) = \frac{(1-R_\infty)^2}{2R_\infty}$ was used to transform the diffuse reflectance data to values proportional to the absorption [22]. For an indirect band gap [23] material like $LaGaO_3$, plotting $[F(R_\infty)h\nu]^{1/2}$ against $h\nu$ can be used to obtain the optical band gap by fitting a linear region and extrapolating this to where it cuts the horizontal axis [24]. Such a plot is presented in Figure 9.6(b), from which the band gap was determined to be 4.65 eV. Preetam *et al.* [25] previously determined the band gap of the $LaGaO_3$ pure host to be 3.59 eV, although our results show that it is much larger. Bingcheng *et al* [23] determined the band gap of $LaGaO_3$ to be 4.48 eV, while Jian *et al*. estimated the optical band gap for $LaGaO_3$ to be 4.40 eV [26]. The differences in band gap values may be due to the different preparation methods which influence the particle size, morphology and defects.

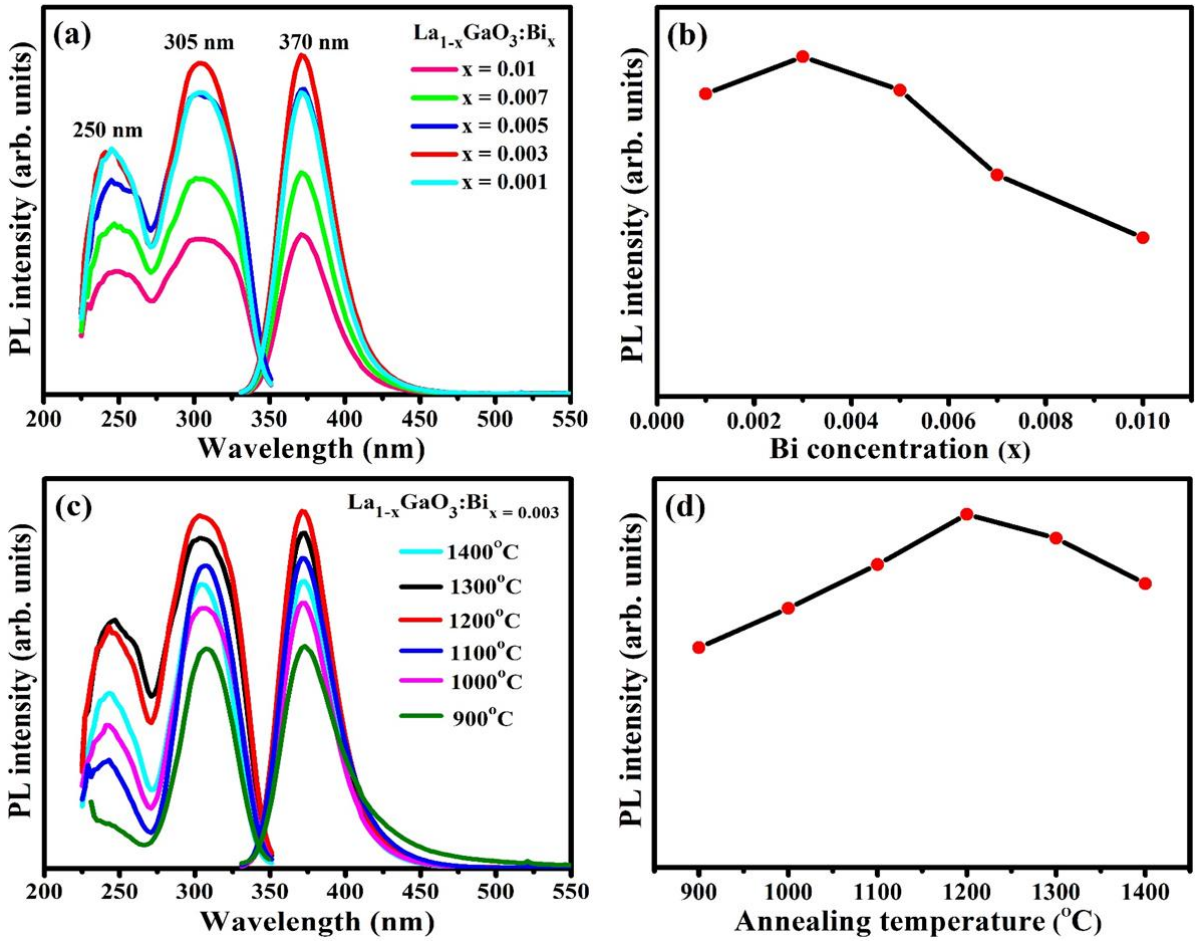

Figure 9.7: (a) Excitation and emission spectra of $La_{1-x}GaO_3:Bi_x$ doped with different Bi concentrations, annealed at 1200 °C. (b) Emission peak intensity as a function of Bi concentration. (c) Excitation and emission spectra of $La_{1-x}GaO_3:Bi_{x=0.003}$ annealed at different temperatures. (d) Emission peak intensity as a function of the annealing temperature.

Figure 9.7(a) presents the PL excitation and emission spectra of $La_{1-x}GaO_3:Bi_x$ doped with different Bi concentrations annealed at 1200 °C, while Figure 9.7(c) shows the PL spectra of $La_{1-x}GaO_3:Bi_{x=0.003}$ annealed at different temperatures. Figure 9.7(b) displays the PL emission intensity as a function of Bi doping concentration. The maximum emission occurred for x = 0.003. The PL emission intensity decreased above that concentration because of concentration quenching, which occurred because of migration of energy between the activators as a result of electric dipole or quadrupole interactions. Appreciable quenching may occur for low dopant concentrations from 0.001 to 0.01 mol% [27], indicating a strong interaction between the Bi^{3+} ions. Figure 9.7(d) shows the PL emission intensity as a function of annealing temperature, for annealing between 900 °C to

1400 °C. The intensity of emission increased with the increasing the heating temperature, reaching the maximum at a heating temperature 1200 °C and then decreased with a further increase in temperature. The emission intensity might be expected to increase as heating temperature increases because of improved the crystalline quality and removal of defects. Jafer *el al* [28] studied the effect of heating temperature on Y_2O_3 doped Bi phosphor powders and attributed the increase of the emission intensity with heating temperature up to a maximum value to segregation effects of the dopant to the particle surface, while the quenching of the luminescence at higher heating temperatures was due to evaporation loss of the dopant from the surface of the sample. The optimum annealing temperature found for $La_{1-x}GaO_3:Bi_x$ phosphor powders in this work (1200 °C) is the same as that reported for $La_{2-x}O_3:Bi_x$ [29].

Two excitation bands have been observed which are centred at 250 nm and 305 nm. The longer wavelength (lower energy) excitation band is attributed to the $^1S_0 \rightarrow {}^3P_1$ transitions, while the excitation band at 250 nm (4.96 eV) may be due to the $^1S_0 \rightarrow {}^1P_1$ transition (C band) or metal-to-metal charge transfer (MMCT) between the Bi^{3+} ions at the La^{3+} cation of the host. Jacquier *et al.* [18] found similar excitation peaks for $LaGaO_3$:Bi and attributed the higher energy excitation peak to the transition from $^1S_0$ to $^1P_1$ or to mixture of both transitions $^1S_0 \rightarrow {}^1P_1$ and $^1S_0 \rightarrow {}^3P_2$. Satya Kamal *et al.* [30] studied the luminescence of $LaGaO_3:Bi^{3+},Cr^{3+}$ and attributed the higher energy excitation band to the charge transfer transition from O^{2-} to Ga^{3+}. In our previous work on La_2O_3:Bi [29] the excitation band at 250 nm was attributed to the metal-to-metal charge transfer (MMCT) transition between the Bi^{3+} ions at the La^{3+} cation. To better understand the origin of the excitation peak at 250 nm (4.96 eV), Wang *et al.* [31] found a relationship between the energies of the A band ($^1S_0 \rightarrow {}^3P_1$) and C band ($^1S_0 \rightarrow {}^1P_1$), namely $E_C = 3.236 + 2.290(E_A - 2.972)^{0.856}$ for values in eV. If the A band excitation transition for $LaGaO_3$:Bi occurs at 305 nm (4.06 eV), then the predicted C band energy would be 5.69 eV (218 nm). Alternatively, the MMCT energy can be determined according to $E_{MMCT} = 55\,000 - 45\,500\chi/d$ (in cm^{-1}) [32], where χ is the electronegativity of the host cations and d is the distance between the Bi^{3+} and host cations (in Å). By using $\chi = 1.28$ and $d = 3.87$ from [32], The MMCT excitation for $LaGaO_3$: Bi can be expected at 39951 cm^{-1} (250 nm). This value matches well with the higher energy excitation band measured in this work, which is therefore attributed to the MMCT band rather than to the C band or the charge transfer transition from O^{2-} to Ga^{3+}. The single broad band of ultraviolet emission which is centred at 370 nm can be

attributed to transitions from the $^3P_1$ excited state back to the $^1S_0$ ground state. For comparison, Samuel *et al.* [33] studied the PL of $LaGaO_3:Bi^{3+},Tb^{3+}$ and attributed the excitation peak at 309 nm to $^1S_0 \rightarrow {}^3P_1$ and the emission peak at 372 nm to the transition $^3P_1 \rightarrow {}^1S_0$ of Bi^{3+} ions.

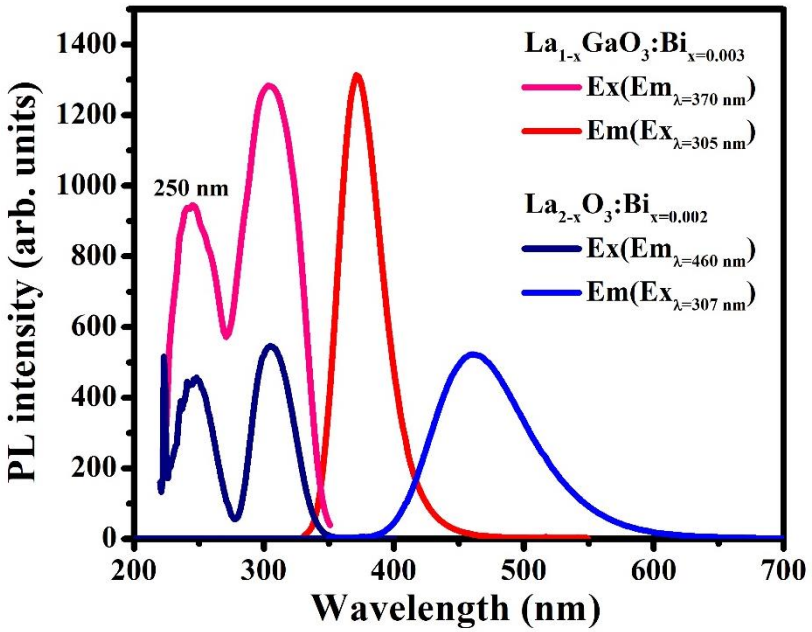

Figure 9.8: PL excitation and emission spectra of $La_{1-x}GaO:Bi_{x=0.003}$ and $La_{2-x}O_3:Bi_{x=0.002}$, annealed at 1200 °C.

For comparison, La_2O_3:Bi has a single broad band of blue emission centred at 462 nm which is attributed to $^3P_1 \rightarrow {}^1S_0$ transitions of the Bi^{3+} ions [29]. Figure 9.8 compares the PL spectra of $La_{1-x}GaO:Bi_{x=0.003}$ powder phosphor directly with $La_{2-x}O_3:Bi_{x=0.002}$, both annealed at 1200 °C. Both compounds have almost similar excitation bands centred at 250 nm and 305 nm. Although the PL emission intensity of $LaGaO_3$:Bi was both more intense as well as stable when exposed to the atmosphere for several months, compared to the PL of La_2O_3:Bi which degrades over several days, the emission spectrum of the $La_{1-x}GaO:Bi_{x=0.003}$ was narrower and shifted compared the corresponding emission spectrum of $La_{2-x}O_3:Bi_{x=0.002}$. The blue PL emission band of $La_{2-x}O_3:Bi_{x=0.002}$ is centred at 460 nm, at significantly longer wavelength in comparison to the PL emission of $La_{1-x}GaO:Bi_{x=0.003}$ which is centred at 370 nm in the UV range.

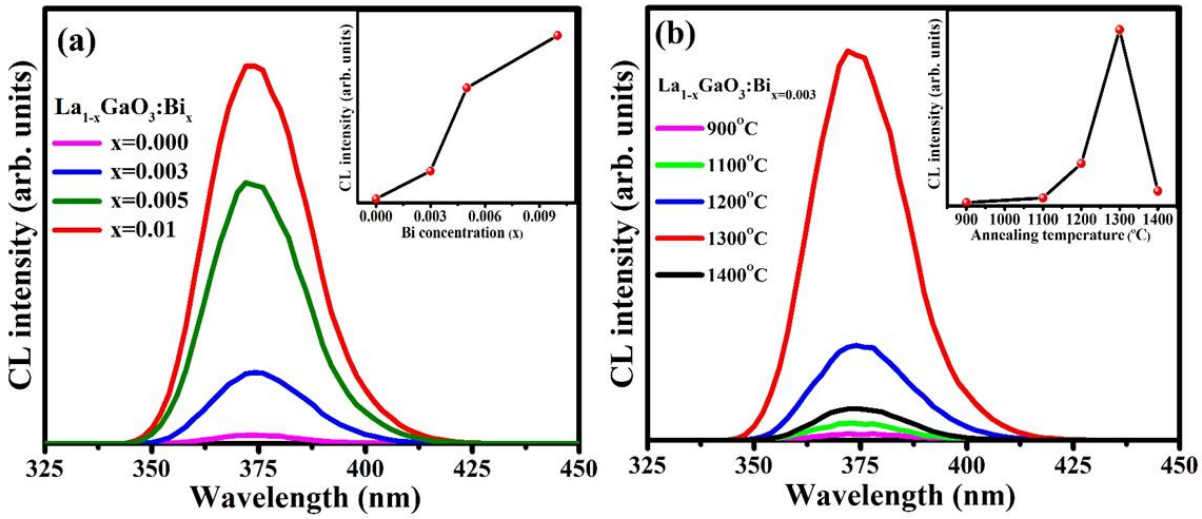

Figure 9.9: (a) CL emission spectra of $La_{1-x}GaO_3:Bi_x$ doped with different Bi concentrations, annealed at 1200 °C. The inset shows the maximum CL intensity as a function of Bi^{3+} concentration, (b) CL emission spectra of $La_{1-x}GaO_3:Bi_{x=0.003}$ annealed at different temperatures. The inset shows the maximum CL intensity as a function of annealing temperature.

Figure 9.9 presents the CL emission spectra of the $La_{1-x}GaO_3:Bi_x$ samples measured with the Gatan system connected to the SEM for an electron energy of 5 keV. The CL emission is centred at 370 nm, similar to the PL emission. Figure 9.9(a) shows the CL emission spectra of $La_{1-x}GaO_3:Bi_x$ doped with different Bi concentrations, annealed at 1200 °C. The inset shows the maximum CL intensity as a function of Bi^{3+} concentration. The CL intensity increased with increasing Bi concentration and the sample doped with maximum Bi concentration used (x = 0.01) had the highest CL intensity. Figure 9.9(b) presents the CL emission spectra of $La_{1-x}GaO_3:Bi_{x=0.003}$ annealed at different temperatures between 900 °C and 1400 °C. The CL intensity initially increased up to the sample annealed at 1300 °C and then decreased, as shown by the inset of Figure 9.9(b). The optimum synthesis parameters for maximum CL emission therefore do not match those found for PL (x = 0.003 and 1200 °C).

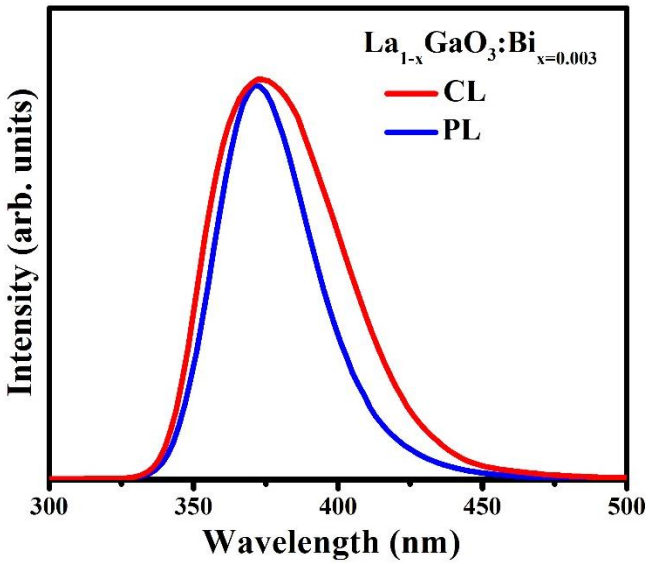

Figure 9.10: Normalized comparison of the PL and CL emission spectra of $La_{1-x}GaO_3:Bi_{x=0.003}$.

Figure 9.10 displays the CL and PL emission intensities of the $La_{1-x}GaO_3:Bi_x$ phosphor powders. The PL emission was excited by 305 nm, while CL emission was excited with an electron beam of 5 keV energy. The PL and CL emission spectra have been normalized because the intensities measured from the CL and PL systems cannot be directly compared. The CL emission spectrum was significantly broader than the PL emission spectrum. The full width at half-maximum (FWHM) of the PL emission band was 43 nm, while for CL emission band it was found to be 53 nm. There is small shift in the wavelength position of the peak maxima between the PL and CL from 370 nm to 374 nm. These differences can be attributed to the large energy difference of the incident photons compared to the electrons and hence the different mechanisms for the excitation.

9.3.3. $LaGaO_3$:Bi phosphor thin films

The $La_{1-x}GaO_3:Bi_{x=0.003}$ annealed at 1200 °C powder was used to create a target for PLD from which thin films were grown as already explained in the experimental details. Figure 9.11 shows the XRD patterns for the $La_{1-x}GaO_3:Bi_{x=0.003}$ thin films on Si substrates deposited in vacuum and different O_2 gas pressures, together with the pattern for the powder from which the PLD target was produced. The films all had the same crystal structure as the powder, indicating good transfer of stoichiometry from the target to the films and no preferential orientation of growth on the substrate.

The broad peak centered at around 29° corresponding to amorphous SiO_2 which might have come from the heated Si substrate and O_2 background gas [34, 35].

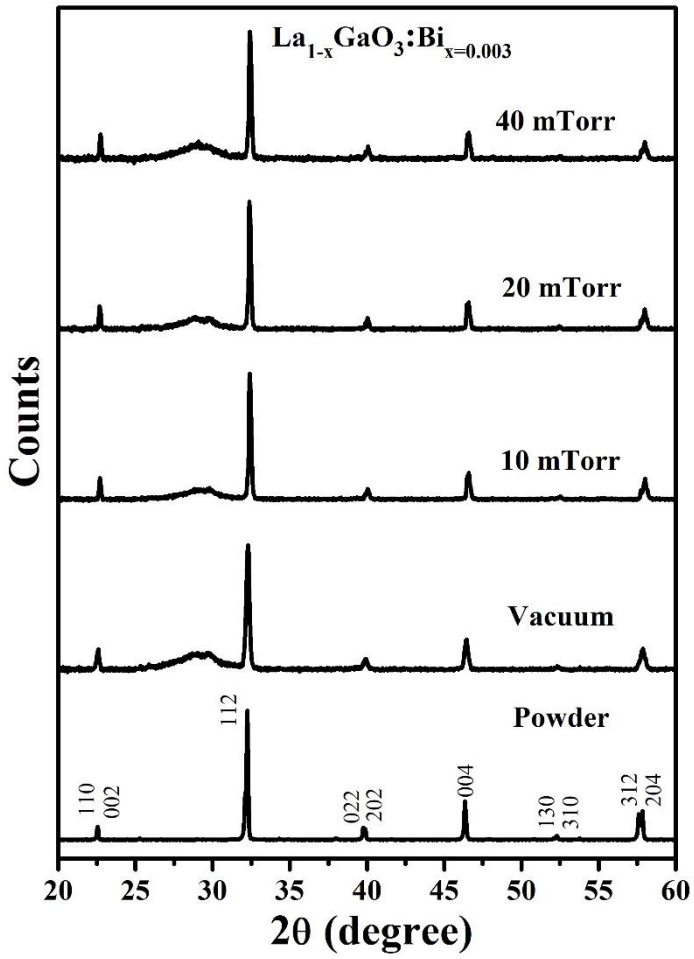

Figure 9.11: XRD patterns of $La_{1-x}GaO_3:Bi_{x=0.003}$ thin films deposited in vacuum and for various O_2 gas pressures.

Figure 9.12 shows the plan-view and cross-sectional SEM images and EDS spectra of the $La_{1-x}GaO_3:Bi_{x=0.003}$ phosphor thin films. Particles of different sizes with spherical shapes were observed. The cross-sectional images of the thin films were similar and clearly reveal the presence of spherical particles in the morphology. The cross-section of the film deposited in vacuum showed that the thickness of the film was not uniform, but ~1.2 μm at the maximum points.

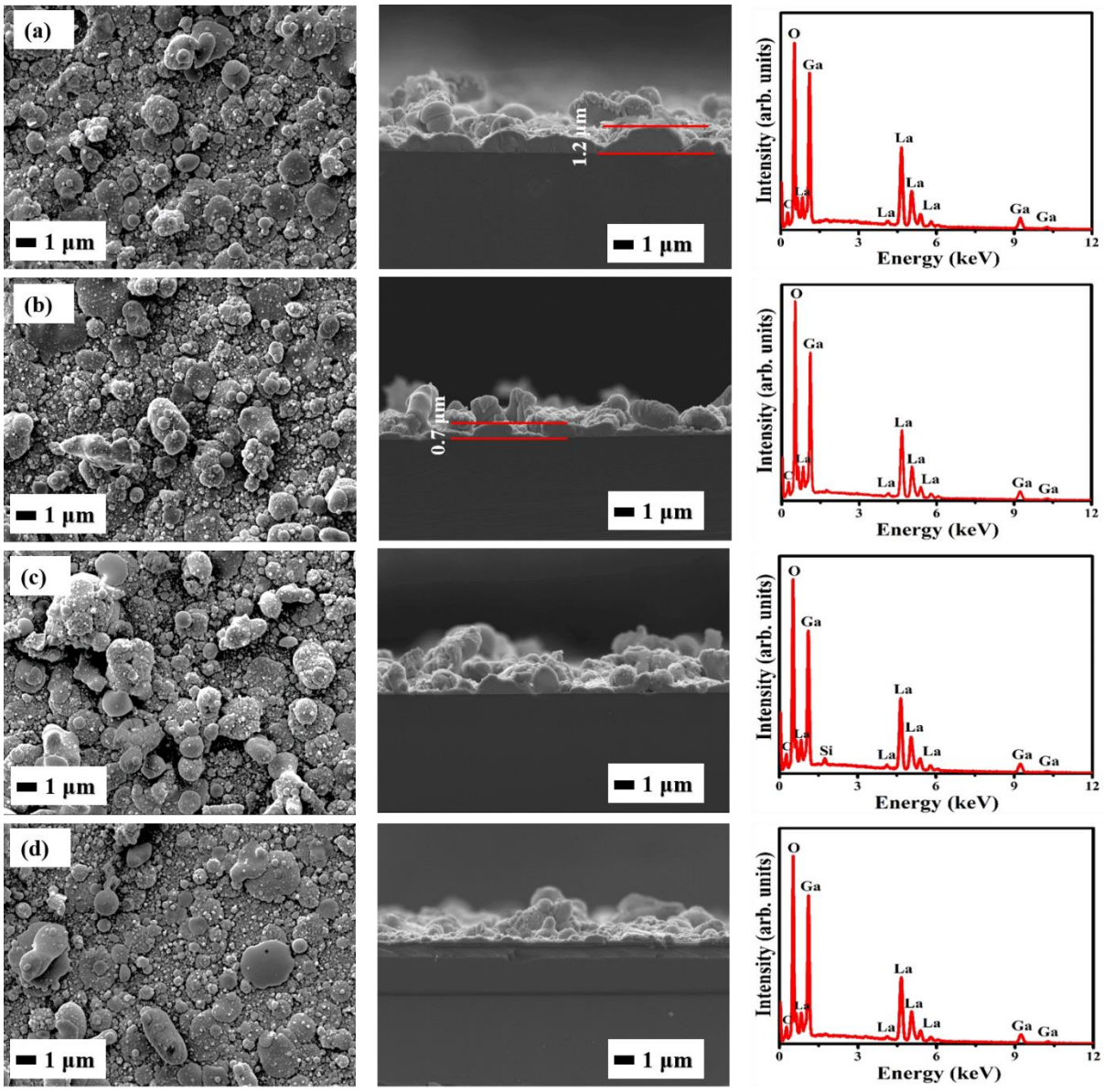

Figure 9.12: The plan-view and cross-sectional SEM images as well as EDS spectra of $La_{1-x}GaO_3:Bi_{x=003}$ thin films prepared (a) in vacuum and in O_2 pressures of (b) 10 (c) 20 (d) 40 mTorr.

The corresponding thickness of the samples fabricated in O_2 gas decreased to ~0.7 µm or less and appear to become less for increasing O_2 pressure. The EDS spectra of the films are similar to the powders, indicating good transfer of stoiciometry from the target to thin film during PLD, except the Ga peak which is lower compared to the O peak in all cases. This indicates some loss of Ga during PLD, possibly because Ga has a lower boiling point than La and does not adhere to the

substrate equally well. The presence of Si on the sample shown in Figure 13 (c) is due to the Si substrate.

Figure 9.13(a) shows the PL emission spectra of $La_{1-x}GaO_3:Bi_{x=0.003}$ thin films measured with a 325 nm He-Cd laser. The film deposited in vacuum showed less intensity compared to those deposited in an oxygen atmosphere, for which the emission intensity decreased as the O_2 pressure increased. Figure 9.13(b) displays the CL emission spectra for the same samples measured with the Gatan system connected to the SEM for an electron energy of 5 keV. The form of the CL emission from the thin films was similar to that obtained earlier from the powder (Figure 9.10). Like for PL, the film deposited in vacuum showed less intensity compared to those deposited in oxygen atmosphere and, for the samples prepared in oxygen, the emission intensity decreased as the O_2 pressure was increased. All the thin film samples displayed a similar crystal structure as well as PL and CL emission spectra as the powder samples.

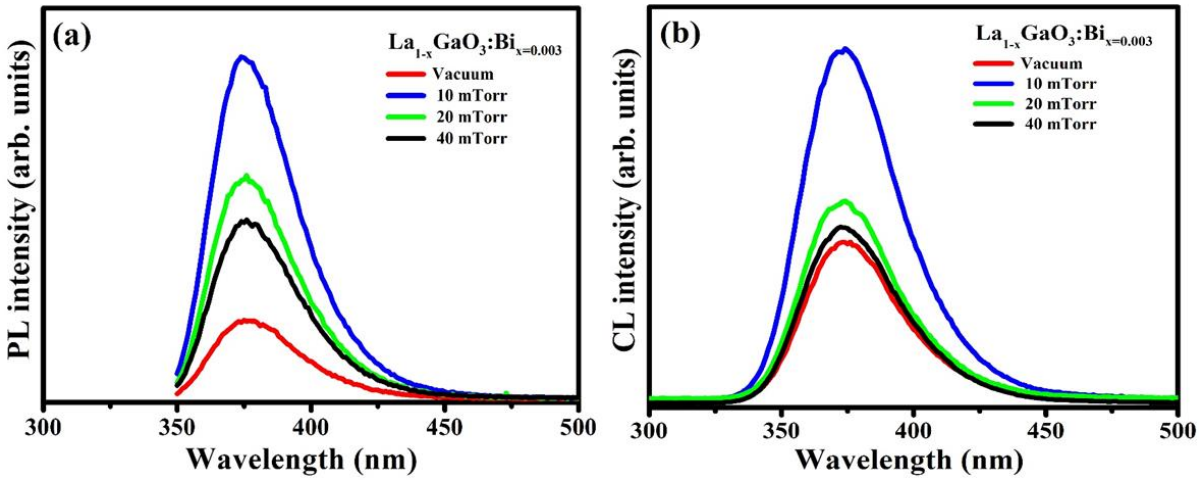

Figure 9.13: (a) PL and (b) CL emission spectra of $La_{1-x}GaO_3:Bi_{x=0.003}$ thin films.

9.4. Conclusion

Bi doped $LaGaO_3$ was successfully synthesized by the citric acid sol-gel combustion synthesis. XRD data confirmed that the structure of $LaGaO_3$ belonged to the orthorhombic crystal structure. SEM images showed that the grain size increased with increasing annealing temperature. The

diffuse reflectance spectra for the doped sample showed three absorption bands centered at around 210 nm, 250 nm and 310 nm. The absorption band centered at 210 nm was also observed for the undoped sample and was attributed to absorption above the band gap. The absorption bands centered at 250 nm and 310 nm were only present in the doped samples and was therefore attributed to absorption by Bi^{3+} ions. From reflectance data of the pure host material the band gap of $LaGaO_3$ was found to be 4.65 eV. A broad UV emission centred at 370 nm was observed when excited at 305 nm, which was attributed to the $^3P_1 \rightarrow {}^1S_0$ transition of Bi^{3+} ions. The emission intensity was measured as a function of Bi doping concentration, with the maximum occurring for x = 0.003. The shift in the wavelength position of the peak maxima between the PL and CL from 370 nm to 374 nm was attributed to the different mechanisms for the excitation. All thin film samples had the same crystal structure as the powder. The cross-section of the film deposited in vacuum showed that the thickness of the film was not uniform, but ~1.2 μm at the maximum points. The corresponding thickness of the films fabricated in O_2 gas decreased to ~0.7 μm or less and appeared to become less for increasing O_2 pressure. The PL and CL emission spectra of the thin films samples were similar to those obtained from the powder. The film deposited in vacuum showed less intensity compared to those deposited in an O_2 atmosphere, for which the emission intensity decreased as the pressure increased.

9.5. References

1. W.A.I. Tabaza, H.C. Swart, R.E. Kroon. Optical properties of Bi and energy transfer from Bi to Tb in $MgAl_2O_4$ phosphor. *Journal of Luminescence* 148 (2014) 192-197. doi: 10.1016/j.jlumin.2013.12.018
2. B.M. Jaffar, H.C. Swart, H.A.A. Seed Ahmed, A. Yousif, R.E. Kroon. Stability of Bi doped La_2O_3 powder phosphor and PMMA composites. *Journal of Physics and Chemistry of Solids* 131 (2019) 156-163. doi: 10.1016/j.jpcs.2019.04.004
3. R.D. Shannon. Revised Effective Ionic Radii and Systematic Studies of Interatomic Distances in Halides and Chaleogenides. *Acta Crystallographica Section A* 32 (1976) 751–767. doi: 10.1107/S0567739476001551

4. Koichi Momma, Fujio Izumi. VESTA 3 for Three-Dimensional Visualization of Crystal, Volumetric and Morphology Data. *Journal of Applied Crystallography* 44 (2011)1272–1276. doi: 10.1107/S0021889811038970
5. A. Vaitkus, A. Merkys and S. Gražulis. Validation of the Crystallography Open Database using the Crystallographic Information Framework. *Journal of Applied Crystallography* 54 (2021) 661-672. doi: 10.1107/S1600576720016532
6. K. Persson. Materials Data on La_2O_3 (SG:164) by Materials Project. (2014). doi: 10.17188/1194889
7. M. Méndez, J.J. Carvajal, Y. Cesteros, M. Aguiló, F. Díaz, A. Giguère, D. Drouin, E. Martínez-Ferrero, P. Salagre, P. Formentín, *et al.* Sol-Gel Pechini Synthesis and Optical Spectroscopy of Nanocrystalline La_2O_3 doped with Eu^{3+}. *Optical Materials* 32 (2010) 1686–1692. doi: 10.1016/j.optmat.2010.02.018
8. G. Chen, J.R. Peterson. Systematics of the Phase Behavior in Lanthanide Sesquioxides. *Journal of Alloys and Compounds* 186 (1992) 233–239. doi: 10.1016/0925-8388(92)90009-X
9. Feng Shi and Hengyang Qiao. Preparations, properties and applications of gallium oxide nanomaterials–A review. *Wiley Nano Select* (2021) 1-26. doi: 10.1002/nano.202100149
10. YidanWei, Xingji Li, JianqunYang, Chaoming Liu, JinyuZhao, Yong Liu & Shangli Dong. Interaction between hydrogen and gallium vacancies in β-Ga_2O_3. *Scientific Reports* 8 (2018) 10142. doi: 10.1038/s41598-018-28461-3
11. M. Zinkevich, S. Geupel, F. Aldinger, A. Durygin, S. K. Saxena, M. Yang, Z.-K. Liu. Phase diagram and thermodynamics of the La_2O_3–Ga_2O_3 system revisited. *Journal of Physics and Chemistry of Solids* 67 (2006) 1901–1907. doi: 10.1016/j.jpcs.2006.03.012
12. M. Kasunič, A. Meden, S. D. Škapin, D. Suvorov, A. Golobič. Order–disorder of oxygen anions and vacancies in solid solutions of La_2TiO_5 and $La_4Ga_2O_9$. *Acta Crystallographica B* 65 (2009) 558–566. doi: 10.1107/s010876810902833x
13. M. C. Martín-Sedeño, E. R. Losilla, L. León-Reina, S. Bruque, D. Marrero-López, P. Núñez, M. A. G. Aranda. Enhancement of Oxide Ion Conductivity in Cuspidine-Type Materials. *Chemistry of Materials* 16 (2004) 4960–4968. doi: 10.1021/cm0487472
14. W. Marti, P. Fischer, F. Altorfer, H. J. Scheel and M. Tadin. Crystal structures and phase transitions of orthorhombic and rhombohedral $RGaO_3$ (R=La, Pr, Nd) investigated by neutron

powder diffraction. *Journal of Physics: Condensed Matter* 6 (1994) 127–135. doi: 10.1088/0953-8984/6/1/014

15. R. Syed, A. Mallavarapu, V. Sudarsan, S. K. Agarwalla, D. K. Singh, V. Kain. Luminescence and structural properties of ytterbium and erbium co-doped $LaGaO_3$ nanophosphor for up-conversion by polyol method. *Solid State Sciences* 117 (2021) 106626. doi: 10.1016/j.solidstatesciences.2021.106626
16. C. Artini. Crystal chemistry, stability and properties of interlanthanide perovskites: A review. *Journal of the European Ceramic Society* 37 (2017) 427–440. doi: 10.1016/j.jeurceramsoc.2016.08.041
17. Xiaoming Liu and Jun Lin. $LaGaO_3$:A (A = Sm^{3+} and/or Tb^{3+}) as promising phosphors for field emission displays. *Journal of Materials Chemistry* 18 (2008) 221–228. doi: 10.1039/b709929k
18. B. Jacquier, G. Boulon, G. Sallavuard, F. Gaume-Mahn. Bi^{3+} center in a lanthanum gallate phosphor. *Journal of Solid State Chemistry* 4 (1972) 374–378. doi: 10.1016/0022-4596(72)90152-1
19. Alok M. Srivastava. Luminescence of Bi^{3+} in $LaGaO_3$. *Materials Research Bulletin* 34 (1999) 1391–1396. doi: 10.1016/s0025-5408(99)00149-x
20. J. Schou. Physical aspects of the pulsed laser deposition technique: The stoichiometric transfer of material from target to film. *Applied Surface Science* 255 (2009) 5191–5198 doi: 10.1016/j.apsusc.2008.10.101
21. F. Xu, H. Zhang, F. Xie, Y. Liao, Y. Li, J. Li, L. Jin, Y. Yang, G. Gan, G. Wang, Q. Zhao. Investigation of grain boundary diffusion and grain growth of lithium zinc ferrites with low activation energy. *Journal of the American Ceramic Society* (2018) 1-9. doi: 10.1111/jace.15739
22. Rosendo López, Ricardo Gómez. Band-Gap Energy Estimation from Diffuse Reflectance Measurements on Sol-Gel and Commercial TiO_2: A Comparative Study. *Journal of Sol-Gel Science and Technology* 61 (2012) 1–7. doi: 10.1007/s10971-011-2582-9
23. Bingcheng Luo, Xiaohui Wang, Enke Tian, Hongzhou Song, Guowu Li, Longtu Li. Electronic, dielectric and optical properties of orthorhombic lanthanum gallate perovskite. *Journal of Alloys and Compounds* 708 (2017) 187-193. doi: 10.1016/j.jallcom.2017.02.267

24. Aman Pandey, Gunisha Jain, Divya Vyas, Silvia Irusta, Sudhanshu Sharma. Nonreducible, Basic La_2O_3 to Reducible, Acidic $La_{2-x}Sb_xO_3$ with Significant Oxygen Storage Capacity, Lower Band Gap, and Effect on the Catalytic Activity. *Journal of Physical Chemistry C* 121 (2017) 481–489. doi: 10.1021/acs.jpcc.6b10821
25. Preetam Singh, Indrani Choudhuri, Hari Mohan Rai, Vikash Mishra, Rajesh Kumar, Biswarup Pathak, Archna Sagdeo and P. R. Sagdeo. Fe doped $LaGaO_3$: good white light emitters. *RSC Advances* 6 (2016) 100230–100238. doi: 10.1039/c6ra21693e
26. Jian Xu, Daisuke Murata, Byoungjin So, Kazuki Asami, Jumpei Ueda, Jong Heob and Setsuhisa Tanabe. 1.2 lm persistent luminescence of Ho3+ in LaAlO3 and LaGaO3 perovskites. *Journal of Materials Chemistry C* 6 (2018) 11374–11383. doi: 10.1039/c8tc04393k
27. D.L. Dexter, James H. Schulman. Theory of Concentration Quenching in Inorganic Phosphors. *Journal of Chemical Physics* 22 (1954) 1063–1070. doi: 10.1063/1.1740265
28. R.M. Jafer, H.C. Swart, A. Yousif, Vinod Kumar, E. Coetsee. The Effect of Annealing Temperature on the Luminescence Properties of Y_2O_3 phosphor Powders doped with a High Concentration of Bi^{3+}. *Journal of Luminescence* 180 (2016) 198–203. doi: 10.1016/j.jlumin.2016.08.042
29. B.M. Jaffar, HC. Swart, H.A.A. Seed Ahmed, A. Yousif, R.E. Kroon. Luminescence properties of Bi doped La_2O_3 powder phosphor. *Journal of Luminescence* 209 (2019) 217–224. doi: 10.1016/j.jlumin.2019.01.044
30. Ch. Satya Kamal, T. K. Visweswara Rao, T. Samuel, P. V. S. S. S. N. Reddy, Jacek B. Jasinski, Y. Ramakrishna, M. C. Raoe and K. Ramachandra Rao. Blue to magenta tunable luminescence from $LaGaO_3$: Bi^{3+}, Cr^{3+} doped phosphors for field emission display applications. *RSC Advances* 7 (2017) 44915–44922. doi: 10.1039/C7RA08864G
31. Lili Wang, Qiang Sun, Qingzhi Liu, Jinsheng Shi. Investigation and Application of Quantitative Relationship between sp Energy Levels of Bi^{3+} ion and Host Lattice. *Journal of Solid State Chemistry* 191 (2012) 142–46. doi: 10.1016/j.jssc.2012.03.015
32. Philippe Boutinaud. Revisiting the Spectroscopy of the Bi^{3+} Ion in Oxide Compounds. *Inorganic Chemistry* 52 (2013) 6028–6038. doi: 10.1021/ic400382k
33. T. Samuel, C. Satya Kamal, S. Ravipati, B. P. Ajayi, V. Veeraiah, V. Sudarsan, K. Ramachandra Rao. High purity green photoluminescence emission from Tb^{3+}, Bi^{3+} co-doped

$LaGaO_3$ nanophosphors. *Optical Materials* 69 (2017) 230–237. doi: 10.1016/j.optmat.2017.04.037

34. Y. S. Katharria, S. Kumar, F. Singh, J. C. Pivin, D. Kanjilal. Synthesis of buried SiC using an energetic ion beam. *Journal of Physics D: Applied Physics* 39 (2006) 3969–3973. doi: 10.1088/0022-3727/39/18/007

35. D. Comedi, O. H. Y. Zalloum, E. A. Irving, J. Wojcik, T. Roschuk, M. J. Flynn, P. Mascher. X-ray-diffraction study of crystalline Si nanocluster formation in annealed silicon-rich silicon oxides. *Journal of Applied Physics* 99 (2006) 023518. doi: 10.1063/1.2162989

Chapter ten

Conclusions and future work

10.1. Summary of the results

The stability and luminescent properties of LaOX (X = Cl, Br and F) and $LaGaO_3$, $LaYO_3$ activated by Bi^{3+} have been successfully investigated as phosphor powders prepared by solid state reaction method and citric acid sol-gel combustion synthesis, respectively. Then LaOX (X = Cl, F) and $LaGaO_3$ doped Bi were investigated as thin films by using the PLD technique. The major aim of this research project is to study the effect of host anion or cation substitution on the luminescence and stability of lanthanum oxide (La_2O_3) based phosphors doped with bismuth (Bi).

The XRD data confirmed that both LaOCl and LaOBr phases belong to the tetragonal crystal structure. SEM images showed that the particles were aggregated and had irregular plate-like shapes. The reflectance spectra showed two absorption bands, located at 255 nm and 308 nm for LaOBr:Bi and 247 nm and 300 nm for LaOCl:Bi. The absorption bands at shorter wavelengths centred at around 255 nm and 247 nm correspond to the $^1S_0 \rightarrow {}^3P_1$ absorption of Bi^{3+} ions, while the longer wavelength absorption bands at around 308 nm and 300 nm may result from Bi-induced defects or Bi-clusters. The band gap energies were estimated to be 5.38 eV for LaOBr and 5.76 eV for LaOCl. The ultraviolet emission peaks were assigned to the $^3P_1 \rightarrow {}^1S_0$ transition of the Bi^{3+} ions, while additional relatively weak emissions in the visible range were attributed to Bi clustering. The PL emission intensity of LaOCl:Bi was about double that of LaOBr:Bi powder phosphor. LaOCl:Bi was found to be slightly unstable when exposed to the atmosphere for several months, while LaOBr:Bi was significantly less stable. The long term degradation was accompanied by a change in XRD patterns. The LaOBr:Bi phosphor was also found to degrade rapidly under 254 nm ultraviolet excitation, while LaOCl:Bi did not degrade under the same conditions. XPS data of the UV-exposed LaOCl:Bi and LaOBr:Bi showed an increase in the concentration of hydroxide on the surface of both the samples and broadening of the peaks associated with the anions. Since only the luminescence of the LaOBr:Bi degraded during UV-exposure, while the LaOCl:Bi did not, the similar changes in XPS results for both samples may indicate that the degradation is not due to a surface reaction, but may be due to non-radiative defects forming more easily in the bulk of LaOBr which has a smaller bandgap than LaOCl.

The X-ray diffraction data of LaOF confirmed that the phosphor powder crystallized in tetragonal and rhombohedral structures, depending on the annealing temperature. The EDS spectra confirmed that the ratios of the oxygen and fluorine changed by changing the annealing temperature. A broad white emission centred at 518 nm was observed when excited at 263 nm, which was attributed to the $^3P_1 \rightarrow {}^1S_0$ transition of Bi^{3+} ions. The emission intensity was measured as a function of Bi doping concentration, with the maximum occurring for x = 0.005. The LaOF:Bi phosphor powder was found to be degraded under 254 nm ultraviolet excitation, while it was found stable when exposed to the atmosphere for several months. XPS data confirmed that the annealing at 1100 °C and exposure of the sample to UV radiation result in segregation of the Bi^{3+} on the surface of the sample.

Bi doped LaOCl and LaOF phosphor thin films were successfully synthesized by the PLD technique. XRD data confirmed that both LaOCl and LaOF phases belong to the tetragonal crystal structure. The SEM images of LaOCl show that the particles had different spherical sizes for the film deposited in a vacuum. The films deposited in different Ar pressures had particles of different spherical sizes as well as flower-like shapes with platelets. The SEM images of LaOF show that the particles had spherical shape with distinct sizes. The LaOF films consisted of much less material than for the corresponding films of LaOCl. The EDS spectra of the films are similar to the powder. Photoluminescence measurements revealed that the films exhibited emission around 344 nm for LaOCl:Bi and 518 nm for LaOF:Bi under excitations of 266 nm and 263 nm, respectively. These excitation and emission peaks have been attributed to the transitions between the $^3P_1$ excited state and $^1S_0$ ground state of the Bi^{3+} ions. For both powder and films, the luminescence from the LaOF:Bi samples was less intense compared to the corresponding LaOCl:Bi samples.

$La_{2-y}Y_yO_3$ was successfully synthesized via the citric acid sol-gel combustion method. Material with composition $La_{0.5}Y_{1.5}O_3$ was single phase with cubic crystal structure and was stable after being exposed to the atmosphere for four months. SEM images showed that the shape of particles

changed from cubic to more round when Bi was doped in host structure. The PL of $La_{0.5-x}Y_{1.5}O_3:Bi_x$ excited at 333 nm consisted of a broad emission from 350 nm to 800 nm that consisted out of two peaks centred at 424 nm and 529 nm which has a maximum intensity for x = 0.005. This emission was attributed to Bi^{3+} ions in C_2 sites of the host. Bi^{3+} also occupied the S_6 sites for which blue emission at 424 nm was obtained for excitation at 371 nm. Although the luminescence from the $La_{0.5-x}Y_{1.5}O_3:Bi_{x=0.005}$ sample was less intense compared to $Y_{2-x}O_3:Bi_{x=0.005}$, there was a significant colour shift and the emission from Bi^{3+} ions at the S_6 site was close to that emitted by unstable La_2O_3:Bi.

Bi doped $LaGaO_3$ was successfully synthesized by the citric acid sol-gel combustion synthesis. XRD data confirmed that the structure of $LaGaO_3$ belonged to the orthorhombic crystal structure. SEM images showed that the grain size increased with increasing annealing temperature. The diffuse reflectance spectra for the doped sample showed three absorption bands centred at around 210 nm, 250 nm and 310 nm. The absorption band centred at 210 nm was also observed for the undoped sample and was attributed to absorption above the band gap. The absorption bands centred at 250 nm and 310 nm were only present in the doped samples and was therefore attributed to absorption by Bi^{3+} ions. From reflectance data of the pure host material the band gap of $LaGaO_3$ was found to be 4.65 eV. A broad UV emission centred at 370 nm was observed when excited at 305 nm, which was attributed to the $^3P_1 \rightarrow {}^1S_0$ transition of Bi^{3+} ions. The emission intensity was measured as a function of Bi doping concentration, with the maximum occurring for x = 0.003. The shift in the wavelength position of the peak maxima between the PL and CL from 370 nm to 374 nm was attributed to the different mechanisms for the excitation.

10.2. Suggestions for future work

1. Trying to solve the problem of the hygroscopic nature of the La_2O_3 by preparing La_2O_3:Bi thin films by using sol-gel spin-coated and PLD and making a layer of PMMA polymer on their surfaces and then comparing their luminescence stability to La_2O_3:Bi.
2. Encapsulating the La_2O_3 in a polymer for applications, thereby shielding it from the atmosphere.
3. Studying the energy transfer between the Bi and other rare earth ions e.g. Yb, Eu in the LaOX (X=Cl, Br, and F) and $LaGaO_3$, $LaYO_3$ and $LaGdO_3$ hosts.

4. Preparing LaGaOCl and LaGaOF doped with Bi powders by using solid state reaction method and comparing the results with the LaOCl, LaOF and $LaGaO_3$ powders in this work.
5. Preparing $LaYO_3$ and LaOBr doped with Bi thin films by using sol-gel spin-coated and PLD and comparing the results with the powders results.
6. Preparing LaOX (X=Cl, F) and $LaGaO_3$ and $LaGdO_3$ doped Bi thin films by using sol-gel spin-coated and comparing the results with the PLD thin films in this work.
7. Preparing $La_2O_2S_2$ host doped with the Bi and comparing the results with LaOX (X=Cl, Br and F) hosts.
8. Alloying other oxide hosts such as Sc_2O_3 and Nd_2O_3 with La_2O_3 and doped with Bi and comparing the results with $LaGaO_3$, $LaYO_3$, and $LaGdO_3$ host.
9. To characterize the phosphors produced during this work using thermoluminescence.

10.3. Publications

1. Babiker. M. Jaffar, H. C. Swart, H.A.A. Seed Ahmed, A. Yousif, R.E. Kroon. *Comparative study of the photoluminescence and cathodoluminescence of Bi doped LaOCl and LaOBr phosphor powders*. Submitted to Journal of Luminescence.
2. Babiker. M. Jaffar, H. C. Swart, H.A.A. Seed Ahmed, A. Yousif, R.E. Kroon. *Luminescence properties of Bi doped LaOF phosphor powder*. Submitted to Optical Materials.
3. Babiker. M. Jaffar, H. C. Swart, H.A.A. Seed Ahmed, A. Yousif, R.E. Kroon. *Bi doped LaOCl and LaOF thin films grown by pulsed laser deposition*. Submitted to Journal of Luminescence.
4. Babiker. M. Jaffar, H. C. Swart, H.A.A. Seed Ahmed, A. Yousif, R.E. Kroon. *Stability and photoluminescence of Bi doped $(La,Y)_2O_3$ phosphor powders*. Submitted to Optical Materials.
5. Babiker. M. Jaffar, H. C. Swart, H.A.A. Seed Ahmed, A. Yousif, R.E. Kroon. *Alloying Bi doped La_2O_3 and Ga_2O_3 for stable phosphor powder and pulsed laser deposited thin films*. Submitted to Journal of Luminescence.